Radio Science Bulletin

ISSN 1024-4530

INTERNATIONAL
UNION OF
RADIO SCIENCE

UNION
RADIO-SCIENTIFIQUE
INTERNATIONALE

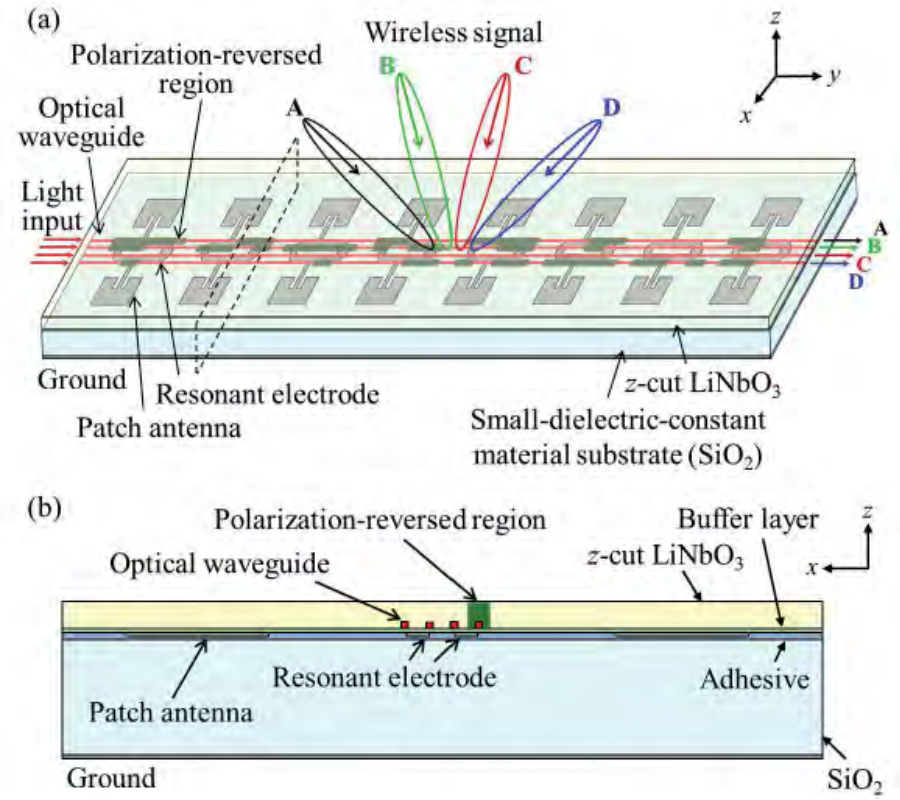

No 349
June 2014

URSI, c/o Ghent University (INTEC)
St.-Pietersnieuwstraat 41, B-9000 Gent (Belgium)

Contents

Front cover. The basic structure of the proposed device (a) a whole view of the device, (b) a cross-sectional view of the device in the xz plane. See the paper by Naohiro Kohmu et al. on pp. 32-39.

Editor-in-Chief
URSI Secretary General
Paul Lagasse
Dept. of Information Technology
Ghent University
St. Pietersnieuwstraat 41
B-9000 Gent
Belgium
Tel.: (32) 9-264 33 20
Fax : (32) 9-264 42 88
E-mail: ursi@intec.ugent.be

Editor
W. Ross Stone
840 Armada Terrace
San Diego, CA92106
USA
Tel: +1 (619) 222-1915
Fax: +1 (619) 222-1606
E-mail: r.stone@ieee.org

For information, please contact :
The URSI Secretariat
c/o Ghent University (INTEC)
Sint-Pietersnieuwstraat 41, B-9000 Gent, Belgium
Tel.: (32) 9-264 33 20, Fax: (32) 9-264 42 88
E-mail: info@ursi.org
http://www.ursi.org

Editorial

Special Section on AP-RASC 2013 Student Paper Competition

The 2013 Asia-Pacific Radio Science Conference (AP-RASC 2013) was held in Taipei, Taiwan, during September 3-7, 2013. This issue contains four papers from the winners of that competition. The Guest Editors have provided a separate introduction to the special section, so I won't repeat that information here. I commend these papers to you: they are most interesting, and cover a fascinating array of radio science topics.

Our Other Papers

Yoshiharu Omura will be presenting the Commission H tutorial lecture at the XXXIth URSI General Assembly and Scientific Symposium in Beijing. He has provided us with an invited paper based on that tutorial lecture. The topic is the state of our current understanding of nonlinear wave-particle interactions in planetary radiation belts. Such interactions generate the whistler-mode chorus emissions and electromagnetic ion-cyclotron-triggered emissions that have been observed in recent years. The paper begins with a review of the basic dynamics of resonant electrons interacting with a whistler-mode wave. The growth in the wave due to the frequency-sweep rate at the equator is explained. The paper uses both experimental observations and a new set of computer simulations that have been successful in reproducing chorus emissions. The simulation of emissions triggered by the whistler mode in the magnetosphere when a triggering wave is injected at the equator is described. It is shown that there is an optimum wave amplitude for triggering emissions. The balance of the paper provides a detailed and quite readily understandable look at the various properties of such emissions, and the phenomena that accompany them. The combination of new simulations and observed data nicely serve to illuminate the underlying mechanisms. This is a particularly fine tutorial, which includes some of the most recent results on phenomena that should be present in the radiation belts of planets with magnetic fields.

C. J. Rodger, M. A. Clilverd, W. Li, M. P. McCarthy, Y. Omura, and C. E. Weaver have provided us with a paper intended to stimulate interest in two Commission H sessions at the URSI GASS in Beijing. The paper deals with energetic electron precipitation from the Van Allen radiation belts around the Earth. The paper begins with a review of the phenomena associated with such precipitation, and why it is of considerable practical interest, particularly because of effects on Earth-orbiting satellites. This is followed by a review of wave-particle interactions, particularly as they relate to the transport of energetic electrons by waves in and out of the Van Allen radiation belts. A review of recent observations of electron precipitation is then given. This is followed by a review of recent advances in the theory of such precipitation. One of the potentially important causes of electron precipitation is the resonant interaction of electromagnetic ion-cyclotron waves with certain populations of electrons, causing pitch-angle scattering of the electrons into the Earth's atmosphere. Recent observations of this are reviewed. The use of low-energy precipitation as a proxy for whistler-mode waves is discussed. Finally, the effects of electron precipitation on the chemical constituents of the atmosphere are explained. This paper provides a nice introduction to the topic of electron precipitation, and a very nice background for the related sessions at the GASS.

Our Other Contributions

Kristian Schlegel has brought us another book review, of a book on reconfigurable antennas. Kristian has informed me that he plans to retire from part of the book review column after the Beijing GASS, continuing only with the Young Scientist reviews for the future. His contributions to the *Radio Science Bulletin* have been greatly appreciated, and I'm glad that he will continue to still be involved.

This issue contains the triennial reports from URSI Commissions A, B, D, F, and H. These provide an overview of what the Commissions have been doing throughout the past three years.

We have reports on a couple of URSI-sponsored conferences, and, sadly, an in memoriam article on Karl Langenberg, who recently passed away. We also have an article on the recipient of the 2014 URSI France medal.

As I write this, the XXXIth URSI General Assembly and Scientific Symposium in Beijing is only a couple of weeks away. I hope to see you there!

In Memoriam

Karl Langenberg
1942 - 2014

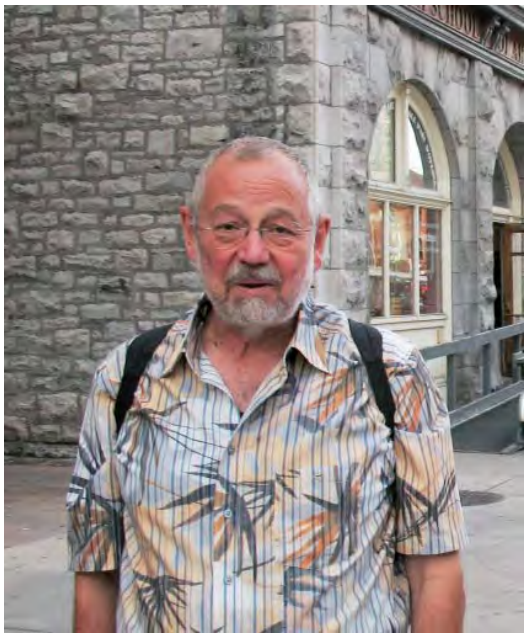

Our dear friend and colleague, Karl J. Langenberg, passed away on May 22, 2014, at the age of 72, after a short battle with cancer. With Karl, we lost a truly international scientific leader in elastodynamic and electromagnetic wave theory, well-known and highly regarded in our scientific community. We will deeply miss him.

Karl Langenberg was born on May 29, 1942, in Augsburg/ Bavaria, Germany. After the war, where he lost his father, his mother moved to Saarbrucken, near the French border. There, he visited the Otto-Hahn-Gymnasium (high school), until his Abitur (high school diploma) in 1961. Karl studied physics at the Saarland University, Germany, and graduated in 1968 as a Diplom-Physiker, with a thesis on electromagnetic wave propagation in one-dimensional inhomogeneous media. He then joined the Institute for Applied Physics and High-Frequency Techniques at Saarland University (Director: Prof. Dr. G. Eckart), where he did research in electromagnetic field theory, particularly, antenna theory and propagation of transient electromagnetic waves in inhomogeneous environments. In 1972, he achieved the PhD (summa cum laude) with a thesis on the transient electromagnetic pulse propagation in a dielectric layer. For his "outstanding dissertation" he received the Prize of the VDE/ ITG in 1975.

Until 1979, he was an Assistant Professor of Electromagnetic Theory at Saarland University. His areas of research and teaching were in electromagnetics and mathematical physics, particularly antenna theory, numerical methods, Fourier transforms and applications, and scattering and diffraction of electromagnetic waves by canonical objects. In 1979, he received the Habilitation degree, with a thesis on transient fields of linear antenna arrays, and the *Venia Legendi* for Electromagnetic Theory. In 1979/80, Karl became Lecturer (Privatdozent) for Electromagnetic Theory at Saarland University, and from 1980 until 1982 he was with the Fraunhofer Institute for Nondestructive Testing in Saarbrücken as a principal scientist. From 1983 until his retirement in 2007, he was Full Professor of Electromagnetic Theory at Kassel University, Germany. His areas of research included the theory of electromagnetic fields, numerical methods, remote sensing, inverse scattering, acousto-elastic wave propagation and scattering, and antenna theory. In 1987, he served as Dean of the Department of Electrical Engineering at Kassel University. In the same year, he neglected an offer of a full professorship at the University of the German Armed Forces, Hamburg, Germany.

Because of his outstanding technical and personal skills, Karl Langenberg was an internationally popular and sought-after lecturer. He served for the AGARD Lecture Series on "Target Classification and Identification" in Italy, Germany, and Norway; directed several workshops on "Inverse Problems in Electromagnetism" in France; and was lecturer of the Ultrasonics International '97 Tutorial on "Ultrasonic Inverse Problems," Delft/Netherlands; and of the CISM course on "Evaluation of Materials and Structures by Quantitative Ultrasonics," Udine/Italy. In 1991, he was Visiting Scientist of the Department of Electrical Engineering at the University of Arizona, Tucson/ Arizona, and of the Department of Electrical Engineering at the Worcester Polytechnic Institute, Worcester/Massachusetts.

Karl Langenberg was an active member of the German Society for Non-Destructive Evaluation (*Deutsche Gesellschaft für zerstörungsfreie Prüfung – DGZfP*), where he served as Chair of the Section on "Theoretical Models in Ultrasonics" since 1990. Many of his (about 250 referred) scientific contributions, including the most recent monograph on *Ultrasonic Nondestructive Testing of Materials: Theoretical Foundations* (by K.-J. Langenberg, R. Marklein, and K. Mayer, Boca Raton, CRC Press, 2012) are in the area of nondestructive evaluation with ultrasonic waves.

Karl was also an outstandingly engaged member of the International Union of Radio Science (URSI). In 1975, he was elected a member of the German Commission F, "Waves in Nonionized Media," but moved to Commission B, "Fields and Waves," in 1981. From 1987 to 1990, he

served as Chair of the German Commission B. In 1992, he was elected Vice Chair, and served from 1999 until 2007 as Chair, of URSI in Germany. In 2001, he also became a member of "B-TAB:" the Technical Advisory Board for International URSI Commission B. In 2007, he convened a session in memory of the late Donald G. Dudley, to be held during the URSI Commission B International Symposium in Ottawa/Canada. From 2005 to 2008, he was elected Vice Chair, and from 2008 to 2011, Chair of URSI International Commission B. Since then, he was active as its past Chair. In 2010, he was Chair of the URSI International Symposium on Electromagnetic Theory (EMT-S) in Berlin, Germany.

Karl Langenberg was a Life Fellow of the IEEE, a member of the German VDE, and a member of many editorial boards, including *Wave Motion* (1989-2006), *Ultrasonics* (since 1995), *Applied Computational Electromagnetics* (since 1992), *Inverse Problems* (1989-1992), *IEEE Transactions on Antennas and Propagation* (1998-2004), *Inverse Problems in Science and Engineering* (since 2004), and *Radio Science* (since 2010). He was also founder and Editor of the *Advances of Radio-Science – Kleinheubacher Berichte* (www.copernicus.org/URSI/ars) until 2007.

Besides his many merits in international scientific work and leadership, Karl was very much what could be called a Cosmopolitan. Together with his wife, Ursula, he loved to travel: to see foreign countries, to socialize with people, and to learn from different cultures. Beginning in the 1980s, he also perfectly organized several Jeep trips for a group of six electromagnetics colleagues to deserts and national parks in Australia, America, and southern Africa. The last one in that series was at the end of March 2014 to Namibia – just a couple of weeks before he had to start his final journey.

Karl's attitude toward life couldn't be much better summarized than by the following poem, which also appeared on the black-edged letter by his family:

You, fortunate eyes,
All you've seen, there,
Let it be as it may,
Yet it was so fair!

(J. W. von Goethe, *Faust II*)

Acknowledgement

The authors are grateful to Dr. Klaus Mayer (Kassel University, Germany) for providing Karl's detailed CV.

Thomas Weiland and Ludger Klinkenbusch
E-mail: thomas@weiland-web.de; lbk@tf.uni-kiel.de

Guest Editors' Introduction to Special Section on AP-RASC 2013 Student Paper Competition

The 2013 Asia-Pacific Radio Science Conference (AP-RASC 2013) was successfully held in Taipei, Taiwan, during the period September 3-7, 2013. For details on the organization, structure, agenda, technical and special programs, and the statistics of the Conference, please refer to [1]. This special section of the *Radio Science Bulletin* publishes four papers from the specialists who were selected from 19 student papers submitted to the Student Paper Competition (SPC) program. All of the submitted papers were peer-reviewed by at least two referees, endorsed by the Official Members of the China (SRS) National Committee of URSI. Five student paper finalists were selected by the Student Paper Competition Committee, and were invited to submit their full papers to the special section in the URSI *Radio Science Bulletin*. The submitted papers were evaluated again in accordance with the publication policy of the *Radio Science Bulletin*, and four of them were accepted for publication in the special section.

The topics of the published papers in this special section are very diverse. The paper authored by Lee et al. discusses wave generation via the cyclotron maser instability by an electron ring distribution, and the associated electron acceleration by the excited Z-mode and whistler-mode waves. The paper by Cheng et al. focuses on the problem of physical layer authentication, aimed at assuring that the current transmission comes from the same entity as the previous transmission. Kohmu et al.'s paper presents a new design for an electro-optic modulator, utilizing an antenna-coupled-electrode array and polarization-reversed structures to achieve higher efficiency in optical modulation. The paper by Wang et al. proposes a numerical homogenization method to extract equivalent electromagnetic parameters of ferromagnetic nanowires. From these exceedingly high-quality student papers, we truly believe that with promising and outstanding young scientists continuously joining the URSI community, the URSI mission of "encouraging and promoting international activity in radio science and its applications, for the benefit of the mankind" can be achieved.

Finally, we would like to extend our sincere gratitude to the many reviewers for their great help in selecting and reviewing the student papers published in this special section.

Reference

L. C. Lee, R. B. Wu, H. C. Chang, T. L. Wu, and K. Kobayashi, "Report on the 2013 Asia-Pacific Radio Science Conference (AP-RASC 2013)," *Radio Science Bulletin*, 348, March 2014, pp. 73-80.

Guest Editors:

Yen-Hsyang Chu, National Central University, Institute of Space Science, Chung-Li, Taiwan; e-mail: yhchu@jupiter.ss.ncu.edu.tw

Ping-Cheng Yeh, National Taiwan University, Department of Electrical and Engineering, Taipei, Taiwan; e-mail: pcyeh@ntu.edu.tw

Electron Acceleration and Diffusion of Ring Distribution by Z-Mode and Whistler-Mode Waves

K.H. Lee[1], Y. Omura[2] and L.C. Lee[3]

[1, 3] Institute of Space Science, National Central University, Zhongli, Taiwan
E-mail: myonezillion@gmail.com; louclee@earth.sinica.edu.tw
[2] Research Institute for Sustainable Humanosphere,
Kyoto University, Uji, Kyoto, Japan
E-mail: omura@rish.kyoto-u.ac.jp
[3] the Institute of Earth Science, Academia Sinica, Nankang, Taiwan

This paper is the invited Second Prize winner from the AP-RASC 2013 Student Paper Competition.

Abstract

In this paper, we present a brief review of wave generation via the cyclotron maser instability by an electron ring distribution, and the associated electron acceleration by the excited Z-mode and whistler-mode waves. The electron ring distribution can excite X-mode waves mainly in the perpendicular direction, Z-mode waves in the perpendicular and parallel directions, and whistler-mode waves in the parallel direction. For parallel propagation, the Z-mode or the whistler-mode waves dominate, depending on the ratio of the electron-plasma to the electron-cyclotron frequencies. These parallel waves can in turn efficiently accelerate the energetic ring electrons. For an initial kinetic energy ranging from 100 keV to 500 keV, the peak energy of the accelerated electrons can reach two to eight times the initial kinetic energy. The acceleration process was then studied via test-particle calculations, in which electrons interacted with one single wave, two counter-propagating waves, or four counter-propagating waves. The efficient acceleration occurred in the multi-wave cases due to simultaneous acceleration of electrons by counter-propagating waves.

1. Introduction

The cyclotron maser instability (CMI) is an important mechanism for radio emissions in plasma physics and astrophysics. Wu and Lee [1] and Lee and Wu [2] proposed the cyclotron maser instability as the radiation mechanism for non-thermal radio emissions from planets, such as the auroral kilometric radiation (AKR). They predicted the growth of X and O modes. The key ingredients for the cyclotron maser instability are (a) the relativistic effect in the resonance condition, and (b) a population-inversion distribution providing free energy. The relativistic resonance condition yields an ellipse or hyperbola in the particle-momentum space, rather than a straight line with constant parallel momentum. A population inversion requires a positive gradient along the perpendicular momentum in the distribution function. For these characteristics, there are various kinds of distributions that can support the cyclotron maser instability, such as loss-cone [1-3], ring-beam [4-18], and horseshoe distributions [19, 20].

The cyclotron maser instability, driven by an electron ring-beam distribution, drew much attention, and has been widely studied [4-18]. Such a distribution can be formed in quasi-perpendicular shocks via magnetic-mirror reflection, as proposed by Wu [12] and Leroy and Mangeney [13]. Wu et al. [14] and Yoon et al. [15] studied the cyclotron maser instability under the assumption of a ring-beam distribution formed by a mirror reflection of an injection of a plasma beam, accelerated by magnetic reconnection in the low corona. Kainer et al. [16] and Lee et al. [17, 18] studied the ring-beam cyclotron maser instability via one-dimensional and two-dimensional simulations, with $\omega_{pe}/\Omega_{ce} \gg 1$ and $\omega_{pe}/\Omega_{ce} < 1$, respectively, where ω_{pe} is the electron plasma frequency, and Ω_{ce} is the electron cyclotron frequency. The ratio ω_{pe}/Ω_{ce} is an important parameter for the cyclotron maser instability, and is usually much less than unity for strong wave emission by the cyclotron maser instability [2, 21].

In our simulation study [22, 23], we further found a strong acceleration of energetic electrons in the case with

a pure ring distribution. The electron ring distribution is a special case of ring-beam distributions. In such cases, the average parallel momentum is zero, and the average pitch angle is 90° with respect to the ambient magnetic field. We carried out a series of particle simulations in which a population of tenuous energetic electrons with a ring distribution was present in a magnetized background plasma. Through the cyclotron maser process, the electron ring distribution excited the X-mode waves, mainly in the perpendicular direction, Z-mode waves in the perpendicular and the parallel directions, and whistler-mode waves in the parallel direction. The parallel Z-mode and whistler-mode waves could further lead to a strong acceleration and diffusion of the energetic ring electrons. The acceleration process was then studied via test-particle calculations. The strong acceleration is related to electron resonant trapping by waves, and wave phase velocity, amplitude, and frequency play important roles. In this paper, the wave generation via the cyclotron maser instability by an electron ring distribution [17, 18], and the associated electron acceleration by the excited Z-mode and whistler-mode waves [22, 23], are briefly reviewed.

2. Simulation Setup

The one-dimensional and two-dimensional electromagnetic particle-in-cell simulation codes were modified from *KEMPO1* [24, 25]. The one-dimensional and two-dimensional simulation boxes were in the *x-y* plane and along the *x* axis, respectively, with periodic boundaries. A constant ambient magnetic field, $\mathbf{B_0} = B_0\hat{x}$, was applied for the two-dimensional case, and $\mathbf{B}_0 = B_0\cos\theta_B\hat{x} + B_0\sin\theta_B\hat{y}$ with $\mathbf{k} \parallel \hat{x}$ was used for the one-dimensional case, where θ_B is the angle between $\mathbf{B}_0$ and $\mathbf{k}$, and $\mathbf{k}$ is a wave vector. In the initial condition, all particles were uniformly distributed in the simulation box. A background electric field was provided for quasi-neutrality by the cold and immobile protons. Electron distributions were studied in the momentum space rather than in the non-relativistic velocity space, and the term "momentum" shall refer to "momentum per unit mass" or "relativistic velocity $\mathbf{u}$."

A ring-beam distribution function in the cylindrical coordinates can be expressed as

$$f_{rb} = n_{rb}a_{rb}\exp\left[-\frac{\left(u_\perp - u_{d\perp}\right)^2 + \left(u_\parallel - u_{d\parallel}\right)^2}{2\left(\Delta u\right)^2}\right], \quad (1)$$

where $u_\perp$ and $u_\parallel$ are the momentum components perpendicular and parallel to $\mathbf{B_0}$, respectively; $u_{d\perp}$ and $u_{d\parallel}$ are the ring-beam momenta perpendicular and parallel to $\mathbf{B_0}$, respectively; Δu is a momentum dispersion of a ring-beam distribution; and a_{rb} is a normalization constant. The density of a ring-beam distribution n_{rb} is taken to be

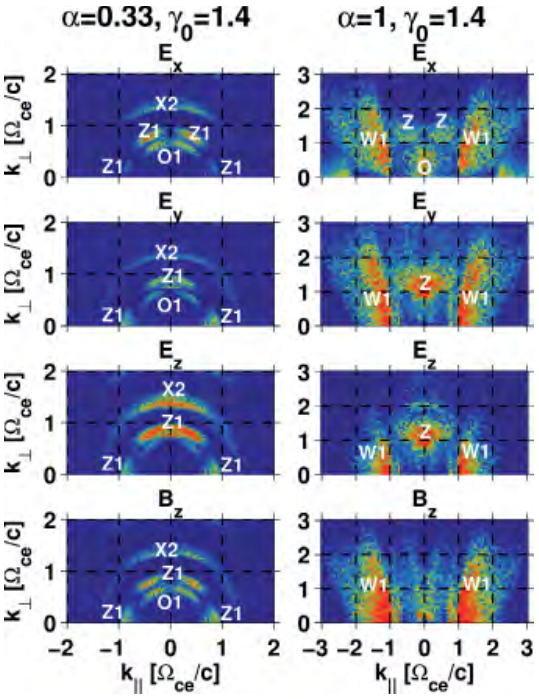

Figure 1. The maximum value of (by rows, top to bottom) (a) the E_x wave amplitude, (b) the E_y wave amplitude, (c) the E_z wave amplitude, and (d) the B_z wave amplitude in the ω domain as a function of $k_\perp$ and $k_\parallel$ for the cases of $\alpha = 1$ and $\alpha = 0.33$, and $\gamma_0 = 1.4$. For $\alpha = 0.33$ the Z mode dominated, and the X mode was subdominant. For $\alpha = 1$, the whistler mode dominated. The Z- and whistler-mode waves with parallel propagation could further accelerate the energetic ring electrons.

5% of the total electron density. The background electrons were assumed to possess a Maxwellian distribution with a thermal momentum $\Delta u = 0.05c$, and the momentum dispersion of a ring-beam distribution was $\Delta u = 0.025c$, where c is the speed of light. The average pitch angle of a ring-beam distribution is defined as $\phi_p = \tan^{-1}\left(u_{d\perp}/u_{d\parallel}\right)$. In the simulations, the primary parameters used were (1) the ratio of electron plasma (ω_{pe}) to cyclotron (Ω_{ce}) frequencies, $\alpha \equiv \omega_{pe}/\Omega_{ce}$; and (2) the average initial kinetic energy, $\varepsilon_0 \equiv \left(\gamma_0 - 1\right)m_e c^2 =$ 100 keV, 200 keV, and 500 keV, corresponding to an initial Lorentz factor of $\gamma_0 \equiv \sqrt{1 + u_{d\perp}^2/c^2 + u_{d\parallel}^2/c^2} = 1.2, 1.4,$ and 2, respectively, where m_e is the electron rest mass.

3. Wave Generation

In the presence of a ring-beam plasma, the beam component can lead to the two-stream or beam instability, and the ring component can trigger the cyclotron maser instability. Lee et al. [18] studied wave generation associated with the cyclotron maser instability for various ring-beam pitch angles, $\phi_p = 15° \sim 90°$. Here, we present the cases with $\phi_p = 90°$, i.e., the pure ring case. In Figure 1, the wave spectra in $k_\perp - k_\parallel$ space showed an overall wave excitation with an arbitrary propagation angle. The diagrams showed

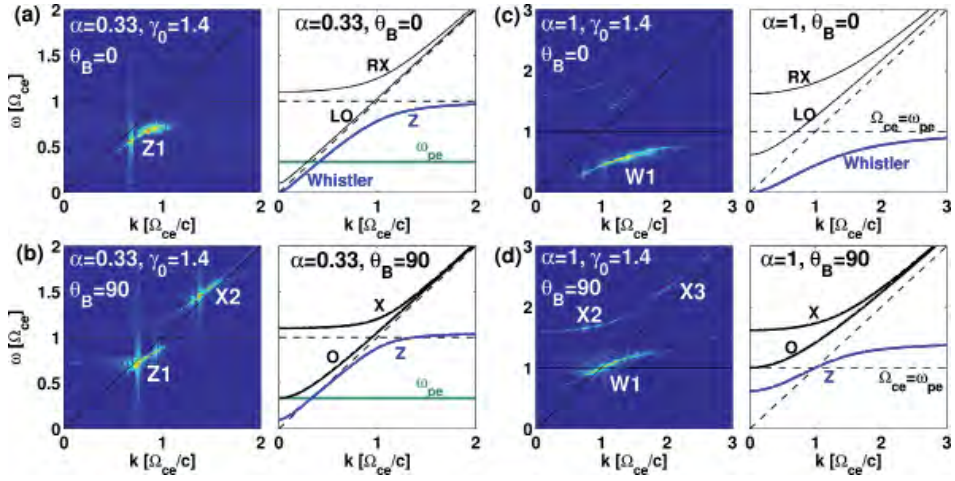

Figure 2. The wave-dispersion diagrams for $\alpha = 0.33$ (left panels) and $\alpha = 1$ (right panels) of two-dimensional simulations with $\theta_B = 0°$ (top panels) and $\theta_B = 90°$ (bottom panels).

the maximum values of E_x, E_y, E_z, and B_z wave intensity in the ω domain as a function of $k_\perp$ and $k_\parallel$, where E_x is the electric component parallel to $\mathbf{B_0}$; B_z and E_z are purely transverse components. The corresponding $\omega - k$ dispersion diagrams with $\theta_B = 0°$ and 90° are shown in Figure 2, and the theoretical cold plasma dispersion relation is also plotted for comparison.

In Figure 1, for $\alpha = 0.33$, the electron ring distribution excited the Z-mode waves in the perpendicular and parallel directions, and the X-mode waves mainly in the perpendicular direction. The Z-mode waves were excited at the first harmonic (Z1), as shown in Figures 2a and 2b. The perpendicular X-mode waves were excited at the second harmonic, as shown in Figure 2b. In Figure 1, for $\alpha = 1$, the whistler-mode waves with parallel and quasi-parallel propagations dominated, and the perpendicular Z-mode waves were subdominant. The parallel whistler-mode waves could be identified in the wave-dispersion diagrams in Figure 2c. The perpendicular Z- and X-mode waves could be identified in Figure 2d. The X-mode waves were too weak, and could only be identified in the wave-dispersion diagrams in Figure 2d. It should be noted that the wave-dispersion diagrams in the pure ring cases were symmetric with respect to the ω axis in Figure 2, and only the right-half part (forward propagation with respect to the ambient magnetic field) of the dispersion diagrams is shown.

4. Electron Acceleration in Simulations

In the cases of an electron pure ring distribution, the simulation results showed a strong acceleration of energetic electrons [22, 23]. The acceleration process was dominated

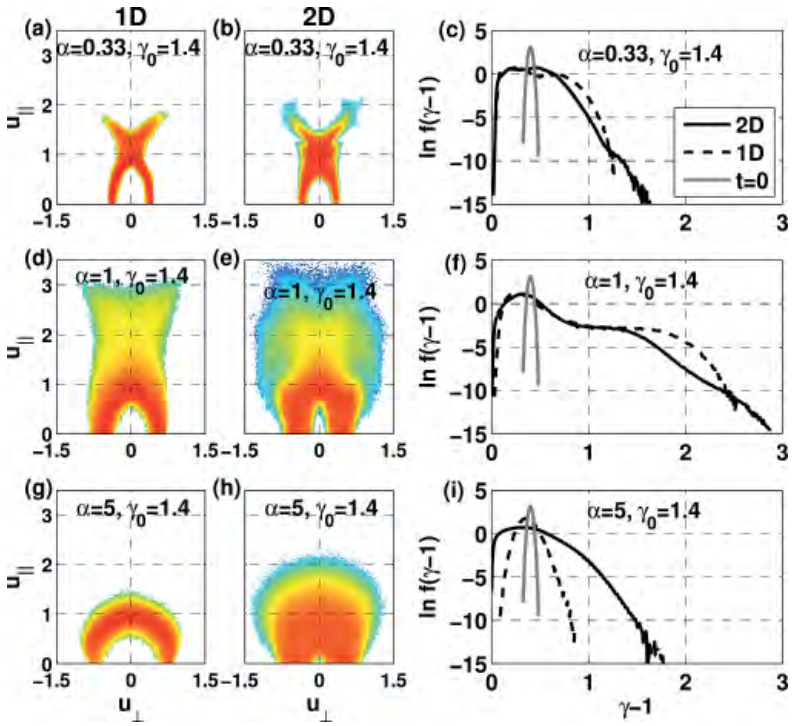

Figure 3. The energetic electron distributions in the $u_\perp - u_\parallel$ momentum space and as functions of $(\gamma - 1)$ after the wave-energy saturation for the one-dimensional and two-dimensional simulations, with $\alpha = 0.33$, $\alpha = 1$, and $\alpha = 5$, and $\gamma_0 = 1.4$.

ε_0 / α	100keV	200keV	500keV
$\alpha = 0.33$	400keV (350keV)	600keV (800keV)	1300keV (1600keV)
$\alpha = 1.0$	800keV (850keV)	1250keV (1400keV)	2750keV (3100keV)
$\alpha = 5.0$	200keV (400keV)	400keV (800keV)	1000keV (2000keV)

Table 1 Peak kinetic energies of accelerated electrons in one-dimensional (2D) simulations as a function of $\alpha = \omega_{pe}/\Omega_{ce}$ and the initial kinetic energy ε_0 [Adapted from K.H. Lee et al., Phys. Plasmas, 2013].

by the Z-mode and whistler-mode waves propagating in the parallel direction ($\theta_B = 0°$).

Figure 3 shows the energetic electron distributions after saturation of the wave energy in the one-dimensional and two-dimensional simulations. Note that the assumption of parallel propagation ($\theta_B = 0°$) was used in the one-dimensional simulations. In the simulations, the initial electron ring distribution evolved into the following three types of electron distributions:

(1) Sharp X-like distribution: The sharp X-like distribution was found in the cases with $\alpha = 0.33$. The patterns of the distributions were similar in both the one-dimensional and two-dimensional cases. Electrons were accelerated in both the parallel and perpendicular directions, and the peak kinetic energy could reach three to four times the initial kinetic energy, as shown in Figure 3c.

(2) Diffusive X-like distribution with a long "neck:" The strongest acceleration occurred in the cases with $\alpha = 1$. The X-like pattern was not discernible, compared with the cases of $\alpha = 0.33$. Electrons were mainly accelerated in the perpendicular direction, and the electron distribution showed a long "neck" in the perpendicular direction. In the two-dimensional case, waves with oblique and perpendicular propagations could be excited, leading to a more-diffusive pattern of the electron distribution. The peak kinetic energy of the accelerated electrons could reach five to six times the initial kinetic energy, as shown in Figure 3b.

(3) Shell-like distribution with little energy variation: The shell-like distribution was found in the cases of $\alpha = 5$ Electrons underwent pitch-angle scattering with little kinetic energy variation. The shell-like distribution could then trigger the cyclotron maser instability for wave excitation in the perpendicular and oblique directions in the two-dimensional simulation, leading to a more-diffusive pattern of the electron distribution.

Table 1 shows the peak kinetic energies of the accelerated electrons in one-dimensional (two-dimensional) simulations as a function of $\alpha = \omega_{pe}/\Omega_{ce}$ and the initial kinetic energy, ε_0. The maximum ratio of the peak to the initial kinetic energies was 8 (8.5), and occurred in the case of $\alpha = 1$ and $\varepsilon_0 = 100$ keV. The maximum energy gain was 2250 keV (2600 keV), and occurred in the case of $\alpha = 1$ and $\varepsilon_0 = 500$ keV.

5. Test-Particle Calculations

The test-particle calculations could be used to further analyze the acceleration process. For an electron interacting with a forward and a backward wave propagating along the ambient magnetic field, the equation of electron motion is

$$m_e \frac{d(\gamma \mathbf{v})}{dt} = -e\left[\mathbf{E}_f + \mathbf{E}_b + \mathbf{v}\times\left(\mathbf{B}_0 + \mathbf{B}_f + \mathbf{B}_b\right)\right] \quad (2)$$

where $\mathbf{B}_{f,b} = \mathbf{k}\times\mathbf{E}_{f,b}/\omega$, with $\mathbf{k} \| \mathbf{B}_0$ and $\mathbf{E}_{f,b} \perp \mathbf{B}_0$; $-e$ is electron charge, and the subscripts f and b respectively indicate forward and backward wave propagation with respect to $\mathbf{B}_0$. Let ϕ be the gyration angle of $\mathbf{v}_\perp$, $\psi_{f,b}$ be the gyration angle of $\mathbf{B}_{f,b}$, and $\zeta_{f,b} \equiv \phi - \psi_{f,b}$ be the gyration angle between $\mathbf{v}_\perp$ and $\mathbf{B}_{f,b}$, as illustrated in Figure 4. One can obtain the time derivative of relativistic parallel velocity,

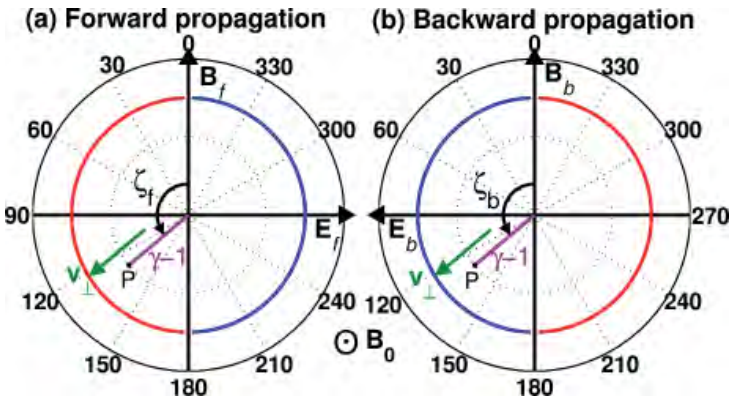

Figure 4 An illustration of the wave fields with forward (f) and backward (b) propagation acting on an electron in the $(\gamma-1, \zeta)$ polar coordinates of the magnetic/electric field frame. The subscripts f and b respectively indicate forward and backward wave propagation with respect to $\mathbf{B}_0$. $\mathbf{E}_f$ and $\mathbf{E}_b$ are wave electric fields; $\mathbf{B}_f$ and $\mathbf{B}_b$ are wave magnetic fields. Electron P had a kinetic energy of $(\gamma-1)m_e c^2$, and its $\mathbf{v}_\perp$ made an angle ζ with the wave's magnetic field. The red and blue curves correspond to the acceleration ($d\gamma/dt > 0$) and deceleration phases ($d\gamma/dt < 0$), respectively [adapted from K. H. Lee et al., *Phys. Plasmas*, 2012].

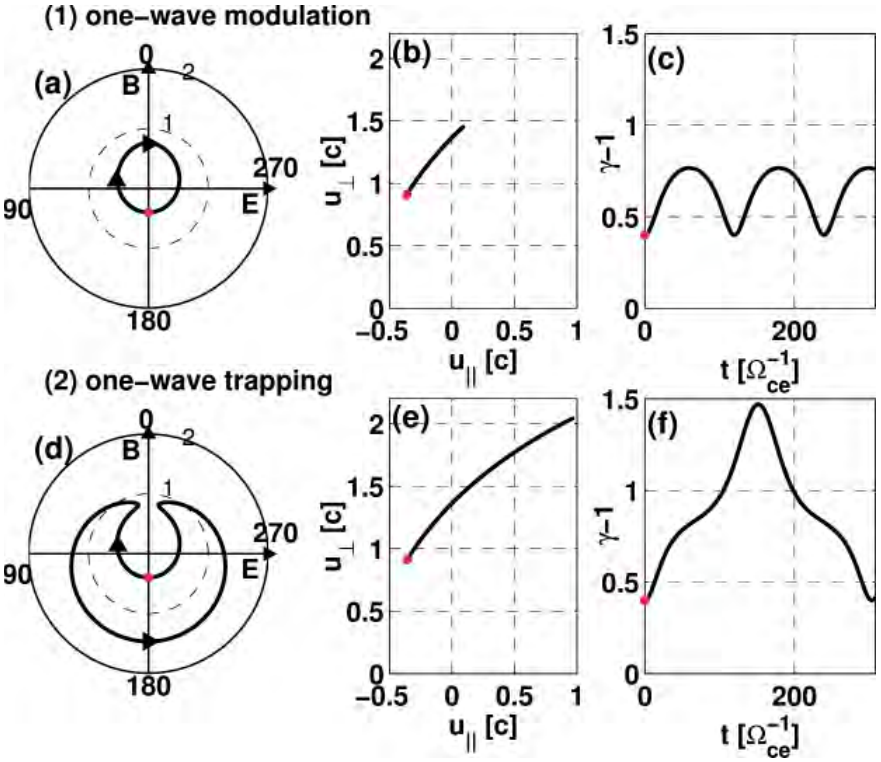

Figure 5 One-wave test-particle results for (1) an un-trapped electron and (2) a trapped electron: (a) and (d) show the trajectories in the $(\gamma-1,\zeta)$ coordinates; (b) and (e) show the trajectories in the $u_\perp - u_{||}$ momentum space; and (c) and (f) show the time histories of $\gamma-1$. The red dots indicate the initial positions.

$$\frac{d\left(\gamma v_{||}\right)}{dt}=\frac{\Omega_w}{v_\perp}\left(\sin\zeta_f+\sin\zeta_b\right), \tag{3}$$

the time derivative of relativistic perpendicular velocity,

$$\frac{d\left(\gamma v_\perp\right)}{dt}=\frac{\omega}{k}\Omega_w\left(\sin\zeta_f-\sin\zeta_b\right)-\Omega_w v_{||}\left(\sin\zeta_f+\sin\zeta_b\right) \tag{4}$$

the time derivative of the Lorentz factor,

$$\frac{d\gamma}{dt}=-\frac{e}{m_e c^2}\mathbf{v}_\perp\cdot\left(\mathbf{E}_f+\mathbf{E}_b\right)=\left(\frac{\omega}{k}\right)\left(\frac{\Omega_w v_\perp}{c^2}\right)\left(\sin\zeta_f-\sin\zeta_b\right) \tag{5}$$

and the time derivative of the electron gyration angle,

$$\frac{d\phi}{dt}=\frac{\Omega_w}{\gamma v_\perp}\left[\cos\zeta_f\left(\frac{\omega}{k}-v_{||}\right)+\cos\zeta_b\left(-\frac{\omega}{k}-v_{||}\right)\right]+\frac{\Omega_{ce}}{\gamma}, \tag{6}$$

where $\Omega_w=\Omega_{ce}B_{f,b}/B_0$. θ is defined as the time derivative of ζ,

$$\theta_f\equiv\frac{d\zeta_f}{dt}=\frac{d\phi}{dt}-\left(\omega-kv_{||}\right), \tag{7}$$

$$\theta_b\equiv\frac{d\zeta_b}{dt}=\frac{d\phi}{dt}-\left(\omega+kv_{||}\right). \tag{8}$$

For simplicity, in the equations it is assumed that both forward and backward waves (two-wave case) have the same wave amplitude, frequency, and wavenumber.

We can obtain equations of electron motion for the one-wave test-particle calculation by omitting the terms associated with the backward wave or the forward wave from Equation (3) to Equation (8). For an electron interacting with a forward (backward) propagating wave, the electron is accelerated if $0<\zeta_f<\pi$ ($\pi<\zeta_b<2\pi$) or decelerated if $\pi<\zeta_f<2\pi$ ($0<\zeta_b<\pi$), as illustrated in Figure 4. An ideal case is that an electron is in the acceleration phase, with $d\zeta/dt=0$ all the time. Nevertheless, the wave field changes the electron velocities, $\mathbf{v}_\perp$ and $\mathbf{v}_{||}$, resulting in $d\zeta/dt\neq 0$, which makes the electron move out of the acceleration phase after some time. However, an effective acceleration can occur if the electron stays long in the acceleration phase.

Figure 5 shows the results of a one-wave test-particle calculation in which an electron interacts with only one forward wave or only one backward wave. In the one-wave test-particle calculations, there were two types of electron trajectories: (1) one-wave modulation, and (2) one-wave trapping. The trapping process will be further discussed later. The example in Figures 5a-5c shows the trajectories of a modulated (untrapped) electron. Figure 5a shows the electron's trajectory in the $(\gamma-1,\zeta)$ polar coordinates. The electron first rotated in the clockwise direction from the red dot and was accelerated. It then traveled into the

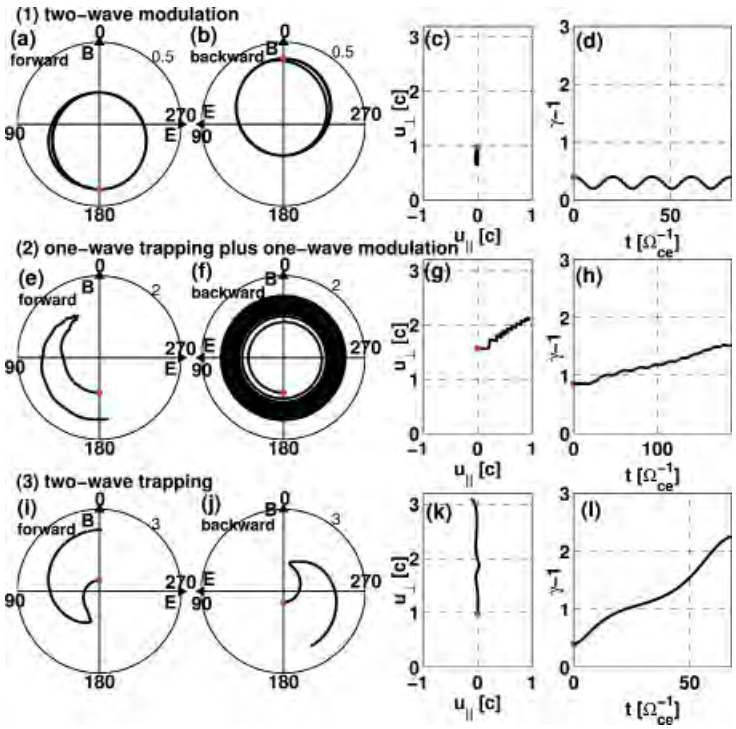

Figure 6. Two-wave test-particle results for electrons undergoing (1) the two-wave modulation, (2) the one-wave trapping plus one-wave modulation, and (3) two-wave trapping. (a) and (b), (e) and (f), and (i) and (j) show the trajectories in the ($\gamma-1, \zeta$) coordinates associated with the forward and the backward waves; (c), (g), and (k) show the trajectories in the $u_\perp - u_{||}$ momentum space; and (d), (h), and (l) show the time histories of $\gamma-1$. The red dots indicate the initial positions

deceleration region, and then reached its initial position. The electron stayed within the acceleration region for only a short time, and was then decelerated. For the modulated electron, its momentum and kinetic energy only underwent a small modulation, as shown in Figures 5b and 5c. The process is called "one-wave modulation."

Figures 5d-5f shows the trajectories of a trapped electron. In Figure 5d, the electron first rotated in the clockwise direction from the red dot, and then the rotation slowed down with a gyration reversal. This electron then rotated in the counterclockwise direction, and was further accelerated until it entered the deceleration region in the 4th and the 1st quadrants. Due to the competition between the relativistic electron cyclotron frequency, Ω_{ce}/γ , and the Doppler-shift wave frequency, ω' , a gyration reversal occurred as $\Omega_{ce}/\gamma - \omega' \approx 0$. Resonant trapping of the electron occurred due to the gyration reversal, and the electron could stay within the acceleration region for a long time, leading to a strong acceleration. For an electron trapped by a wave, it could be accelerated considerably with $\gamma - 1 \simeq 1.5$, as shown in Figures 5e and 5f. The process is called "one-wave resonant trapping acceleration," or simply called "one-wave trapping."

For the two-wave test-particle calculation, two waves with opposite propagating directions (counter-propagating) were imposed. The Doppler-shift frequencies of the two waves were $\omega - kv_{||}$ (forward) and $\omega + kv_{||}$ (backward). Due to the opposite signs of the wave vectors, it was hard for an electron to stay within the acceleration phases of both waves for a long time if $v_{||}$ was large.

In the two-wave test-particle calculation, an electron could be trapped by neither the forward wave nor the backward wave, as per the example in Figures 6a-6d. The electron trajectories in the ($\gamma-1, \zeta$) polar coordinates associated with the forward and the backward waves in Figures 6a and 6b were similar to the case of the one-wave un-trapping modulation. Since the electron was not trapped by any wave, its kinetic energy and momentum only underwent small modulation, as shown in Figures 6c and 6d. The process is called "two-wave un-trapping modulation," or simply called "two-wave modulation."

In the two-wave test-particle calculation, as an electron was trapped by either the forward wave or the backward wave, the electron motion was a combination of the one-wave resonant trapping acceleration and the one-wave un-trapping modulation. The electron trajectory in the ($\gamma-1, \zeta$) polar coordinates associated with the wave that trapped the electron shown in Figure 6e was similar to the case of one-wave resonant trapping, while the electron motion associated with another wave shown in Figure 6f went rapidly through the acceleration and the deceleration regions, and obtained a small modulation of kinetic energy and momentum, as shown in Figures 6g and 6h. The process is called "one-wave resonant trapping acceleration plus one-wave un-trapping modulation," or simply called "one-wave trapping plus one-wave modulation."

In the two-wave test-particle calculation, as an electron was trapped by both the forward and the backward waves, its trajectories in the ($\gamma-1, \zeta$) polar coordinates associated with both waves in Figures 6i and 6j were similar to the case of the one-wave resonant trapping acceleration. Gyration reversals occurred in the polar plots associated with both waves, and the electron stayed within

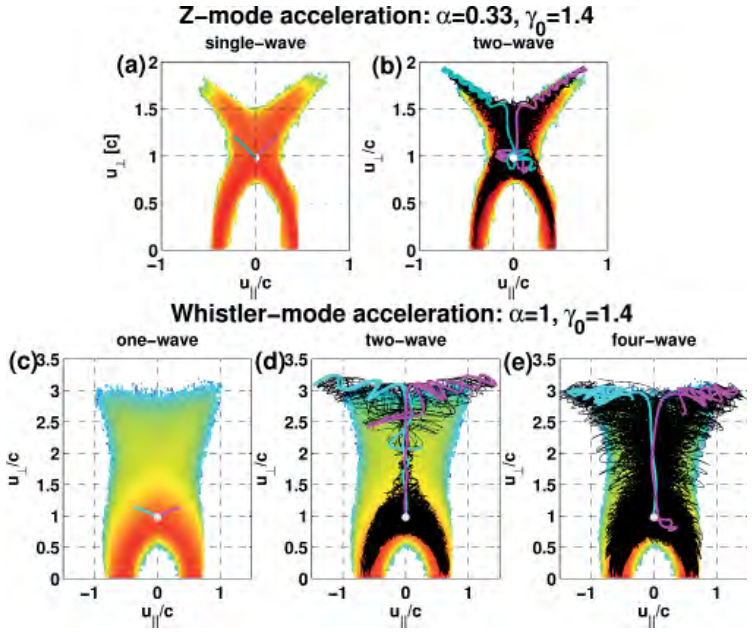

Figure 7. The test-particle trajectories in the $u_\perp - u_\parallel$ momentum space for $\alpha = 0.33$ with (a) one wave and (b) two waves, and for $\alpha = 1$ with (c) one wave, (d) two waves, and (e) four waves. The wave frequencies and the wave numbers corresponded to the most intensive waves of the one-dimensional simulations with $\alpha = 1$ and $\gamma_0 = 1.4$. The corresponding energetic electron momentum distributions after wave-energy saturation of the simulation ($t = 512\Omega_{ce}^{-1}$) are also shown as color contours, for comparison.

the acceleration region of both waves for a long time. The process is called "two-wave resonant trapping acceleration," or simply called "two-wave trapping." During the two-wave trapping process, a strong acceleration of electrons occurred, and electrons were mainly accelerated in the perpendicular direction, as shown in Figures 6k and 6l.

Figure 7 shows the superposition of test-particle trajectories in the $u_\perp - u_\parallel$ momentum space for the whistler-mode and Z-mode cases corresponding to the simulation cases with $\alpha = 1$ and $\alpha = 0.33$. In the test-particle calculations, electrons interacted with one wave, two counter-propagating waves, and four counter-propagating waves (two forward waves and two backward waves). The corresponding energetic electron distribution at the end of the simulation was also drawn as color contours for comparison. The wave frequencies and vectors corresponded to the most intensive waves in the one-dimensional simulation. In the cases with one, two, or four waves, the wave amplitude was determined by conservation of total wave energy, which was about the wave peak energy in the one-dimensional simulation.

In Figures 7a and 7c, the purple and blue curves corresponded to two one-wave test-particle calculations in which electrons interacted with a forward wave and a backward wave, respectively. In the two examples here, each of the electrons was not trapped, and underwent the one-wave modulation. The trajectory in the momentum space for the one-wave test-particle calculation was always along the diffusion curve [26], which is defined as the curve with constant kinetic energy in the frame of reference moving with the wave's phase velocity. The difference between the one-wave trapping case and the one-wave un-trapping case is that an trapped electron can travel much further along the diffusion curve, while the motion of an un-trapped electron shows only a small oscillation in kinetic energy and momentum.

Figures 7b-7d show two-wave test-particle calculations in which one forward and one backward wave were imposed. For $\alpha = 0.33$, the superposition of all test-particle trajectories formed an X-like pattern, which resembled the simulation result. Part of the electrons were initially accelerated through the two-wave trapping in the perpendicular direction for a short time, and then underwent the one-wave trapping plus one-wave modulation. During the two-wave trapping stage, the electric field of the forward wave and the electric field of the backward wave were nearly in phase, and hence electrons were simultaneously accelerated by both the forward and the backward waves. The formation of each branch of the X-like distribution was dominated by either the forward or the backward wave. However, the formation of the whole X-like distribution required both the forward- and the backward-propagating waves. For $\alpha = 1$, the strong perpendicular acceleration by the two-wave trapping led to the formation of a long and thin "neck," although the thin neck was different from the simulation result with a thick "neck." The peak energy of the accelerated electrons in the two-wave calculations for the Z-mode ($\alpha = 0.33$) acceleration could reach four times the initial kinetic energy, while that for the whistler-mode ($\alpha = 1$) acceleration could reach six times the initial kinetic energy.

Figure 7e shows a four-wave test-particle calculation in which two forward and two backward waves were imposed. The superposition of all test-particle trajectories showed a more-diffusive pattern, which resembled the simulation result with a thick "neck." The purple and blue trajectories corresponded to two electron trajectories of strong acceleration. Each electron was initially simultaneously trapped and accelerated by all the four waves, and its trajectory showed strong perpendicular acceleration in the momentum space. It then deviated from the four-wave resonant trapping process, and was trapped by one wave or two waves of the same propagating direction, while other

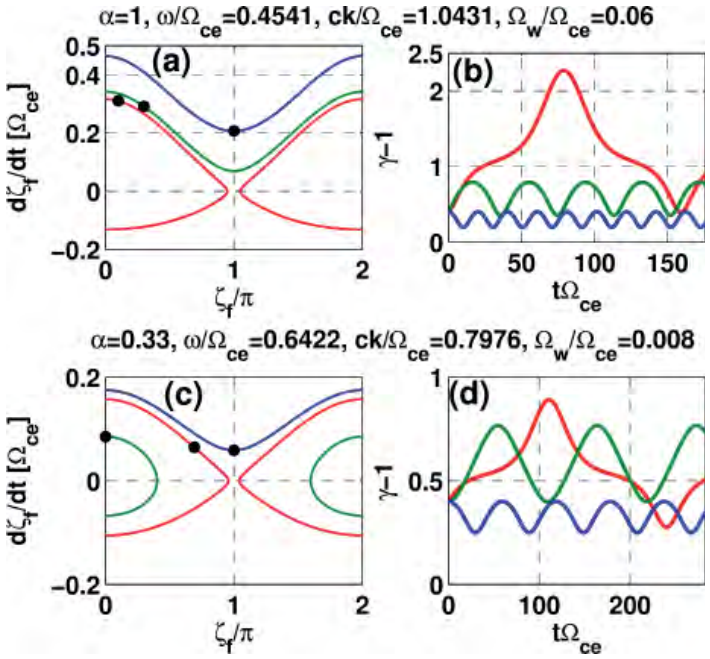

Figure 8. The test-particle results of two-wave cases corresponding to $\alpha = 0.33$ (bottom panels) and $\alpha = 1$ (top panels). It was assumed that $v_{||} = 0$ and $\zeta_b = \zeta_f + \pi$. The red curve in (a) and the red and green curves in (c) corresponded to trapped electrons. The black dots indicate initial positions. Strong acceleration occurred for trapped electrons, while un-trapped electrons only had small energy variations.

waves gave small modulation to electron kinetic energy and momentum. In the four-wave calculation, for an electron simultaneously trapped by all of the four waves or by one forward and one backward waves, the acceleration process was similar to the two-wave resonant trapping acceleration of the two-wave calculation. For an electron trapped by one of the four waves or simultaneously trapped by two waves with the same propagating direction, the acceleration process was similar to the one-wave trapping plus one-wave modulation in the two-wave calculation. For an electron un-trapped by all waves, the electron motion showed only a small variation in kinetic energy and momentum. For the whistler-mode acceleration case ($\alpha = 1$), the peak energies of the accelerated electrons in the two- and four-wave cases were similar, and could reach six times the initial kinetic energy.

In the two-wave and four-wave calculations, the huge energy boost of electrons in the perpendicular direction was predominantly due to simultaneous acceleration by all the counter-propagating waves. Electrons were mainly accelerated in the perpendicular direction during this stage. After that, the electron motion was dominated by waves propagating in one direction, while the waves in the opposite direction gave a small modulation in energy and momentum. In Figures 7b, 7d, and 7e, the purple and blue curves showed strong acceleration in the perpendicular direction at the initial stage, and were dominated by the forward and the backward waves, respectively, at a later stage.

For the two-wave resonant trapping acceleration in the two-wave calculation, an ideal case was that an electron kept $v_{||} = 0$ to stay long in both the acceleration phases of the two counter-propagating waves. In Equation (5), the variation of electron energy is associated with the wave's electric field, and a strong acceleration occurs under the conditions that (1) $\zeta_f - \zeta_b = \pi \pm 2n\pi$ (n is an integer), and (2) ζ_f and ζ_b are within the acceleration phases. By assuming $\zeta_f - \zeta_b = \pi \pm 2n\pi$ and $v_{||} = 0$ in the initial condition, Equations (3), (7), and (8) lead to

$$\frac{d\left(\gamma v_{||}\right)}{dt} = 0\,, \tag{9}$$

$$\theta_f - \theta_b = 2kv_{||} = 0\,. \tag{10}$$

Equations (9) and (10) further ensure that the two conditions, $v_{||} = 0$ and $\zeta_f - \zeta_b = \pi \pm 2n\pi$, stay true at all time. Based on the assumption that $\zeta_f - \zeta_b = \pi \pm 2n\pi$ and $v_{||} = 0$, an ideal two-wave trapping can occur, and the equation of motion can be simplified as

$$\frac{du_\perp}{dt} = 2\frac{\omega}{k}\Omega_w \sin\zeta_f\,, \tag{11}$$

$$\frac{d\gamma}{dt} = 2\frac{\omega}{k}\frac{\Omega_w u_\perp}{\gamma c^2}\sin\zeta_f\,, \tag{12}$$

$$\theta_f \equiv 2\frac{\omega}{k}\frac{\Omega_w}{u_\perp}\cos\zeta_f + \frac{\Omega_{ce}}{\gamma} - \omega\,. \qquad (13)$$

Taking the time derivative of Equation (13) leads to the pendulum-like second-order resonance condition

$$\frac{d\theta_f^2}{d\zeta_f} + \omega_{tr}^2 \sin\zeta_f = 0\,. \qquad (14)$$

$$\omega_{tr}^2 = 4\left(\frac{\omega\Omega_w\Omega_{ce}}{ck}\right)\left(\frac{c}{u_\perp}\right)$$

$$\left(4\frac{\omega}{k}\frac{\Omega_w}{\Omega_{ce}u_\perp}\cos\zeta_f - \frac{\omega}{\Omega_{ce}} + \frac{1}{\gamma} + \frac{u_\perp^2}{\gamma^3c^2}\right). \qquad (15)$$

By ignoring the term $4\omega\Omega_w\cos\zeta_f/k\Omega_{ce}u_\perp$ for small wave amplitudes ($\Omega_w \ll \Omega_{ce}$), the square of the trapping frequency, ω_{tr}^2, can be written as

$$\omega_{tr}^2 \simeq 4\left(\frac{\omega\Omega_w\Omega_{ce}}{ck}\right)\left(\frac{c}{u_\perp}\right)\left(-\frac{\omega}{\Omega_{ce}} + \frac{1}{\gamma} + \frac{u_\perp^2}{\gamma^3c^2}\right). \qquad (16)$$

The numerical solution of Equations (11), (12), and (13) shows pendulum-like trajectories in the $(d\zeta/dt, \zeta)$ phase space. Figure 8 shows the two-wave test-particle results of the ideal two-wave trapping corresponding to the simulation cases of $\alpha = 0.33$ and 1. The red curves in Figure 8a and the green and red curves in Figure 8c correspond to trapped electrons. Strong acceleration occurs for trapped electrons, while un-trapped electrons only have small energy variations, as shown in Figures 8b-8d. In the case of $\alpha = 0.33$, most electrons were trapped, but the maximum energy increment from $\gamma_0 = 1.4$ was only $\Delta\gamma \approx 0.5$. In the case of $\alpha = 1$, although the number of trapped electrons was lower, the energy increment of all these trapped electrons could reach $\Delta\gamma \approx 2$ with $\gamma_0 = 1.4$. In the case of $\alpha = 5$, no electron with $\gamma_0 = 1.4$ was trapped by the two-wave resonance, and hence the electron motion in this case showed only a small variation in kinetic energy.

In the above discussions, the two initial conditions, $\zeta_f - \zeta_b = \pi \pm 2n\pi$ and $v_\parallel = 0$, led to the ideal two-wave trapping. The first assumption, the phase difference between ζ_f and ζ_b, can be rewritten as

$$\zeta_f - \zeta_b = (\phi - \psi_f) - (\phi - \psi_b)$$

$$= \psi_f - \psi_b$$

$$= (\omega t - kx + \psi_{f0}) - (\omega t + kx + \psi_{b0})$$

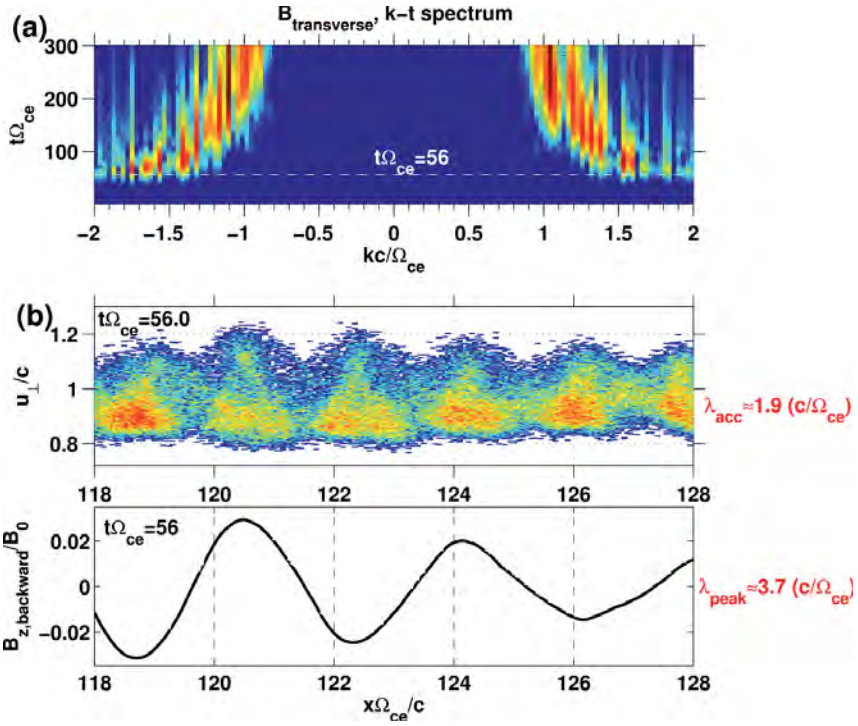

Figure 9. (a) The $k-t$ power spectrum for the transverse magnetic field, (b) the energetic electron distribution in the $u_\perp - x$ phase space and wave spatial profile at $t\Omega_{ce} = 56$ for the case with $\alpha = 1$ and $\gamma_0 = 1.4$. At $t\Omega_{ce} = 56$, the wavelength of the most-intensive whistler-mode waves was $\lambda_{peak} \approx 3.7\,c/\Omega_{ce}$, and the strong two-wave resonant acceleration occurred at a wavelength of $\lambda_{acc} \approx 1.9\,c/\Omega_{ce}$.

$$= -2kx + \left(\psi_{f0} - \psi_{b0}\right), \qquad (17)$$

where ψ_f and ψ_b are the phases of the forward and backward waves, respectively, and ψ_{f0} and ψ_{b0} are the phase constants of the forward and backward waves, respectively. In Equation (17), there is no time dependence in the phase difference. A strong two-wave resonant acceleration occurs as the condition, $\zeta_f - \zeta_b = \pi \pm 2n\pi$ is satisfied. Efficient acceleration therefore takes place at a spatial interval corresponding to a wavenumber of $2k$. In the simulation case with $\alpha = 1$ and $\gamma_0 = 1.4$, at $t\Omega_{ce} = 56$, the wavenumber of the most intensive waves was $ck_{peak}/\Omega_{ce} \approx 1.7$, corresponding to a peak wavelength $\lambda_{peak} \approx 3.7\, c/\Omega_{ce}$, as shown by Figure 9a. Figure 9b shows a comparison between the electron distribution at $t\Omega_{ce} = 56$ in the $u_\perp - x$ phase space and the wave's spatial profile. The perpendicular acceleration of electrons led to a wavy structure in the electron distribution, and occurred at the location of wave crests and troughs. As $-2kx + \left(\psi_{f0} - \psi_{b0}\right)$ varied in space, a strong two-wave resonant acceleration took place at a spatial interval λ_{acc}, which was equal to half of the peak wavelength, λ_{peak}, of the most intensive wave mode ($\lambda_{acc} \approx 0.5\lambda_{peak}$).

6. Summary

In the presence of a tenuous electron ring distribution on top of a magnetized background plasma, the ring component can trigger the cyclotron maser instability and excite waves. Part of the waves can further accelerate the energetic electrons. A series of one-dimensional and two-dimensional simulations were carried out to study the wave emission and electron acceleration. The acceleration process was then studied via test-particle calculation. Efficient acceleration occurred in the multi-wave cases due to simultaneous acceleration of electrons by counter-propagating waves.

The main results can be summarized as follows:

(1) The electron acceleration in the one-wave and two-wave test-particle calculations could be classified into five types. In the one-wave case, we had (A1) one-wave modulation, and (A2) one-wave trapping. In the two-wave case, we had (B1) two-wave modulation, (B2) one-wave trapping plus one-wave modulation, and (B3) two-wave trapping. The acceleration processes in the four-wave calculations were similar, and could be related to the above five types of acceleration.

(2) The strong perpendicular acceleration in the multi-wave cases was due to resonant trapping of electrons by counter-propagating waves.

(3) The resonant acceleration by counter-propagating waves occurred at a spatial interval λ_{acc}, which was about half of the peak wavelength, λ_{peak}, of the most intensive wave mode ($\lambda_{acc} \approx 0.5\lambda_{peak}$).

(4) In the particle simulations with $\alpha = 0.33$ and $\gamma_0 = 1.2$, 1.4, and 2, the peak energy of the accelerated electrons was about three to four times the initial kinetic energy. With $\alpha = 1$, it could reach six to eight times the initial kinetic energy. With $\alpha = 5$, it could reach only two to three times the initial kinetic energy.

7. Acknowledgements

This work was supported by Grant-in-Aid 23340147 of the Ministry of Education, Science, Sports, and Culture of Japan, by the National Science Council in Taiwan (NSC 101-2628-M-001-007-MY3), and by the Center for Computational Geophysics of NCU in Taiwan (CCG Contribution Number: NCU-CCG102-0003).

8. References

1. S. Wu and L. C. Lee, "A Theory of the Terrestrial Kilometric Radiation," *Astrophysical Journal*, **230**, 1, December 1979, pp. 621-626.

2. L. C. Lee and C. S. Wu, "Amplification of Radiation Near Cyclotron Frequency Due to Electron Population Inversion," *Physics of Fluids*, **23**, 7, March 1980, pp. 1348-1354.

3. J. S. Wagner, T. Tajima, L. C. Lee, and C. S. Wu, "Computer Simulation of Auroral Kilometric Radiation," *Geophysical Research Letters*, **10**, 6, June 1983, pp. 483-486.

4. H. P. Freund, H. K. Wong, C. S. Wu, and M. J. Xu, "An Electron Cyclotron Maser Instability for Astrophysical Plasmas," *Physics of Fluids*, **26**, 8, August 1983, pp. 2263-2270.

5. C. S. Wu and H. P. Freund, "A Kinetic Cyclotron Maser Instability Associated with a Hollow Beam of Electrons," *Radio Science*, **19**, 2, March 1984, pp. 519-525.

6. P. L. Pritchett, "Relativistic Dispersion and the Generation of Auroral Kilometric Radiation," *Geophysical Research Letters*, **11**, 2, February 1984, pp. 143-146.

7. R. J. Strangeway, "Wave Dispersion and Ray Propagation in a Weakly Relativistic Electron Plasma: Implications for the Generation of Auroral Kilometric Radiation," *Journal of Geophysical Research*, **90**, A10, October 1985, pp. 9675-9687.

8. A. O. Benz, and G. Thejappa, "Radio Emission of Coronal Shock Waves," *Astronomy and Astrophysics*, **202**, 1-2 , August 1988, pp. 267-274.

9. W. M. Farrell, "Direct Generation of O-mode Emission in a Dense, Warm Plasma: Applications to Interplanetary Type II Emissions and Others in its Class," *Journal of Geophysical Research*, **106**, A8, August 2001, pp. 15701-15709.

10. Y. P. Chen, G. C. Zhou, P. H. Yoon, and C. S. Wu, "A Beam-maser Instability: Direct Amplification of Radiation," *Physics of Plasmas*, **9**, 6, June 2002, pp. 2816-2821.

11. P. H. Yoon, C. B. Wang, and C. S. Wu, "Ring-Beam Driven Maser Instability for Quasiperpendicular Shocks," *Physics of Plasmas*, **14**, 2, January 2007, pp. 022901-022901.6.

12. C. S. Wu, "A Fast Fermi Process: Energetic Electrons Accelerated by a Nearly Perpendicular Bow Shock," *Journal of Geophysical Research*, **89**, A10, October 1984, pp. 8857-8862.

13. M. M. Leroy and A. Mangeney, "A Theory of Energization of Solar Wind Electrons by the Earth's Bow Shock," *Annals of Geophysics*, **2**, 4, July 1984, pp. 449-456.

14. C. S. Wu, C. B. Wang, P.H. Yoon, H. N. Zheng, and S. Wang, "Generation of Type III Solar Radio Bursts in the Low Corona by Direct Amplification," *Astrophysical Journal*, **575**, 2, April 2002, pp. 1094-1103.

15. P. H. Yoon, C. S. Wu, and C. B. Wang, "Generation of Type III Solar Radio Bursts in the Low Corona by Direct Amplification. II. Further Numerical Study," *Astrophysical Journal*, **576**, 1, May 2002, pp. 552-560.

16. S. Kainer and R. J. MacDowall, "A Ring Beam Mechanism for Radio Wave Emission in the Interplanetary Medium," *Journal of Geophysical Research*, **101**, A1, January 1996, pp. 495-508.

17. K. H. Lee, Y. Omura, L. C. Lee, and C. S. Wu, "Nonlinear Saturation of Cyclotron Maser Instability Associated with Energetic Ring-beam Electrons," *Physical Review Letters*, **103**, 10, August 2009, pp. 105101-105101.4.

18. K. H. Lee, Y. Omura, and L. C. Lee, "A 2D Simulation Study of Langmuir, Whistler, and Cyclotron Maser Instabilities Induced by an Electron Ring-beam Distribution," *Physics of Plasmas*, **18**, 9, July 2011, pp. 092110-092110.7.

19. P. L. Pritchett, R. J. Strangeway, C. W. Carlson, R. E. Ergun, J. P. McFadden, and G. T. Delory, "Free Energy Sources and Frequency Bandwidth for the Auroral Kilometric Radiation," *Journal of Geophysical Research*, **104**, A5, May 1999, pp. 10317-10326.

20. P. L. Pritchett, R. J. Strangeway, R. E. Ergun, and C. W. Carlson, "Generation and Propagation of Cyclotron Maser Emissions in the Finite Auroral Kilometric Radiation Source Cavity," *Journal of Geophysical Research*, **107**, A12, May 2002, pp. SMP13.1-SMP13.17.

21. L. C. Lee, "Theories of Non-Thermal Radiations from Planets," in *Plasma Waves and Instabilities at Comets and in Magnetospheres*, Washington, DC, American Geophysical Union, 1989, pp. 239-249.

22. K. H. Lee, Y. Omura, and L. C. Lee, "Electron Acceleration by Z-mode Waves Associated with Cyclotron Maser Instability," *Physics of Plasmas*, **19**, 12, December 2012, pp. 122902-122902.5.

23. K. H. Lee, Y. Omura, and L. C. Lee, "Electron Acceleration by Z-mode and Whistler-mode Waves," *Physics of Plasmas*, **20**, 11, November 2013, pp. 112901-112901.10.

24. Y. Omura and H. Matsumoto, "KEMPO1: Technical Guide to One-Dimensional Electromagnetic Particle Code," in

Collaborative Non-Cryptographic Physical-Layer Authentication Schemes in Wireless Networks

Hao-Chung Cheng, Sheng-Yi Ho, and Ping-Cheng Yeh

Department of Electrical Engineering and Graduate Institute of Communication Engineering
National Taiwan University,
Taipei 10617, Taiwan
E-mail: f99942118@ntu.edu.tw.

This paper is the invited Third Prize winner from the AP-RASC 2013 Student Paper Competition.

Abstract

Recently, many lower-layer characteristics, such as clock skew, channel response, and frame sequence number, have been utilized to achieve wireless security. The physical-layer characteristics of the wireless medium serve as a rich source of location-specific information that can be used to complement or enhance traditional security schemes. In this paper, we focus on the problem of physical-layer authentication (PHY authentication), which aims at assuring that the current transmission comes from the same entity as the previous transmission. In other words, the receiver analyzes the physical-layer characteristics to discriminate among different transmissions coming from different devices. Two physical-layer characteristics are considered separately: the frequency response of the wireless channel, and the propagation delay. Collaborative authentication is also treated in this paper. First, we consider collaborative authentication between different receivers observing the same physical-layer characteristic. We next combine the authentication results from different characteristics to formulate generalized multi-feature authentication. Although they are described under the discussion of physical-layer characteristics, it is possible to apply the proposed scheme to formulate a collaborative cross-layer non-cryptographic authentication mechanism with moderate modifications. Numerical results showed that the physical-layer authentication is valid, and the proposed collaborative authentication schemes further improved the authentication performance.

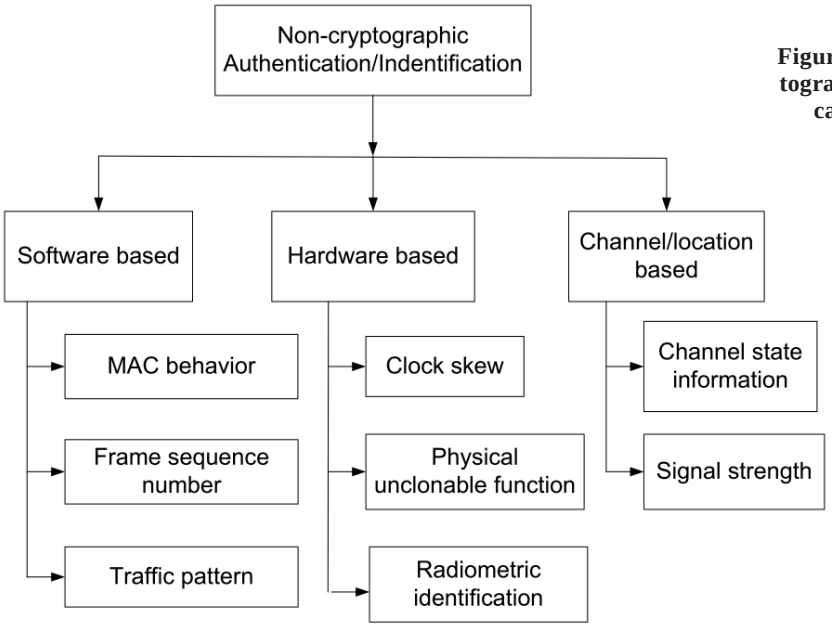

Figure 1. A classification of non-cryptographic authentication and identification in wireless networks [4].

1. Introduction

As wireless devices become increasingly prevalent and powerful, they are becoming both the targets of attacks and the very tools for performing such attacks. Due to the broadcast essence of wireless communications, the attackers can perform eavesdropping or even inject messages into legitimate transmissions to spoof the receiver, in a manner rather easier than with wired networks. Numerous attacks on wireless networks have been addressed in the literature [1-3]. Among the various attacks, identity-based attacks (e.g., medium-access-control (MAC) access spoofing) are easy to launch, and are thus considered the first step for intruder attack attempts, including denial-of-service (DoS), session hijacking, man-in-the-middle attacks, data modification, and sniffing. Although conventional cryptographic security mechanisms are essential for securing wireless networks, these mechanisms are either inefficient or fall short in certain existing scenarios [4].

- Existing 802.11 security techniques only provide authentication for data frames. Management and control frames are usually not protected.
- Cryptographic techniques are ill-suited for a less-well-equipped device, due to high computational complexity.
- It is difficult in ad-hoc networks to perform key management, such as distributing, refreshing, and revoking keys.
- In emerging wireless networks, such as cognitive radio networks, the identification of primary users will be performed at the signal level, without relying on higher-layer cryptographic methods.

In view of these circumstances, many researchers have proposed utilizing the lower-layer characteristics (fingerprinting) for non-cryptographic authentication and identification [4]. The classifications of non-cryptographic authentication schemes are summarized in Figure 1.

We further focus on channel/location-based authentication schemes. Due to the scattering properties of the wireless environment, the physical characteristics of the wireless medium serve as a rich source of location-specific information, which can be used to complement and enhance traditional security mechanisms. Both the received signal-strength indication (RSSI) and the channel response are considered a form of channel state information (CSI) for authentication or detecting identity-based attacks. In [4] and [5], the temporal RSSI and RSSI variations were utilized, and in [6-8], the frequency-domain channel response (sub-channel gains in a multi-carrier system) were utilized. In addition to channel state information, another physical-layer characteristic that contains the location-specific information is the propagation delay. A further explanation of propagation-delay-based authentication will be addressed in Section 2.

In addition to seeking new physical-layer characteristics for authentication, we consider the possibility of performing collaborative physical-layer authentication. The collaborative authentication could be performed among different receiving terminals observing the same physical characteristic (in Section 2) or observing multiple characteristics (in Section 3). The numerical results showed that physical-layer authentication is valid, and collaborative schemes can further improve authentication accuracy. Although the collaborative schemes addressed in this work are focused on physical-layer authentication, it is possible to adapt joint authentication schemes for allowing cross-layer authentication with moderate modifications.

The rest of this paper is organized as follows. Section 2 introduces the physical-layer authentication schemes, including channel-response-based authentication and the propagation-delay-based method. A generalized multi-feature collaborative authentication scheme is addressed in Section 3. The numerical results are shown in Section 4. Finally, we conclude this paper in Section 5.

2. Physical-Layer Authentication Schemes

In this section, two physical-layer authentication schemes (channel-response based, propagation-delay based) are proposed. We can utilize these physical-layer authentication methods to enhance traditional cryptographic authentication schemes.

2.1 Channel-Response-Based Authentication

In the following, we consider the static channel and the time-varying channel separately. In both cases, we use hypothesis testing to discriminate whether the transmitting terminal is Alice or not. The null hypothesis, $\mathcal{H}_0$, denotes that the transmission attempts come from Alice, and the alternative hypothesis, $\mathcal{H}_1$, claims that the transmission comes from someone else.

2.1.1 Static Channel

When the transmitting terminal (Alice) and the receiving terminal (Bob) remain static, the channel response between Alice and Bob will also be static (time-invariant, but still frequency selective). The sub-channel's gains will thus not change with time. We assume Bob first measures and stores the channel's frequency response from Alice. Denote the true channel response as $H_{AB}(f)$, and the noisy version of Bob's measurement as $\hat{H}_{AB}(f)$. Bob stores the sampled noisy response $\hat{\mathbf{h}}_{AB}$, which is the sampled version of $\hat{H}_{AB}$. We use the notation $\mathbf{x} = [x_1, \ldots, x_N]^T$ to express the sampled version of $X(f)$, where $x_n = X(f)|_{f = f_c - W/2 + n\Delta f}$, N denotes the sample

size, f_c is the central frequency, W is the system bandwidth, and the subcarrier spacing is $\Delta f = W/N$. When the next frame arrives, Bob also measures and samples the channel response $\hat{\mathbf{h}}_t$.

The noisy measurements $\hat{\mathbf{h}}_{AB}$ and $\hat{\mathbf{h}}_t$ are modeled as

$$\hat{\mathbf{h}}_{AB} = \mathbf{h}_{AB} e^{j\phi_{AB}} + \mathbf{n}_{AB}, \tag{1}$$

$$\hat{\mathbf{h}}_t = \mathbf{h}_t e^{j\phi_t} + \mathbf{n}_t .$$

ϕ_{AB} and ϕ_t denote the phase mismatches between transmitter and receiver. We denote the thermal noise by $\mathbf{n}_{AB}$ and $\mathbf{n}_t$, the elements of which are i.i.d. (independent and identically distributed) circularly symmetric complex Gaussian noise samples $\mathcal{CN}\left(0, \sigma_N^2\right)$.

With $\hat{\mathbf{h}}_{AB}$ and $\hat{\mathbf{h}}_t$, Bob uses a simple hypothesis testing to authenticate the current transmission:

$$\mathcal{H}_0 : \mathbf{h}_t = \mathbf{h}_{AB}, \tag{2}$$

$$\mathcal{H}_1 : \mathbf{h}_t \neq \mathbf{h}_{AB} .$$

Note that the number of complex sub-channel gains used for authentication (the size of $\mathbf{h}_t$ and $\mathbf{h}_{AB}$) do not have to equate to the whole number of sub-channels. To avoid ambiguity, let M denote the number of subcarriers used for authentication, with $M \leq N$, which is the sample size of an OFDM symbol. The test statistic is chosen to be

$$T = \min_{\phi} \frac{1}{\sigma_N^2} \left\| \hat{\mathbf{h}}_t - \hat{\mathbf{h}}_{AB} e^{j\phi} \right\|^2, \tag{3}$$

where the minimization argument, ϕ, aims at correcting the potential phase mismatch, even though the transmission attempts come from Alice. The argument ϕ_{min} minimizing Equation (3) is

$$\phi_{min} = \mathrm{Arg}\left(\hat{\mathbf{h}}_t \bullet \hat{\mathbf{h}}_{AB}^c \right), \tag{4}$$

where $(\bullet)^c$ denotes the complex conjugate operation.

When the transmission comes from Alice, the channel response measured by Bob will be

$$\hat{\mathbf{h}}_{AB} = \mathbf{h}_{AB} e^{j\phi_{AB}} + \mathbf{n}_{AB}, \tag{5}$$

$$\hat{\mathbf{h}}_t = \mathbf{h}_{AB} e^{j\phi_t} + \mathbf{n}_t .$$

From the derivations in [6], the conditional test statistic can be derived as

$$T_{\mathcal{H}_0} = \frac{1}{\sigma_N^2} \left\| \hat{\mathbf{h}}_t - \hat{\mathbf{h}}_{AB} e^{j\phi^*} \right\|^2 \tag{6}$$

$$= \sum_{m=1}^{M} \left(\frac{\Delta n_{mr}}{\sigma_N} \right)^2 + \sum_{m=1}^{M} \left(\frac{\Delta n_{mi}}{\sigma_N} \right)^2 \sim \chi_{2M,0}^2 ,$$

where ϕ^* is the correction of phase mismatch, Δn_{mr} and Δn_{mi} are independent with distribution $\mathcal{N}\left(0, \sigma_N^2\right)$, and we denote $\Delta n_{mr} + \Delta j n_{mi} \coloneqq n_{tm} - n_{ABm} e^{j\phi^*}$ since $n_{tm} - n_{ABm} e^{j\phi^*} \sim \mathcal{CN}\left(0, 2\sigma_N^2\right)$.

Similarly, when the transmission comes from Eve,

$$\hat{\mathbf{h}}_{AB} = \mathbf{h}_{AB} e^{j\phi_{AB}} + \mathbf{n}_{AB}, \tag{7}$$

$$\hat{\mathbf{h}}_t = \mathbf{h}_{EB} e^{j\phi_t} + \mathbf{n}_t .$$

In this case,

$$\mathbf{h}_t e^{j\phi_t} = \mathbf{h}_{EB} e^{j\phi_t} \neq \mathbf{h}_{AB} e^{j\phi_{AB}} e^{j\phi^*}, \tag{8}$$

and the resulting test statistic, $T_{\mathcal{H}_1}$, is no longer chi-squared-distributed, but should be derived as

$$T_{\mathcal{H}_1} = \frac{1}{\sigma_N^2} \left\| \hat{\mathbf{h}}_t - \hat{\mathbf{h}}_{AB} e^{j\phi^*} \right\|^2$$

$$= \frac{1}{\sigma_N^2} \left\| \mathbf{h}_{EB} e^{j\phi_t} - \mathbf{h}_{AB} e^{j\phi_{AB}} e^{j\phi^*} + \mathbf{n}_t - \mathbf{n}_{AB} e^{j\phi^*} \right\|^2$$

$$= \frac{1}{\sigma_N^2} \left\| \Delta \mathbf{h} + \Delta \mathbf{n} \right\|^2 \tag{9}$$

$$= \frac{1}{\sigma_N^2} \sum_{m=1}^{M} \left| \left(\Delta h_{mr} + j\Delta h_{mi} \right) + \left(\Delta n_{mr} + j\Delta n_{mi} \right) \right|^2$$

$$= \sum_{m=1}^{M} \left(\frac{\Delta h_{mr} + \Delta n_{mr}}{\sigma_N} \right)^2 + \sum_{m=1}^{M} \left(\frac{\Delta h_{mi} + \Delta n_{mi}}{\sigma_N} \right)^2 \sim \chi^2_{2M,\delta},$$

since $\Delta h_{mr} + \Delta n_{mr} \sim \mathcal{N}\left(\Delta h_{mr}, \sigma_N^2 \right)$ and $\Delta h_{mi} + \Delta n_{mi} \sim \mathcal{N}\left(\Delta h_{mi}, \sigma_N^2 \right)$. $T_{\mathcal{H}_1}$ is a non-central chi-squared random variable with non-centrality parameter

$$\delta = \frac{1}{\sigma_N^2} \sum_{m=1}^{M} \left| h_{EBm} e^{j\phi_t} - h_{ABm} e^{j\phi_{AB}} e^{j\phi^*} \right|^2. \quad (10)$$

In summary, the test statistic, *T*, has different distributions under $\mathcal{H}_0$ and $\mathcal{H}_1$:

$$T_{\mathcal{H}_0} \sim \chi^2_{2M,0}, \quad (11)$$

$$T_{\mathcal{H}_1} \sim \chi^2_{2M,\delta}.$$

Consequently, the *false alarm rate* (Type I error) can be expressed as

$$\alpha = \Pr\left(T_{\mathcal{H}_0} > T_0 \right) \quad (12)$$

$$= 1 - F_{\chi^2_{2M,0}}\left(T_0 \right),$$

and the *miss rate* (Type II error) is

$$\beta = \Pr\left(T_{\mathcal{H}_1} \le T_0 \right)$$

$$= F_{\chi^2_{2M,\delta}}\left(T_0 \right).$$

F denotes the cumulative density function (CDF), and T_0 is the test threshold to be decided. In practice, Bob should not obtain any information from Eve in advance, so the statistical distribution of $T_{\mathcal{H}_1}$ is unknown. In this case, one way to determine T_0 is by first assigning the required false alarm rate, and then calculating the corresponding test threshold,

$$T_0 = F^{-1}_{\chi^2_{2M,0}}\left(1 - \alpha \right). \quad (14)$$

2.1.2 Time-Variant Channel

The general time-variant channel response is considered, consisting of three parts:

a) the fixed part, which is the long-term average of the channel response containing spatial variability information;

b) the time-variant part, with zero mean;

c) the thermal noise at the receiving end, which is modeled by the circularly symmetric complex Gaussian random variable, $\mathcal{CN}\left(0, \sigma_N^2 \right)$.

Without loss of generality, the time-variant part and the thermal noise are considered to be independent. The *n*th element of the sampled frequency response from Alice to Bob, $\mathbf{h}_{AB}[k]$, at time *kT* from some arbitrary time origin, is thus decomposed as

$$h_{ABn}[k] = \bar{h}_{ABn} + \varepsilon_{ABn}[k] + n_{ABn}[k], \; 1 \le n \le N, \quad (15)$$

where $x_n[k] = X\left(kT; f_c - W/2 + n\Delta f \right)$ denotes the sample of $X\left(t; f \right)$ at the *n*th subcarrier and time *kT*.

We apply the wide-sense stationary uncorrelated scattering (WSSUS) model to provide the statistical description of the short-term temporal variation of a wireless channel [9]. The wide-sense stationary uncorrelated scattering channel can be represented as a tapped delay line:

$$h\left(t, \tau \right) = \sum_{l=1}^{L} c_l\left(t \right) \delta\left(\tau - \tau_l \right), \quad (16)$$

where *L* is the number of taps, $c_l\left(t \right)$ are the time-dependent complex coefficients for the taps, and τ_l is the delay of the *l*th tap. Since the receiver cannot resolve two signal components with temporal spacing smaller than $\Delta\tau = 1/W$ (*W* is the system bandwidth,) Equation (16) is modified to

$$h\left(t, \tau \right) = \sum_{l=1}^{L} c_l\left(t \right) \delta\left(\tau - l\Delta\tau \right). \quad (17)$$

The time-variant part, $\varepsilon_{ABn}[k]$, is the Fourier transform of $h(t,\tau)$ with respect to τ:

$$\varepsilon_{ABn}[k] = \mathcal{F}\{h(t,\tau)\}\Big|_{t=kT,\, f=f_c-\frac{W}{2}+n\Delta f}$$

$$= \sum_{l=0}^{\infty} c_l[k] e^{-j2\pi\left(f_c-\frac{W}{2}+n\Delta f\right)l\Delta\tau}.$$

Similarly, the complex channel gain from Eve to Bob of the *n*th subcarrier at time *kT* is

$$h_{EBn}[k] = \bar{h}_{EBn} + \varepsilon_{EBn}[k] + n_{EBn}[k],\ 1 \le n \le N \quad (18)$$

We follow the assumptions in [7], which are briefly summarized below:

a) $E[c_l(t)] = 0$.

b) The power-delay spectrum of $c_l[k]$ is modeled by the one-sided exponential distribution, i.e.,

$$P_\tau[l] = \mathrm{Var}\{c_l[k]\} = \sigma_T^2\left(1-e^{-2\pi B_c\Delta\tau}\right)e^{-2\pi Wl\Delta\tau}$$

where $c_l[k] = c_l(kT)$ is the amplitude sample of the *l*th multipath component at time *kT*, σ_T^2 is the average power of $c_l[k]$ over all taps, and B_c is the channel coherence bandwidth.

c) The temporal process of $c_l[k]$ is characterized by an autoregressive model of order 1 (AR-1) as

$$c_l[k] = ac_l[k-1] + \sqrt{\left(1-a^2\right)P_\tau[l]}u_l[k], \quad (20)$$

where the AR-1 coefficient, *a*, denotes the similarity of two c_l values temporally spaced by *T*, and the random component $u_l[k] \sim \mathcal{CN}(0,1)$ is independent of $c_l[k-1]$.

Two relationships [7] can be derived based on these assumptions.

Relationship 1:

$$\mathbf{h}_{AB}[k] - \mathbf{h}_{AB}[k-1] \sim \mathcal{CN}(\mathbf{0},\mathbf{R}), \quad (21)$$

where

$$\mathbf{R} = \mathrm{Cov}\{\mathbf{h}_{AB}[k] - \mathbf{h}_{AB}[k-1]\}$$

$$= \left[r(m-n)\right]_{mn},\ 1 \le m,n \le M$$

$$r(0) = 2(1-a)\sigma_T^2 + 2\sigma_N^2,$$

$$r(x) = \frac{2\sigma_T^2(1-a)\left(1-e^{-2\pi B_c/W}\right)}{1-e^{-2\pi B_c/W - j2\pi x/M}},$$

$$1-M \le x \le M-1.$$

Relationship 2:

$$\mathbf{h}_{EB}[k] - \mathbf{h}_{AB}[k-1] \sim \mathcal{CN}\left(\bar{\mathbf{h}}_{EB} - \bar{\mathbf{h}}_{AB}, \mathbf{G}\right), \quad (22)$$

where

$$\mathbf{G} = \mathrm{Cov}\{\mathbf{h}_{EB}[k] - \mathbf{h}_{AB}[k-1]\}$$

$$= \begin{bmatrix} 2\sigma_T^2+2\sigma_N^2 & \frac{r(-1)}{1-a} & \cdots & \frac{r(1-M)}{1-a} \\ \frac{r(-1)}{1-a} & 2\sigma_T^2+2\sigma_N^2 & \cdots & \frac{r(2-M)}{1-a} \\ \vdots & \vdots & \ddots & \vdots \\ \frac{r(1-M)}{1-a} & \frac{r(M-2)}{1-a} & \cdots & 2\sigma_T^2+2\sigma_N^2 \end{bmatrix}$$

As in the case of the static channel, Bob uses a simple hypothesis testing to decide whether the current transmission comes from Alice or someone else, with the verified channel-response measurement, $\mathbf{h}_{AB}[k-1]$, and the current measurement, $\mathbf{h}_t[k]$:

$$\mathcal{H}_0 : \mathbf{h}_t[k] = \mathbf{h}_{AB}[k],$$

$$\mathcal{H}_1 : \mathbf{h}_t[k] \ne \mathbf{h}_{AB}[k].$$

Again, M sub-channels are used for authentication. To simplify the discussion, we assume Bob knows the key parameters, including the AR-1 coefficient, a, the channel-coherence bandwidth, B_c, and the average tap power, σ_T. The test statistic is chosen as

$$T = \mathbf{t}^H \mathbf{t}$$

$$= 2\left(\mathbf{h}_t[k] - \mathbf{h}_{AB}[k-1]\right)^H \mathbf{R}^{-1}\left(\mathbf{h}_t[k] - \mathbf{h}_{AB}[k-1]\right) \quad (23)$$

where $\mathbf{t} = \sqrt{2}\mathbf{R}_d^{-H}\left(\mathbf{h}_t[k] - \mathbf{h}_{AB}[k-1]\right)$, and $\mathbf{R}_d$ is the Cholesky factorization of $\mathbf{R}$, with $\mathbf{R} = \mathbf{R}_d^H \mathbf{R}_d$.

When the transmission comes from Alice ($\mathcal{H}_0$ holds), the elements of $\mathbf{t}$ will be independent and identically distributed circularly symmetric complex Gaussian distributed $\mathcal{CN}(0,2)$, and thus the test statistic, $T_{\mathcal{H}_0}$, is chi-squared distributed with degrees of freedom *2M*:

$$T_{\mathcal{H}_0} = \mathbf{t}^H \mathbf{t} \sim \chi^2_{2M,0}. \quad (24)$$

The false alarm rate can be expressed as

$$\alpha = \Pr\left(T_{\mathcal{H}_0} > T_0\right)$$

$$= 1 - F_{\chi^2_{2M,0}}(T_0),$$

and the miss rate is

$$\beta = \Pr\left(T_{\mathcal{H}_1} \le T_0\right). \quad (25)$$

The test threshold, T_0, can be decided by first determining the required false alarm rate, and then computing the inverse cumulative density function

$$T_0 = F^{-1}_{\chi^2_{2M,0}}(1-\alpha). \quad (26)$$

2.1.3 Collaborative Authentication Schemes

According to the discussions above, the test statistic under the null hypothesis $\mathcal{H}_0$ is chi-squared distributed with $2M$ degrees of freedom. Now, consider that there are K independent authentication terminals (Bob_1, Bob_2, ..., Bob_K.) At first, all terminals individually compute the test statistic, and then the resulting test statistics, the T_k s, and the number of subcarriers used for authentication, the M_k s, are collected by the central terminal. The central terminal adds all the test statistics up to obtain a joint test statistic, $T_J = T_1 + T_2 + \ldots + T_K$. Under the null hypothesis, the test statistics calculated by different terminals will be independent chi-squared random variables. From the additive property, the joint test statistic will also be chi-squared distributed under $\mathcal{H}_0$:

$$T_{J|\mathcal{H}_0} = \sum_{k=1}^{K} T_k \sim \chi^2_{Q,0}, \quad (27)$$

where

$$Q = 2\sum_{k=1}^{K} M_k. \quad (28)$$

In this case, the false alarm rate can be obtained as

$$\alpha = P\left(T_{J|\mathcal{H}_0} > T_0\right) \quad (29)$$

and the miss rate is

$$\beta = P\left(T_{J|\mathcal{H}_1} \le T_0\right). \quad (30)$$

Under a specific assigned false alarm rate, the simulation results (in Section 4) showed that the collaborative scheme has a lower miss rate, and the ratio of miss-rate reduction was quite significant.

2.2 Propagation-Delay-Based Authentication

In the following, two scenarios are discussed. If the link propagation delay is measurable (for example, each radio frame has a time stamp attached to it), the delay pattern is considered to be the radio signature for physical-layer authentication. Otherwise, the delay difference between different receivers serves as an alternative.

2.2.1 Delay-Based Scheme

Denote the moving speed of Alice as v_A, and the temporal spacing of contiguous-frame transmissions as T_s. The propagation-delay variation, δ_k, can then be

expressed as

$$\delta_k = -\frac{v_A T_s}{c}\cos\theta_k , \tag{31}$$

where c is the velocity of light. We model the angle θ_k, included by the moving direction of Alice and the line-of-sight (LOS) direction to Bob_k (in the counterclockwise manner), as a uniform random variable $\Theta_k \sim U[0, 2\pi)$. The delay pattern is demonstrated in Figure 2.

We perform the simple hypothesis testing as

$\mathcal{H}_0$: The transmission attempts come from Alice

$\mathcal{H}_1$: The transmission attempts DO NOT come from Alice,

and the test statistic is chosen to be

$$t = \sum_{k=1}^{K}\left(\frac{\delta_k}{v_a T_s / c}\right)^2 , \tag{32}$$

where K denotes the number of receiving terminals involved in the collaborative authentication. With Equation (31), the test statistic can be rewritten under the null hypothesis, $\mathcal{H}_0$, as

$$T_{\mathcal{H}_0} = \sum_{k=1}^{K}\cos^2\Theta_k = \sum_{k=1}^{K} Y_k \tag{33}$$

Let $Y_k = \cos^2\Theta_k$. The moment-generating function $M_{Y_k}(x)$ of Y_k can be derived as

$$M_{Y_k}(x) = \frac{1}{\sqrt{\pi}} e^{\frac{x}{2}}\Gamma\left(\frac{1}{2}\right) I_0\left(-\frac{x}{2}\right), \tag{34}$$

where $\Gamma(z)$ is the gamma function, and $I_0(z)$ is the modified Bessel function:

$$\Gamma(z) = \int_0^\infty t^{z-1}e^{-t}dt ,$$

$$I_\alpha(z) = \sum_{m=0}^{\infty}\frac{1}{m!\Gamma(m+\alpha+1)}\left(\frac{z}{2}\right)^{2m+\alpha} .$$

Without loss of generality, the Θ_k s can be considered independent, and so can the transformed random variable Y_k s. By the principle of the *sum of independent random variables*, the moment-generating function of T is the product of the individual moment-generating functions:

$$M_{T|\mathcal{H}_0}(x) = \prod_{k=1}^{K} M_{Y_k}(x) . \tag{35}$$

With the statistical distribution of the test statistic, the hypothesis testing can be performed as in Section 2. Although the one-to-one mapping relationship holds among the probability density function, the cumulative density function, and the moment-generating function obtained from the same random variable, the inverse transform from the moment-generating function to the probability/cumulative density function, or, specifically, the test threshold value, is a difficult task. A practical method to obtain the threshold value based on the moment-generating function was described in the appendix of [10]. In addition,

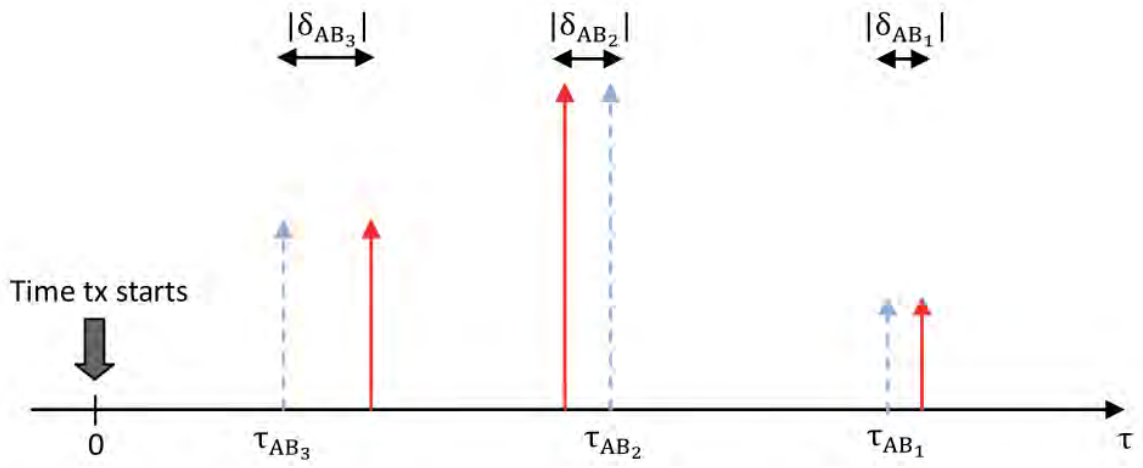

Figure 2. The propagation-delay pattern and delay variation.

we especially emphasize that the delay-based physical-layer authentication can be performed by a single receiver.

2.2.2 Delay-Difference-Based Scheme

When the propagation delay is not available, an alternative for physical-layer authentication is the delay-difference pattern, which is shown in Figure 3. The delay-difference pattern is built up from the absolute frame arrival times, measured by all receivers involved. In Figure 3, the blue dotted lines denote the verified frame reception, and the red solid lines denote the frame reception to be verified. The delay difference, $\delta_{1,2}$ and $\delta_{2,3}$, are used to verify the next frame reception. Under the null hypothesis, the delay-difference patterns of the next reception, $\delta'_{1,2}$ and $\delta'_{2,3}$, should remain like the verified pattern; otherwise, the two patterns would be unalike. Although the propagation delays, the τ_{AB_k} s, are unknown, they are useful for expressing the delay difference:

$$\delta_{k,l} = \tau_{AB_l} - \tau_{AB_k}, \tag{36}$$

$$\delta'_{k,l} = \tau'_{AB_l} - \tau'_{AB_k}$$

$$= \left(\tau_{AB_l} + \delta_l\right) - \left(\tau_{AB_k} + \delta_k\right) \tag{37}$$

$$= \left(\tau_{AB_l} - \tau_{AB_k}\right) + \left(\delta_l - \delta_k\right)$$

$$= \delta_{k,l} + \left(\delta_l - \delta_k\right),$$

where δ_k is the delay change. As mentioned in the previous section, the difference of delay change is defined as

$$\Delta\delta_{k,l} \triangleq \delta'_{k,l} - \delta_{k,l}$$

$$= \delta_l - \delta_k \tag{38}$$

$$= \left(-\frac{v_A T_s}{c}\cos\theta_l\right) - \left(-\frac{v_A T_s}{c}\cos\theta_k\right)$$

$$= \frac{v_A T_s}{c}\left(\cos\theta_k - \cos\theta_l\right),$$

so the test statistic is chosen to be

$$t = \sum_{k=1}^{K-1}\left(\frac{\Delta\delta_{k,k+1}}{v_A T_s / c}\right)^2. \tag{39}$$

Under $\mathcal{H}_0$, t can be further expressed as

$$T_{\mathcal{H}_0} = \sum_{k=1}^{K-1}\left(\cos\Theta_k - \cos\Theta_{k+1}\right)^2. \tag{40}$$

The $K-1$ terms in Equation (39) are now correlated random variables, so a closed form of the distribution $f_{T|\mathcal{H}_0}(z)$ is difficult to obtain as the test threshold. We adopt the simulation method to determine the test threshold and evaluate authentication performance.

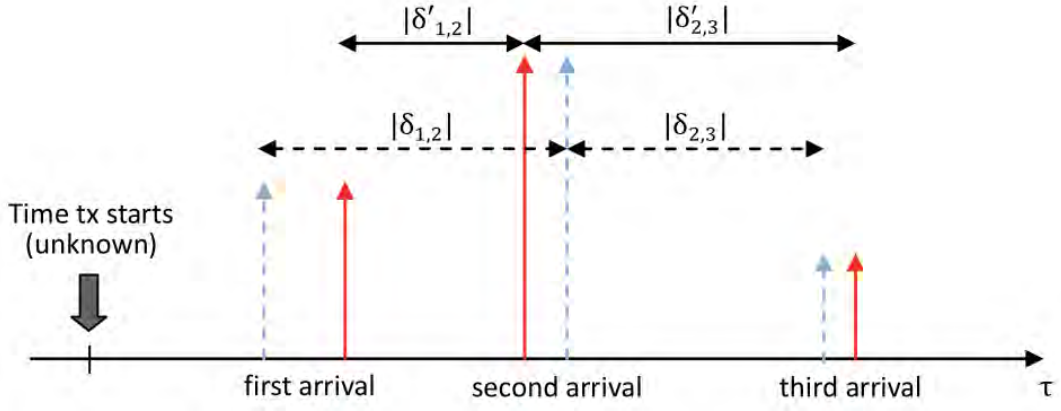

Figure 3. The delay-difference pattern

Section 3. Generalized Multi-Feature Authentication

In this section, we propose a manner of performing a collaborative authentication scheme, especially when multiple physical-layer characteristics (multi-feature) are treated. A hypothesis testing is applied to decide whether the current transmission comes from the same entity as the verified transmissions. The proposed scheme may also be adapted to formulate a cross-layer collaborative authentication scheme.

Assume there are authentication test statistics $T_1, T_2, \ldots T_S$ from different *S* physical characteristics. As mentioned in the previous section, the underlying distributions of the test statistics are known only when the null hypothesis holds. We apply a linear combination to the *S* statistics as

$$T = \sum_{s=1}^{S} w_s T_s , \tag{41}$$

where the w_s s are weighting factors with constraint $\sum_{s=1}^{S} w_s = 1$.

Under the null hypothesis, we denote the conditional moment-generating functions as $M_{T_1|\mathcal{H}_0}(x_1), M_{T_2|\mathcal{H}_0}(x_2), \ldots, M_{T_S|\mathcal{H}_0}(x_S)$. The moment-generating function of the jointly formulated test statistic, *T*, can be obtained as

$$M_{T|\mathcal{H}_0}(x) = \prod_{s=1}^{S} M_{T_s}(w_s x). \tag{42}$$

With the conditional moment-generating function, we then fix the required false alarm probability, α, to find the test critical value, η, and the hypothesis testing is performed as

$$\text{if } T \le \eta \Rightarrow \mathcal{H}_0 , \tag{43}$$

$$\text{if } T > \eta \Rightarrow \mathcal{H}_1 .$$

However, how to determine the weighting factors? Intuitively, a larger weighting factor, w_s, implies that we have more confidence in the validity of the test statistic, T_s. In other words, the assignment of weighting factors depends on the degrees of trust we have in the corresponding test statistics. Figure 4 shows three typical scenarios of a measured test statistic, $T(x)$, compared to the conditional expectation $\mu_{T(X)|\mathcal{H}_0}$. As mentioned above, although the underlying statistical distribution of $T(X)|\mathcal{H}_1$ is unknown, its realization is usually larger than $T(X)|\mathcal{H}_0$. When the measured statistic is smaller than $\mu_{T(X)|\mathcal{H}_0}$, as in Figure 4a, we can somewhat judge that the measurement tends to retain the null hypothesis. If $T(X)$ and $\mu_{T(X)|\mathcal{H}_0}$ are comparable, the uncertainty of which hypothesis holds rises. In another case, when $T(X)$ is larger than $\mu_{T(X)|\mathcal{H}_0}$, we tend to reject $\mathcal{H}_0$. In light of these discussions, we conclude that when the test statistic $T(x)$ is farther from the conditional expectation $\mu_{T(X)|\mathcal{H}_0}$, it brings stronger evidence no matter rejecting $\mathcal{H}_0$ or $\mathcal{H}_1$. The weighting factor is thus determined in a heuristic manner as

$$w_s = \frac{\left| T_s(x) - \mu_{T_s(X)|\mathcal{H}_0} \right|}{\sigma_{T_s(X)|\mathcal{H}_0}}, \tag{44}$$

where $\sigma_{T_s(X)|\mathcal{H}_0}$ denotes the standard deviation of $T_s(X)|\mathcal{H}_0$, which is used for normalization. After all weighting factors are computed by Equation (44), they are normalized by the constraint $\sum_{s=1}^{S} w_s = 1$:

$$w_s = \frac{w_s}{\sum_{j=1}^{S} w_j} . \tag{45}$$

Entry	Value
Central carrier frequency	2 GHz
Bandwidth	20 MHz
Coherence bandwidth (for time-varying channel)	333 kHz
Subcarrier spacing	15 kHz
Number of carriers used for physical-layer authentication	3 tones
Distance between Alice and Eve	0.2λ, 0.5λ, 0.8λ
SNR	7 dB, 10 dB, 13 dB

Table 1. The simulation parameters in the scenarios of both the static and time-varying channels.

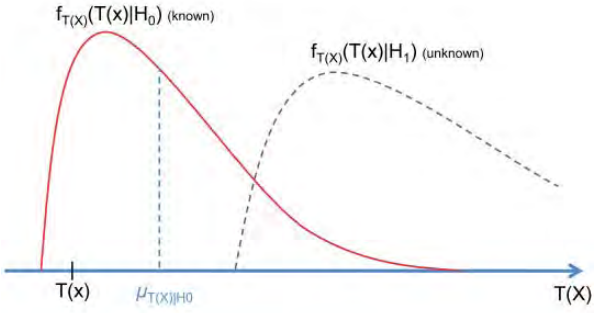

Figure 4a. a diagram of the test-statistic realization: The test statistic is smaller than the expectation $\mu_{T(X)|\mathcal{H}_0}$

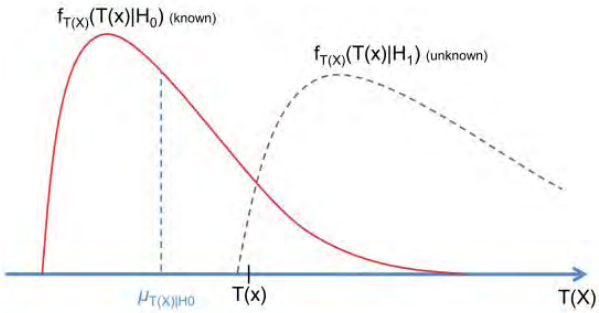

Figure 4b. A diagram of test statistic realization: The test statistic is comparable with the expectation of

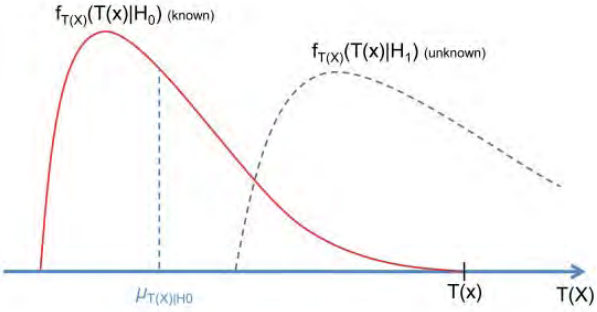

Figure 4c. A diagram of test statistic realization: The test statistic is larger than the expectation of $\mu_{T(X)|\mathcal{H}_0}$.

Section 4. Numerical Results

In this section, we show the performance of the proposed physical authentication methods. To capture the spatial correlation of the wireless channel, we exploited the 3GPP Spatial Channel Model (SCM)[11] to generate the channel response from Alice/Eve to Bob(s). The simulation parameters are summarized in Table 1.

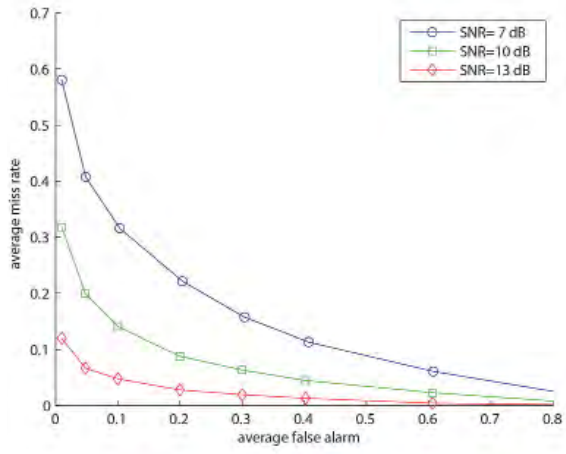

Figure 5. The receiver operating characteristic (ROC) curves for a single authentication terminal, with the distance between Alice and Eve fixed at 0.2λ.

4.1 The Performance of Channel-Response-Based Authentication

Figure 5 shows the receiver operating characteristic (ROC) curve under different signal-to-noise ratios (SNRs): the distance between Alice and Eve was fixed at 0.2λ (3 cm). As the false alarm rate was increased, the decision tended to reject the null hypothesis $\mathcal{H}_0$ (regarding the transmission from someone else): this lowered the test threshold as well as the miss rate. Another factor that influences the receiver operating characteristic curve is the SNR value. A lower SNR value gives a smaller non-centrality, which makes the corresponding non-central chi-squared random variable $T_{\mathcal{H}_1}$ approach the central chi-squared random variable $T_{\mathcal{H}_0}$: therefore, the miss rate rises.

The effect of changing the distance between Alice and Eve is shown in Figure 6. We only considered highly correlated scenarios. Again, by Equation (10), the higher correlation between $\mathbf{h}_{AB}$ and $\mathbf{h}_{EB}$ made the non-centrality δ smaller, and thus the miss rate was raised for a smaller Alice/Eve distance.

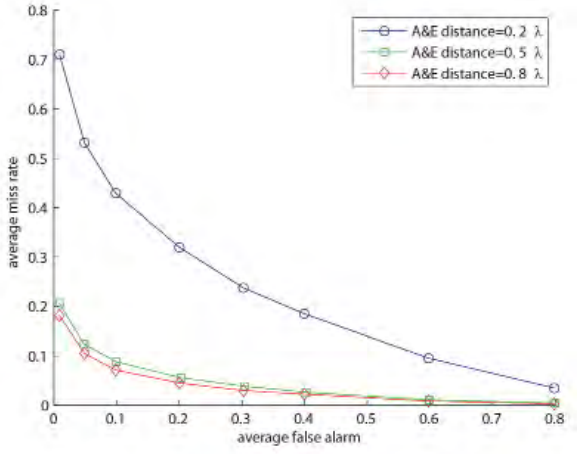

Figure 6. The receiver operating characteristic curves for a single authentication terminal, with the SNR value fixed at 7 dB.

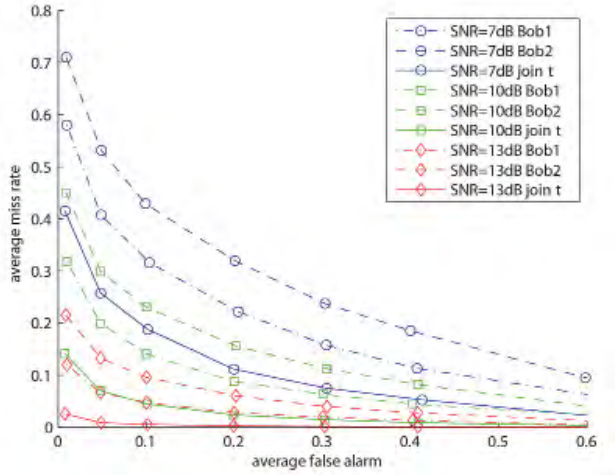

Figure 7a. Multiple authentication terminals in the static channel scenario (the distance between Alice and Eve was fixed at 0.2λ): the receiver operating characteristic curves for multiple authentication terminals.

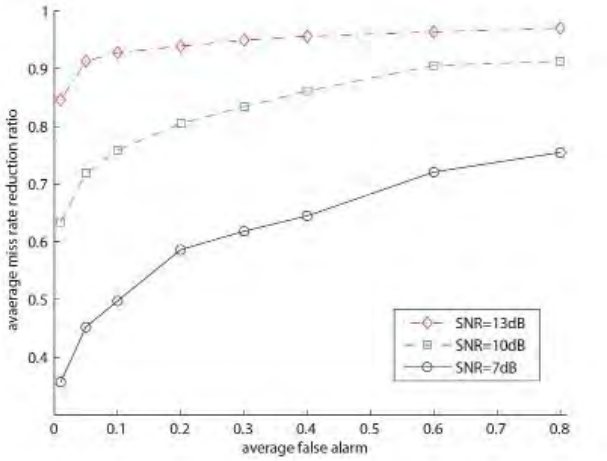

Figure 7b. Multiple authentication terminals in the static channel scenario (the distance between Alice and Eve was fixed at 0.2λ): the miss-rate reduction ratio. The baseline (single Bob) was obtained by averaging the performance of Bob_1 and Bob_2 .

We then examined the performance of collaborative authentication. In Figure 7, it was obvious that the collaborative scheme (solid curves) greatly improved authentication performance. Given the same false alarm rate, the collaborative scheme achieved a lower miss rate, regardless of the SNR value.

Entry	Value
Central carrier frequency	2 GHz
Moving speed of Alice	3 km/hr
Frame time spacing	100 ms
Distance between Alice and Eve	1.0λ , 1.5λ , 2.0λ

Table 2. The simulation parameters in the propagation-delay-based authentication.

Figure 7b highlights the reduction ratio of the average miss rate, which is defined as

$$\text{miss rate reduction ratio} = 1 - \frac{\text{multiple-Bob miss rate}}{\text{single-Bob miss rate}} . \quad (46)$$

It can be shown that the ratio of miss rate reduction is quite significant.

For the scenario of a time-variant channel, the time-variant part of the channel response equivalently enlarges the noise variance. The authentication performance therefore becomes worse compared to the static case, even though the SNR values are comparable. Nevertheless, the collaborative scheme still provided significant performance

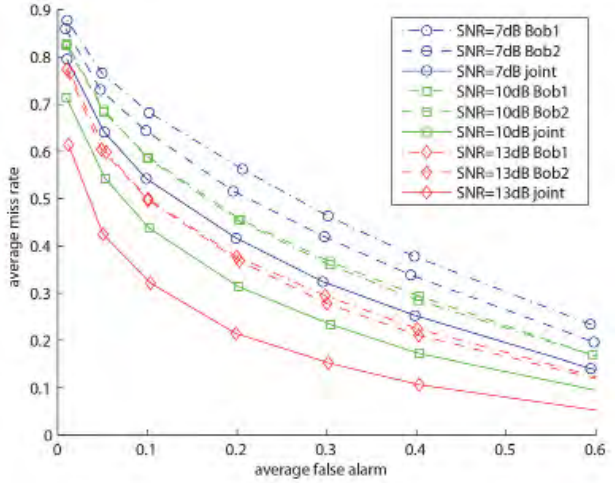

Figure 8a. Multiple authentication terminals in the time-variant channel scenario (the distance between Alice and Eve was fixed at 0.8λ): the receiver operating characteristic curves for multiple authentication terminals.

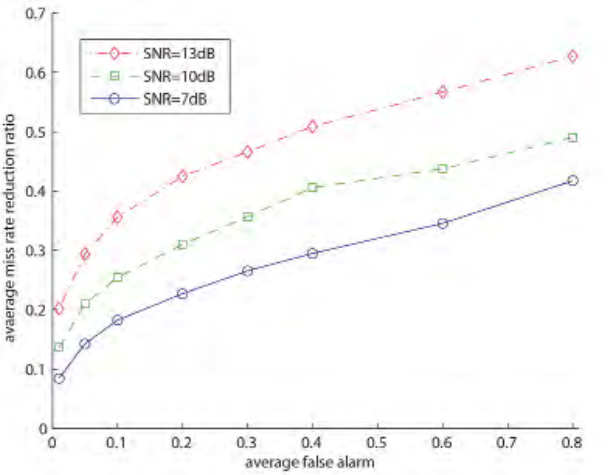

Figure 8b. Multiple authentication terminals in the time-variant channel scenario (the distance between Alice and Eve was fixed at 0.8λ): the miss-rate reduction ratio. The baseline (single Bob) was obtained by averaging the performance of Bob_1 and Bob_2 .

improvement, as shown in Figure 8. Figure 8b further highlights the ratio of miss rate reduction as defined in Equation (46).

4.2 The Performance of Propagation-Delay-Based Authentication

For the scenario of propagation delay, the parameters were as shown in Table 2. First, we demonstrated the performance evaluation (see Figure 9) of delay-based physical-layer authentication with respect to a different number of receivers. The initial distance between Alice and Eve was 1.5λ. Intuitively, when more receivers are involved, it is more difficult for Eve to falsify the propagation-delay signature from Alice, so the miss rate should be significantly reduced when the number of receivers increases.

The performance evaluation of delay-difference-based authentication is given in Figure 10. Note that the delay-difference signature cannot be obtained by a single receiver, so the delay-difference-based scheme must be performed in a collaborative manner. We changed the Alice-Eve distance and receiver numbers to evaluate the performance, and the simulation results conformed to our thoughts. Finally, we give a brief comparison of the two schemes, which is shown in Figure 11. Here, the term *degrees of freedom* means the count of summations performed to compute the test statistic (Equations (32) and (39)). For example, when three receivers are involved, the delay-based scheme possesses exactly three terms in the summation, whereas the delay-difference-based scheme has only two terms in the summation. The number of receivers was separately set to 2/3 in the delay-based/delay-difference-based schemes to obtain the same degrees of freedom.

In Figure 11, the blue lines denote the receiver operating characteristic curves of delay-based schemes, and the red lines denote the delay-difference-based schemes. Obviously, even under the same number of degrees of freedom, the delay-based scheme significantly outperformed the delay-difference-based scheme, especially when Alice and Eve were rather near. An intuitive explanation considers how the test statistics were formulated in the two schemes. When the degrees of freedom is K, the test statistics under $\mathcal{H}_0$ will be

$$T_{\text{delay}|\mathcal{H}_0} = \sum_{k=1}^{K} \cos^2 \Theta_k ,$$

and

$$T_{\text{delayDiff}|\mathcal{H}_0} = \sum_{k=1}^{K} \left(\cos\Theta_k - \cos\Theta_{k+1}\right)^2$$

$$= \sum_{k=1}^{K} \left[\cos^2\Theta_k + \cos^2\Theta_{k+1} - 2\cos\Theta_k \cos\Theta_{k+1}\right].$$

The expectations of $T_{\text{delay}|\mathcal{H}_0}$ and $T_{\text{delayDiff}|\mathcal{H}_0}$ are related by

$$E\left[T_{\text{delayDiff}|\mathcal{H}_0}\right] = \left(2 - \frac{2}{K}\right) E\left[T_{\text{delay}|\mathcal{H}_0}\right] \text{ if } K \geq 2 , \quad (47)$$

which means the realization of $T_{\text{delayDiff}|\mathcal{H}_0}$ is about twice the value of $T_{\text{delayDiff}|\mathcal{H}_0}$, on average. When the required

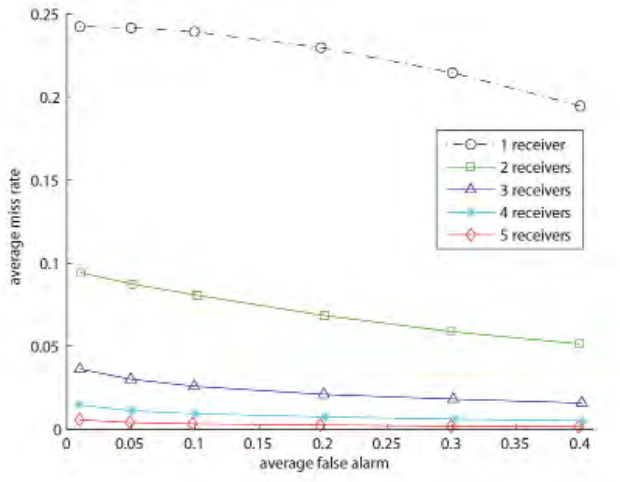

Figure 9. The performance evaluation of delay-based authentication for different numbers of

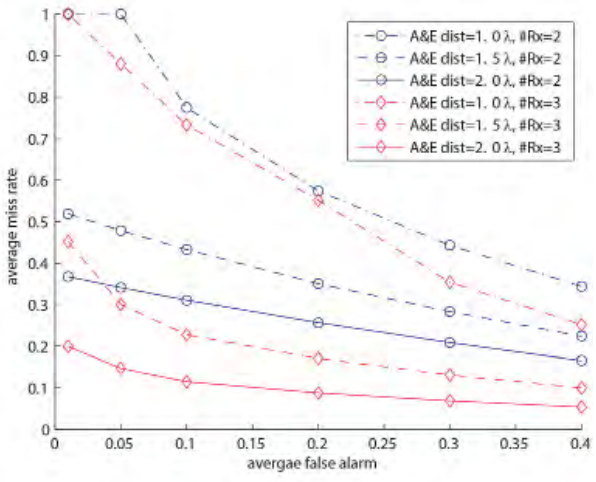

Figure 10. The performance evaluation of delay-difference-based authentication.

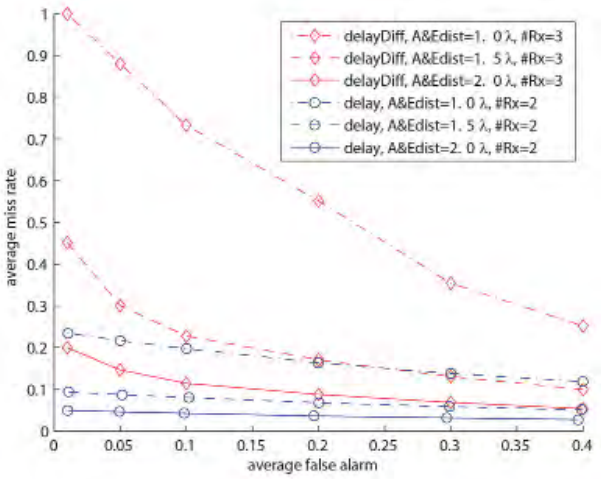

Figure 11. A comparison of the delay-based scheme and the delay-difference-based scheme. The degrees of freedom were both set to two.

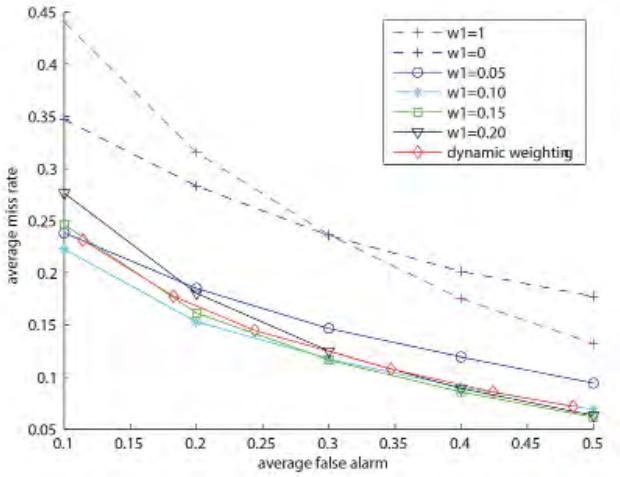

Figure 12. The receiver operating characteristic curves with respect to different weighting factors.

false alarm rate is fixed, the test threshold of the delay-difference-based scheme will be higher, which leads to a higher probability of accepting the authentication, thus making the miss rate higher.

4.3 The Performance of Generalized Multi-Feature Authentication

Figure 12 demonstrates the performance of the proposed multi-feature collaborative authentication scheme. Here, we performed the collaborative authentication by adopting two independent authentication processes. T_1 is the test statistic based on the time-variant channel response in Section 2.1, and T_2 is from the propagation-delay-based scheme in Section 2.2. The SNR was set to 10 dB, six tones were used to compute T_1, the Alice-Eve distance was set to 0.8λ (12 cm), and two receiving terminals were involved. Since only two test statistics were present, we had two weighting factors, w_1 and w_2, with constraint $w_1 + w_2 = 1$. Different weighting-factor settings were used to show how the authentication performance was influenced. The receiver operating characteristic curve labeled $w_1 = 1$ means only T_1 was exploited for authentication. Obviously, as w_1 decreased, the performance was improved, with a lower miss rate, which demonstrated the effectiveness of collaborative authentication. The simulation results showed that the optimum receiver operating characteristic curve was achieved when w_1 was approximately 0.1. If we kept on decreasing w_1, the miss rate again rose. The curve labeled *dynamic* means that we dynamically changed the weighting factors based on Equation (44). We could see that the performance was comparable with the optimum weighting. In fact, the optimum weighting depends on the statistical distributions of the test statistics. A large performance improvement could only be achieved when the weighting factors were properly determined. The proposed weighting-factor selection scheme determined the coefficients from the test statistics themselves, without manual adjustment, but the authentication accuracy was comparable to the optimum weighting.

Section 5. Conclusion

In this work, we utilized the physical-layer characteristics to enhance and complement traditional cryptographic authentication schemes. The physical-layer characteristics carry location-specific information, so it is more difficult for malevolent devices to spoof legitimate devices. Two characteristics, the frequency-domain channel response and the propagation delay, were considered, and the performance evaluation showed their validity. More specifically, we considered the possibility of collaborative authentication schemes. First, we improved the authentication accuracy by combining the same type of characteristic measurements from multiple receiving terminals. We then combined authentication results from different types of characteristic measurements to provide a stronger physical-layer authentication. The proposed multi-feature collaborative authentication process is general.

In our opinion, it could be adapted to a cross-layer collaborative authentication process with moderate modification, to formulate a more-powerful non-cryptographic cross-layer authentication mechanism.

6. References

1. N. Borisov, I. Goldberg, and D. Wagner, "Intercepting Mobile Communications: The Insecurity of 802.11," Proceedings of The 7th Annual International Conference on Mobile Computing and Networking, MobiCom '01, ACM, 2001, pp. 180-189.

2. W. Arbaugh, N. Shankar, Y. Wan, and K. Zhang, "Your 802.11 Wireless Network Has No Clothes," *Transactions on IEEE Wireless Communications*, **9**, 6, December 2002, pp. 44-51.

3. J. R. Walker, S. P. J. Walker, and I. Corporation, "Unsafe At Any Key Size; An Analysis of The WEP Encapsulation," *Transactions on Intelligence/Sigart Bulletin*, 2000.

4. K. Zeng, K. Govindan, and P. Mohapatra, "Non-Cryptographic Authentication and Identification in Wireless Networks," *Transactions on IEEE Wireless Communications*, **17**, October 2010, pp. 56-62.

5. M. Demirbas and Y. Song, "An RSSI-Based Scheme for Sybil Attack Detection in Wireless Sensor Networks," Proceedings of the 2006 International Symposium on World of Wireless, Mobile and Multimedia Networks, WOWMOM '06, 2006, pp. 564-570.

6. L. Xiao, L. J. Greenstein, N. B. Mandayam, and W. Trappe, "Fingerprints in the Ether: Using the Physical Layer for Wireless Authentication," IEEE International Conference on Communications (ICC), 2007, pp. 4646-4651.

7. L. Xiao, L. Greenstein, N. Mandayam, and W. Trappe, "Using the Physical Layer For Wireless Authentication in Time-variant Channels," *Transactions on IEEE Wireless Communications*, **7**, 7, July 2008, pp. 2571-2579.

8. L. Xiao, L. J. Greenstein, N. B. Mandayam, and W. Trappe, "A Physical-Layer Technique to Enhance Authentication for Mobile Terminals," Proceedings of IEEE International Conference on Communications (ICC), May 2008, pp. 1520-1524.

9. . Molisch, *Wireless Communications*, New York, Wiley, 2005.

10. A. Martinez, A. Guillen i Fabregas, and G. Caire, "Error Probability Analysis of Bit-Interleaved Coded Modulation," *Transactions on IEEE Information Theory*, **52**, 1, January 2006, pp. 262-271.

11. "Spatial Channel Model for Multiple Input Multiple Output MIMO Simulations (Release 6)," 3rd Generation Partnership Project (3GPP), Tech. Rep., September 2003.

Electro-Optic Modulator Using an Antenna-Coupled-Electrode Array and a Polarization-Reversed Structure for a Radar Tracking System

Naohiro Kohmu, Hiroshi Murata, and Yasuyuki Okamura

Graduate School of Engineering Science
Osaka University
Osaka, Japan
E-mail: naohiro.kohmu@gmail.com; murata@ee.es.osaka-u.ac.jp

This is one of the invited Finalist papers from the AP-RASC 2013 Student Paper Competition.

Abstract

We have proposed an electro-optic (EO) modulator utilizing an antenna-coupled-electrode (ACE) array and polarization-reversed structures. For effective optical modulation in millimeter-wave (MMW) frequency ranges, a thin (~50 μm-thick) $LiNbO_3$ (LN) crystal stacked structure on a low-k material substrate is adapted to the device. By using the thin LN stacked structure, an effective electrical length/volume of the device becomes large compared with the EO crystal substrate devices, and a large antenna aperture size and long standing-wave modulation electrode are obtainable. Furthermore, the degradation of the modulation efficiency by substrate-mode resonance can also be reduced. Higher-efficiency optical modulation is therefore expected. In addition, by utilizing polarization-reversed structures and multiple optical waveguides in the EO antenna-coupled-electrode modulator, direction-of-arrival estimation of a wireless signal can also be obtained. The proposed modulator was designed in the 60 GHz band. Its basic operation was successfully demonstrated, with an improvement of ~10 dB modulation efficiency compared to the conventional device using only an LN substrate. The control of the EO modulation directivity in four-channel optical waveguides was also successfully demonstrated for the first time, as far as we know. The measured peak conversion angles for the four-optical-channel waveguides were −30°, −15°, 0°, and 15°, respectively, and the channel crosstalk was below −13 dB. Applications of the proposed device to a radar tracking system are also discussed.

1. Introduction

Recently, millimeter-wave (MMW) radar systems are attracting a lot of interest. This is because millimeter-wave radar systems have higher resolution compared to microwave (MW) radar systems, owing to the short wavelength of a millimeter-wave signal [1]. However, millimeter-wave signals are affected by large transmission loss in both free space and metal cables, compared with microwave signals. To the contrary, the silica optical fiber has the lowest transmission loss (~0.2 dB/km ($\lambda = 1.55$ μm)) in any transmission cable. Huge transmission bandwidth (over a THz) and negligible crosstalk are also advantages of the optical fiber. By using the optical fiber for millimeter-wave signal transmission, the transmission loss of millimeter-wave signals can be drastically reduced [2, 3]. The conversion of wireless millimeter-wave signals to light-wave signals is therefore important in constructing millimeter-wave radar systems using radio-over-fiber (ROF) technology.

Electro-optic (EO) antenna-coupled-electrode (ACE) modulators for converting wireless microwave/millimeter-wave signals to light-wave signals have been proposed and developed [4-9]. EO antenna-coupled-electrode modulators have many advantages: they have a simple and compact structure, and require no external power supply for their operation. In addition, the microwave/millimeter-wave signals received by an array of these antennas can be synthesized without specific signal-synthesis circuits, since the synthesis can be done through successive EO

modulation by microwave/millimeter-wave signals during the light-wave propagation under the antenna-coupled-electrode array.

Recently, we have proposed EO modulators using an antenna-coupled-electrode array and a polarization-reversed structure of ferroelectric crystals [6, 8]. In the EO antenna-coupled-electrode array modulators adopting polarization-reversed structures, the phase of signal synthesis between the microwave/millimeter-wave signal and the light-wave signal can be controlled by the polarization-reversed structure. By only changing the polarization-reversed patterns in these modulators, the directivity in the conversion from wireless millimeter-wave signals to light-wave signals can therefore be designed. In addition, by utilizing multiple optical waveguides with different polarization-reversed structures in these modulators, direction-of-arrival estimation of a wireless signal is also possible. The basic operations of these interesting devices were demonstrated in the 15 GHz to 40 GHz frequency range [6, 8].

However, there are remaining issues in the EO antenna-coupled-electrode modulators for higher-frequency-range applications. The reported EO antenna-coupled-electrode modulators were fabricated on ferroelectric crystals like $LiNbO_3$ (LN) and $LiTaO_3$ (LT). Since their dielectric constants in the millimeter-wave ranges are rather large ($\varepsilon_r = 23$ to 43), an effective electrical length/volume of the device is rather small. An antenna aperture size and an interaction length between the millimeter-wave and light-wave therefore becomes small. In addition, the effect of substrate resonant modes may cause degradation of the device's performance [10, 11]. Owing to these issues, their modulation efficiency was small in the higher frequency ranges [9, 10].

In this paper, we report a new EO modulator using a thin LN-crystal-stacked structure on a small-dielectric-constant material substrate (SiO_2) for high-efficiency optical modulation in the higher frequency ranges. By using the stacked structure, an effective electrical length/volume of the device becomes large compared with EO crystal substrate devices, and a large antenna aperture size and long standing-wave modulation electrode are obtainable. In addition, by using a thin (~50 μm) LN crystal, the effect of substrate resonant modes can be reduced [11]. High-efficiency optical modulation is therefore expected. The basic operations of the proposed device in the 60 GHz band were experimentally demonstrated.

In the following sections, the device's structure, operational principle, analysis, design, fabrication, and experiments are presented. Applications of the EO antenna-coupled-electrode modulator to a radar tracking system are also discussed.

2. Device Structure

Figure 1 shows the basic structure of the proposed EO antenna-coupled-electrode modulator. A thin *z*-cut LN crystal is stacked on a small-dielectric-constant-material substrate such as SiO_2. They can be attached by use of an adhesive. On the reverse surface of the thin LN crystal, optical waveguides and the antenna-coupled-electrode array are fabricated, as shown in Figure 1b.

The antenna-coupled-electrode is composed of a pair of patch antennas and a one-wavelength-long standing-wave resonant electrode, using a coupled-microstrip line

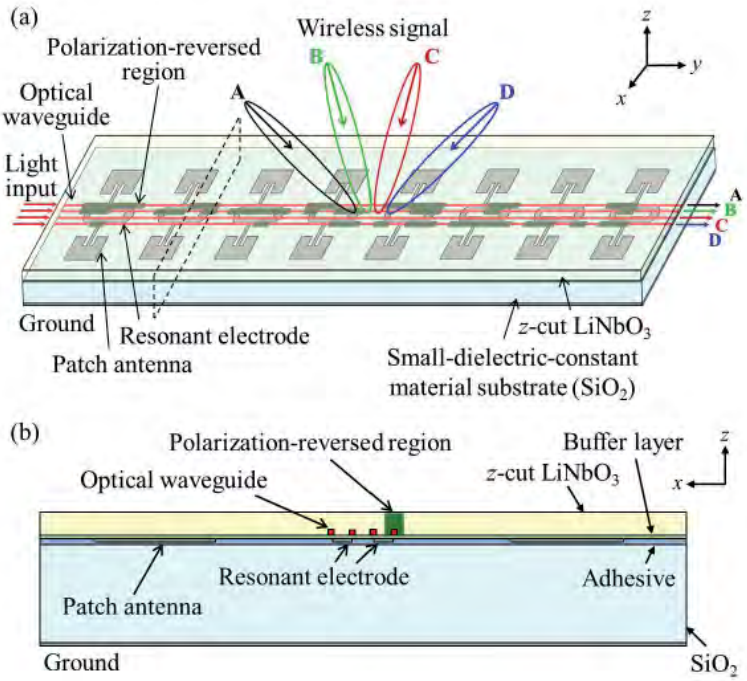

Figure 1. The basic structure of the proposed device (a) a whole view of the device, (b) a cross-sectional view of the device in the *xz* plane.

(CMSL) with shorted ends [9]. The patch antennas and the resonant electrode are connected to each other by use of a microstrip line (MSL) with the symmetric configuration shown in Figure 1a, that is, a mirroring configuration from the center line between the two microstrip lines in the coupled-microstrip line. Several straight single-mode optical waveguides are fabricated on the reverse side of the LN crystal. The waveguides are precisely aligned so as to be onto the edges of the coupled-microstrip line resonant electrodes, as shown in Figure 1b. By utilizing polarization-reversed structures in each optical waveguide, several wireless millimeter-wave signals, coming from different directions to this device, can be discriminated among at the same time according to their irradiation angles, as shown in Figure 1a [6, 8]. This is applicable to radar tracking systems.

By using the thin (~50 μm) LN crystal stacked structure on the SiO_2 substrate, an effective electrical length/volume of the device becomes large compared with LN substrate devices. The antenna aperture size of the proposed device becomes four times larger than that of the LN substrate device.

The effect of the substrate mode can also be reduced, since the thin LN crystal is used. A high-efficiency optical modulation is therefore expected.

There are odd and even modes in the coupled-microstrip line. The odd mode in the coupled-microstrip line is utilized for optical modulation in the proposed device, since the odd mode has strong electric fields near the optical waveguides [12]. In the proposed devise, we utilized the selective coupling technique to the odd mode from a pair of the two patch antennas described below.

When an *x*-polarized wireless millimeter-wave signal is irradiated onto the device with patch antennas, in-phase surface currents are induced on them along the *x* axis. The induced current signals are transferred from the pair of antennas to the coupled-microstrip-line resonant electrode through the microstrip lines with the same length.

It should be noted that their feeding points from the pair of patch antennas are in the opposite sides compared with the surface current flow directions on the antennas. Therefore, the supplied signals from the two patch antennas to the coupled-microstrip-line resonant electrode are out of phase. As a result, effective coupling to the odd mode in the coupled-microstrip line can be obtained. On the contrary, the coupling to the even mode in the coupled-microstrip line is very small, since the feeding conditions from the two patch antennas to the coupled-microstrip-line electrode are out of phase. High-efficiency optical modulation by use of strong electric fields in the odd mode is therefore obtained [9].

3. Operational Principle

Figure 2 shows the cross-sectional view of the device along the optical waveguide, when a wireless millimeter-wave signal is irradiated onto the device at an angle of θ. The wireless signal is received by the patch antennas, and the received millimeter-wave signal is transferred to the modulation electrode. A standing-wave electric field is then induced on each resonant electrode, as shown in Figure 2b. The standing-wave electric field at the *h*th modulation electrode can be expressed by the following equation [8]:

$$E_m^h(y,t,\theta) = E_0 \sin\left\{n_m k_m \left[y-(h-1)d\right]\right\}, \quad (1)$$

$$\cos\left[\omega_m t - n_0 k_m (h-1) d \sin\theta\right]$$

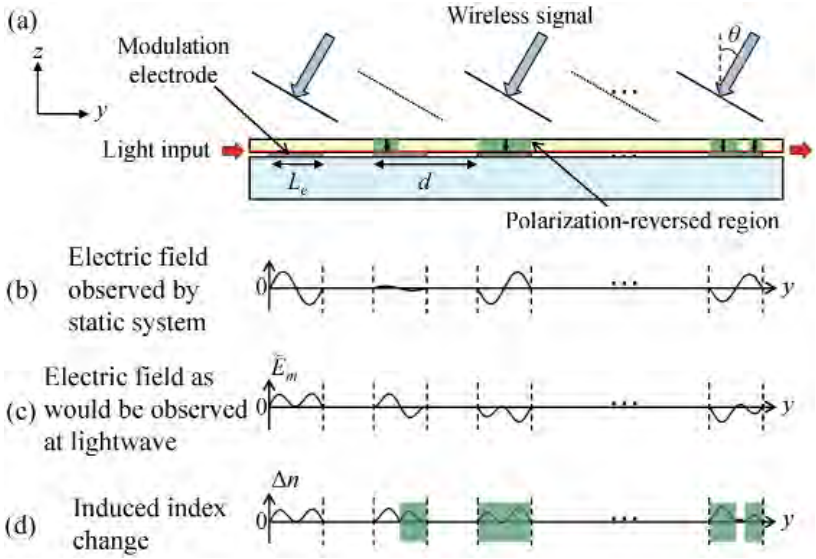

Figure 2. (a) A cross-sectional view of the EO antenna-coupled-electrode modulator, (b) the standing-wave electric field, (c) the modulation electric field as would be observed at a propagating light wave, and (d) the induced refractive index change through the Pockels effect.

where E_0 is amplitude of the electric field on the electrode, n_m is the effective refractive index of the millimeter wave in the coupled-microstrip-line resonant electrode, d is the distance between the antenna-coupled electrodes, k_m is the wavenumber of the millimeter wave in vacuum, ω_m is the angular frequency of the millimeter-wave signal, and n_0 is the refractive index of the millimeter wave in air ($=1$).

In order to obtain optical the modulation characteristics in the proposed devise, the electric field as it would be observed in the propagating light in the waveguide should be considered, since it takes a finite time for the light wave to pass through the waveguide [13-15]. This can be obtained by taking into account the transit time of the light wave, as follows. Using the transformation of $y' = y - v_g t$ (where y' is the point of the light wave in the coordinate system moving with the light wave, and v_g is the group velocity of the light wave), Equation (1) is transformed into the following equation:

$$\tilde{E}_m^h(y; f_m) = E_m^h\left(y, \frac{y-y'}{v_g}, \theta\right)$$

$$= E_0 \sin\left\{n_m k_m \left[y-(h-1)d\right]\right\}$$

$$\cos\left[n_g k_m y - n_0 k_m (h-1) d \sin\theta + \varphi\right], \qquad (2)$$

where n_g is the group index of the light wave propagating in the waveguide, and $\phi = n_g k_m t$ is an initial phase. The fields expressed by Equation (2) are plotted in Figure 2c.

The modulation index (depth), D, of the EO modulator using an antenna-coupled-electrode array is calculated by the integration of the electric field as would be observed by the light wave. The modulation index, D, can therefore be expressed by the following equation, when a TM-polarized light wave is used:

$$D(\theta) = \frac{\pi r_{33} n_e^3}{\lambda} \Gamma \sum_{h=1}^{N} \int_{(h-1)d}^{(h-1)d+L_e} f_{pol.}(y) \tilde{E}_z(y, \theta; h)\, dy, \quad (3)$$

where λ is the wavelength of the light wave in vacuum, n_e is the extraordinary refractive index of the suspended LN, γ_{33} is the Pockels coefficient for the suspended LN, Γ is the overlapping factor between distributions of the light-wave guided mode and the modulation electric field distribution, L_e is the length of the resonant electrode, and N is the total number of antenna-coupled electrodes. $f_{pol.}(y)$ expresses the pattern of the spontaneous polarization distribution along the optical waveguide. $f_{pol.}(y)$ is defined as $+1$ at a non-polarization-reversed region, and -1 at a polarization-reversed region.

The electric field as would be observed at the propagating light wave contains positive and negative regions, as shown in Figure 2c. The modulation index may therefore be reduced by the effect of the negative region if a non-polarization-reversed scheme is used. By utilizing a polarization-reversed scheme, as shown in Figures 2a and 2d, the modulation efficiency can be enhanced from wireless the millimeter-wave signal of the angle, θ. This means that the modulation index, $D(\theta)$, depends on the angle of incidence, θ, when the polarization-reversed structure is fixed. The directivity of the EO antenna-coupled-electrode modulator in the conversion from millimeter-wave signals to light-wave signals can therefore be controlled by changing the polarization-reversed patterns.

4. Analysis and Design

4.1 Directivity

The polarization-reversed patterns for a required irradiation angle, θ, can be designed using Equation (3).

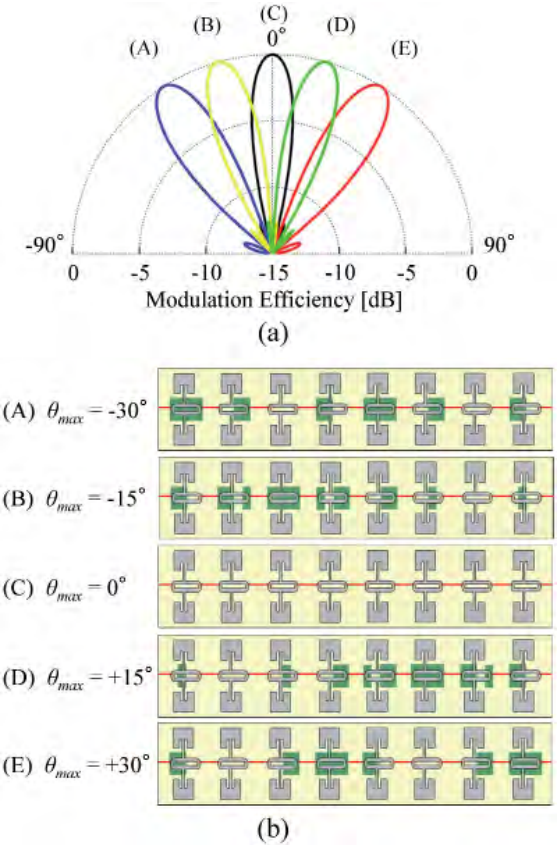

Figure 3. (a) The calculated directivities in millimeter-wave light-wave conversion, and (b) the corresponding polarization-reversed patterns.

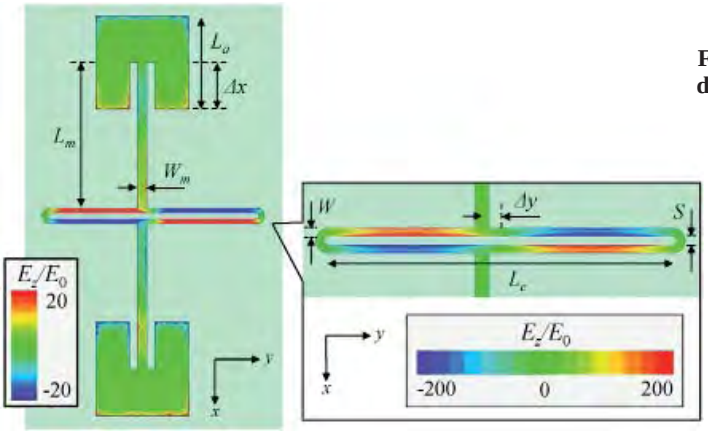

Figure 4. The calculated electric-field distributions on the antenna-coupled-electrode's surface at 58 GHz.

Figure 3a shows the calculated directivities in the conversion from millimeter-wave signals to light-wave signals, when the design parameters in Table 1 were assumed for the proposed device. Figure 3b also shows the corresponding polarization-reversed patterns. By utilizing polarization-reversed structures in the LN crystal, a peak angle (main-beam angle) in millimeter-wave – light-wave conversion can be almost arbitrarily designed. This characteristic is useful for radar tracking systems.

4.2 Antenna-Coupled Electrode

In the design of the proposed device, precise tuning of resonant frequencies of the patch antennas and the coupled-microstrip-line resonant electrode and their impedance matching are important for effective operation. They were therefore analyzed in detail by use of the three-dimensional field-analysis software, Ansoft *HFSS ver. 12*.

First, the operational frequency was set at 58 GHz. The thickness of the z-cut LN crystal was assumed to be 50 μm. The relative permittivity tensor of the LN was set to be $(\varepsilon_{rx}, \varepsilon_{ry}, \varepsilon_{rz}) = (43, 43, 28)$. The small-dielectric-constant material was assumed to be 0.25 mm-thick fused silica (SiO_2), with a relative permittivity of $\varepsilon_r = 4$. The length of the square patch antenna was set at a half wavelength, based on standard antenna theory [16, 17]. The length of the coupled-microstrip-line standing-wave electrode was set at one wavelength with shorted ends, as shown in Figure 1. The electrodes were assumed to be composed of a 1 μm-thick Al film. A 0.2 μm-thick SiO_2 buffer layer was also inserted between the antenna-coupled-electrode and the LN crystal.

Effective index of modulation wave, n_m	4.25
Group index of light wave, n_g	2.19
Resonant electrode length, L_e	1.217 mm
Distance between the ACEs, d	2.358 mm
Total number of the ACEs, N	8
Peak conversion angle, θ_{max}	–30°, –15°, 0°, 15°, 30°

Table 1. The parameters used in the design of the directivities.

The patch antennas and the coupled-microstrip-line resonant electrode were next uncoupled, and dummy input ports were set to them through 50 Ω matched microstrip lines. After that, they were independently analyzed in detail. The conditions for the resonance at 58 GHz and impedance matching at 50 Ω were derived by monitoring their reflection coefficients.

Finally, the tuned patch antennas and coupled-microstrip line electrode were connected and analyzed again. Figure 4 shows the calculated electric-field distribution on the electrode's surface in the antenna-coupled electrode when an *x*-polarized plane-wave millimeter-wave signal at 58 GHz normally irradiated the antenna-coupled-electrode from free space. We could see that the patch antennas were operating in the fundamental mode, and a resonant standing-wave electric field was induced along the coupled-microstrip-line electrode. The maximum electric field at the coupled-microstrip-line electrode was ~200 times that of the input electric field.

Figure 5 shows the calculated distributions of the *z* component of the electric field for optical modulation, E_z, at the edge of the coupled-microstrip line electrodes. For comparison, the E_z for our previous device was also plotted [9]. It was shown that the amplitude of the standing wave in the proposed device was enhanced ~1.4 times compared to the previous device. A high-efficiency optical modulation was therefore expected. The parameters of the designed antenna-coupled electrode are summarized in Table 2.

5. Device Fabrication

Based on the design, the proposed devices were fabricated using a *z*-cut LN and SiO_2. The LN crystal and the SiO_2 substrates were 0.25 mm thick and 20 mm long.

First, the polarization-reversed structures were fabricated in the LN crystal using the pulse-voltage application method. The four different polarization reversal patterns shown in Figure 3b were fabricated.

Operational frequency, f_m	58 GHz
Al patch/electrode metal thickness	1 μm
z-cut $LiNbO_3$ relative permittivity tensor, $(\varepsilon_{rx}, \varepsilon_{ry}, \varepsilon_{rz})$	(43, 43, 28)
z-cut $LiNbO_3$ thickness, t_{LN}	50 μm
SiO_2 relative permittivity, ε_r	4
SiO_2 thickness, t_{SiO2}	0.25 mm
Patch antenna length, L_a	546 μm
Recessed microstrip line feeding position, Δx	271 μm
Resonant electrode length, L_e	1.217 mm
Resonant electrode separation, S	30 μm
Resonant electrode width, W	30 μm
Feeding position to coupled-microstrip line, Δy	66 μm
Microstrip line width, W_m	50 μm
Microstrip line length, L_m	850 μm

Table 2. The parameters of the designed antenna-coupled electrode.

Second, four straight single-mode optical waveguides for 1.55 μm-wavelength light waves were fabricated on the LN crystal by using the annealed-proton-exchange method, with melted benzoic acid at 240° C for 90 minutes [18]. A 0.2 μm-thick SiO_2 buffer layer was deposited on the surface of the LN crystal after the proton-exchange process. The SiO_2 buffer layer was fabricated by use of magnetron RF sputtering.

Third, the antenna-coupled-electrode array was fabricated on the LN crystal using a 1 μm-thick Al film. The Al film was formed by use of electron-beam vapor deposition, and the liftoff technique was used for the patterning of the antenna-coupled-electrode array. A thermal annealing process at 350° C for one hour was also done to improve the optical waveguide performance after the electrode forming.

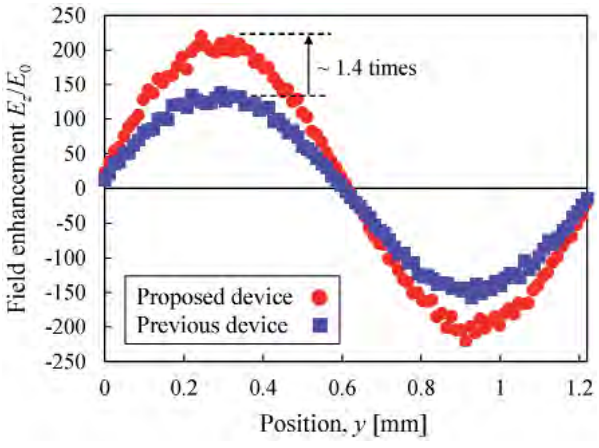

Figure 5. The calculated electric-field distributions along the coupled-microstrip-line resonant electrode at 58 GHz.

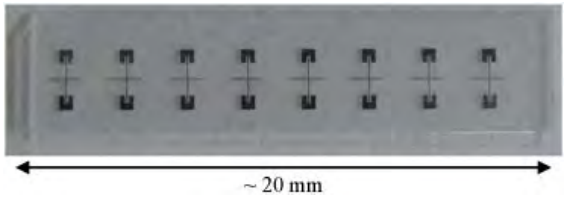

Figure 6. A photograph of the fabricated device, just before the final deposition of the reverse side for the ground electrode.

Fourth, the LN with the antenna-coupled-electrode array was flipped over, and was connected to the SiO_2 using a UV adhesive. After that, by polishing, the thickness of the LN crystal was reduced from 0.25 mm to 50 μm.

Finally, a 1 μm-thick Al film was deposited on the reverse side of the SiO_2 substrate for the ground electrode. A photograph of the fabricated devices just before the final deposition on the reverse side for the ground electrode is shown in Figure 6.

6. Experiment

The performance of the fabricated device was measured using the experimental setup shown in Figure 7. A continuous-wave light wave with a wavelength of 1.55 μm from a distributed-feedback laser was input to the optical waveguide of the fabricated device. A wireless millimeter-wave signal from an oscillator was amplified and irradiated onto the device using a standard horn antenna (Flann Microwave Ltd. Model 25240-20, ~19 dBi gain at 58 GHz). The modulated light wave from the device was measured by use of an optical spectrum analyzer.

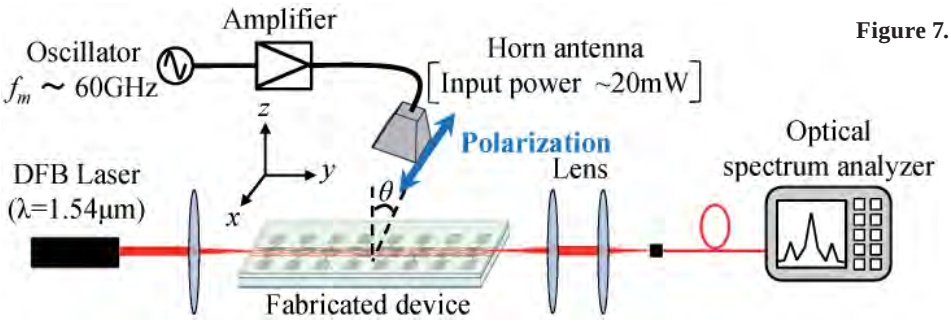

Figure 7. The experimental setup.

The examples of the measured optical spectrum are shown in Figure 8, when the millimeter-wave signal's frequency was 57.3 GHz, the irradiation angle was 0°, and the supplied millimeter-wave signal power to the horn antenna was 20 mW. The optical sidebands were clearly observed. The measured spectrum ratio between the optical carrier, P_c, and the first sideband, P_{s1}, was −38 dB.

Figure 9 shows the measured frequency dependence of the optical modulation efficiency. We defined the optical modulation efficiency as the ratio between the intensities of the optical carrier and the first sideband (P_{S1}/P_c). It was shown that the modulation efficiency was improved by ~10 dB compared to the previous device.

The measured directivities in four optical waveguides are shown in Figure 10. The measured peak conversion angle for the four-channel optical waveguides were −30° , −15° , 0°, and 15°, respectively, and the channel crosstalk was below −13 dB. These were in good agreement with the theoretically calculated values.

7. Discussion and Conclusions

The basic operation of the proposed device was successfully verified in the experiments. The modulation efficiency at the peak frequency was improved by ~10 dB compared with our previous device. In addition, the measured peak conversion angle for the four-channel optical waveguides and the channel crosstalk were in good agreement with the designed values.

The proposed device is an optical phase modulator. In order to apply this device to radar tracking systems, several photonic technologies can be used, as follows. Phase-modulated light-wave signals from the device can be filtered by use of an optical sharp-cut filter to cut the lower or upper sideband. After that, the filtered signals are amplified by an erbium-doped optical-fiber amplifier. The amplified light-wave signals are then detected by use of a high-speed photodetector. By monitoring the detected signals, the proposed EO modulator can identify the direction of wireless millimeter-wave signals.

This modulator can therefore be used in radar tracking systems. In addition, by launching the light-wave signals from both sides of the EO modulator with optical circulators, wireless signals coming from eight different directions can be identified at the same time, and wide-angle radar tracking can be expected.

We are now trying to measure the performance of the fabricated EO modulator for millimeter-wave radar tracking applications in detail.

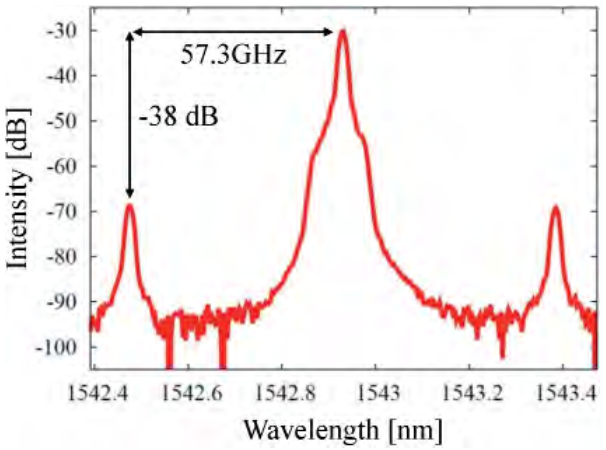

Figure 8. The measured output spectrum.

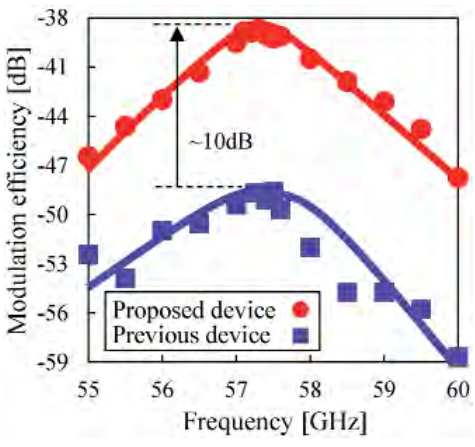

Figure 9. The measured and calculated frequency dependencies.

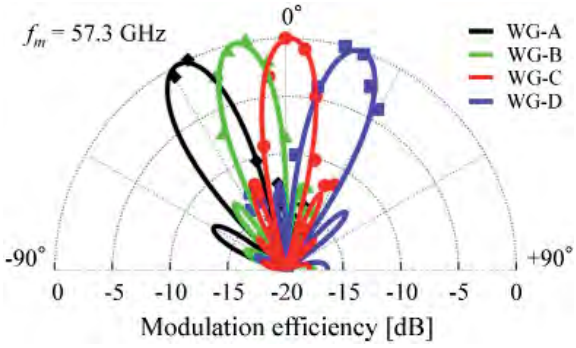

Figure 10. The measured and calculated directivities in the four-channel optical waveguide.

6. Acknowledgements

The authors thank Drs. Hidehisa Shiomi, Kazuhiro Kitatani, and Yusuf Nur Wijayanto for their helpful advice and comments on the analysis and experiments. This work was supported in part by Grants-in-Aid Scientific Research from the Ministry of Education, Science, Sports, and Culture, Japan, and a Research Grant from the Support Center for Advanced Telecommunications Technology Research, Foundation.

7. References

1. N. Currie and C. Brown, *Principles and Applications of Millimeter-Wave Radar*, Norwood, MA, Artech House, December, 1987.

2. A. J. Seeds and K. J. Williams, "Microwave Photonics," *IEEE/OSA J. Lightwave Technol.*, **24**, 12, December 2006, pp. 4628-4641.

3. S. Iezekiel, *Microwave Photonics: Device and Applications*, Wiltshire, John Wiley & Sons, Ltd., March, 2009.

4. F. T. Sheehy, W. B. Bridges, and J. H. Schaffner, "60 GHz and 94 GHz Antenna-Coupled $LiNbO_3$ Electrooptic Modulators," *IEEE Photon. Tech. Lett.*, **5**, 3, March 1993, pp. 307-310.

5. S. Shinada, T. Kawanishi, T. Sakamoto, M. Adachi, K. Nishikawa, S. Kurokawa, and M. Izutsu, "A 10-GHz Resonant-Type $LiNbO_3$ Optical Modulator Array," *IEEE Photon. Tech. Lett.*, **19**, 10, May 2007, pp. 735-737.

6. H. Murata, N. Suda, and Y. Okamura, "Electro-Optic Modulator Using Patch Antenna-Coupled Resonant Electrodes and Polarization-Reversed Structure for Radio-On-Fiber Systems," The Conference on Lasers and Electro-Optics 2009 (CLEO2009), Baltimore, USA, May 2009, CTuT5.

7. Y. N. Wijayanto, H. Murata, and Y. Okamura, "Electro-Optic Microwave-Lightwave Converters Utilizing Quasi-Phase-Matching Array of Patch Antennas with Gap," *IEE Electronics Lett.*, **48**, 1, January 2012, pp. 36-38.

8. H. Murata, R. Miyanaka, and Y. Okamura, "Wireless Space-Division-Multiplexed Signal Discrimination device Using Electro-Optic Modulator with Antenna-Coupled Electrodes and Polarization-Reversed Structures," *International Journal of Microwave and Wireless Technologies*, 4, October 2012, pp. 399-405.

9. N. Kohmu, H. Murata, Y. Okamura, "Electro-Optic Modulators Using Double Antenna-Coupled Electrodes for Radio-Over-Fiber Systems," *IEICE Trans. Electron.*, **E96-C**, 2, February 2013, pp. 204-211.

10. K. Goverdhanam, "Effect of Substrate Modes in 40 Gbit Travelling Wave $LiNbO_3$ Modulators," The IEEE MTT-S International Microwave Symposium (IMS2002), Seattle, USA, 2(IF-WE-35), June 2002, pp. 1285-1288.

11. A. Kanno, T. Sakamoto, A. Chiba, T. Kawanishi, K. Higuma, M. Sudou, and J. Ichikawa, "120-Gb/s NRZ-DQPSK Signal Generation by a Thin-Lithium Niobate-Substrate Modulator," *IEICE Electronics Express*, **7**, 11, June 2010, pp. 817-822.

12. A. Enokihara, H. Furuya, H. Yajima, M. Kosaki, H. Murata, and Y. Okamura, "60 GHz Guided-Wave Electro-Optic Modulator Using Novel Electrode Structure of Coupled Microstrip Line Resonator," The IEEE MTT-S International Microwave Symposium (IMS2004), Fort Worth, USA, 3(THIF-59), June 2004, pp. 2055-2058.

13. A. Yariv, *Quantum Electronics, Third Edition*, New York, Wiley, January, 1989.

14. H. Murata, S. Matsunaga, A. Enokihara, and Y. Okamura, "Resonant Electrode Guided-Wave Electro-Optic Phase Modulator Using Polarization-Reversed Structures", *IEE Electron. Lett.*, **41**, 8, April 2005, pp. 497-498.

15. . Enokihara, H. Yajima, H. Murata, and Y. Okamura, "Guided-Wave EO Intensity Modulator Using Coupled Microstrip Line Electrode of Higher-Order Harmonic Resonance Combined with Polarization-Reversed Structure," *IEICE Trans. Electron*, **E-90C**, 5, May 2007, pp. 1096-1104.

16. C. A. Balanis, *Antenna Theory, Third Edition: Analysis and Design*, Wiltshire, John Wiley & Sons, Inc., March, 2005.

17. K. F. Lee and K. M. Luk, *Microstrip Patch Antennas*, London, Imperial Collage Press, September, 2010.

18. K. Tada, T. Murai, T. Nakabayashi, T. Iwashita, and T. Ishikawa, "Fabrication of $LiTaO_3$ Optical Waveguide by H^+ Exchange Method," *Jpn. J. Appl. Phy.*, **26**, March 1987, pp. 503-504.

Ferromagnetic Nanowires : Homogenization and Applications

Jue Wang[1], Zhen Peng[2], and Jin-Fa Lee[1]

[1]Department of Electrical and Computer Engineering
The Ohio State University
Columbus, OH, USA
E-mail: wang.1453@buckeyemail.osu.edu; jinlee@esl.eng.ohio-state.edu

[2] Department of Electrical and Computer Engineering
the University of New Mexico
Albuquerque, NM, USA

This is one of the invited Finalist papers from the AP-RASC 2013 Student Paper Competition.

Abstract

A numerical homogenization method for extracting the equivalent electromagnetic parameters – in particular, the dispersive and nonreciprocal permeability tensor – of ferromagnetic nanowires (FMNW) is presented in this paper. With the effective material property obtained, the performance of ferromagnetic-nanowire microwave devices, such as integrated double-band isolators and self-biased circulators, etc., were analyzed using a full-wave numerical simulation approach. Numerical examples validated the proposed homogenization method, and demonstrated the integration of the multi-physics solution strategy for characterizing the effects of ferromagnetic nanowires employed in RF devices.

1. Introduction

Metamaterials can be broadly defined as artificial effective structures composed of small units achieving exotic responses that are not readily available in natural or conventional materials. Extensive research conducted on metamaterials has led to many innovative theories and devices over the years [1-4]. Coming to the second decade of the new century, the development of artificial structural materials is at the stage where interdisciplinary interest is taking place, such as multi-scale metamaterials, reconfigurable metamaterials, and their combinations with nanotechnology. Compared with the earlier generation of metamaterials, the new generation of metamaterials incorporates finer structural scales, for instance, on the nanometer or even atomic scale, which suffer less from scattering losses as well as fabrication difficulties.

While the potentials of metamaterials and their possible applications are appealing, it is often difficult to accurately model them, due to the inherently very fine and complex structures involved. However, by observing that metamaterials usually consist of (most often periodically) positioned inclusions much smaller than the electromagnetic wavelength of interest, a homogenized description of the structure can be adopted as an accurate alternative. Among numerous works already existing in the literature on homogenization, we would like to highlight a few here. In [5], the authors presented a homogenization method by calculating the reflection and transmission coefficients on finite lengths of electromagnetic metamaterials. In [6], the authors determined the effective material constants based on averaging the local fields. In [7], a homogenized description was derived of periodic metamaterials, which were made of magneto-dielectric inclusions; the author subsequently obtained closed-form expressions for the effective constitutive parameters. Finally, in [8] the author combined the physical insight and a Whitney-like interpolation to form a new homogenization theory of metamaterials, through which coarse-grained fields are defined.

In this paper, we are interested in a ferromagnetic nanowire (FMNW) array. We exploit its magnetic properties, as well as investigate its integration with microwave/RF components and devices. Due to their tailored electromagnetic responses, ferromagnetic-nanowire metamaterials exhibit novel properties, such as double ferromagnetic resonance (FMR), anisotropy control, and self-bias. Compared to traditionally bulky ferromagnets, the utilization of ferromagnetic nanowire metamaterials can significantly reduce the size of microwave devices. The major previous works referred by

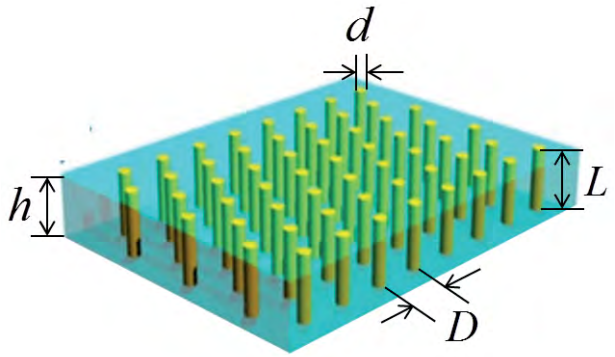

Figure 1. A sketch of a ferromagnetic-nanowire substrate structure.

this paper are [9] and [10], in which the authors presented a Maxwell-Garnett-like formulation for extracting the effective permeability tensor for non-saturated/saturated arrays of axially magnetized ferromagnetic nanowires, as well as enumerating several applications of ferromagnetic nanowires in microwave devices. Instead of adopting the analytical model, we propose here in this paper a three-dimensional (3D) full-wave numerical process, more generally to extract the macroscopic effective permeability tensor, by first computing the static magnetic-field distribution with the acceleration of the two-dimensional fast Fourier transformation method (two-dimensional-FFT) [11], and then conducting a small-signal analysis [12]. With that, we analyze the performance of microwave components and devices integrated with ferromagnetic-nanowire-based metamaterial structures through full-wave electromagnetic computations.

This paper begins with an introduction to put in context the definition and development of metamaterial structures, and the demand and challenge of modeling them. It then proceeds to state the homogenization methodology, and a numerical result section is included afterwards.

2. The Proposed Homogenization Method

We consider an array of ferromagnetic nanowires of diameter d and length L ($L \gg d$), embedded in a porous membrane with height h and inter-wire distance D, as shown in Figure 1. Our goal is to obtain the effective dynamic permeability of the array in a complex tensorial form.

The proposed homogenization procedure can be divided into the following major steps.

2.1 Setting Up the Biasing/ Operating Point

The ferromagnetic nanowire array is subjected externally to an axially-aligned (set to be the z direction in this scenario) dc magnetic field, $\mathbf{H}_{dc}^{ext}$, and a transverse ac signal, $\mathbf{h}$. The initial magnetization, $\mathbf{M}_{dc}$, can therefore be obtained from the hysteresis loop of the ferromagnetic nanowire metamaterial, which relates the magnetization to the applied static magnetic field, $\mathbf{H}_{dc}^{ext}$. Figure 2 shows a schematic hysteresis curve.

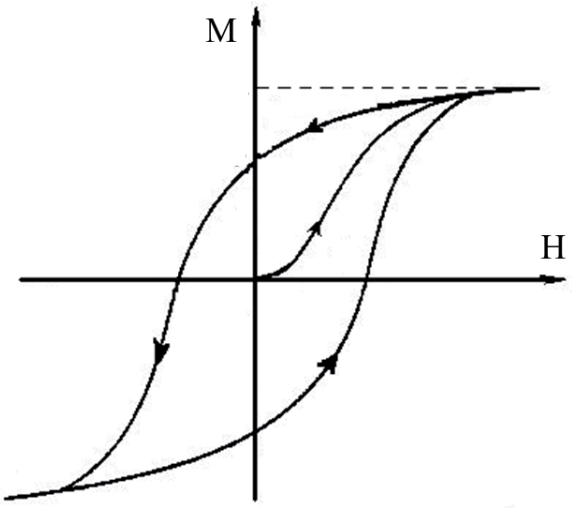

Figure 2. A schematic of a hysteresis loop.

2.2 Computation of the Demagnetization Field

With the magnetization, $\mathbf{M}_{dc}$, obtained, the volume/surface magnetic charge density, ρ_v / ρ_s , in/on the tube is calculated as

$$\rho_v = -\nabla \bullet \mathbf{M}_{dc} \tag{1}$$

and

$$\rho_s = \mathbf{M}_{dc} \bullet \hat{\mathbf{n}} , \tag{2}$$

with $\hat{\mathbf{n}}$ being the surface normal of the tube pointing in the outward direction. Consequently, the magnetic potential, Φ , can be computed via

$$\Phi(\vec{r}) = \frac{1}{4\pi}\int_V \frac{\rho_v}{|\vec{r}-\vec{r}'|}dv' + \frac{1}{4\pi}\int_S \frac{\rho_s}{|\vec{r}-\vec{r}'|}ds' . \tag{3}$$

Since in our case, $\mathbf{M}_{dc}$ is constant, this results in $\rho_v = 0$, and thus Equation (3) can be simplified as

$$\Phi(\vec{r}) = \frac{1}{4\pi}\int_S \frac{\rho_s}{|\vec{r}-\vec{r}'|}ds' . \tag{4}$$

In general, there would be millions or even billions of nanowires involved in the structure, and the direct computation of Equation (4) would require prohibitive computational resources. Fortunately, as stated previously, these nanowires are usually distributed in a periodic lattice. We can therefore accelerate the computation of Equation (4) by employing the two-dimensional FFT method [11].

Observing Equation (4), the magnetic potential, Φ due to the magnetic charge can be decomposed into near and far interaction terms:

$$\Phi(\vec{r}) = \Phi_n(\vec{r}) + \Phi_f(\vec{r}). \quad (5)$$

In Equation (5), Φ_n is the potential contributed by the disk charge residing on the top and bottom surfaces of the tube, and evaluated on the axis of the disk. A closed-form expression for the near term can be written as

$$\Phi_n(z) = \frac{\rho_s}{2}\left[\sqrt{(z-z_0)^2 + R^2} - |z-z_0|\right], \quad (6)$$

where ρ_s is the surface magnetic charge density, R is the radius of the disk, and z and z_0 are the potential evaluation location and the center of the magnetic charge disk, respectively.

Φ_f in Equation (5) can be approximately derived from the point charge of $\rho_s \pi R^2$, with R being the radius of the cylindrical tube. Assume that $R \ll |\vec{r} - \vec{r}'|$, where $\vec{r}$ and $\vec{r}'$ are the locations of the charge and the observation point, respectively. We have,

$$\Phi_f(\vec{r}) \approx \frac{1}{4\pi}\sum_{\vec{r}\neq\vec{r}'} \frac{\rho_s \pi R^2}{|\vec{r} - \vec{r}'|}. \quad (7)$$

It has already been pointed out before that the nanotubes are distributed in a Cartesian grid, with source charges of the same value but opposite sign residing on the top and bottom surfaces of each tube. Combined with the fact that the static Green's function is translationally invariant, namely,

$$g(\vec{r}, \vec{r}') = \frac{1}{|\vec{r} - \vec{r}'|} = g(|\vec{r} - \vec{r}'|),$$

this leads to a two-dimensional block-Toeplitz matrix structure for Equation (7). The computations of the magnetic potentials can therefore be speeded up significantly using the two-dimensional FFT for the summation of the far-term contributions. Adding the near-term correction, Equation (6), at the end completes the computations of the magnetic potentials on the Cartesian grids.

The demagnetization field, $\mathbf{H}_m$, is then readily available for every ferromagnetic nanowire from the magnetic potential:

$$\mathbf{H}_m(\vec{r}) = -\nabla\Phi(\vec{r}). \quad (8)$$

2.3 Computation of the Small-Signal Solution of the LLG Equation

Assuming that the corresponding ac magnetization field, $\mathbf{h}$, is much smaller than the external dc bias, a decomposition of the total effective magnetization field, $\mathbf{H}_{eff}$, into the dc and the small ac signal hence proves to be beneficial. Namely,

$$\mathbf{H}_{eff} = \mathbf{H}_{dc} + \mathbf{h}, \quad (9)$$

$$\mathbf{H}_{dc} = \mathbf{H}_{dc}^{ext} + \mathbf{H}_m.$$

We note here that other contributions to the effective magnetic field, $\mathbf{H}_{eff}$, such as the exchange interaction, the anisotropic field, and the thermal field, are neglected, since they are much less significant compared to the demagnetization field.

Similarly, the total magnetization moment, $\mathbf{M}$, is separated into dc and ac components, as well:

$$\mathbf{M} = \mathbf{M}_{dc} + \mathbf{m}. \quad (10)$$

Note that the dc magnetization, $\mathbf{M}_{dc}$, is mainly in the z direction in the current consideration. Moreover, the ac magnetization moment, $\mathbf{m}$, can be computed from the equation of magnetization motion, or the Landau-Lifshitz-Gilbert (LLG) equation:

$$\frac{\partial \mathbf{M}}{\partial t} = -\mu_0 |\gamma_g| \mathbf{M} \times \left(\mathbf{H}_{eff} + \frac{\alpha_G}{\mu_0 |\gamma_g| M_s}\frac{\partial \mathbf{M}}{\partial t}\right), \quad (11)$$

where μ_0 is the permeability of free space, γ_g is the gyromagnetic ratio, α_G is the damping factor, and M_s is the magnitude of the saturation magnetization.

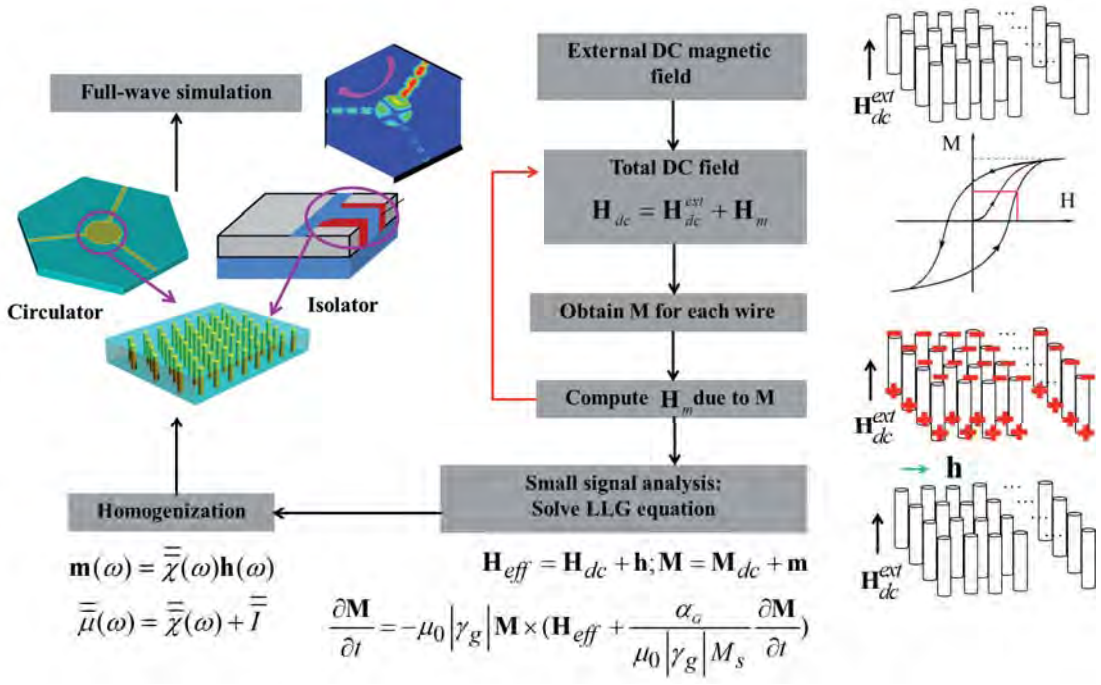

Figure 3. A flowchart of the ferromagnetic-nanowire-based metamaterial homogenization process and application enumeration.

Substituting Equations (9) and (10) into Equation (11), assuming a time-harmonic dependence of $e^{j\omega t}$, and applying the small-signal approximation model in [12] by neglecting higher-order terms, Equation (11) can be written as

$$j\omega\mathbf{m} = -\mu_0 |\gamma_g| \left(M\,\hat{\mathbf{z}} \times \mathbf{h} + \mathbf{m} \times \mathbf{H}_{dc}\right) - j\omega\alpha_G \frac{M}{M_s} \hat{\mathbf{z}} \times \mathbf{m}, \quad (12)$$

with M being the magnitude of $\mathbf{M}$.

Equation (12) can be written as

$$j\omega m_x = -\mu_0 |\gamma_g| \left(-Mh_y + m_y H_z - m_z H_y\right) + j\omega\alpha_G \frac{Mm_y}{M_s}$$

$$j\omega m_y = -\mu_0 |\gamma_g| \left(Mh_x + m_z H_x - m_x H_z\right) - j\omega\alpha_G \frac{Mm_x}{M_s} \quad (13)$$

$$j\omega m_z = -\mu_0 |\gamma_g| \left(m_x H_y - m_y H_x\right).$$

The 2×2 matrix form of the x and y components is

$$\begin{bmatrix} \mathcal{A}_{xx} & \mathcal{A}_{xy} \\ \mathcal{A}_{yx} & \mathcal{A}_{yy} \end{bmatrix} \begin{bmatrix} m_x \\ m_y \end{bmatrix} = \mu_0 |\gamma_g| M \begin{bmatrix} h_x \\ h_y \end{bmatrix} \quad (14)$$

$$\mathcal{A}_{xy} = \frac{j\left(H_x{}^2 |\gamma_g|^2 \mu_0{}^2 - \omega^2\right)}{\omega}$$

$$\mathcal{A}_{yx} = \frac{j\left(-H_y{}^2 |\gamma_g|^2 \mu_0{}^2 + \omega^2\right)}{\omega}$$

$$\mathcal{A}_{yy} = \frac{jH_x H_y M_s |\gamma_g|^2 \mu_0{}^2 + H_z M_s |\gamma_g| \mu_0 \omega - jM\alpha_G \omega^2}{\omega M_s}$$

where H_x, H_y, and H_z are the components of $\mathbf{H}_{dc}$ in the x, y, and z directions, respectively, and m_x, m_y, and m_z are the components of $\mathbf{m}$. The notations h_x and h_y are also similarly defined.

2.4 Extraction of the Equivalent/ Effective Permeability Tensor

With the small-signal magnetization moment, $\mathbf{m}$, computed in response to given external applied ac magnetic field, $\mathbf{h}$ (through the excitation of three different polarizations), it follows that the 3×3 magnetic susceptibility tensor $\bar{\bar{\chi}}_\omega$ can be determined. Consequently, the relative equivalent/effective homogenized permeability tensor $\bar{\bar{\mu}}_\omega$ of the ferromagnetic nanowires is also available,

and we note that the extracted permeability tensor is nonreciprocal and dispersive.

$$\mathbf{m}(\omega) = \bar{\bar{\chi}}_{\omega}\mathbf{h}(\omega), \tag{15}$$

$$\bar{\bar{\chi}}_{\omega} = \begin{bmatrix} \dfrac{\mu_0 |\gamma_g| M}{\begin{bmatrix} \mathcal{A}_{xx} & \mathcal{A}_{xy} \\ \mathcal{A}_{yx} & \mathcal{A}_{yy} \end{bmatrix}} & 0 \\ 0 & 0 \end{bmatrix},$$

and

$$\bar{\bar{\mu}}_{\omega} = \bar{\bar{\chi}}_{\omega} + \bar{\bar{I}} = \begin{bmatrix} \mu_{xx} & \mu_{xy} & 0 \\ \mu_{yx} & \mu_{yy} & 0 \\ 0 & 0 & 1 \end{bmatrix}. \tag{16}$$

It is worth commenting that in the proposed procedure, in cases where the magnetization moment locally is not largely homogeneous, the extracted macroscopic effective material properties can further be made inhomogeneous within the bulk of the ferromagnetic nanowires.

2.5 Integration with Microwave/ RF Components/Devices – Performance Analysis

The extracted electromagnetic material parameters will be directly employed for microwave/RF components utilizing ferromagnetic nanowire substrates. With the macroscopic material properties readily available, a full-wave three-dimensional electromagnetic simulation will be applied to analyze the microwave/RF components, such as isolators, circulators, etc.

Figure 3 summarizes the methodology and scope of this work, including procedures for performing the homogenization technique of ferromagnetic-nanowire-based metamaterials and their applications as RF components in microwave devices.

3.2 Numerical Results

3.1 Validation of Extracted Permeability Tensor

We first validate the proposed numerical homogenization procedure by comparing the effective

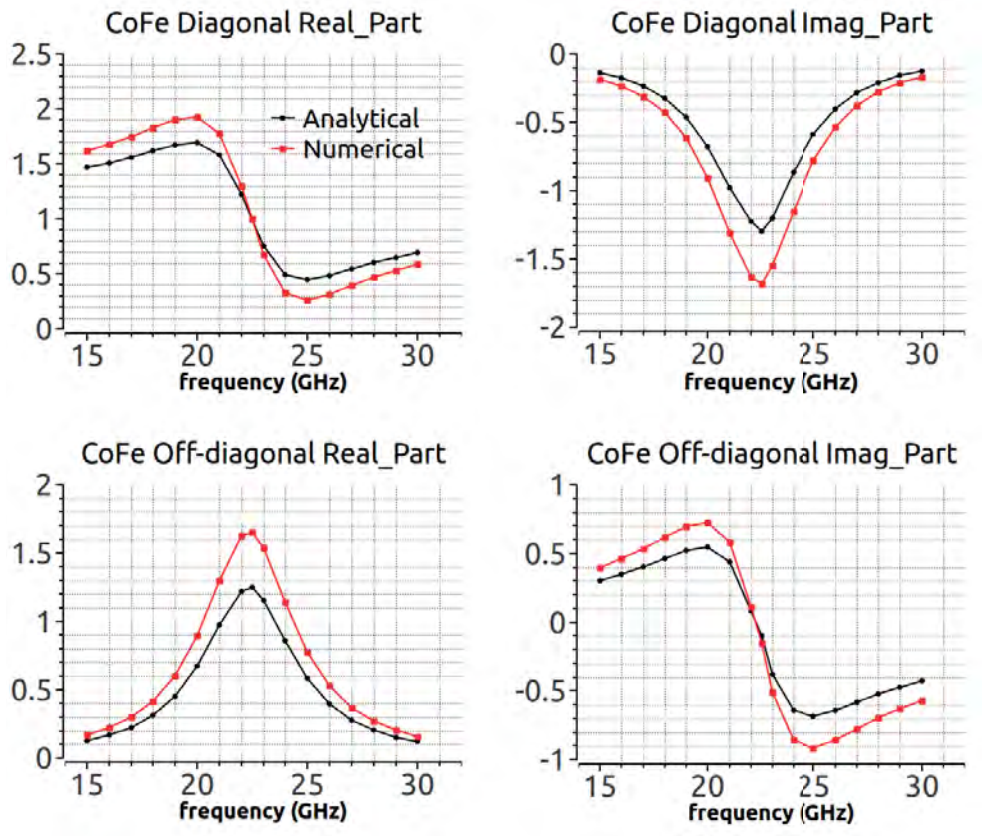

Figure 4. Comparisons of the effective relative permeability tensor of a CoFe nanowire membrane obtained by different methods.

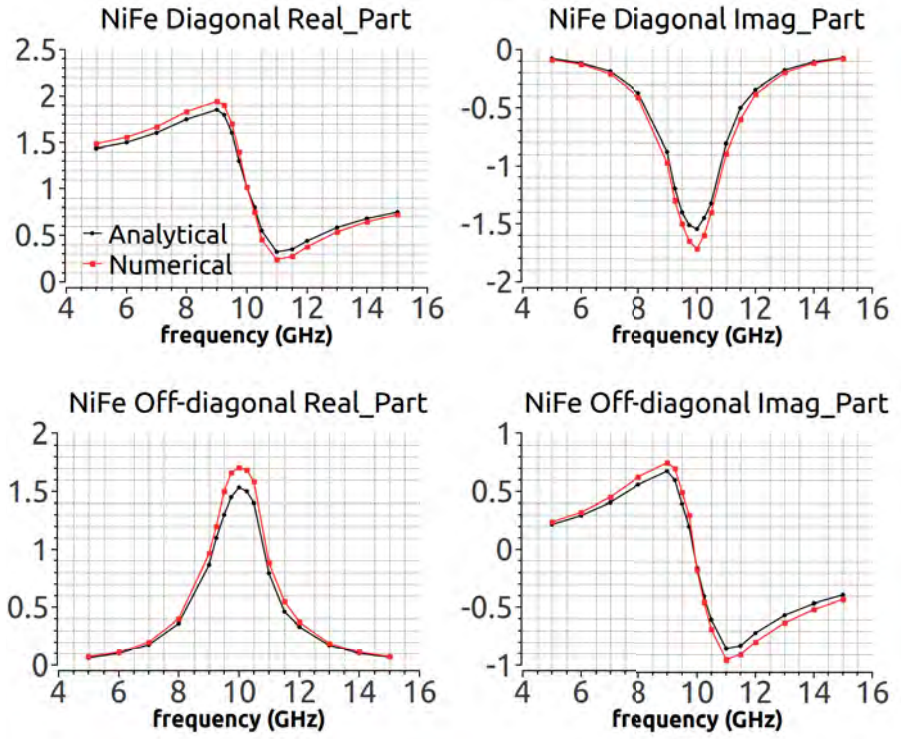

Figure 5. Comparisons of the effective relative permeability tensor of an NiFe nanowire membrane obtained by different methods.

material property computed against an analytical model proposed in [13] for a nanowired substrate of different magnetic alloys. Specifically, a nonreciprocal microstrip phase shifter on a substrate with two different magnetic nanowires (CoFe and NiFe) was designed and analyzed. The substrate was fabricated via electro-deposition of CoFe and NiFe nanowires into 100 μm thick porous anodic alumina membranes with a pore diameter of 35 nm and a membrane porosity of $P = 12\%$. In order to enhance the nonreciprocal behavior of the device, CoFe and NiFe nanowires were grown into different heights of the membrane thickness, with $h_{CoFe} = 0.68$ and $h_{NiFe} = 0.84$, respectively.

The analytical homogenized model proposed in [13] for the nanowires has the form

$$\bar{\bar{\mu}} = \begin{bmatrix} \mu & -j\kappa & 0 \\ j\kappa & \mu & 0 \\ 0 & 0 & 1 \end{bmatrix}, \qquad (17)$$

with

$$\mu = 1 + \frac{2\pi M_s \gamma P h f_{FMR}\left(m^2+1\right)}{f_{FMR}^2 - f^2}, \qquad (18)$$

$$\kappa = \frac{4\pi M_s \gamma P h f m}{f_{FMR}^2 - f^2},$$

where $f_{FMR} = \gamma\left[H_{DC} + 2\pi M_s\left(1-3P\right)\right] + j\alpha f$ is the ferromagnetic resonance frequency, $m = M/M_s$ is the normalized magnetization, α is the damping factor, H_{DC} is the applied static field parallel to the axial direction of the nanowires (for the self-bias case, it will be zero), f is the operating frequency, M_s is the saturation magnetization, and, finally, P is the porosity.

Figures (4) and (5) show comparisons of the effective relative permeability tensors obtained from the proposed homogenization procedure and the reference analytical model in the self-bias situation. From these figures, we observed that the two models predicted resonances at almost the same frequency for both CoFe and NiFe nanowire substrates, with $f_{res\_CoFe} = 22.3\,\text{GHz}$ and f_{res_NiFe} around 10 GHz.

3.2 Double Ferromagnetic Resonance Phenomenon

Ferromagnetic resonance has been extensively studied due to its applications in microwave devices. Specifically, in ferromagnetic-nanowire arrays, the ferromagnetic resonance phenomenon has drawn great attention, mainly due to the following reasons. First of all, the ferromagnetic-resonance frequency is easily tunable by either adjusting the external magnetic field or by applying various demagnetizing cycles so as to make the remanent state programmable. Secondly, it is predicted by analytical model and observed through experiments that

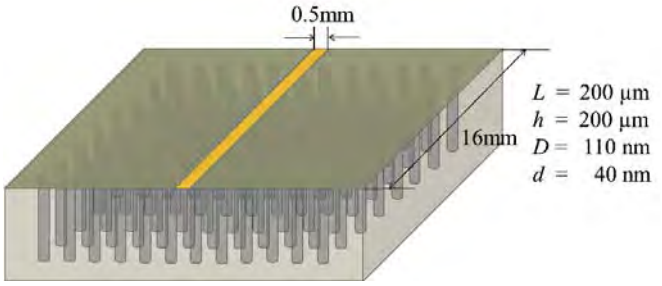

Figure 6. A sketch of the microstrip line.

for applied magnetic fields below saturation, there exist two sets of ferromagnetic-resonance frequencies. The existence of double ferromagnetic-resonance frequencies can potentially lead to applications with dual working-frequency bands.

A schematic drawing of a microstrip line with a substrate of ferromagnetic nanowires embedded in a porous alumina membrane is included in Figure 6. As shown in the figure, the microstrip line is 0.5 mm wide and 16 mm long, and the bottom of the membrane is covered with metal as a ground. We shall study the electromagnetic-wave propagates along the microstrip line over a wide frequency band, and under a range of externally applied magnetic fields.

We took the hysteresis-loop figure from [14] and re-plotted it in Figure 7. In particular, in Figure 7 we highlighted the realized magnetization branch within the hysteresis loop. Through the figure, we obtained the pairs of the applied external dc magnetic field, H_{dc}^{ext}, and the normalized magnetization, $M_n \left(M_n = M_{dc}/M_s\right)$. Note that the saturation magnetization, M_s, for the ferromagnetic nanowires was 1400 kA/m. We conducted the studies of ferromagnetic resonance by sweeping the external dc bias field from -5.0 KOe to 5.0 KOe with a step of 500 Oe, following the specified branch indicated in Figure 7. Table 1 summarizes the $\left(H_{dc}^{ext}, M_n\right)$ pairs read from the hysteresis loop.

With the initial dc magnetization obtained from the hysteresis loop, we performed the homogenization process previously described in full and outlined in Figure 3 to extract the relative effective permeability tensors of the ferromagnetic nanowires from 20 GHz to 40 GHz. The extracted permeability tensors were subsequently employed to compute the S_{21} coefficients through full-

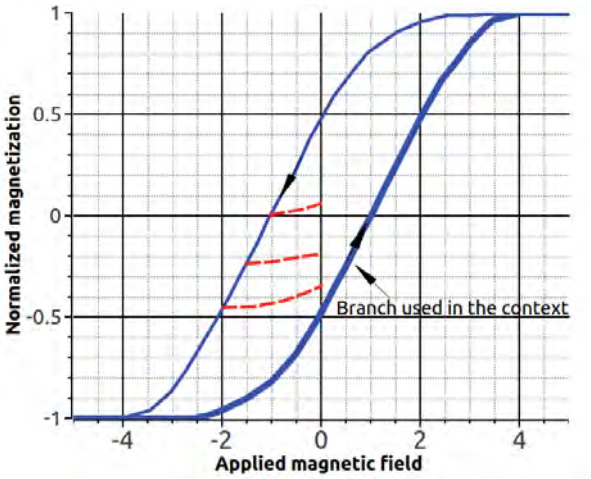

Figure 7. The major hysteresis loop (solid blue) and the minor hysteresis curves (dashed red).

wave electromagnetic computations. However, it is worth mentioning that in order to account for the fabrication imperfections, fringe-field effects, and the measurement uncertainties, we adopted a similar adjustment as suggested in [9, 14]. Namely,

$$\overline{\overline{\mu}}_c = \overline{\overline{I}} + q\left(\overline{\overline{\mu}}_h - \overline{\overline{I}}\right), \tag{20}$$

where $\overline{\overline{\mu}}_c$ is the effective permeability tensor that is used in the full-wave simulations, and $\overline{\overline{\mu}}_h$ is the permeability tensor extracted from the homogenization process. The parameter q is a geometrical filling factor, which is determined experimentally according to references [9, 14]. Herein, we had $q = 0.13$. Note that in references [9, 14], the ferromagnetic nanowires were approximated as a reciprocal and isotropic material with the effective permeability given by

H_{dc}^{ext} [KOe]	–2.5	–2.0	–1.5	–1.0	–0.5	0.0	0.5
M_n	–1.0	–0.96	–0.9	–0.82	–0.68	–0.48	–0.25
H_{dc}^{ext} [KOe]	1.0	1.5	2.0	2.5	3.0	3.5	4.0
M_n	–0.002	0.24	0.48	0.69	0.85	0.97	1.0

Table 1. The external dc magnetic field as a function of the normalized magnetization.

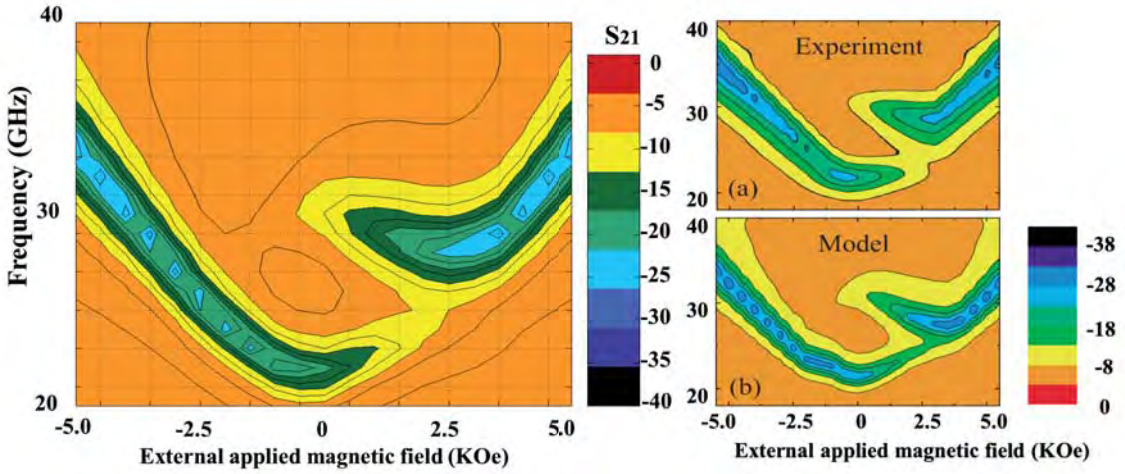

Figure 8. (l): A contour plot of the S_{21} parameter from the simulated result. (r): The (a) reference experiment and (b) model results copied from Figure 2 in [14].

$$\mu_c = 1 + q\left(\mu_h - 1\right), \tag{21}$$

where μ_h is the diagonal component of the permeability tensor of the ferromagnetic-nanowire substrate.

By extending Equation (21) to Equation (20), we aim to capture the non-reciprocal effects of the ferromagnetic nanowires. However, with the adjustment introduced, the non-reciprocal effects induced will not be significant. For example, we had the effective permeability $\overline{\overline{\mu}}_c$ at 33 GHz, and the external applied magnetic field $H_{dc}^{ext} = -5$ KOe, giving

$$\overline{\overline{\mu}}_c = \begin{bmatrix} 1.068 - j0.2 & -0.2 - j0.055 & 0. \\ 0.2 + j0.055 & 1.068 - j0.2 & 0. \\ 0. & 0. & 1. \end{bmatrix}. \tag{22}$$

In Figure 8, we compared our numerical results against the measurements and the results from [9]. The numerical results computed using the proposed approach are shown on the left of Figure 8, whereas the reference experimental and analytical-model results are included on the right of Figure 8. As could be seen from the figure, very good agreement was established between these three sets of results. As a consequence, through this example, we therefore demonstrated the validity of the proposed numerical homogenization process. Furthermore, judging from the figure, it could be argued that the proposed homogenization procedure produced results that resembled the measurements more than the analytical model proposed in the reference.

We also observed from the figures in Figure 8 that with the external applied dc magnetic field above saturation, $\left|H_{dc}^{ext}\right| \geq 2.5$ KOe, there would be only a single ferromagnetic-resonance peak. Additionally, in the region above the saturation, the resonant frequency increased almost linearly with the magnitude of the external applied dc magnetic field. However, it was in the region where the applied field is below saturation, $0 < H_{dc}^{ext} < 2.5$ KOe, that two sets of peaks corresponding to two ferromagnetic-

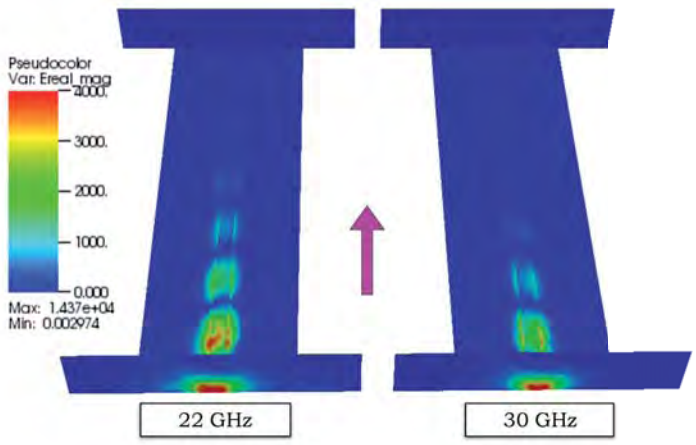

Figure 9. The electric-field distributions along the microstrip line with a ferromagnetic-nanowire substrate, biased with the same external bias field, $H_{dc}^{ext} = 0.5$ KOe, at two different resonance frequencies.

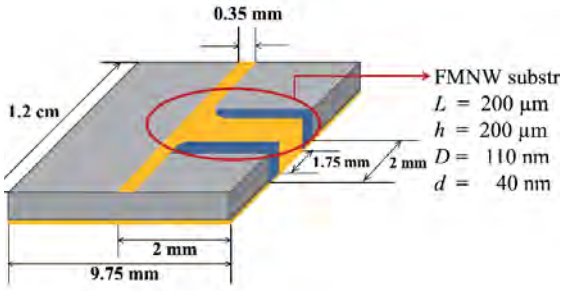

Figure 10. The structure of the ferromagnetic-nanowire isolator.

resonance frequencies existed. The existence of two ferromagnetic-resonance frequencies could result in potential applications for dual-band microwave devices. In Figure 9, we plot the electric-field distributions along the microstrip line, with a single external bias field set to be 0.5 KOe. As could be seen from the figure, there were two different frequencies, 22 GHz and 30 GHz, at which the electromagnetic energy was absorbed almost completely by the ferromagnetic-nanowire substrate.

3.3 Dual-Band Integrated Edge-Mode Isolator

In this section, we first compute the homogenized relative permeability tensor of a ferromagnetic-nanowire substrate previously illustrated in [9]. This substrate was utilized in a dual-band integrated edge-mode isolator in [10], which will be discussed in detail following the validation of the homogenized material properties. The dimensions of the substrate as well as the geometrical description of the isolator are included in Figure 10.

3.3.1 Comparison of the Homogenized Relative Permeability of the Ferromagnetic-Nanowire Substrate

The nanowire array was embedded in a porous alumina membrane by selective deposition. The wires were distributed in a symmetrical network. The average diameter and length of the nanowires were 40 nm and 200 μm, respectively, with an inter-wire distance of about 110 nm. Referring to Figure 1, we have d = 40 nm, $L = h = 200$ μm, and $D = 110$ nm, as documented in Figure 10.

With the external biased magnetic field being –0.5 KOe in the axial direction, subsequently the corresponding average magnetization moment was 350 kA/m ($M_s = 1400$ kA/m). Following the same procedure in [9], we obtained the relative characteristic permeability, μ_c , from the homogenized relative permeability tensor via $\mu_c = 1 + q(\mu_h - 1)$, with μ_h being the diagonal component

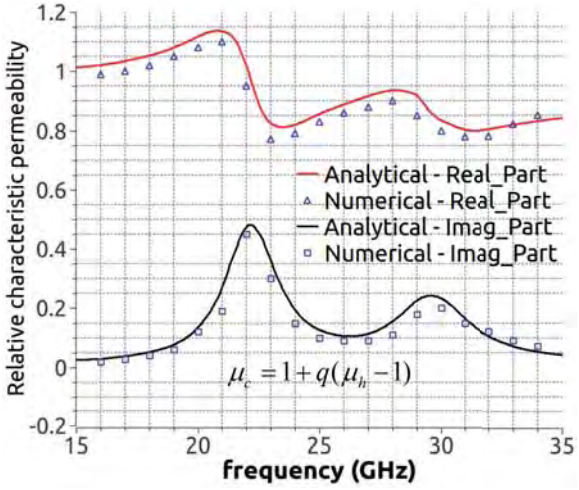

Figure 11. A comparison of the relative characteristic permeability. The solid lines stand for the analytical model in [9], while the triangles and squares denote the results of the proposed numerical homogenization method.

of the tensor here. The comparison of μ_c at a few frequency points to the results obtained from [9] is plotted in Figure 11. As could be seen, the computed results from the proposed method agreed well with the reference.

3.3.2 A Dual-Band Integrated Edge-Mode Isolator

After validating the proposed homogenization procedure, we were ready to investigate some interesting properties of ferromagnetic nanowires employed in microwave devices. Particularly, herein we considered a dual-band integrated edge-mode isolator designed in [10]. Figure 10 elucidates the geometry and the corresponding dimensions of the isolator. The relative permittivity of the porous alumina membrane (without ferromagnetic nanowires) was 5.3, and that of the alumina membrane with ferromagnetic-nanowire inclusions was $6.15 - j0.25$

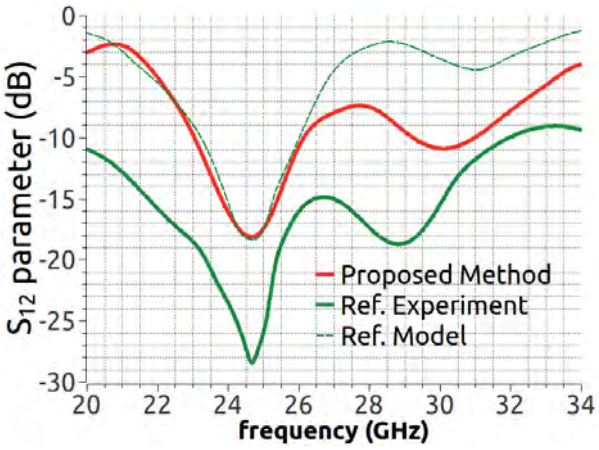

Figure 12. The S_{12} parameter comparison.

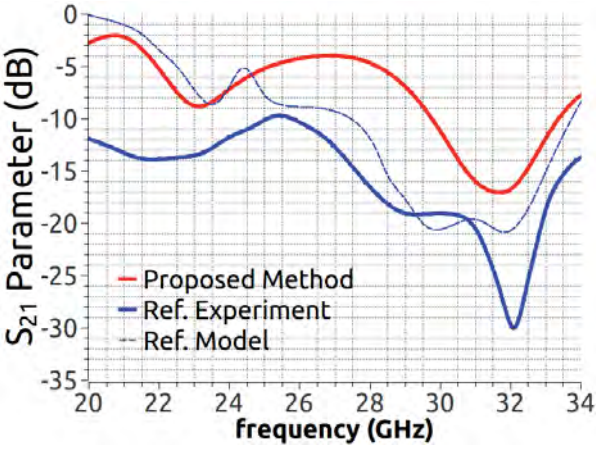

Figure 13. The S_{21} parameter comparison.

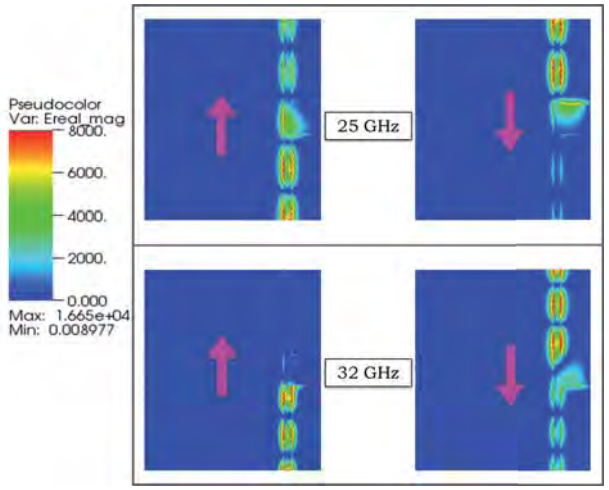

Figure 14. The electric-field distributions along the microstrip line of the isolator at two different working frequencies.

. The operational bias point of the isolator was set to be $\mathbf{H}_{dc}^{ext} = -1.3$ KOe, and the corresponding magnetization moment was -140 kA/m. Figures 12 and 13 plot the *S* parameters of the isolator obtained by different methods. As could be seen, compared against the measurements, all simulation results had a lower insertion loss. This may have been due to the neglect of loss incurred in the physical realization of the device and the measurement process.

Moreover, as shown in Figures 12 and 13, the isolator worked at two isolation frequency bands, centered at 25 GHz and 32 GHz, respectively. At the two working frequency bands, the isolation directions were reversed. Subsequently, we plotted the electric field distributions along the microstrip line of the isolator in Figure 14 for these two center frequencies.

3.3.2 A Dual-Band Self-Biased Circulator

Shown in Figure 15 is a planar dual-band self-biased circulator integrated with a ferromagnetic-nanowire substrate. The ferromagnetic-nanowire substrate utilized by the circulator was taken directly from reference [15]. The porous alumina substrate was 220 μm thick, with an average pore diameter and inter-pore distance of 40 nm and 100 nm, respectively. Magnetic nanowires were selectively electro-deposited into the membrane. The saturation magnetization of the nanowire array was 1400 kA/m, and the remanent magnetization was $M_r = 0.48M_s$. The back of the template was covered with a perfect electric

Figure 15. A detailed description of a dual-band self-biased circulator.

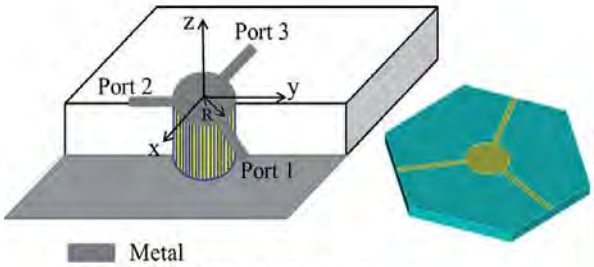

Metal
Nanowire Substrate
Porous Alumina Membrane

Geometry of the circulator	
Disc radius	2.5 mm
Length of port access	8 mm
Width of port access	0.5 mm
FMNW substrate operation point	
Biased field	0
M	627 kA/m

	FMNW nanowire substrate
Membrane height	220μm
Wire diameter	40μm
Porosity	12%
Saturation magnetization	1400 kA/m
Damping factor	0.06
Permittivity used	
Membrane without FMNW	5.3
Membrane with FMNW	6.15-j0.25

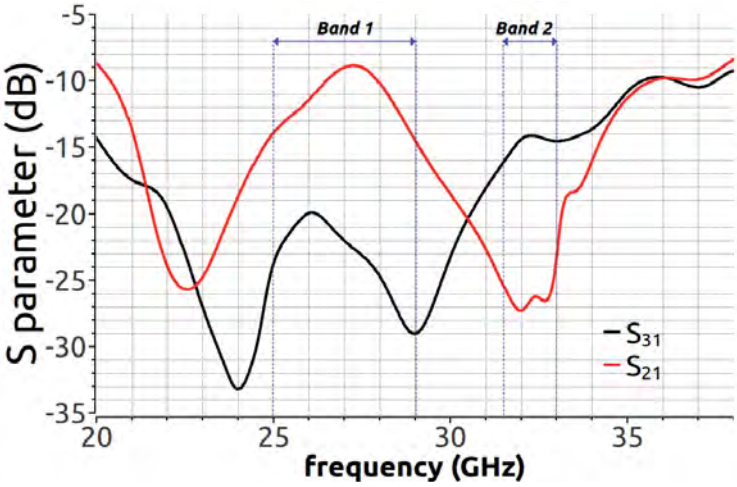

Figure 16. The *S*-parameter plots of the full-wave simulation results for the conceptual microstrip circulator.

conductor (PEC) as the ground plane. Furthermore, a PEC circular mask was aligned on top, and underneath the disk was the nanowire-array region. The radius of the disk was 2.5 mm, and the three-port access microstrip was 8 mm long and 0.5 mm wide.

With the effective permeability tensor of the ferromagnetic-nanowire substrate obtained through the proposed homogenization procedure, and the relative permittivity of the porous alumina membrane with and without magnetic-nanowire filling set to be $6.15 - j0.25$ and 5.3 [15], respectively, we were ready to launch the full-wave numerical simulation and evaluate the performance of the circulator.

Figure 16 plots the transmission coefficients, with Port 1 being excited over the frequency range from 20 GHz to 40 GHz. As evidenced from the figure, the circulator had two working frequency bands: 25 GHz to 29 GHz, and 31.5 GHz to 33 GHz. In the first frequency band, 25 GHz to 29 GHz, the electromagnetic-wave energy circulated clockwise, whereas in the higher frequency band, 31.5 GHz to 33 GHz, it circulated counterclockwise. The reversing of the circulation direction in these two frequency bands was clearly demonstrated in Figure 17, where the distributions of the electric field are plotted for 27 GHz and 32 GHz, respectively.

With a modest isolation of roughly 10 dB, the performance of the circulator was yet to be enhanced. However, as a proof of concept, the proposed circulator demonstrated the capability of utilizing a ferromagnetic-nanowire substrate in an integrated microwave device to achieve novel properties and new applications.

4. Conclusion

A numerical homogenization procedure was proposed in this paper to study the unique properties of ferromagnetic-nanowire metamaterials. Numerical results validated the proposed approach. The double ferromagnetic-resonance phenomenon of a ferromagnetic-nanowire array was demonstrated. Moreover, two microwave components – a microwave edge-mode isolator and a dual-band self-biased circulator – were analyzed using the homogenized material properties in full-wave time-harmonic electromagnetic field computations.

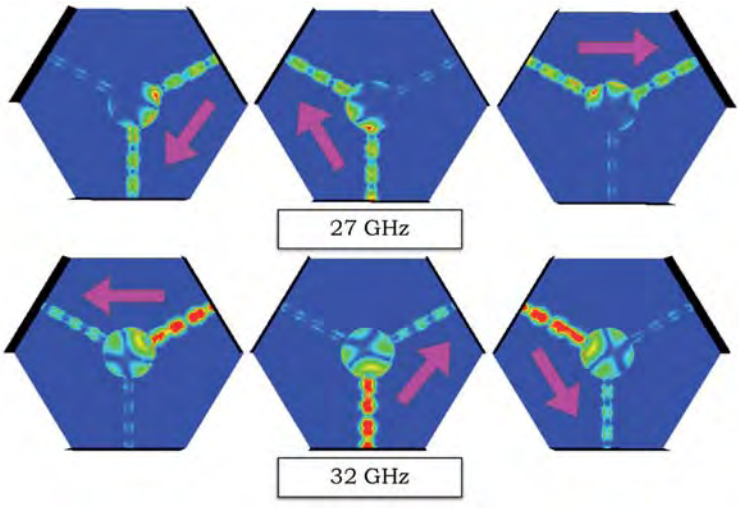

Figure 17. The electric-field plots of the full-wave simulation results of the conceptual microstrip circulator.

5. Acknowledgments

The authors would like to thank Dr. Louis-Philippe Carignan and Prof. Christophe Caloz at École Polytechnique de Montréal, Canada, for their help in preparing the edge-mode isolator.

6. References

1. V. G. Veselago, "The Electrodynamics of Substances with Simultaneously Negative Values of ε and μ," *Physics-Uspekhi*, **10**, 4, February, 1968, pp. 509-514.

2. D. R. Smith, W. Padilla, D. C. Vier, S. C. Nemat-Nasser and S. Schultz, "Composite Medium with Simultaneously Negative Permeability and Permittivity," *Physical Review Letters*, **84**, 18, May, 2000, pp. 4184-4187.

3. C. Caloz, and T. Itoh, "Application of the Transmission Line Theory of Left-handed (LH) Materials to the Realization of a Microstrip LH Line," IEEE International Symposium on Antennas and Propagation, **2**, 2002, pp. 412-415.

4. J. B. Pendry, D. Schurig and D. R. Smith, "Controlling Electromagnetic Fields," *Science*, **312**, 5781, April, 2006, pp. 1780-1782.

5. D. R. Smith, S. Schultz, P. Markoš and C. M. Soukoulis, "Determination of Effective Permittivity and Permeability of Metamaterials from Reflection and Transmission Coefficients," *Physical Review B*, **65**, 19, April, 2002.

6. D. R. Smith and J. P. Pendry, "Homogenization of Metamaterials by Field Averaging," *Journal of the Optical Society of America B*, **23**, 3, March, 2006, pp. 391-403.

7. A. Alu, "First-Principle Homogenization Theory for Periodic Metamaterials," *Physical Review B*, **84**, 7, August, 2011.

8. I. Tsukerman, "Effective Parameters of Metamaterials: A Rigorous Homogenization Theory via Whitney Interpolation," *Journal of the Optical Society of America B*, **28**, 3, March, 2011, pp. 577-586.

9. V. Boucher, L-P Carignan, T. Kodera, C. Caloz, A. Yelon and D. Menard, "Effective Permeability Tensor and Double Resonance of Interacting Bistable Ferromagnetic Nanowires," *Physical Review B*, **80**, 22, December, 2009.

10. L-P Carignan, A. Yelon, D. Menard and C. Caloz, "Ferromagnetic Nanowire Metamaterials: Theory and Applications," *IEEE Transactions on Microwave Theory and Techniques*, **59**, 10, October, 2011, pp. 2568-2586.

11. S. M. Seo and J-F Lee, "A Fast IE-FFT Algorithm for Solving PEC Scattering Problems," *IEEE Transactions on Magnetics*}, **41**, 5, May, 2005, pp. 1476-1479.

12. J. Ramprecht and D. Sjoberg, "Biased Magnetic Materials in RAM Applications," *Progress in Electromagnetics Research*, **75**, 2007, pp. 85-117.

13. G. Hamoir, J. De La Torre Medina, L. Piraux and I. Huynen, "Self-Biased Nonreciprocal Microstrip Phase Shifter on Magnetic Nanowired Substrate Suitable for Gyrator Applications," *IEEE Transactions on Microwave Theory and Techniques*, **60**, 7, July, 2012, pp. 2152-2157.

14. L-P Carignan, V. Boucher, T. Kodera, C. Caloz, A. Yelon and D. Menard, "Double Ferromagnetic Resonance in Nanowire Arrays," *Applied Physics Letters*, **95**, 6, August, 2009.

15. L-P Carignan, T. Kodera, A. Yelon, C. Caloz and D. Menard, "Integrated and Self-biased Planar Magnetic Microwave Circuits based on Ferromagnetic Nanowire Substrates," IEEE EuMC, 2009, pp. 743-746.

Theory and Simulations of Nonlinear Wave-Particle Interactions in Planetary Radiation Belts

Yoshiharu Omura

Research Institute for Sustainable Humanosphere
Kyoto, University, Gokasho, Uji,
Kyoto, 611-0011, Japan
E-mail: omura@rish.kyoto-u.ac.jp

This invited paper is based on the Commission H tutorial lecture to be given at the XXXIth URSI General Assembly and Scientific Symposium, Beijing, China, August, 2014.

Abstract

There has been significant progress in understanding the generation mechanism of whistler-mode chorus emissions in recent years. This is partly due to the successful reproduction of chorus emissions by computer simulations, and partly due to precise observations of the emissions by spacecraft in planetary radiation belts. We give a brief account of the nonlinear theory of the generation mechanism of chorus emissions, which has been revealed by the simulations and observations. We describe the nonlinear dynamics of resonant electrons, and the formation of the electromagnetic electron "hole" that results in resonant currents generating rising-tone emissions. In contrast, falling-tone emissions are generated through the formation of electron "hills." We also describe the mechanism of nonlinear wave damping due to quasi-oblique propagation, which results in the formation of a gap at half the electron cyclotron frequency. The nonlinear wave-growth theory of chorus emissions can also be applied to the generation mechanism of electromagnetic ion-cyclotron- (EMIC) triggered emissions, recently found in spacecraft observations. Hybrid code simulations have confirmed that coherent rising-tone emissions are generated by energetic protons at frequencies below the proton cyclotron frequency. Electromagnetic ion-cyclotron waves can also interact with relativistic electrons. Both chorus emissions and electromagnetic ion-cyclotron-triggered emissions play important roles in controlling radiation-belt particle dynamics.

1. Introduction

Whistler-mode chorus emissions have several important nonlinear physical processes as their generation mechanisms. In this tutorial, we review different nonlinear processes related to the generation of the rising-tone emissions of whistler-mode chorus emissions and electromagnetic ion-cyclotron- (EMIC) triggered emissions, in the course of theoretical developments in recent years. Both whistler-mode chorus emissions and electromagnetic ion-cyclotron-triggered emissions have significant influence on the dynamics of relativistic electrons in the radiation belts. The nonlinear acceleration and pitch-angle scattering mechanisms are also reviewed. This is not intended as a comprehensive review paper: the relevant papers are listed as references for understanding the basic physical processes.

2. Basic Dynamics of Resonant Electrons and Formation of an Electron Hole

The basic dynamics of energetic electrons interacting with a whistler-mode wave, propagating parallel to the magnetic field, has been studied by many papers (see the reviews in [1-3]). When the energy of the electrons is less than a few hundred keV, the electrons interact with a whistler-mode wave propagating in the opposite direction through cyclotron resonance. When the wave is generated around the equator, electrons moving toward the equator interact with the wave at the resonance velocity V_R. Most of these are scattered to lower pitch angles, while a fraction of them are trapped by the wave, being effectively accelerated [4]. The nonlinear trajectories of these resonant electrons are described by the pendulum equations, expressed as

$$\frac{\mathrm{d}\zeta}{\mathrm{d}t} = \theta, \tag{1}$$

$$\frac{\mathrm{d}\theta}{\mathrm{d}t} = \omega_{tr}^2 \left(\sin\zeta + S\right), \tag{2}$$

where S is an inhomogeneity factor given by

$$S = -\frac{1}{s_0 \omega \Omega_w}\left(s_1 \frac{\partial \omega}{\partial t} + c s_2 \frac{\partial \Omega_e}{\partial h} \right). \quad (3)$$

The variable h is the distance along the magnetic field line from the equator.

The variable ζ is the phase angle between the perpendicular velocity vector and the wave's magnetic-field vector. θ is the difference between the parallel velocity and the resonance velocity, defined by $\theta = k\left(v_{\|} - V_R\right)$, where k is the wavenumber. The parameter ω_{tr} is the trapping frequency, and the parameters s_0, s_1, and s_2 are functions of the wave's frequency, ω, and the average perpendicular velocity, respectively [5]. The inhomogeneity factor consists of two terms: the frequency sweep rate, and the gradient of the background magnetic field, expressed by the cyclotron frequency Ω_e. They are divided by the wave's amplitude, Ω_w, normalized by the cyclotron frequency. Since the majority of resonant electrons are un-trapped, there arises a hole in the velocity phase space, (ζ, θ), which we call an electromagnetic electron hole. This is because the wave potential is formed by the electromagnetic Lorentz force due to the cross product of the perpendicular velocity and the wave magnetic field acting in the direction parallel to the background magnetic field.

3. Wave Growth Due to the Frequency Sweep Rate at the Equator

As shown in Figure 1a, the electron hole can form a transverse resonant current that is decomposed into two components: J_E parallel to the wave's electric field, and J_B parallel to the wave's magnetic field. From Maxwell's equations, we can derive an equation describing the evolution of the wave's amplitude, B_w, controlled by J_E and the dispersion relation between the wave's frequency and the wavenumber including J_B, which we may call a nonlinear dispersion relation. Depending on the magnitude of the inhomogeneity factor S, the ratio of J_B and J_E changes.

The maximum value of a negative J_E can be attained when $S = -0.4$, which maximizes the wave's growth. Since the interaction takes place near the magnetic equator, where the flux of the energetic electrons maximizes because of the lowest value of the resonance velocity, the gradient of the magnetic field, the second term in Equation (3), can be neglected. To realize maximum wave growth, we need to assume a finite frequency-sweep rate, given by

$$\frac{\partial \omega}{\partial t} = 0.4 \frac{s_0}{s_1} \omega \Omega_w, \quad (4)$$

which shows that the frequency-sweep rate is proportional to the wave's frequency and the wave's amplitude [6].

A series of electron hybrid simulations [7] were conducted with different densities of the energetic electrons generating chorus emissions with different wave amplitudes [8]. We found that frequency-sweep rates varied depending on the wave amplitudes. We also found that the waves were progressively generated at the equator, indicating that the chorus emission is due to the absolute instability near the equator.

We can rewrite the wave-amplitude equation based on the initial unperturbed distribution function of energetic electrons. Combining this with the frequency-sweep-rate Equation (4), we have a set of equations that describe the initial phase of the chorus-wave growth, which we call the chorus equations [5]. We have the threshold wave amplitude for the absolute instability occurring at the equator. It is noted that the chorus equations are valid only for the initial phase of the nonlinear wave growth, and the saturation mechanisms are not included in the equations.

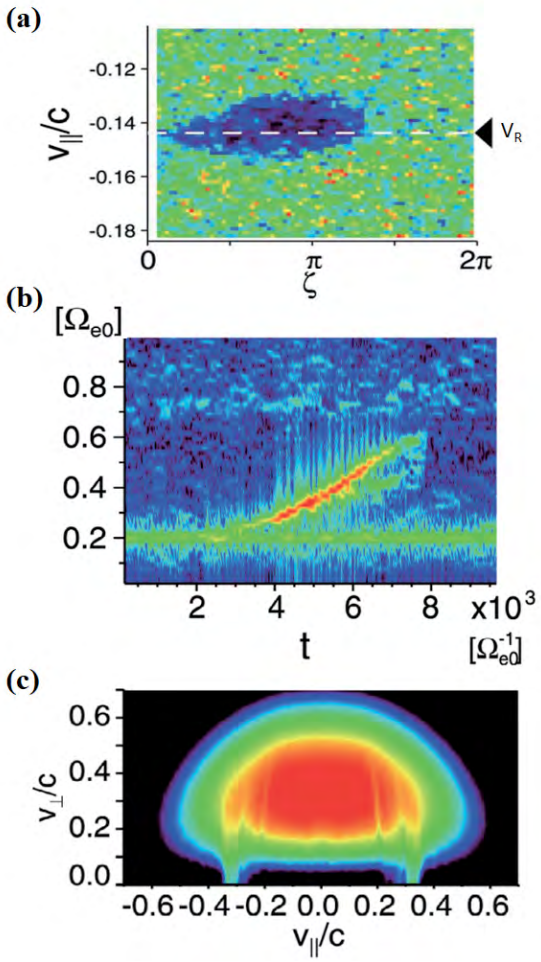

Figure 1. An electromagnetic full-particle simulation by Hikishima and Omura (2012) [10]: (a) An electron hole in the velocity phase space, (b) a whistler-mode rising-tone emission, (c) the velocity distribution function of energetic electrons at the equator.

4. Simulation of Triggered Emissions

Self-consistent electromagnetic particle simulations were performed to analyze whistler-mode triggered emissions in the magnetosphere [9], where we injected a triggering wave at the equator. In addition to the triggering wave with a constant frequency, very clear rising-tone emissions, propagating in the northward and southward directions, appeared, together with the formation of electron holes in the velocity phase space, as shown in Figure 1 [10]. The time evolution of the velocity distribution function, $f\left(v_{\|}, v_{\perp}\right)$, at the equator was also analyzed [9, 11]. Corresponding to the northward and southward waves, nearly vertical depletion regions, corresponding to the electron holes, appeared in the negative and the positive parallel velocity regions, as shown in Figure 1c. They moved inward to the smaller parallel velocities. It was also interesting that some of them, at higher perpendicular velocities, were effectively trapped, and accelerated to higher pitch angles, as we found two bumps at smaller parallel velocities [9].

5. Optimum Wave Amplitude for Triggering Rising-Tone Emissions

We varied the amplitude of the triggering waves, but the frequency-sweep rates of triggered emissions, which are related to the wave amplitudes by Equation (4), were nearly the same, indicating that the excited wave amplitudes did not depend on the amplitude of a triggering wave [10]. A very large triggering wave cannot excite rising-tone emissions, implying that there exists an optimum wave amplitude for triggering emissions. We have examined the relationship between the wave amplitude and the triggering process of a rising-tone emission. By separating the wave frequency into a solution of the linear dispersion relation, ω_0, and its deviation, ω_1, we obtained a relationship between the deviation and the component current, J_B, divided by the wave amplitude [12]. In the formation process of an electron hole, J_B is gradually formed over a time T_N, which we call the nonlinear transition time, of the same order as the nonlinear trapping period. The frequency increase, ω_1, is induced over the time T_N, which is equivalent to the average frequency sweep rate determined by the wave amplitude. We checked the importance of the foregoing formation of J_B in the Vlasov hybrid code [13], in which we explicitly solved the wave equations with J_B and J_E. In the code without J_B, we could not reproduce the rising tone, clearly indicating the importance of J_B in triggering the rising-tone emissions. Solving for the wave amplitude in the nonlinear wave-growth condition maximizing the value of J_E, we obtained the optimum wave amplitude for triggering a rising-tone emission (the black solid lines in Figure 2c). We have also derived the optimum wave amplitude for the electromagnetic ion-cyclotron-triggered emissions [14].

6. Formation of Subpackets

The optimum amplitudes and the threshold amplitudes were plotted as functions of frequency [12] for various parameters used in the simulations [7, 15] and observations [16-18]. As the frequency increased, the optimum amplitude decreased. The frequency range of the emission roughly corresponded to the ranges of the frequency for which the optimum amplitude was greater than the threshold amplitude. The wave could not grow much beyond the optimum value, because the inhomogeneity could not be kept close to $S = -0.4$ with the increasing wave amplitude. Once the amplitude exceeded the optimum value as a result of the absolute instability,

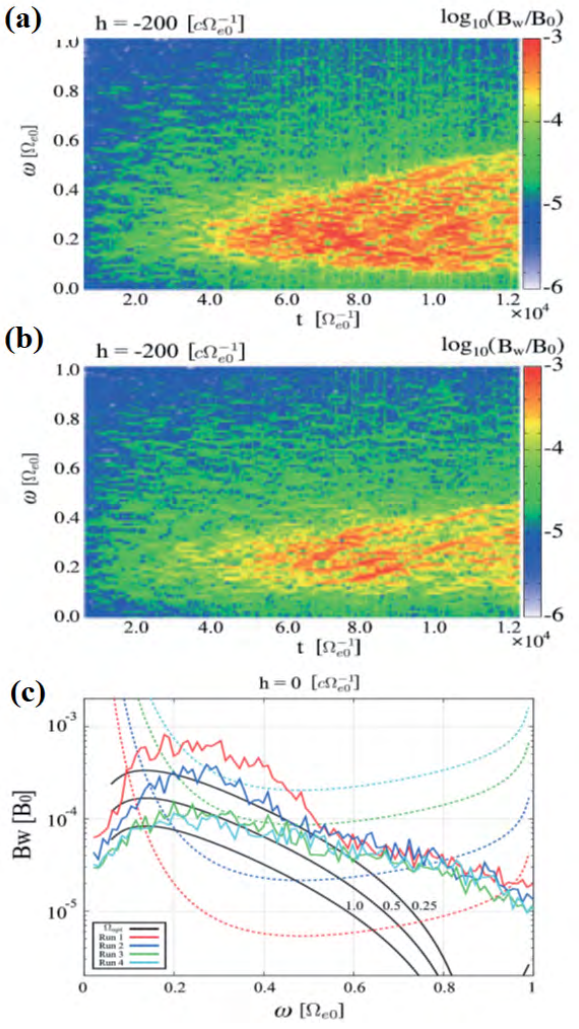

Figure 2. An electron hybrid simulation by Katoh and Omura (2013) [20]: (a) Run 1, with a smaller magnetic-field gradient reproducing broadband hiss-like emissions originating from concurrent chorus emissions; (b) Run 2, with a larger magnetic-field gradient generating chorus emissions; (c) The maximum wave amplitudes of the frequency spectra at the equator observed in Runs 1-4. The threshold amplitudes were plotted in colored dashed lines, and the optimum amplitudes were plotted in black solid lines.

the wave growth was terminated, and then the triggering started from a slightly higher frequency. It was noted that an incoming flux of energetic electrons was modulated by the frequency of the triggered emission as the trigged emission propagated away from the equator. Therefore, the electrons modulated in their gyrophase could generate a seed of triggering waves, even in the region slightly upstream of the equator. This process is related to the formation of subpacket structures in the chorus elements. In an observation of chorus emissions by the THEMIS spacecraft [18], we found that the observation was made almost at the equator, because we did not find any gap at half the cyclotron frequency in the spectra of rising-tone emissions, as explained in Section 8. Using the observed particle data, we calculated the threshold and optimum wave amplitudes, and we also compared the frequency-sweep rate with the wave's amplitude relation. As we observed in the time history of the rising-tone emission, we found that a rising-tone element consisted of many "triggerings" of the absolute instability at progressively increasing frequencies. Each triggering corresponded to the formation of a subpacket. A recent observation by the Van Allen Probes has also identified detailed structures of many subpackets in a single chorus element [19].

7. Nonlinear Convective Instability

We now describe how the chorus elements excited near the magnetic equator propagate away from the equator. The frequency-sweep rate established at the equator is preserved through propagation, and the nonlinear instability due to the nonlinear current J_E should continue even away from the equator. However, as the wave amplitude grows, the relative contribution of the frequency-sweep rate to the value of S becomes small. Instead, the gradient of the magnetic field, which occurs in the second term in S, increases as a function of the distance from the equator. The value of S can therefore be kept close to -0.4, resulting in efficient nonlinear wave growth through propagation. This is the nonlinear convective instability. The magnitude of the wave amplitude should increase with increasing latitude as long as the flux of energetic electron exists, as we also found in the simulation [11, 15].

8. Nonlinear Wave Damping at Half the Cyclotron Frequency

There is another prominent nonlinear effect in the process of wave propagation away from the equator. The wave-normal angles are parallel at the equator, but they gradually become oblique through propagation along the dipole magnetic field, while we assumed purely parallel propagation in the simulations of chorus generation. In the simulation, we did not find any gap at half the cyclotron frequency, while we found the gap in most of the chorus observations. The mechanism of the gap formation is due to nonlinear wave damping of the chorus element at the local half cyclotron frequency, when the wave normal angle satisfies the quasi-parallel propagation condition [5]. The group velocity and phase velocity of whistler-mode waves coincide at half the cyclotron frequency in the quasi-parallel propagation. The parallel electric field appears even at a small oblique angle, and the electric field forms a static potential in the frame of reference moving with the phase velocity and the group velocity.

The electrostatic potential can trap the energetic electrons moving with the phase velocity. There arises a mirror force in the parallel direction that acts as a secular term in the pendulum equations of the nonlinear trapping. In other words, the phase velocity increases, and the electrons are accelerated in the parallel direction. Because of the acceleration, the wave loses its energy to the trapped electrons, resulting in damping at half the local cyclotron frequency.

9. Concurrent Triggering of Chorus Emissions and Broadband Hiss-Like Emissions

We have considered formation of a chorus element due to the sequential triggering of rising-tone emissions, when the threshold amplitude is below the optimum wave amplitude. The threshold amplitude is controlled by the gradient of the background magnetic field, which is modeled by a parabolic function, $\Omega_e = \Omega_{EQ}\left(1+ah^2\right)$, where Ω_{EQ} is the electron cyclotron frequency at the equator. In a series of the electron hybrid-code simulations (Runs 1 and 2 out of Runs 1-4 are shown in Figures 2a and 2b) [20], we varied the value of the parabolic coefficient, a, in these simulations. A smaller value makes the threshold smaller. With the smaller threshold amplitude, we found that many triggerings of rising-tone emissions occur at the same time at different locations and different frequencies, as shown in Figure 2a. This indicates that the broadband hiss-like emissions [21] may also consist of the nonlinear wave-growth processes that we find in the chorus emissions. When the gap between the threshold and the optimum amplitudes is large, the triggering becomes concurrent. Theoretically, this is possible if the electron holes are formed at different locations in the velocity phase space. When concurrent triggering takes place with a lower threshold amplitude due to a lower gradient of the magnetic field, the wave amplitude appears enhanced, because of overlap of several chorus elements being excited at the same time (Figure 2c).

10. Electromagnetic Ion Cyclotron Triggered Emissions

The same nonlinear process as for R-mode whistler emissions can take place for the L-mode electromagnetic ion-cyclotron waves below the proton cyclotron frequency by energetic protons with temperature anisotropy, as

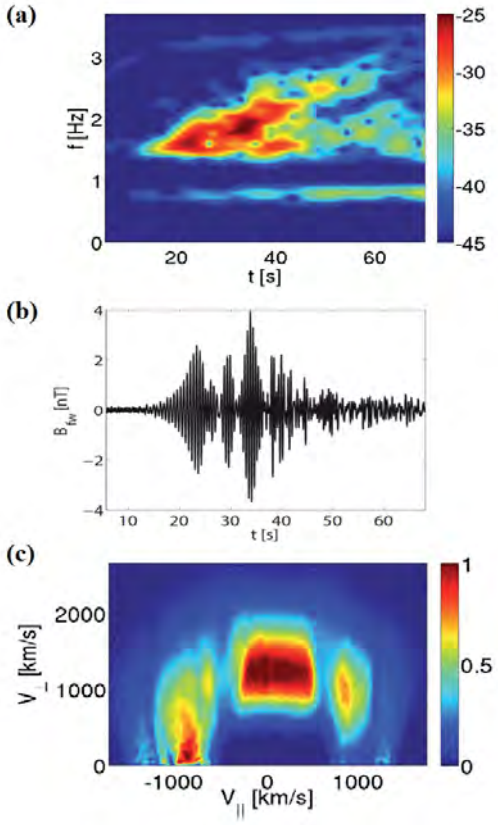

Figure 3. An ion hybrid simulation by Shoji and Omura (2013) [14]: (a) The dynamic spectrum of an electromagnetic ion-cyclotron-triggered emission; (b) the waveforms of the emission, showing subpackets; (c) the velocity distribution function of energetic protons generating the emission.

reported as electromagnetic ion-cyclotron-triggered emissions observed by the Cluster spacecraft [22]. The nonlinear wave-growth theory [23] was developed in the process of the data analysis of electromagnetic ion-cyclotron waves. The nonlinear wave growth of rising-tone emissions and associated precipitation of energetic protons was confirmed by the hybrid-code simulation [24, 25], as shown in Figure 3. We also derived the optimum wave amplitude for the electromagnetic ion-cyclotron-triggered emissions, and confirmed the formation of subpackets due to saturation of the nonlinear wave growth and repeated triggering process, shown in Figure 3b [14]. In the process of nonlinear wave growth, a substantial amount of energetic protons is precipitated in the loss cone, as we found in Figure 3c. The electromagnetic ion-cyclotron triggered emissions also cause significant precipitation of relativistic electrons, as discussed in the next section.

11. Acceleration and Pitch-Angle Scattering of Relativistic Electrons

Whistler-mode waves can interact with a wide range of energies, because of the relativistic effect that appears in the cyclotron resonance condition,

$$\omega - kV_R = \frac{\Omega_e}{\gamma}, \qquad (5)$$

by virtue of the Lorentz factor, γ. Chorus emissions in the magnetosphere are excited by electrons of energy $1 \sim 100$ keV. In the energy range greater than 100 keV, the Lorentz factor, γ, deviates from unity, substantially changing the resonance condition. When the frequency satisfies the condition $\omega < \Omega_e/\gamma$, the resonance velocity, V_R, takes a negative value. A fraction of the electrons moving toward the equator at a velocity close to the resonance velocity is trapped by the nonlinear wave potential, and they are accelerated due to the spatial inhomogeneity of the magnetic field. As the trapped electrons are accelerated to higher energies, the Lorentz factor increases to satisfy the equation $\omega = \Omega_e/\gamma$. The resonance velocity then becomes zero, while the trapped electrons are accelerated further to have a positive resonance velocity with a condition $\omega > \Omega_e/\gamma$. This process is called "relativistic turning acceleration" (RTA) [26, 27]. The small resonance velocity, close to zero, makes the interaction time longer, and the acceleration becomes very effective. An electron with an energy of a few hundred keV can be accelerated to 1 MeV energy within a short time. Relativistic electrons of a few MeV can also be accelerated by the nonlinear trapping by a wave packet moving together in the same direction. Because of the longer interaction period, the acceleration of the trapped electrons becomes significant, generating the several MeV electrons forming the radiation belts. We call this acceleration "ultra-relativistic acceleration" (URA) [28]. The long time evolution of the relativistic electron flux due to relativistic turning acceleration and ultra-relativistic acceleration has been demonstrated by a test particle simulation [29].

Pitch-angle scattering of energetic electrons ($1 \sim 100$ keV) takes place in the process of chorus-wave generation. Un-trapped resonant electrons are effectively scattered into the loss cone, as demonstrated in the chorus-generation simulation [30]. The higher-energy electrons are not scattered much by chorus emissions, because the un-trapped resonant electrons go only around the wave potential, and the change of the pitch angles and energies induced by the resonance are not significant. On the other hand, the electrons at energies greater than 100 keV are effectively scatted to lower pitch angles through nonlinear wave trapping by electromagnetic ion-cyclotron waves. The pitch-angle scattering becomes very effective, especially by an electromagnetic ion-cyclotron rising-tone emission [31, 32]. As we find with the chorus-wave generation, the finite inhomogeneity due to the rising tone plays a critical role in inducing the pitch-angle variation.

12. Falling Tone Emissions

When the triggering wave is injected into the region upstream from the equator, the triggering of falling-tone emissions is possible, as demonstrated by the Vlasov hybrid

simulation [33]. In the upstream region, an electron hill with an enhanced density is formed in the velocity phase space, instead of an electron hole. The electron hill generates a resonant current, J_B, with the reversed sign, inducing a negative frequency deviation $\omega_1 < 0$. The frequency-sweep rate is reversed, because of the negative ω_1, and the gradient of the magnetic field also becomes negative, because of the upstream location. Because of these effects, the sign of the inhomogeneity factor, S, for the trapped resonant electrons forming the hill is reversed. The electron hill can be regarded as an electron hole with a negative density depression. The electron hole with the reversed sign of S and the negative density depression induce a negative J_E causing wave growth, as we find in the case of rising-tone emissions. Therefore, generation of falling-tone emissions can take place in the upstream region. When the wave packet of the falling-tone emission propagates toward the equator, the propagation angle substantially deviates from the parallel direction [34]. The obliquity prevents the wave packet from further interaction with the resonant electrons that may turn the emission into a rising-tone emission.

13. Conclusion

The nonlinear wave-growth process of whistler-mode emissions is triggered by a wave with an amplitude above the threshold of the absolute instability. When the triggering waves are naturally excited by the instability driven by the temperature anisotropy, the emissions are called "chorus." Chorus emissions are also observed in the magnetospheres of Jupiter [35] and Saturn [36]. The nonlinear processes of whistler-mode and electromagnetic ion-cyclotron wave generation and associated relativistic electron dynamics should be operative in radiation belts of magnetized planets.

Nonlinear wave growth can be triggered by an artificially transmitted wave from an antenna located near the magnetic equator, or by waves radiated from an ionospheric current modulated at a designated frequency produced by heating facilities from the ground. Since both chorus emissions and electromagnetic ion-cyclotron triggered emissions have significant impact on the relativistic electron flux of the radiation belts through nonlinear wave-trapping processes, artificial excitation of these waves may make it possible in the future to control the radiation belts.

14. Acknowledgments

This work was supported by Grant-in-Aid 23340147 of the Ministry of Education, Science, Sports and Culture of Japan. The author thanks David Nunn, Danny Summers, Ondrej Santolik, Yuto Katoh, Mitsuru Hikishima, and Masafumi Shoji for their useful comments for revision of the manuscript.

15. References

1. Y. Omura, D. Nunn, H. Matsumoto and M. J. Rycroft, "A Review of Observational, Theoretical and Numerical Studies of VLF Triggered Emissions," *Journal of Atmospheric and Terrestrial Physics*, **53**, 1991, pp. 351-368.

2. S. Sazhin and M. Hayakawa, "Magnetospheric Chorus Emissions – A Review," *Planetary and Space Science*, **40**, 1991, pp. 681-697.

3. Y. Omura, D. Nunn, and D. Summers, "Generation Processes of Whistler-Mode Chorus Emissions: Current Status of Nonlinear Wave Growth Theory," *Geophysical Monograph Series*, **199**, "Dynamics of the Earth's Radiation Belts and Inner Magnetosphere," American Geophysical Union, 2012, pp. 243-254.

4. Y. Omura and D. Summers, "Dynamics of High Energy Electrons Interacting with Whistler-Mode Chorus Emissions in the Magnetosphere," *Journal of Geophysical Research*, **111**, 2006, A09222.

5. Y. Omura, M. Hikishima, Y. Katoh, D. Summers, and S. Yagitani, "Nonlinear Mechanisms of Lower Band and Upper Band VLF Chorus Emissions in the Magnetosphere," *Journal of Geophysical Research*, **114**, 2009, A07217.

6. Y. Omura, Y. Katoh, and D. Summers, "Theory and Simulation of the Generation of Whistler-Mode Chorus," *Journal of Geophysical Research*, **113**, 2008, A04223.

7. Y. Katoh and Y. Omura, "Computer Simulation of Chorus Wave Generation in the Earth's Inner Magnetosphere," *Geophysical Research Letters*, **34**, 2007, L03102.

8. Y. Katoh and Y. Omura, "Amplitude Dependence of Frequency Sweep Rates of Whistler Mode Chorus Emissions, *Journal of Geophysical Research*, **116**, 2011, A07201.

9. M. Hikishima, Y. Omura, and D. Summers, "Self-Consistent Particle Simulation of Whistler Mode Triggered Emissions," *Journal of Geophysical Research*, **115**, 2010, A12246.

10. M. Hikishima and Y. Omura, "Particle Simulations of Whistler-Mode Rising-Tone Emissions Triggered by Waves with Different Amplitudes," *Journal of Geophysical Research*, **117**, 2012, A04226.

11. M. Hikishima, S. Yagitani, Y. Omura, and I. Nagano, "Coherent Nonlinear Scattering of Energetic Electrons in the Process of Whistler-Mode Chorus Generation," *Journal of Geophysical Research*, **114**, 2009, A10205.

12. Y. Omura and D. Nunn, "Triggering Process of Whistler Mode Chorus Emissions in the Magnetosphere," *Journal of Geophysical Research*, **116**, 2011, A05205.

13. D. Nunn, "A Novel Method for the Numerical Simulation of Hot Collision-Free Plasmas; Vlasov Hybrid Simulation," *Journal of Computational Physics*, **109**, 1993, pp. 180-196.

14. M. Shoji and Y. Omura, "Triggering Process of Electromagnetic Ion Cyclotron Rising Tone Emissions in the Inner Magnetosphere," *Journal of Geophysical Research*, **118**, 2013, pp. 5553-5561.

15. M. Hikishima, S. Yagitani, Y. Omura, and I. Nagano, "Full Particle Simulation of Whistler-Mode Rising Chorus Emissions in the Magnetosphere," *Journal of Geophysical Research*, **114**, 2009, A01203.

16. O. Santolik, D. A. Gurnett, J. S. Pickett, M. Parrot, and N. Cornilleau-Wehrlin, "Spatio-Temporal Structure of Storm-Time Chorus," *Journal of Geophysical Research*, **108**, July 2003, 1278.

17. O. Santolik, "New Results of Investigations of Whistler-Mode Chorus Emissions," *Nonlinear Processes in Geophysics*, **15**, 2008, pp. 621-630.

18. S. Kurita, Y. Katoh, Y. Omura, V. Angelopoulos, C. M. Cully, O. Le Contel, and H. Misawa, "THEMIS Observation of Chorus Elements Without a Gap at Half the Gyrofrequency," *Journal of Geophysical Research*, **117**, 2012, A11223.

19. O. Santolik, C. A. Kletzing, W. S. Kurth, G. B. Hospodarsky and S. R. Bounds, "Fine Structure of Large-Amplitude Chorus Wave Packets," *Geophysical Research Letters*, **41**, 2014, pp. 293-299.

20. Y. Katoh and Y. Omura, "Effect of the Background Magnetic Field Inhomogeneity on Generation Processes of Whistler-Mode Chorus and Broadband Hiss-Like Emissions," *Journal of Geophysical Research*, **118**, 2013, pp. 4189-4198.

21. W. Li, R. M. Thorne, J. Bortnik, X. Tao, and V. Angelopoulos, "Characteristics of Hiss-Like and Discrete Whistler-Mode Emissions," *Geophysical Research Letters*, **39**, 2012, L18106.

22. J. S. Pickett, B. Grison, Y. Omura, M. J. Engebretson, I. Dandouras, A. Masson, M. L. Adrian, O. Santolik, P. M. E. Decreau, N. Cornilleau-Wehrlin, and D. Constantinescu, "Cluster Observations of EMIC Triggered Emissions in Association with Pc1 Waves Near Earth's Plasmapause," *Geophysical Research Letters*, **37**, 2010, L09104.

23. Y. Omura, J. Pickett, B. Grison, O. Santolik, I. Dandouras, M. Engebretson, P. M. E. Decreau, and A. Masson, "Theory and Observation of Electromagnetic Ion Cyclotron Triggered Emissions in the Magnetosphere," *Journal of Geophysical Research*, **115**, 2010, A07234.

24. M. Shoji and Y. Omura, "Simulation of Electromagnetic Ion Cyclotron Triggered Emissions in the Earth's Inner Magnetosphere," *Journal of Geophysical Research*, **116**, 2011, A05212.

25. M. Shoji and Y. Omura, "Precipitation of Highly Energetic Protons by Helium Branch Electromagnetic Ion Cyclotron Triggered Emissions," *Journal of Geophysical Research*, **117**, 2012, A12210.

26. Y. Omura, N. Furuya, and D. Summers, "Relativistic Turning Acceleration of Resonant Electrons by Coherent Whistler-Mode Waves in a Dipole Magnetic Field," *Journal of Geophysical Research*, **112**, 2007, A06236.

27. Y. Katoh, Y. Omura, and D. Summers, "Rapid Energization of Radiation Belt Electrons by Nonlinear Wave Trapping," *Annales Geophysicae*, **26**, 2008, pp. 3451-3456.

28. D. Summers and Y. Omura, "Ultra-Relativistic Acceleration of Electrons in Planetary Magnetospheres," *Geophysical Research Letters*, **34**, 2007, L24205.

29. N. Furuya, Y. Omura, and D. Summers, "Relativistic Turning Acceleration of Radiation Belt Electrons by Whistler Mode Chorus," *Journal of Geophysical Research*, **113**, 2008, A04224.

30. M. Hikishima, Y. Omura, and D. Summers, "Microburst Precipitation of Energetic Electrons Associated with Chorus Wave Generation," *Geophysical Research Letters*, **37**, 2010, L07103.

31. Y. Omura and Q. Zhao, "Nonlinear Pitch-Angle Scattering of Relativistic Electrons by EMIC Waves in the Inner Magnetosphere," *Journal of Geophysical Research*, **117**, 2012, A08227.

32. Y. Omura and Q. Zhao, "Relativistic Electron Microbursts Due to Nonlinear Pitch-Angle Scattering by EMIC Triggered Emissions," *Journal of Geophysical Research*, **118**, 2013, pp. 5008-5020.

33. D. Nunn and Y. Omura, "A Computational and Theoretical Analysis of Falling Frequency VLF Emissions," *Journal of Geophysical Research*, **117**, 2012, A08228.

34. K. Yamaguchi, T. Matsumuro, Y. Omura, and D. Nunn, "Ray Tracing of Whistler-Mode Chorus Elements: Implications for Generation Mechanisms of Rising and Falling Tone Emissions," *Annales Geophysicae*, **31**, 2013, pp. 665-673.

35. F. V. Coroniti, F. L. Scarf, C. F. Kennel, and W. S. Kurth, "Analysis of Chorus Emissions at Jupiter," *Journal of Geophysical Research*, **89**, 1984, pp. 3801-3820.

36. G. B. Hospodarsky, T. F. Averkamp, W. S. Kurth, D. A. Gurnett, J. D. Menietti, O. Santolik, and M. K. Dougherty, "Observations of Chorus at Saturn Using the Cassini Radio and Plasma Wave Science Instrument," *Journal of Geophysical Research*, **113**, 2008, A12206.

Drivers, Detection, and Impacts of Precipitation from the Radiation Belts

C.J. Rodger[1], M.A. Clilverd[2], W. Li[3], M.P. McCarthy[4], Y. Omura[5], and C.E. Weaver[6],

[1]Department of Physics, University of Otago, Dunedin, New Zealand
E-mail: crodger@physics.otago.ac.nz

[2] British Antarctic Survey (NERC), Cambridge, United Kingdom
E-mail: macl@bas.ac.uk

[3]Atmospheric and Oceanic Sciences, UCLA, Los Angeles, CA, USA
E-mail: moonli@atmos.ucla.edu

[4]Department of Earth and Space Sciences, University of Washington, Seattle, USA
E-mail: mccarthy@ess.washington.edu

[5]Research Institute for Sustainable Humanosphere, Kyoto University, Kyoto, Japan
E-mail: omura@rish.kyoto-u.ac.jp

[6]University of Calgary, Calgary, Canada
E-mail: carol.weaver@unh.edu

Abstract

Particle precipitation into the atmosphere is believed to be one of the dominant mechanisms for the loss of energetic electrons from the Van Allen radiation belts. Wave-particle interactions involving ULF through to VLF waves are thought to be important drivers of these loss events. There is growing interest in energetic electron precipitation (EEP). Much of the renewed interest comes from NASA's recent Van Allen Probes mission, which has stimulated new experimental and theoretical research and opened up new understanding into the fundamental physical processes of radiation-belt dynamics. There is also a new focus on the impact of the energetic electron precipitation on the polar atmosphere, with increasing evidence of significant changes in upper-atmospheric chemistry, and coupling to polar-surface climate.

1. Background Information

The Earth is surrounded by regions of magnetospherically trapped high-energy particles, with intense fluxes of relativistic energy electrons (>1 MeV). These regions are known as the inner and outer Van Allen radiation belts, named after their discoverer, James A. Van Allen, of the University of Iowa. The first observations of the Van Allen belts date back to the very beginning of the Space Age, undertaken by Explorer-1 and Explorer-3 in early 1958, as part of the International Geophysical Year. This was unexpected, with the early observations prompting one of Van Allen's research team to proclaim, "My God, Space is Radioactive." A schematic showing the basic location of the radiation belts relative to the Earth and inner magnetosphere is shown in Figure 1.

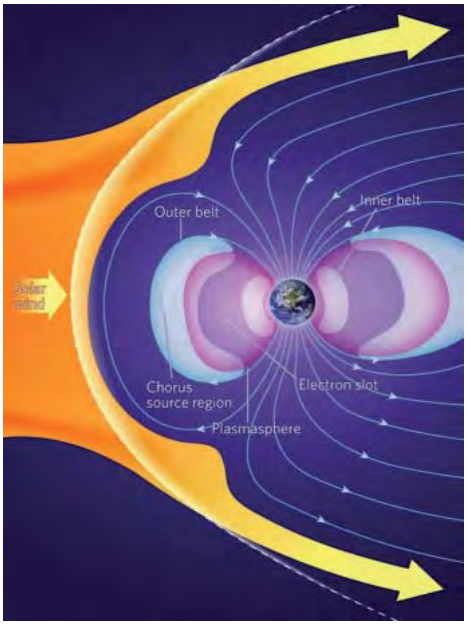

Figure 1. A schematic view of "Geospace:" that region of space closest to the Earth that includes the Van Allen Radiation Belts and is dominated by the geomagnetic field (image adapted from [1]).

As most satellites spend their lives inside the radiation belts, they are directly affected by this environment. Earth-orbiting satellites can be damaged or even lost due to increased high-energy electron fluxes in the Earth's radiation belts. In particular, the outer radiation belt (located 3.5 to eight Earth radii from the Earth's center) is highly dynamic, with fluxes changing by a factor as large as 1000 on timescales of hours to days. These changes are triggered by processes originating from the sun, and, in particular, by fluctuations in the solar wind, themselves reflecting conditions in the sun's outer atmosphere. While originally discovered in the dawn of the space age, there are still significant questions surrounding the relativistic electrons in the radiation belts. Many scientists around the world are investigating how the flux of outer radiation-belt electrons can change by so much, and so quickly.

The upcoming URSI General Assembly and Scientific Symposium (Beijing, PRC, August 16-23, 2014) features two sessions directly focused on the energetic radiation belts: H01 – "Wave-Particle Interactions and Their Effects on Planetary Radiation Belts," and HG03 – "Drivers, Detection, and Ionospheric Impacts of Precipitation from the Radiation Belts," as well as Commission H's tutorial by Prof. Yoshiharu Omura of Kyoto University ("Theory and Simulations of Nonlinear Wave-Particle Interactions in the Planetary Radiation Belts). The session descriptions for the two sessions are copied below:

1.1 H01/02/03/05 Description

Wave-particle interactions are a ubiquitous physical phenomenon that allow the exchange of energy and momentum between natural plasma waves, and energetic radiation-belt particles. In so doing, the wave can act as an energy conduit between different particle energies, species, or both. In this session, we discuss the various plasma waves that control planetary radiation-belt dynamics; their specific effects on the particles, both individually and in concert; and the various modes of wave-particle interactions, for instance, linear, quasi-linear, nonlinear, and non-resonant. We welcome both theoretical and observational studies involving the radiation belts of the Earth or other planets. We particularly encourage early results from the Van Allen Probes. Note that studies directed towards radiation-belt particle precipitation and its effects are likely better suited to the complementary session HG1.

1.2 HG03/04 Description

Particle precipitation into the atmosphere is believed to be one of the dominant mechanisms for the energetic electron loss from the Van Allen radiation belts, as well as ring-current ions. Wave-particle interactions with ULF through to VLF waves are thought to be important drivers of these loss events. This session is targeted at both ground-based and satellite experimental observations, as well as theoretical investigations, into the precipitation of energetic (>20 keV) and relativistic electrons or ring-current ions. Papers considering wave-particle interactions driving losses, measurement of loss fluxes, or the effects of this precipitation on the ionosphere are welcome. We particularly welcome early results from the Van Allen Probes, the BARREL campaign, or studies from existing ground and space-based experiments. Note that studies directed towards radiation-belt electron acceleration or transport are likely better suited to the complementary session H1.

In this *Radio Science Bulletin* paper, we report on the growing interest in energetic electron precipitation (EEP) from the Van Allen radiation belts, which has led to the HG03 session in the upcoming GASS. This is an area in which electromagnetic waves are core to all the physical mechanisms of acceleration, transport, and loss of radiation-belt energetic electrons. In addition, multiple experimental techniques have been employed to monitor the occurrence and properties of energetic electron precipitation as it strikes the ionosphere. These tend to rely either upon the energy released (by measuring X-rays, for example by high-altitude balloons), or by monitoring the electrical conductivity of the upper atmosphere, which is increased by energetic electron precipitation (and sensed by waves ranging from over frequencies from VLF through to the L-band employed by GNSS in total electron content measurements). We include information from each one of the invited speakers from the HG03 session, as well as where energetic electron precipitation fits into the wider scientific picture.

2. Wave-Particle Interactions

Wave-particle interactions are an ubiquitous physical phenomenon that allow the exchange of energy and momentum between natural plasma waves, and energetic radiation-belt particles. In so doing, the wave can act as an energy conduit between different particle energies, species, or both. The basic physics of the propagation of these waves through the magneto-active plasma leads the waves to be circularly polarized. For waves in the VLF range, the polarization is right-hand circular. This has become known as the "whistler mode," as some of the most common forms are whistlers, caused by the electromagnetic waves from lightning propagating through the plasma. A number of naturally occurring whistler-mode waves exist, with chorus and hiss being examples with high importance to the radiation belts. The whistler mode is sometimes referred to as the electron cyclotron mode, as it has the same "sense" as an electron gyrating in a magnetic field. In the ULF-ELF range, the wave's propagation is left-hand circularly polarized, commonly termed the ion-cyclotron mode (which assumes a positively charged ion). An example of these waves is an electromagnetic ion-cyclotron mode (EMIC) wave, which is also important in radiation-belt dynamics.

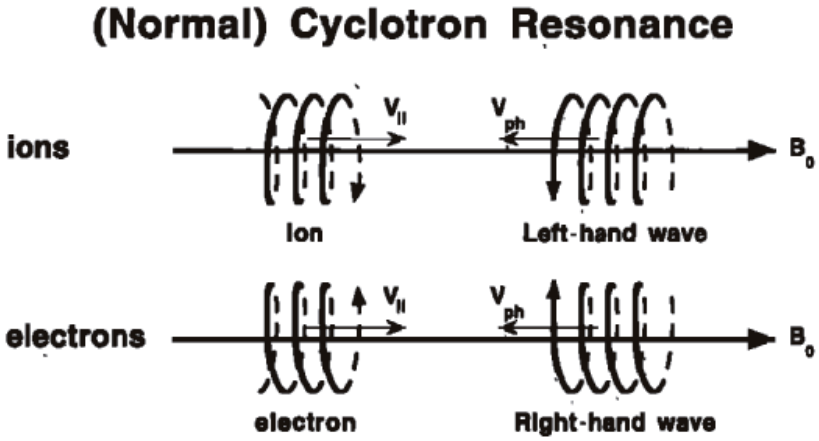

Figure 2. For normal resonance, the relative motion between the wave and particle Doppler-shifts the wave up to the cyclotron frequency of the particle (image adapted from [4]).

As the whistler and ion-cyclotron mode waves are circularly polarized, they may resonate with the gyrating electrons and ions found within the Van Allen Radiation Belts. The so-called "Normal" resonance occurs between the Doppler-shifted wave and the particle, with electrons resonating with whistler-mode waves and protons with ion-cyclotron-mode waves (Figure 2). The interactions between an electron and a right-hand polarized wave depend on the energy of the electron, such that there are relativistic considerations. If $\gamma < \Omega_c/\omega$, the wave and particle propagate in opposite directions, as in Figure 2 (i.e., counter-streaming), where γ is the Lorentz factor, Ω_c is the angular cyclotron frequency, and ω is the angular wave frequency. However, if the particle energy is still higher, such that $\gamma > \Omega_c/\omega$, the wave and particle will move in the same direction. While this is still normal cyclotron resonance, the electron does not overtake the wave packet, because $V_R < V_p < V_g$ (for $\omega < 0.5\Omega_c$), where V_R is the particle's resonance velocity, V_p is the wave's phase velocity, and V_g is the wave's group velocity.

These wave-particle interactions lead to the exchange of energy and momentum, which can amplify or attenuate the wave, with a corresponding momentum change in the particle and/or a change in the vector quantity, leading to pitch-angle scattering. It is important to note that so-called anomalous, or "parasitic resonances" [2], can also occur, particularly when a particle overtakes a circularly polarized wave. This is possible for relativistic particles, and waves traveling at comparatively low speeds due to the refractive index of the plasma. An example of this is the interaction between relativistic electrons and electromagnetic ion-cyclotron-mode waves, where the overtaking electron sees the electromagnetic ion-cyclotron-mode wave as being right-hand circularly polarized.

During geomagnetic storms, both VLF and ULF waves are enhanced, which, in turn, can enhance the transport of electrons within the outer radiation belt and also drive wave-particle interactions between energetic electrons and magnetospheric waves. Here "transport" refers to radial diffusion, which occurs as a result of drift-resonance between ULF waves and the drifting electrons. These interactions are known to accelerate electrons from seed populations of ~30 keV to energies of >1 MeV, while at the same time perturbing a fraction of the trapped population onto paths that are likely to interact with the Earth's atmosphere [3]. Electrons that magnetically mirror at altitudes that are so low that they will hit the neutral atmosphere and be lost are said to be in the bounce-loss cone, precipitating into the atmosphere at ~100 km altitude.

3. Recent Observations of Precipitation

Radiation-belt electron losses can be profitably studied from a stratospheric balloon platform [5]. Precipitating electrons scatter electromagnetically from atmospheric atomic nuclei, and the resulting bremsstrahlung X-radiation penetrates, with little loss, to near 30 km, an altitude readily accessible to balloons. While electron energy and temporal features are reliably inferred from the recovered X-ray spectra, electron pitch-angle information is lost, excepting that loss-cone electrons alone contribute to X-ray production. As with ground-based observations of radiation-belt losses, and unlike space-based observations, balloons are effectively stationary. That is, with stratospheric winds of the order of 10 m/s, the primary motion of a balloon originates in the Earth's spin.

Because extended observations can be collected from a single location, it is possible to study slower low-frequency aspects of loss mechanisms. Furthermore, time series from still platforms are purely temporal, exhibiting no confusing component of platform motion through spatial gradients. Because bremsstrahlung production is immediate, and X-rays travel at light speed, the sole time scale introduced by the balloon-bremsstrahlung technique is a delay of the order of 100 microseconds. Consequently, balloon measurement of radiation-belt electron precipitation can span the time range from 10^{-4} to 10^{4} seconds.

The BARREL project was conceived to augment the Radiation Belt Storm Probe (RBSP) mission, by providing

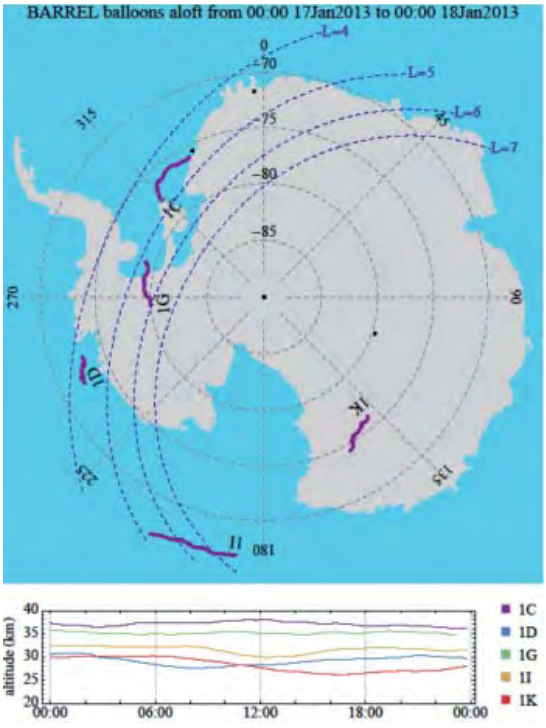

Figure 3. The upper panel shows the positions of five balloon payloads over a 24 hour interval: the dots mark the two launch sites and the geomagnetic pole. Circumpolar winds moved the balloons westward in magnetic latitude and longitude. Together with the two launch sites, these winds endowed an L-shell and local time extent to the array. The lower panel shows that balloon altitude, although relatively constant over a day, varied as much as a pressure scale height.

an extended and extensive observation of radiation-belt losses to the atmosphere. The RBSP spacecraft, renamed the Van Allen probes, cannot accurately measure fluxes inside the small equatorial loss cone. The absence of loss measurements strongly limits one's ability to connect losses with in situ observations of particle fluxes and wave spectra. BARREL achieves extensive observations by employing multiple stratospheric platforms at once. The polar vortex and a staggered launching schedule together confer a local time separation between balloons. Payloads were launched from two Antarctic sites to provide L-shell spread (i.e., a spread in geomagnetic latitude), and to reduce risks from logistical or surface-weather problems. BARREL achieved extended observations through two campaign periods, the Antarctic summers of 2013 and 2014, with up to 40 instruments deployed altogether, and an average data collection time of about eight days per balloon. The launch bases were chosen to immediately position balloons where radiation-belt electron loss flux measurements are most probable [6]. Figure 3 shows flight paths and altitudes of five balloons over a 24-hour period in January 2013. Stratospheric winds transported the balloons westward from their launch sites, marked as two spots along the upper coastline (constant L-curves were derived from the IGRF model). Altitude was important, because the amount of atmosphere between the X-ray source and the detector varied diurnally. The lower panel shows that altitude variation was about a scale height, due to near-constant sunlight during the campaign period.

The accumulated dataset from BARREL was used to identify and characterize radiation-belt losses. For example, Figure 4 shows X-ray spectrograms during the same 24-hour period of Figure 3. Annihilation radiation at 511 keV produced the horizontal band at the top of each panel. Flux variations extended throughout the depicted energy range of 50 keV to 550 keV at three of the five balloons, but only in the $L = 4.5$ to 6.5 range. Therefore, electrons of energy exceeding 500 keV were lost to the atmosphere on this day. The X-ray differential energy spectra could be inverted into electron spectra to quantify those losses. Episodes of elevated precipitation were seen to last for the order of 10 minutes and occurred several times. Episodes could extend

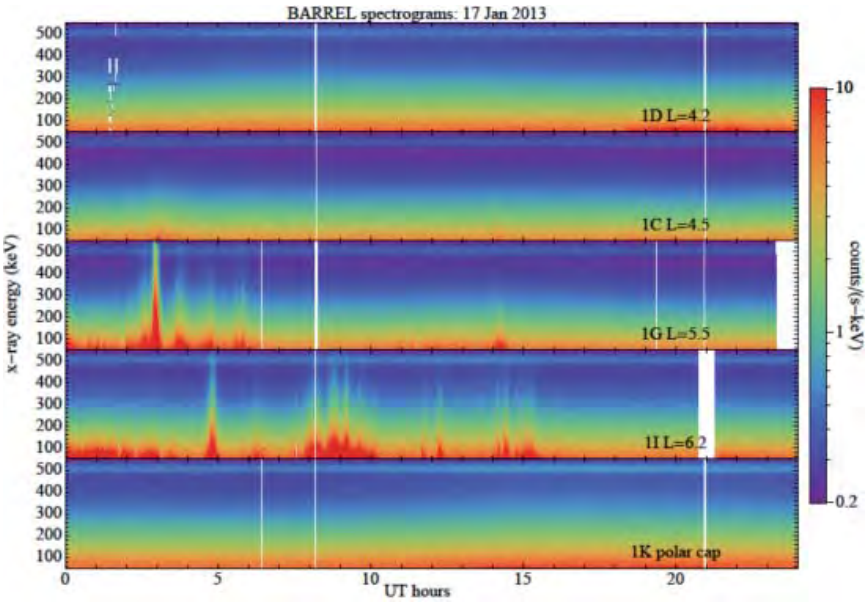

Figure 4. Simultaneous x-ray spectrograms from five payloads, showing different features due to different geomagnetic locations. In the polar cap (bottom panel), there was no flux change, and therefore no variation in energetic electron precipitation. At lower L-shell (middle panels), there were multiple intervals of electron precipitation – to several hundred keV energy – during this day. Enhanced electron precipitation, below 100 keV, was seen as low as $L = 4.2$ (top panel). The faint band at 511 keV in all spectrograms was the positron annihilation line, which was used as an absolute calibration source.

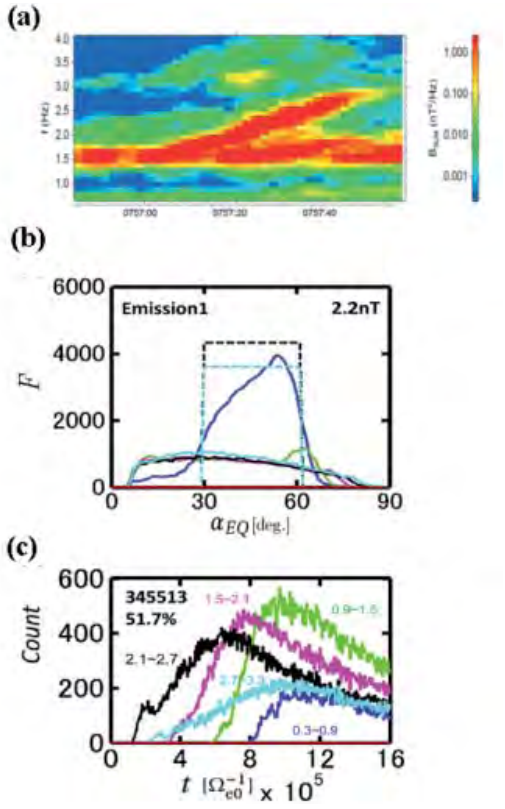

Figure 5. (a) Electromagnetic ion-cyclotron-mode-triggered emissions observed by the Cluster spacecraft [9, 10]. (b) Equatorial pitch-angle-distribution functions of trapped relativistic electrons (solid lines), after interaction with electromagnetic ion-cyclotron-mode-triggered emissions, and (c) the numbers of precipitating electrons of different energy ranges of 0.3-0.9 MeV, 0.9-1.5 MeV, 1.5-2.1 MeV, 2.1-2.7 MeV, and 2.7-3.3 MeV in blue, green, magenta, black, and cyan, respectively (results of test particle simulations with the initial uniform distributions 30-60 degrees by dashed lines) [12].

over six hours of magnetic local time, for instance, at 14:30; although most episodes exhibited smaller spatial extent. These measurements will become even more useful when combined with data from the Van Allen probes.

While difficult to observe from spacecraft, low-frequency modulation (Pc-4 to Pc-5, or several minutes period) of radiation-belt precipitation is sometimes observed from balloon platforms [7]. These modulation frequencies are well below those of the electromagnetic ion-cyclotron or whistler modes, the modes regarded by many as responsible for pitch-angle scattering electrons into the loss cone. Hence, the low-frequency observations have stimulated recent theoretical work to understand the role of low-frequency waves in loss processes [8]. The main idea investigated in this recent simulation work is that magnetic-field compressional variation lowers the mirroring altitude, resulting in loss. Results compared well with balloon-borne X-ray measurements. Much work remains to be done in investigating the role of Pc4/Pc5 waves and radiation-belt electron losses.

4. Recent Advances in Theory Describing Precipitation

Recently, it has been shown that the anomalous cyclotron resonance between relativistic electrons and the electromagnetic ion-cyclotron-mode-triggered emissions [9, 10] takes place very effectively near the magnetic equator, because of the rising-tone frequency (Figure 5a) and the variation of the ambient magnetic field. Efficient precipitation is caused by nonlinear trapping of relativistic electrons by electromagnetic wave potentials formed by electromagnetic ion-cyclotron-mode-triggered emissions. Frequency-sweep rates of rising-tone emissions and the inhomogeneous magnetic field play essential roles in the nonlinear trapping of resonant electrons, transferring them to lower pitch angles [11]. The necessary conditions of the wave amplitude, kinetic energies, and pitch angles that must be satisfied for the nonlinear wave trapping have recently been derived. This has led to test particle simulations with a large number of relativistic electrons undergoing mirror motion in a parabolic magnetic field near the magnetic equator [12]. In the presence of coherent electromagnetic ion-cyclotron-mode-triggered emissions with increasing frequencies, a substantial amount of relativistic electrons are trapped by the wave, and the relativistic electrons at high pitch angles are guided to lower pitch angles within a short time scale, much less than a second (Figure 5b), resulting in rapid precipitation of relativistic electrons or relativistic electron microbursts (Figure 5c). Up to this point, it has been widely assumed that relativistic electron microbursts were caused by whistler-mode chorus elements, although the observed relativistic electron microbursts' energy signature was inconsistent with that expected from chorus [13]. It seems possible that whistler-mode chorus may cause some fraction of relativistic electron microbursts [14], especially those seen on the dayside [16]. Nonetheless, the new theoretical understanding may help explain the apparent inconsistency, while also giving greater importance to the role of electromagnetic ion-cyclotron-mode waves. The arrival of observations from the Van Allen Probes is also allowing electromagnetic ion-cyclotron-mode-driven scattering to be examined in a new light [16].

5. EMIC Observations

As noted above, electromagnetic ion-cyclotron (EMIC) waves are able to resonate with ring-current ion populations as well as relativistic electrons, causing pitch-angle scattering into the Earth's atmosphere. Recent experimental studies have shown that electromagnetic ion-cyclotron-mode wave growth occurs at all local times, and can persist for hours and sometimes even days [17, 18]. With such longevity and broad growth regions, the potential for electromagnetic ion-cyclotron-mode waves to be an important cause of radiation-belt particle loss increases. An array of satellite instrumentation, including the Van Allen Probes, GOES, and POES, in conjunction

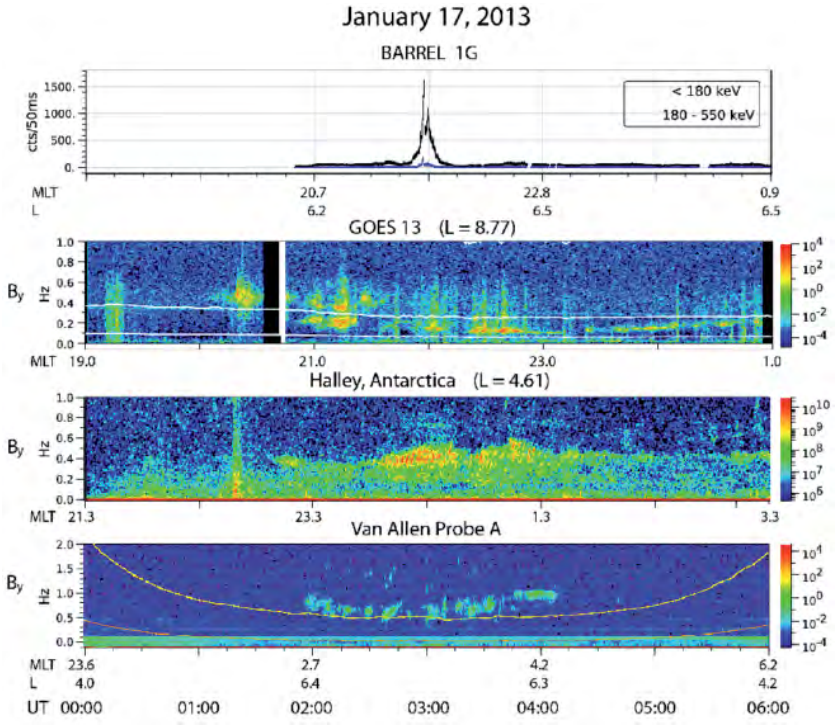

Figure 6. Data from BARREL balloon 1G, GOES 13, Halley, Antarctica, and Van Allen Probe A on January 17, 2013. The BARREL balloon data showed counts per 50 ms of Bremsstrahlung X-rays from which electron precipitation was inferred. The next three plots show magnetometer data with the helium and oxygen cyclotron frequencies superimposed on the GOES and Van Allen Probe plots. The proton cyclotron frequency was above the range of the plots.

with BARREL balloons and ground-based instruments, have allowed new insights into the spatial and temporal extent of electromagnetic ion-cyclotron-mode waves, the propagation from the generation region to satellites and ground instruments, and particle-loss processes resulting from interactions with ions and electrons [19]. Figure 6 shows an example of the widespread nature of the electromagnetic ion-cyclotron-mode waves and the concurrent precipitation of electrons. Electromagnetic ion-cyclotron-mode waves are detected simultaneously for about two hours across at least five hours of MLT on the nightside magnetosphere and cover about four L-shells. Additional data, not shown here, increase the range in MLT to at least 12 hours of MLT. This significantly expands the MLT range reported in previous studies. For example, a recent examination of large-scale electromagnetic ion-cyclotron-mode wave precipitation using ground-based aurora cameras to examine the electromagnetic ion-cyclotron-mode precipitated protons concluded this was occurring over approximately four hours of MLT [20], emphasizing the need for global observations to determine the true spatial size.

These new observational studies are calling into question the current understanding of electromagnetic ion-cyclotron-mode waves being detected primarily in the dusk region, and the conditions under which the waves can be generated. Experimental observations indicate that the temporal and spatial range of the generation region appears to be much larger than studies have previously suggested [17]. In addition, Antarctic ground-based observations show that electromagnetic ion-cyclotron-mode waves occur more often and are detected at higher frequencies (>1 Hz), contrary to previous studies stating electromagnetic ion-cyclotron-mode waves peak at solar minimum. It appears that increased solar activity is driving temperature anisotropies closer to the Earth (at larger magnetic-field strength), thus elevating the wave frequency [21]. A number of recent studies call into question the canonical understanding of electromagnetic ion-cyclotron-mode waves, and their understanding with respect to the precipitation of relativistic electrons from the radiation belts. Several theoretical and modeling studies have predicted electromagnetic ion-cyclotron-mode wave-driven electron precipitation through pitch-angle scattering into the loss cone [22], but it has only been in the last few years that direct evidence of this interaction has been detected [23, 24]. An area of active research concerns how much of an impact the electromagnetic ion-cyclotron-mode waves make on the radiation belts when they are able to resonate with the relativistic electrons.

6. Low-Energy Precipitation as a Proxy for Whistler-Mode Waves

In the last year, a new approach has been put forward, using comparatively low-energy precipitation (tens of keV) observations in an exciting innovative way. As noted above, whistler-mode waves resonate with electrons over a wide energy range, leading to precipitation. One can thus use precipitation as a proxy for the wave activity.

Whistler-mode chorus waves have received intense attention recently due to the important dual role they play in acting both as loss and acceleration processes for energetic electrons [25]. Since chorus-driven electron scattering and energization is fundamentally important for radiation-belt electron dynamics, it is crucial to understand the global evolution of chorus-wave intensity. Although statistical

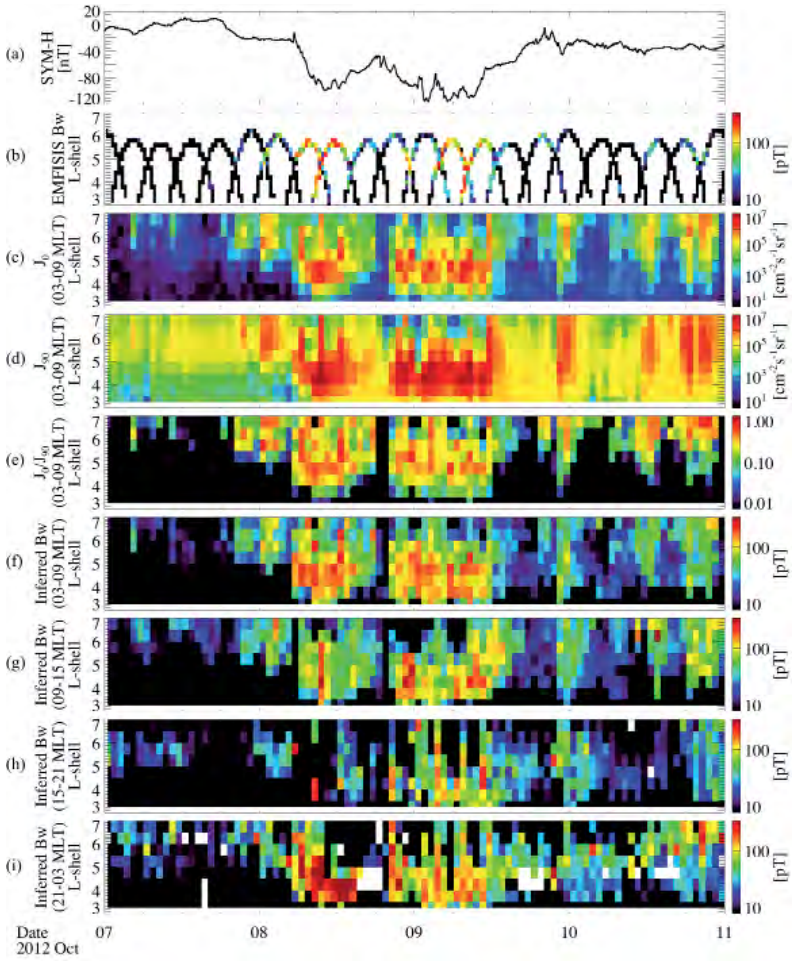

Figure 7. The evolution of whistler-mode chorus-wave intensity measured by Van Allen Probes and low-altitude electron measurements by multiple POES satellites during October 7-10, 2012. (a) The Sym-H index, (b) chorus-wave amplitudes integrated over $0.1 f_{ce}$ to $0.5 f_{ce}$ measured by the EMFISIS instruments on both Van Allen Probes A and B, where f_{ce} is the equatorial electron cyclotron frequency. (c) The precipitated electron flux (J_0), (d) trapped electron flux (J_{90}), and (e) the ratio of J_0/J_{90} in the 30 keV to 100 keV energy channel near the dawn sector over 03-09 MLT measured by multiple POES satellites. (f)-(i) The inferred chorus-wave intensity from the ratio of precipitated and trapped electron fluxes in various MLT ranges.

chorus wave distributions were previously used to simulate radiation-belt electron dynamics during a geomagnetic storm, chorus-wave distributions from statistical results may not accurately represent the true, instantaneous global wave evolution in a particular event.

Low-altitude electron measurements by multiple POES satellites have been used in a recent study to infer whistler-mode chorus-wave amplitudes using a physics-based technique [26]. POES satellites have two particle detectors, which can measure both precipitated and trapped electron fluxes [27], and multiple satellites are distributed in a broad MLT region to provide extensive coverage in both L-shell and MLT. Quasi-linear theory [28] and the UCLA full diffusion code [29] were applied to quantify the electron scattering process near the loss cone driven by chorus waves. The ratio of precipitated and trapped electron fluxes, in turn, was used to infer chorus-wave amplitudes [26]. This technique has been validated by analyzing conjunction events between the Van Allen Probes' measuring chorus-wave amplitudes near the equator and POES satellites measuring the 30 keV to 100 keV electron population at the conjugate low altitudes.

This technique was used to construct the global distribution of chorus-wave intensity as a function of L-shell in various MLT ranges during a double-dip storm, which occurred during October 7-10, 2012 (Figure 7). The precipitated (Figure 7c) and trapped electron fluxes (Figure 7d), and their ratio (Figure 7e), increased during the double dips in SYM-H. The chorus-wave amplitudes inferred from the ratio of precipitated and trapped electron fluxes over 03-09 MLT (Figure 7f) agreed well with the conjugate measurements of chorus-wave amplitudes from the Van Allen Probes (Figure 7b) in the similar MLT sector. The evolution of the whistler-mode wave intensity inferred from low-altitude electron measurements can provide real-time global estimates of the wave intensity over a broad L-MLT region (Figure 7f-7i), which cannot be obtained from in-situ wave measurements by equatorial satellites alone, but is crucial in quantifying radiation-belt electron dynamics.

7. Precipitation Affecting the Wider Earth System

Due to the Earth's magnetic-field configuration, energetic particle precipitation occurs mainly in the polar auroral and sub-auroral regions, i.e., at latitudes higher than 45º. The altitudes at which these particles deposit their momentum is dependent on their energy spectrum, with lower-energy particles impacting the atmosphere at higher altitudes, and higher-energy particles penetrating

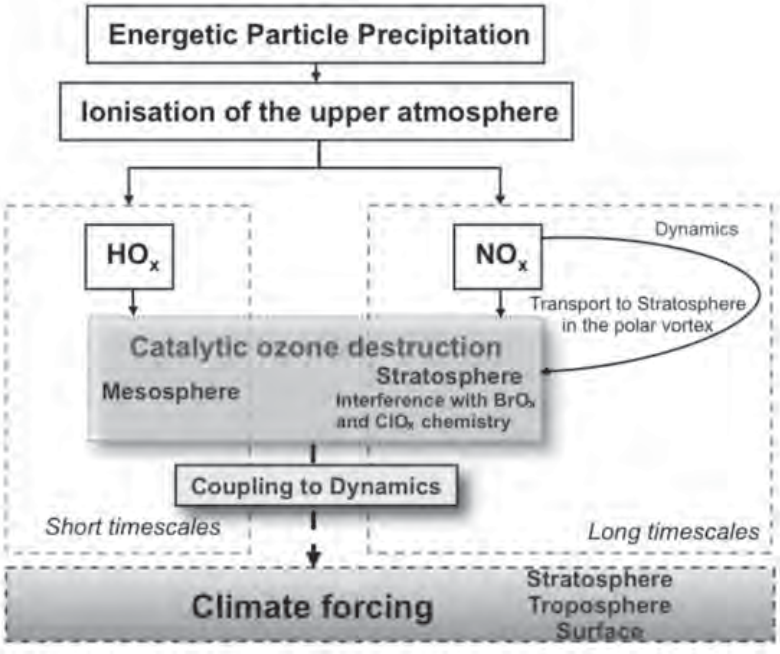

Figure 8. A schematic of the effects of energetic particle precipitation into the upper atmosphere, flowing down through the stratosphere to effect tropospheric climate.

more deeply. Precipitating charged particles produce NO_x ($NO_x = NO + NO_2$) and HO_x ($HO_x = OH + HO_2$) through ionization or dissociative ionization of N_2 and O_2 molecules, which results in the formation of N^+, O^+, N^+, O^+, and NO^+. Energetic particle precipitation has been observed to cause significant increases in NO_x and HO_x in the polar atmosphere [30-32]. These chemicals are particularly important in that they catalytically destroy ozone [33].

There has also been growing evidence that geomagnetic storms produce high fluxes of energetic electron precipitation [34], with modeling suggesting energetic electron precipitation can also lead to significant mesospheric chemical changes in the polar regions [35] affecting the chemical makeup of the polar atmosphere. The radiative balance of the atmosphere is driven by its composition, particularly through the abundance of ozone and its capability of absorbing solar UV radiation efficiently [33]. As NO_x and HO_x influence the ozone abundance at upper stratosphere and mesospheric levels, the radiative balance can be altered and temperature gradients are modified. Through this mechanism, atmospheric wind patterns can be altered, influencing the propagation of planetary and gravity waves within the stratosphere and troposphere. As Figure 8 shows, this step-by-step process provides a pathway to link geomagnetic storm perturbations in the radiation belts with chemical changes in the upper atmosphere, and, ultimately, with the dynamics of the lower atmosphere.

8. References

1. C. J. Rodger and M. A. Clilverd, "Magnetospheric Physics: Hiss from the Chorus," *Nature*, **452**, 7183, 2008, pp. 41-42, doi:10.1038/452041a.

2. L. R. Lyons and R. M. Thorne, "Parasitic Pitch Angle Diffusion of Radiation Belt Particles by Ion Cyclotron Waves," *J. Geophys. Res.*, **77**, 28, 1972, pp. 5608-5616, doi:10.1029/JA077i028p05608.

3. R. M. Thorne, "Radiation Belt Dynamics: The Importance of Wave-Particle Interactions," *Geophys. Res. Lett.*, **37**, 2010, L22107, doi:10.1029/2010GL044990.

4. B. T. Tsurutani and G. S. Lakhina, "Some Basic Concepts of Wave-Particle Interactions in Collisionless Plasmas," *Rev. Geophys.*, **35**, 4, 1997, pp. 491-501, doi:10.1029/97RG02200.

5. G. K. Parks, T. J. Freeman, M. P. McCarthy, and S. H. Werden, "The Discovery of Auroral X-Rays by Balloon-Borne Detectors and Their Contributions to Magnetospheric Research," in R. L. Lysak (ed.), *Auroral Plasma Dynamics*, Washington, DC, American Geophysical Union, 1993, doi: 10.1029/GM080p0017.

6. R. M. Millan, M. P. McCarthy, J. G. Sample, D. M. Smith, L. D. Thompson, D. G. McGaw, L. A. Woodger, J. G. Hewitt, M. D. Comess, K. B. Yando, A. X. Liang, B. A. Anderson, N. R. Knezek, W. Z. Rexroad, J. M. Scheiman, G. S. Bowers, A. J. Halford, A. B. Collier, M. A. Clilverd, R. P. Lin, and M. K. Hudson, "The Balloon Array for RBSP Relativistic Electron Losses (BARREL)," *Space Sci. Rev.*, 2013, doi 10.1007/s11214-013-9971-z.

7. J. E. Foat, R. P. Lin, D. M. Smith, F. Fenrich, R. Millan, I. Roth, K. R. Lorentzen, M. P. McCarthy, G. K. Parks, and J. P. Treilhou, "First Detection of a Terrestrial MeV X-Ray Burst," *Geophys. Res. Lett.*, **25**, 1998, DOI: 10.1029/1998GL900134.

8. T. Brito, L. Woodger, M. Hudson, and R. Millan, "Energetic Radiation Belt Electron Precipitation Showing ULF Modulation," *Geophys. Res. Lett.*, **39**, 2012, doi:10.1029/2012GL053790.

9. J. S. Pickett et al., "Cluster Observations of EMIC Triggered Emissions in Association with Pc1 Waves Near Earth's Plasmapause," *Geophys. Res. Lett.*, **37**, 2010, L09104.

10. Y. Omura, J. Pickett, B. Grison, O. Santolik, I. Dandouras, M. Engebretson, P. M. E. Décréau, and A. Masson, "Theory and Observation of Electromagnetic Ion Cyclotron Triggered

Emissions in the Magnetosphere," *J. Geophys. Res.*, **115**, 2010, A07234.

11. Y. Omura and Q. Zhao, "Nonlinear Pitch-Angle Scattering of Relativistic Electrons by EMIC Waves in the Inner Magnetosphere," *J. Geophys. Res.*, **117**, 2012, A08227.

12. Y. Omura and Q. Zhao, "Relativistic Electron Microbursts Due to Nonlinear Pitch-Angle Scattering by EMIC Triggered Emissions, *J. Geophys. Res.*, 2013, doi:10.1002/jgra.50477.

13. C. J. Rodger, M. A. Clilverd, D. Nunn, P. T. Verronen, J. Bortnik, and E. Turunen, "Storm-Time Short-Lived Bursts of Relativistic Electron Precipitation Detected by Subionospheric Radio Wave Propagation," *J. Geophys. Res.*, **112**, 2007, A07301, doi:10.1029/2007JA012347.

14. T. P. O'Brien, K. R. Lorentzen, I. R. Mann, N. P. Meredith, J. B. Blake, J. F. Fennell, M. D. Looper, D. K. Milling, and R. R. Anderson, "Energization of Relativistic Electrons in the Presence of ULF Power and MeV Microbursts: Evidence for Dual ULF and VLF Acceleration," *J. Geophys. Res.*, **108**, 2003, p. 1329, doi:10.1029/2002JA009784.

15. S. Saito, Y. Miyoshi, and K. Seki, Relativistic Electron Microbursts Associated With Whistler Chorus Rising Tone Elements: GEMSIS-RBW Simulations, *J. Geophys. Res.*, **117**, 2012, A10206, doi:10.1029/2012JA018020.

16. M. E. Usanova, et al., "Effect of EMIC Waves On Relativistic and Ultrarelativistic Electron Populations: Ground-Based and Van Allen Probes Observations," *Geophys. Res. Lett.*, **41**, 2014, pp. 1375-1381, doi:10.1002/2013GL059024.

17. C. E. Weaver, M. R. Lessard, J. L. Gannon, M. J. Engebretson, C. J. Farrugia, and V Pilipenko, "Persistent Occurrence of EMIC Waves Around Magnetic Noon After a High Speed Solar Stream," *AGU Fall Meeting Abstracts*, December 2011, p. B2112.

18. K. W. Paulson, C. W. Smith, M. R. Lessard, M. J. Engebretson, R. B. Torbert, and C. A. Kletzing, "In Situ Observations of Pc1 Pearl Pulsations by the Van Allen Probes," *Geophys. Res. Lett.*, **41**, 2014, doi:10.1002/2013GL059187.

19. C. E. Weaver, M. R. Lessard, M. J. Engebretson, R. M. Millan, A. Halford, R. B. Horne, H. J. Singer, and J. C. Green, "Ground and Satellite EMIC Wave Observations in Conjunction with BARREL Electron Precipitation," AGU Fall Meeting Abstracts, 2013.

20. K. Sakaguchi, Y. Miyoshi, E. Spanswick, E. Donovan, I. R. Mann, V. Jordanova, K. Shiokawa, M. Connors, and J. C. Green, "Visualization of the Visualization of Ion Cyclotron Wave and Particle Interactions in the Inner Magnetosphere via THEMIS-ASI Observations," *J. Geophys. Res.*, **117**, 2012, A10204, doi:10.1029/2012JA018180.

21. C. E. Weaver, E. Lindgren, M. R. Lessard, and M. J. Engebretson, "Observations of Increasing EMIC Waves Frequency With the Increasing Solar Cycle," AGU Fall Meeting Abstracts, 2012.

22. D. Summers, and R. M. Thorne, "Relativistic Electron Pitch-Angle Scattering by Electromagnetic Ion Cyclotron Waves During Geomagnetic Storms," *J. Geophys. Res.*, **108**, 2003, 1143, doi:10.1029/2002JA009489, A4.

23. C. J. Rodger, T. Raita, M. A. Clilverd, A. Seppälä, S. Dietrich, N. R. Thomson, and T. Ulich, "Observations of Relativistic Electron Precipitation From the Radiation Belts Driven by EMIC Waves," *Geophys. Res. Lett.*, **35**, 2008, L16106, doi:10.1029/2008GL034804.

24. Y. Miyoshi, K. Sakaguchi, K. Shiokawa, D. Evans, J. Albert, M. Conners, and V. Jordanova, "Precipitation of Radiation Belt Electrons by EMIC Waves, Observed From Ground and Space," *Geophys. Res. Lett.*, **35**, 2008, L23101, doi:10.1029/2008GL035727.

25. R. M. Thorne, et al., "Rapid Local Acceleration of relativistic Radiation Belt Electrons by Magnetospheric Chorus," *Nature*, **504**, 2013, pp. 411-414, doi:10.1038/nature12889.

26. W. Li, B. Ni, R. M. Thorne, J. Bortnik, J. C. Green, C. A. Kletzing, W. S. Kurth, and G. B. Hospodarsky, "Constructing the Global Distribution of Chorus Wave Intensity Using Measurements of Electrons by the POES Satellites and Waves by the Van Allen Probes," *Geophys. Res. Lett.*, **40**, 2013, pp. 4526-4532, doi:10.1002/grl.50920.

27. C. J. Rodger, M. A. Clilverd, J. C. Green, and M. M. Lam, "Use of POES SEM-2 Observations to Examine Radiation Belt Dynamics and Energetic Electron Precipitation into the Atmosphere," *J. Geophys. Res.*, **115**, 2010, A04202, doi:10.1029/2008JA014023.

28. C. F. Kennel, and H. E. Petschek, "Limit on Stably Trapped Particle Fluxes," *J. Geophys. Res.*, **71**, 1, 1966, pp. 1-28, doi:10.1029/JZ071i001p00001.

29. B. Ni, R. M. Thorne, Y. Y. Shprits, and J. Bortnik, "Resonant Scattering of Plasma Sheet Electrons by Whistler-Mode Chorus: Contribution to Diffuse Auroral Precipitation," *Geophys. Res. Lett.*, **35**, 2008, L11106, doi:10.1029/2008GL034032.

30. D. A. Newnham, P. J. Espy, M. A. Clilverd, C. J. Rodger, A. Seppälä, D. J. Maxfield, P. Hartogh, C. Straub, K. Holmén, and R. B. Horne, "Observations Of Nitric Oxide in the Antarctic Middle Atmosphere During Recurrent Geomagnetic Storms," *J. Geophys. Res.*, **118**, 2013, pp. 7874-7885, doi:10.1002/2013JA019056.

31. Y. Isono, A. Mizuno, T. Nagahama, Y. Miyoshi, T. Nakamura, R. Kataoka, M. Tsutsumi, M. Ejiri, H. Fujiwara, and H. Maezawa, "Variations of Nitric Oxide in the Mesosphere and Lower Thermosphere Over Antarctica Associated With a Magnetic Storm in April 2012," *Geophys. Res. Lett.*, **41**, 2014, doi:10.1002/2014GL059360.

32. M. E. Andersson, P. T. Verronen, S. Wang, C. J. Rodger, M. A. Clilverd, and B. R. Carson, "Precipitating Radiation Belt Electrons and Enhancements of Mesospheric Hydroxyl During 2004-2009," *J. Geophys. Res.*, **117**, 2012, D09304, doi:10.1029/2011JD017246.

33. G. P. Brasseur, and Solomon, S., *Aeronomy of the Middle Atmosphere, Third Edition*, Dordrecht, Springer, 2005.

34. C. J. Rodger, M. A. Clilverd, N. R. Thomson, R. J. Gamble, A. Seppälä, E. Turunen, N. P. Meredith, M. Parrot, J.-A. Sauvaud, and J.-J. Berthelier, "Radiation Belt Electron Precipitation Into the Atmosphere: Recovery From a geomagnetic Storm," *J. Geophys. Res.*, **112**, 2007, A11307, doi:10.1029/2007JA012383.

35. C. J. Rodger, M. A. Clilverd, A. Seppälä, N. R. Thomson, R. J. Gamble, M. Parrot, J.-A. Sauvaud, and T. Ulich, "Radiation Belt Electron Precipitation due to Geomagnetic Storms: Significance to Middle Atmosphere Ozone Chemistry," *J. Geophys. Res.*, **115**, 2010, A11320, doi:10.1029/2010JA015599.

2012 - 2014
Triennial Reports Commissions

COMMISSION A

1. In Memoriam and Concerns

There were no friends and colleagues from the URSI Commission A community that have been reported to me as passing away during the triennium. However, our sympathies go out to those we have missed and others in the URSI community, such as Prof. Karl J. Langenberg of the University of Kassel, Germany, who passed away on May 22 after a losing battle with cancer.

It is felt that a special concern and wishes for the best should be provided for those who are struggling with turmoil in their countries. It seems that so many countries have come to see bloodshed and all members living in those areas or having family in those areas are in our concerns and prayers.

2. Chair's Comments

2.1 General

I would like to thank the GASS conveners and reviewers, as well as all of those who submitted papers to make the 2014 GASS a success. My Vice Chair, Yasuhiro Koyama, and my immediate past Chair, Parmeswar Banerjee, have provided much needed assistance and helpful advice. Dr. Koyama has been very helpful in the activities in the Pacific region, particularly with the 2013 AP-RASC.

One of my goals was to move Commission A to a more active role of assistance to other commissions in the concepts of measurement. There has been some movement in this direction this triennium, in addition to continuing to support the classic areas of metrology in time and synchronization. A list of topics was developed for the 2014 GASS:

- Universal Coordinated Time: The International Reference Time Scale and Possible Redefinition
- Time Scale
- Time and Frequency Transfer
- Metrology of Optical Frequencies and Optical-Dimensional Measuring Techniques
- Quantum-Based Metrology
- Education and Training in Metrology
- Recent Advances in Antenna Measurement Techniques
- Advances in Sensor Development and Applications
- Global Navigation Systems (Overview of the Timing Techniques in the Various Satellite Systems)
- Nonlinear Measurements and Characterization
- Mode-Stir Chambers
- Pulsars and the Application to Time Scales
- Bioeffects and Medical Applications
- EMC and EM Metrology/Pollution
- Interconnect and Packaging Evaluation
- Material Measurement and Characterization
- Microwave to Sub-Millimeter Measurements/Standards
- Noise Measurements and Standards
- Time-Domain Metrology
- Techniques for Remote Sensing
- Measurements and Calibration in Propagation
- RFID
- Signal Enhancement for EM Metrology
- Scattering Calibration
- References (Bistatic)

Several of these areas overlap with other Commissions, with the potential for support in the concepts of measurements.

2.2 Funding

The URSI board provides to the Commission Chairs a sum of money at the start of each triennium, to be administered for the good of the community. During this triennium a sum of EUR 9000 was made available. Approximately EUR 1000 was spent in supporting various meetings. Support was provided to the past Chair to assist in attending the GASS, and the remainder was requested for support of Young Scientists.

2.3 Mailing Lists

Commission A uses the electronic mailing list maintained by URSI and available at the Commission link on the URSI Web site. The Chair has tried to keep updated information provided to URSI, as well as to send separate e-mails to a complementary list, particularly if attachments are desired for the transmission. Developing a list for all members of Commission A who wish to be notified of events

worldwide might be considered. An alternative would be to establish a Facebook page, but that may be limited in distribution due to the nature of the media. It is still an area to be considered for the next triennium.

2.4 Meetings

The Beijing GASS Program: Commission A has ~102 papers at the GASS. This includes 72 submitted directly and 30 in joint sessions. The submitted papers included one student paper and 19 Young Scientists. A panel session on "Education and Training in Metrology" is also planned. It was hoped that a new topic, "Quantum-Based Metrology," would generate interest, but it did not bring enough papers for a session. It is still a topic to watch for future growth and small sensor systems. Quantum systems was the topic of the plenary session of the 2014 National Radio Science Meeting in Boulder, CO, USA, sponsored by Commission A in the USA.

One move that was tried for the 2014 GASS was to introduce open sessions, allowing individuals to submit general papers for consideration in open oral sessions. The other sessions were formed primarily from the invited papers requested by conveners. The future AP-RASC and AT-RASC have all open sessions, and the larger list of topics was submitted for consideration at those meetings.

The Commission technically sponsored several other conferences and had sessions in some of these conferences, such as the 2013 ICEAA–IEEE APWC–EMS in Torino, Italy. Plans are also being made to participate in the 2015 AT-RASC.

The future might be worthy of establishing working groups in the areas of "Time Scale" and the need for a redefinition, as well as in the area of quantum-based metrology.

3. Vice Chair's Comments

In the field of "Time and Frequency Metrology," discussion about the redefinition of Coordinated Universal Time (UTC) has been an important issue, and some important conferences were held. In 2012, the Radiocommunications Assembly of ITU-R discussed the issue and deferred the decision until 2015. ITU-R requested member nations and scientific organizations, including URSI, to provide their opinions to ITU-R. The ITU/BIPM Workshop Future of the International Time Scale, held in 2013, was one of the important conferences for such discussions. In the next GASS, a special session about UTC will be organized. I think it's worth mentioning in the report of Commission A.

The report provides the following information (reference list deleted), and is included because of the importance:

3.1 A1. Time and Frequency Standards and Time Transfer Technique

The research and development on "Time and Frequency Standards and Time Transfer" in Japan has been mainly carried out in the National Institute of Information Technology (NICT) and National Metrology Institute of Japan (NMIJ).

In NICT, Kumagai et al. are going to upgrade NICT-CsF1, aiming the operation at the 10^{-16} level (currently operating with 1.4×10^{-15}). They are also developing the second fountain (NICT-CsF2), with which a frequency stability of $3\times10^{-13}/\tau^{1/2}$ was obtained. They completed evaluations of most systematic frequency shifts and their uncertainties for CsF2 at the level below 5×10^{-16}.

A microwave frequency standard using the $^{171}Yb^{+}$ is under development at NICT. For this purpose, Shiga et al. constructed an experimental apparatus, and the absolute frequency of the $^{171}Yb^{+}$ hyperfine transition was measured with 4×10^{-14} uncertainty. This apparatus was used to demonstrate a new measurement method using atomic phase lock.

The time difference between UTC (NICT) and UTC has been kept almost within +25 ns to -19 ns for the last three years. NICT has 29 Cs clocks and seven H-masers. UTC (NICT) is generated by using 18 high-performance Cs clocks and three H-masers. Other Cs clocks are in operation at two LF stations and at the Advanced ICT Research Institute of NICT. UTC (NICT) has been used as the reference for frequency calibration services

NICT was certified to be in accordance with the ISO/IEC 17025 for the frequency calibration system from National Institute of Technology and Evaluation (NITE) in March 2001. NITE provided an accreditation of ISO/IEC 17025 to NICT on January 31, 2003, and also provided an accreditation of ISO/IEC 17025 of the frequency remote calibration system and the time scale difference to NICT on May 2, 2006, and on September 30, 2011, respectively. BMC of carried in system was changed to 5×10^{-14} in April 2007. The measurement range of frequency calibration was expanded from 1 Hz to 100 MHz in September 2011. NICT received surveillance by NITE in February and renewed IAJapan certificate dated April 26, 2013, from NITE.

Fujieda et al. [Fujieda et al. 2011] developed an all-optical link system for making remote comparisons of two distant ultra-stable optical clocks. An optical carrier transfer system based on a fiber interferometer was employed to compensate the phase noise accumulated during the propagation through a fiber link. Transfer stabilities of 2×10^{-15} at 1 s and 4×10^{-18} at 1 s were achieved in a 90-km link.

NICT has performed various experiments using two-way satellite time and frequency transfer (TWSTFT). Gotoh et al. [Gotoh et al. 2011] have developed a new two-way time transfer modem to improve the time transfer precision of remote clock comparison. For the real-time digital signal processing stages implemented in software, they relied on a graphics processing unit (GPU) and performed two-way satellite time transfer experiments using these modems between Japan and Taiwan. The results obtained were consistent within 200 ps with respect to the results of GPS carrier phase time transfer. The first international TWSTFT experiment using a new software-defined modem with dual pseudo-random noise (DPN) codes were performed over a period of six months [Wen-Hung et al., 2012]. The results of DPN exhibited excellent performance, which was competitive with the GPS precise point positioning (PPP) technique in the short-term and consistent with the conventional TWSTFT. Time deviations of less than 75 ps were achieved for averaging times from 1 s to 1 d. Fujieda et al. [Fujieda et al., 2012] started to implement a carrier-phase information to improve the short-term stability of TWSTFT. The experiments in a domestic short baseline were performed. The short-term stability of 4×10^{-13} at 1 s was achieved.

NICT also performed direct time comparisons using the first Quasi-Zenith Satellite (QZS-1) in order to monitor the onboard clock as a part of the satellite navigation system [Nakamura et al., 2013]. The NICT system achieved a measurement precision of about 25 ps, which was an order of magnitude better than the precision of the clock parameters obtained from the combined orbit and clock estimation.

A study via VLBI simulation for evaluating the potential of the time and frequency transfer was performed by assuming use of the next-generation VLBI technique, which is the "VGOS (VLBI2010 Global Observing System)" including the wideband receiver and data-acquisition system, small antenna, antenna slew-speed improvement, and phase-delay measurement. This simulation indicated that feasibility of the frequency stability with the VLBI measurement would be at the order of 10^{-16} at a one-day interval [Hobiger 2011a,b]. A further feasibility-study campaign experiment was performed by using 11 m antennas between Kashima-Koganei (100 km distance) on February 19-23, 2012. The clock difference between two hydrogen masers at each site was compared with multiple techniques: GPS, VLBI, and TWSTFT (code). It was notable that the increase of VLBI observation bandwidth from 500 MHz to 1 GHz improved the precision of clock comparison. This result encourages developing a new wideband VLBI system [Sekido 2012a,b, 2013a,b, Koyama 2012, 2013, Takefuji 2012a,b,c, 2013].

The development of the new wideband VLBI system for T&F transfer, named "Gala-V," started since 2012 [Ichikawa 2011, Kondo 2012]. The system is designed in a composition of a transportable small-diameter antenna pair and a large-diameter antenna. Its observation frequency range was selected so that it coincides with that of the next-generation international geodetic VLBI system (VGOS) for future joint observation with international VLBI stations [Ujihara 2011, 2012a,b]. A wide frequency (6.4 GHz to 15 GHz) feed for a Cassegrain 34 m diameter antenna was originally designed and installed on the Kashima 34 m radio telescope in 2013. A test evaluation experiment with the Gala-V system is being planned in 2014.

In NMIJ, following research has been conducted:

- Primary frequency standards at NMIJ: NMIJ has made a calibration of the International Atomic Time (TAI) four times between November 2010 and March 2011 with the Cs atomic-fountain frequency standard, NMIJ-F1, with a combined uncertainty of 3.9×10^{-15} [Circular T, Takamizawa et al. 2010, Takamizawa et al., 2012]. However, the resonance frequencies of the microwave cavities were shifted out of the atomic resonance due to the huge earthquake. Moreover, the cesium source was exhausted. Therefore, we opened the vacuum chamber to replace the microwave cavities and to supply a new cesium ampoule. Here, the microwave cavities are parts of the vacuum chamber in the new version. Ultrahigh vacuum was then obtained. Now we are again making the optical setup. In parallel, our second fountain, NMIJ-F2, has been developed, aiming at an uncertainty of $<1\times10^{-15}$ as an immediate goal [Takamizawa et al. 2010, Takamizawa et al. 2012, Takamizawa et al. 2013]. In addition, the large frequency corrections for the second-order Zeeman shift, the blackbody radiation shift, and the collisional shift have been evaluated. Therefore, we are now in a position to compare NMIJ-F2 with TAI and the other primary frequency standards at the 1×10^{-15} level. Ultra-stable microwave oscillator: One of the two CSOs was modified with the addition of a low-vibration pulse-tube cryocooler to be employed as a local oscillator for the fountains. No liquid helium refills are needed for the cryocooled version of the CSOs. Phase noise standards: We have developed a phase noise standard [Watabe et al. 2012, Yanagimachi et al. 2013a, Yanagimachi et al. 2013b, Yanagimachi et al., 2013c].

- Time keeping at NMIJ: All atomic clocks ran down due to power failure from the Great East Japan Earthquake in 2011. Since then, NMIJ has been trying to recover the damaged equipment. At present, four active hydrogen-maser frequency standards and two cesium atomic clocks with high-performance beam tubes (Agilent 5071A) are being operated for time keeping. Those atomic clocks are kept in individual chambers the temperatures of which are kept to within 0.2° C. One of the hydrogen masers is used as a source oscillator for the generation of UTC (NMIJ) to improve the short-term stability. UTC (NMIJ) is created by frequency-steering the hydrogen maser output signal to UTC using a frequency stepper. Time and Frequency Transfer: In NMIJ, a dual-frequency carrier phase GPS receiver is one of the main international time and frequency transfer tools.

- NMIJ has the Two Way Satellite Time and Frequency Transfer (TWSTFT) facilities for the Asia Pacific link and for the Asia-European link. An optical-fiber bidirectional frequency-transfer system, using wavelength-division multiplexing technology, is being studied as one future precise time and frequency comparison system. In addition, NMIJ started research on a precise frequency-comparison system using an optical carrier. Technical challenges and solutions for the system were investigated on the issues such as propagation delay limit, burst noise, interferometer noise, and so on (Wada et al. 2014).

- Frequency Calibration Service at NMIJ: NMIJ has been providing the remote frequency calibration service using the GPS common-view method and Internet since 2006. The CMCs of the service are 1.1×10^{-13} (baseline: 50 km), 1.4×10^{-13} (baseline: 500 km), and 4.9×10^{-13} (baseline: 1,600 km), with an averaging time of one day. The number of users was 16 in 2014; it is on the rise year by year.

3.2 A2. Laser Stabilization and Frequency Measurement

The research and development on laser stabilization and frequency measurement in Japan has been mainly carried out at the National Institute of Information Technology (NICT), National Metrology Institute of Japan (NMIJ), and the RIKEN group.

In NICT, optical frequency standards using the Sr atom and Ca^{+} ion have been developed. Yamaguchi et al. developed the frequency standard based on the $^{87}Sr\,^{1}S_0$-$^{3}P_0$ transition frequency, using atoms in an optical lattice [Yamaguchi, 2012]. Matsubara et al. reduced the uncertainty of the absolute frequency of the $^{40}Ca^{+}$ $^{2}S_{1/2}$-$^{2}D_{5/2}$ transition down to 3×10^{-15}, and the ratio of the $^{40}Ca^{+}$ and Sr transition frequencies with an uncertainty of 2×10^{-15} [Matsubara, 2012]. A new optical frequency standard based on the $^{115}In^{+}$ $^{1}S_0$-$^{3}P_0$ transition frequency is under development to a higher accuracy than that of $^{40}Ca^{+}$. For this purpose, techniques for generating ion chains consisting of $^{115}In^{+}$ and $^{40}Ca^{+}$ have been developed [Hayasaka, 2012].

A new frequency standard in the THz (0.1 THz to 10 THz, wavelength 30 μm to 3 mm) domain has started in NICT. Ito et al. developed a THz frequency comb for absolute THz frequency measurements. Its measurement accuracy has attained the 10^{-17} level around 0.3 THz [Ito, 2013]. Nagano et al. demonstrated microwave synthesis from a continuous-wave THz oscillator [Nagano, 2013]

Some proposals for new frequency standards in the THz and infrared area were also given in NICT. Kajita et al. proposed the precise measurement of the vibrational transition frequencies of alkali earth-H^{+} molecular ions eliminating the Stark shift induced by probe lasers. [Kajita et al., 2011a, 2012b]. They also proposed to measure the vibrational transition frequencies of alkali earth-alkali diatomic molecules trapped in an optical lattice [Kajita et al., 2011b, 2012a, 2013].

NMIJ has developed an Yb optical lattice clock. In 2012, they demonstrated an improved frequency measurement of the $^{1}S_0 - ^{3}P_0$ clock transition in ^{171}Yb bound in the Stark-shift-free optical lattices with an uncertainty of 3.9×10^{-15} that was limited by UTC-NMIJ [Yasuda et al., 2012]. Consequently, the clock transition in Yb was selected as one of the secondary representations of the second by the International Committee for Weights and Measures (CIPM). In order to evaluate the optical clocks that exceed the performance of the Cs fountain primary standards, one needs to measure the frequency ratio between optical clock transitions in the different types of the optical clocks. Therefore, at NMIJ, an Sr optical lattice clock has also been developed and, furthermore, an Yb/Sr dual optical lattice clock project is now underway.

At NMIJ, optical frequency combs play an important role in their optical clock project. In the clock laser system, the highly stabilized fiber comb is able to transfer the linewidth and frequency stability from one laser frequency to another, and it plays the role of an ultra-stable local oscillator for multiple wavelengths. Using the linewidth transfer technique with high-speed controllable fiber-based frequency combs, a cooling laser operated at 689 nm for Sr and clock lasers operated at 578 nm and 698 nm for Yb and Sr, respectively, are stabilized and successfully used for atomic spectroscopy [Akamatsu et al. 2012, Iwakuni et al. 2012, Inaba et al. 2013].

In order to reduce the effect of the thermal noise on the optical cavity that could give frequency stability limits for short averaging times, a long cavity would be one of attractive solutions. For the long cavity, a new spacer material with high specific rigidity would be required, because a long cavity would be sensitive to the seismic noise in laboratories. At NMIJ, they have developed an optical cavity with an ultra-low-expansion ceramic spacer, and investigated the thermal properties of the ceramic [Hosaka et al., 2013].

The Katori group at the University of Tokyo and RIKEN has been developing optical lattice clocks with Sr Hg atoms, and an optical frequency-transfer system using a telecom fiber link between these two sites.

In 2011, the University of Tokyo developed a scheme to compare two clocks with high stability by canceling out the laser noise. They succeeded in comparing two clocks with the Allan deviation of $\sigma_y(\tau) = 4\times10^{-16}/\sqrt{\tau}$, and reached 1×10^{-17} with an averaging time of 2,000 s, which corresponds to the quantum projection noise limit of optical lattice clocks with 1,000 atoms [Takamoto et al., 2011].

A frequency comparison between two remote Sr optical lattice clocks, operated at the University of Tokyo and NICT, was performed via a phase-stabilized optical-fiber link [Yamaguchi et al., 2011]. The frequency comparison of two remote clocks with their distance of 24 km measured the relative frequency difference to be $(1.0 \pm 7.3) \times 10^{-16}$ and the gravitational red shift of ≈ 2.6 Hz due to the height difference of 56 m.

Prof. Katori with theorists [Ovsiannikov et al., 2013] discussed the multipolar and higher-order light shift for Sr atoms.

RIKEN has developed two cryogenic strontium (Sr) lattice clocks since 2011. Thus far, the accuracy of Sr lattice clocks has been limited by the uncertainty of the ambient blackbody radiation shift. By installing a cryogenic chamber, they have succeeded in suppressing the blackbody radiation, and comparing two cryogenic Sr lattice clocks with an uncertainty of 10^{-18} level [Ushijima et al., to be published].

A frequency-transfer system between RIKEN and the University of Tokyo has been developed to compare remote cryogenic Sr lattice clocks at the uncertainty of 10^{-18} [Akatsuka et al., to be published]. The link stability was evaluated to be 1×10^{-17} at 1 s, and reached 1×10^{-18} at 100 s, which corresponds to the gravitational red shift for a height difference of 1 cm.

RIKEN is also developing a lattice clock with mercury (Hg) atoms. Hg atoms have one-order-of-magnitude smaller sensitivity to the blackbody radiation than Sr and Yb atoms. This enables an accuracy of 10^{-18}, even in a room-temperature environment. They have succeeded in trapping Hg atoms in a magic optical lattice and precise spectroscopy of Hg clock transition, and started frequency comparison between Hg and Sr lattice clocks.

The Sugiyama group at Kyoto University is developing single Yb^{+} ion clocks. They succeeded in single-ion spectroscopy of the $^{2}S_{1/2} - ^{2}D_{5/2}$ transition in ^{174}Yb with a spectral width of 5 kHz [Imai et al., 2013]. They also studied laser frequency stabilization to 6S-8S two-photon transitions in Cs in a gas cell, in order to pursue high-frequency stability. They obtained a root Allan variance of 4.4×10^{-14} at an averaging time of 16 s [Uehara et al., 2012].

3.3 A3. Realization of Electrical Unit (dc and LF)

Research work and development on dc and low- frequency electrical standards, that is, standards for dc voltage, dc resistance, ac resistance, capacitance, inductance, ac/dc transfer, etc., have been implemented in the Electricity and Magnetism (EM) Division of the National Metrology Institute of Japan (NMIJ), partly in collaboration with several other institutes in the Advanced Industrial Science and Technology (AIST). The EM division has two sections: the Applied Electrical Standards Section and the Quantum Electrical Standards Section. The Applied Electrical Standards Section takes charge of the ac/dc transfer, the low value impedance, and the power standards. The Quantum Electrical Standards Section covers the Josephson voltage, the quantum Hall resistance, and the high-value impedance standards.

NMIJ has been studying a quantum-based Johnson noise thermometry in quest of a world-record electronic measurement of Boltzmann's constant, and an absolute temperature measurement in collaboration with the Thermometry Section of NMIJ and the NIST (Boulder and Gaithersburg). A Josephson-junction chip dedicated for JNT and other components required for JNT measurement, such as a data-acquisition system, have been developed. Up to now, we have succeeded in measuring the cross power spectra of a 100 ohm resistor at the triple point of water temperature and a reference signal generated with the quantum voltage noise source (QVNS). However, we found that there is some error in the cross spectra data obtained in our present system. We are now trying to improve our system and suppress the error (Urano et al., 2012, 2014)

A programmable Josephson voltage standard (PJVS) system has been optimized for ac waveform synthesis, and adopted for sampling measurements using a calibrator and a thermal converter. The low-frequency characteristics of a thermal converter at below 10 Hz have been successfully evaluated using the sampling measurement. We are now trying to increase the voltage level from 3 Vrms to 10 Vrms, replacing the PJVS chip, in collaboration with CMS (Taiwan). Development of a calibration system for Zener voltage standards using a liquid-helium-free PJVS has been finalized. The system has being checked through direct and indirect comparisons with our conventional JVS (CJVS) system. A bilateral comparison of PJVS systems in NMIJ (Japan) and CMS (Taiwan) (APMP.EM.BIPM-K11.5) is now in progress, with support by KRISS (Korea). Another experiment for evaluating the linearity characteristics of commercial digital voltage meters (DVMs) has been started using the system. Development of a highly stable and user-friendly dc voltage generator, based on a rack-mounted PJVS system with a small cryocooler, is also in progress in collaboration with the Nanoelectronics Research Institute (NeRI), AIST (Kaneko et al., 2011, 2012a, Maruyama et al., 2014a, 2014b, 2014c, 2014d, Amagai et al., 2013, 2014a, Chen et al., 2014).

A compact and ultra-stable 100 Ω standard resistor has been finished, its development and development of resistors (1 Ω to 10 kΩ) with other decade values are in progress. This 100 Ω standard resistor – for which the temperature coefficient is extremely low, less than 0.1 ppm/K at room temperature, and the resistance values are very stable, less than 0.1 ppm/year – has been successfully manufactured and marketed. The pressure coefficients are typically less

than +0.01(μ Ω/Ω)/(-250hPa) and the humidity coefficients of those resistors are immeasurable level (Kanko et al., 2012b, 2012c). The current coefficients are lower than the measurement limit, as well (Domae et al, 2013a). A trilateral comparison of four Alpha Electronics 100 Ω using QHR and CCC was carried out with KRISS (Korea) and NIST (USA). The calibrated values agreed within a few parts in 10^{-8} at a rough estimate. Detailed data processing is now in progress (Kaneko et al., 2014b).

By using the fabrication technology of a highly stable 100 Ω metal-foil resistor component, developed in collaboration between the NMIJ and Alpha Electronics Corp., 100 Ω standard resistors with a four-terminal-pair design, which enables ac measurements, have been fabricated. For the ac characteristics, the frequency dependence of the resistance and phase angle have been evaluated (Domae et al, 2012a, 2013a, 2014).

NMIJ also developed a trial model of 1 kΩ metal-foil resistor with a four-terminal-pair design. The resistance and phase angle of the resistor were measured as a function of frequency (Domae et al, 2014).

Conventional single Hall bar QHR devices have been fabricated, and several devices have been provided for several NMIs.

Newly designed 10 kΩ quantum Hall array resistance standard devices also have been fabricated. This device consists of 16 Hall bars, and its nominal value has only 0.0342 ppm difference based on R_{K-90} from the integer value of 10^4. We observed a clear 10 kΩ plateau, and the measured value agreed with its nominal value within a few ppb (Oe et al, 2011, 2013).

Test devices of ac-QHR with on-chip double-shielding have been fabricated at NMIJ, and their ac characteristic was evaluated at PTB (Kaneko et al., 2012e, 2013a).

A resistive voltage divider, which was constructed from a binary-segmented series array of QHR bars fabricated on one chip, named the "QHR voltage divider," has been developed. From the preliminary tests, the results of the Hall resistance measurement showed large and well-defined plateaus, deviations from nominal voltage ratios that were measured to be less than 1.4×10^{-6}, and the expanded uncertainty of the voltage ratio measurement was estimated to be less than 4.1×10^{-6} (Domae et al, 2012b, 2012c).

One researcher of NMIJ stayed at NIST Gaithersburg for collaboration work on graphene. Shubnikov-de Haas (SdH) oscillation was observed in graphene synthesized on the Si-terminated surface of SiC. The carrier density in SiC graphene was successfully controlled with photochemical gating and the QHE plateau ($i = 2$) was observed. The QHE plateau was observed in graphene, made at NIST Boulder with the CVD technique and fabricated at Gaithersburg (Shimamoto et al., 2012, 2013, Fukuyama et al., 2014).

SINIS (super/insulator/normal/insulator/super) turnstile devices for single electron pumping have been fabricated. This device consisted of a single pumping device and 14 parallel pumping devices. A measurement system has been also developed in a dilution refrigerator. At present, we succeeded in pumping a current of 160 pA (100 MHz) with a standard deviation of 1 part in 10^4. To achieve metrological requirements, the influence of environments such as the temperature and magnetic fields have also been studied. We also have studied different types of devices, such as a tunable barrier-pumping device and a small Josephson junction device (Kaneko, 2012d, 2013b, 2014a, Nakamura et al., 2014a, 2014b, Akiyama 2014c).

In order to maintain a high reliability of the capacitance standard, NMIJ has been performing long-term monitoring of standard capacitors and of capacitance differences among a number of standard capacitors. After the massive earthquake on March 11, 2011, validation of calibration and measurement capabilities (CMCs) of the capacitance standard based on the analysis of these monitoring results was conducted (Domae et al, 2013b).

We have developed a capacitance-scaling bridge using a current comparator and an inductive voltage divider for calibrating 4TP-defined capacitance standards of 100 μF. The expanded uncertainties of the capacitance and the dissipation factor of 100 μF at 120 Hz were 11 μF/F and 14 μrad, respectively. The bridge was recently modified aiming to calibrate standards of 1 mF. The expanded uncertainties of the capacitance and the dissipation factor of 1 mF at 120 Hz were 260 μF/F and 270 μrad, respectively (Sakamoto N. et al., 2010).

NMIJ has started development of precision measuring techniques for diagnosis of energy-storage devices, such as lithium-ion batteries (LIBs) and super-capacitors, by using an impedance spectroscopy method. We have a plan to establish a metrology for evaluating storage-power devices. We have developed the impedance spectrum measurement system that is suitable for testing LIB cells using a frequency response analyzer and a potentio-/galvanostat. Results for LIBs of the 18650-type in the range of 10 mHz to 10 kHz demonstrated that the impedance spectra for unused cells are clearly distinguished from those for used-up cells (Sakamoto N. et al., 2014).

NMIJ has provided ac-dc voltage difference transfer calibration of thermal converters in the voltage range from 10 mV to 1000 V, and in the frequency range from 10 Hz to 1 MHz. A comparison system for ac-dc current difference transfer standards up to 5 A has been developed.

Practical thin-film multi-junction thermal converters (MJTC) have been developed at NMIJ/AIST in collaboration with NIKKOHM Co. Ltd. A high-current thin-film multijunction thermal converter up to 200 mA for ac-dc current transfer standards has been developed (Fujiki et al., 2013, 2014).

A differential sampling measurement system using a 3 V rms ac-programmable Josephson voltage standard (AC-PJVS) system has been developed, and ac-dc transfer differences of thermal voltage converters have been successfully characterized down to 1 Hz [Amagai et al., 2013]. To expand the voltage range from 3 V to 10 V for this technique, we are now developing a differential sampling system using a 10 V rms AC-PJVS system, in collaboration through the Nanoelectronics Research Institute (NeRI), AIST [Amagai et al., 2014a]. The low-frequency property of a single-junction thermal converter down to 1 Hz has been successfully simulated using an improved electro-thermal model [Amagai et al., 2012a, b, c, 2014b]. The long-term stability of our thin-film multijunction thermal converter has been improved by fabricating a new thermopile pattern. To further improve the sensitivity and low-frequency property, the thin-film multijunction thermal converter has been characterized under vacuum conditions, in collaboration with NIKKOHM Co. Ltd [Amagai et al., 2012d, 2014c, d]. The study on absolute measurements of the Seebeck coefficient using an ac-dc measurement technique has started. At present, we have measured the Thomson coefficient of Pt thin wire at room temperature [Amagai et al., 2014e,f]. With regard to a calibration service, we have provided a calibration service of ac voltmeters using a thermal converter in the frequency range from 4 Hz to 10 Hz, 40 Hz to 100 kHz at an rms voltage of 1 V and10 V.

NMIJ had developed a calibration system for non-sinusoidal voltage, current, and power sources at 100 V/5 A of fundamental wave and at 10 V/3 A of higher harmonics in 2011. The extension of the range of the system was delayed because of the temporary transfer of the person in charge (Yamada et al., 2012a).

We also developed an ac shunt calibration system at 5 A and 50 Hz to 60 Hz. The system has been expanding up to 1 kHz at this moment. NMIJ has some plans for expanding up to 100 A and 10 kHz by 2015, according to requests from industries that need power calibration and antenna calibration. To realize the expansion, the NMIJ ac current ratio standard has been re-checked, and its calibration frequency has been expanded up to 4 kHz by improvement of its uncertainty estimation (Kon et al., 2011, 2012a, 2013c, 2014b, 2014d). In addition, the application systems of power measurement using shunt and IVD standards have been developed (Kon et al., 2012b, 2013a, 2013b, 2013d, 2014a, 2014c, 2014e).

Using the NMIJ standards of shunt and current transformer, an evaluation system for electronic current transformers (ECTs), accompanied by merging units (MUs) in accordance with IEC 61850 and IEC 60044-8 for automated substations, has been developed. The system allows long-term evaluation of the ECT/MU of 80 and 256 samples/cycle (Yamada et al., 2012b).

3.4 A4. EM Field, Power Density and Antenna Measurement

A dipole antenna has a simple linear structure, and this improves the measurement accuracy. However, since an ordinary dipole antenna employed for the measurement is a half-wavelength dipole and the total length becomes approximately 5 m at the low-end frequency of EMC measurements, a shortened dipole antenna is used for the measurement in an anechoic chamber. The antenna factor (AF) for a shortened dipole antenna is usually calibrated by the reference antenna method at a finite separation. To estimate the uncertainty of the reference-antenna method, the measured and calculated results were compared [Morioka et al., 2013].

The response of a field probe is calibrated by the well defined standard field. Such a field strength is generated in a transverse electromagnetic (TEM) waveguide, sufficiently below the cutoff frequency of the waveguide. However, above the cutoff frequency, the higher-order modes perturb the field distribution. For this frequency range, a dipole antenna is employed to calibrate the E-field strength at a location in the anechoic chamber [Morioka, 2011a]. Although the field generation in an anechoic chamber has an advantage in the frequency band, TEM waveguides are still useful in terms of compactness. For the use of a TEM cell as a standard field generator, the electromagnetic field distribution should be accurately evaluated. The response of a dipole-like probe against the nonuniform field distribution of the TEM cell was simulated and compared with the measured results [Morioka, 2011b].

A continuous antenna factor in a wide frequency range is convenient to use, and such a broadband antenna as a log-periodic antenna (from 300 MHz to 1 GHz), a biconical antenna (from 30 MHz to 300 MHz), and a biconical and log-periodic hybrid super broadband antenna (from 30 MHz to 1 GHz) were evaluated for a metrology standard [Kurokawa et al., 2012]. A new method was proposed for evaluating a far-field gain and far-field free-space antenna factor in the near distance. The method is based on a technique of a time-frequency analysis to determine the frequency-dependent antenna distance [Kurokawa et al., 2013]. The method was examined for calculating the free-space antenna factor of EMI broadband antennas.

The developments of calibration techniques for loop antennas were carried out by AIST. AIST started to develop the calibration method in 2002. AIST has been providing a calibration service for small loop antennas the diameters of which are 10 cm and 60 cm in the frequency range from 9 kHz to 30 MHz since 2007. The lowest frequency of the loop-antenna calibration service was expanded to 20 Hz for a loop antenna with 133 mm diameter in March, 2008. AIST and NICT have been engaging to improve and simplify the loop-antenna calibration since 2012.

The development of calibration techniques for short monopole antennas were carried out by AIST. There have been a number of measurement methods proposed for electrically short monopole antennas. A case in point is the equivalent capacitance substitution method, which is commonly used for monopole antenna measurements. On the other hand, we have proposed a near-field three-antenna method for electrically short monopole antennas. These two absolute measurement methods are of quite different origins. In light of this fact, a comparison was made between the two measurement methods by means of experiments and simulations, and the differences observed between the antenna factors was discussed [Ishii et al., 2011]. These studies are in progress.

AIST started to develop an ac magnetic field strength standard in 2008. They started the calibration service at 50 Hz, 55 Hz, and 60 Hz in 2011. The method depends on the "Standard Field Method," using a Helmholtz coil [Ishii et al., 2012]. An ac magnetic-field sensor calibration service has been expanded from 1 μT up to 150 μT at 50 Hz and 60 Hz, and the uncertainties were also improved [Ishii, 2013]. This calibration service was started in April 2013.

Calibration services for the gains of standard horn antennas are being performed from 1 GHz to 40 GHz at 21 specified frequency points using the transfer method. An antenna-gain calibration service for standard-gain horn antennas (1.7 GHz to 2.6 GHz, 18 GHz to 26.5 GHz, 50 GHz to 110 GHz) has been prepared using the three-antenna extrapolation method. An antenna-factor calibration service for ridged-guide broadband horn antennas (1 GHz to 6 GHz at 3 m) has been prepared. A far-field antenna-gain measurement method was proposed in antenna measurements using the amplitude-center location in the Friis transmission formula from the Kern transmission formula using the phase centers of the antennas [Hirose et al., 2012, 2013]. An antenna-pattern measurement system above 50 GHz using a photonic technology was proposed. This system can minimize the influence of waveguide components, because an optical fiber is used as the mm-wave transmission line [Ameya et al., 2012].

In the EMC field, the frequency range of the EMI regulations was expanded from 1 GHz to 6 GHz in EU and Japan in 2010. To evaluate the EMI anechoic chamber performance above 1 GHz, we have proposed an optical-feeding radiating antenna for site validation proficiency testing of EMI anechoic rooms [Ameya et al., 2012 b].

3.5 A5. Power Attenuation and Impedance Measurements

NMIJ organized three international comparisons as the pilot laboratory. In the APMP.EM-RF.K8.CL regional metrology organization key comparison (KC) of RF power measurement, eleven countries participate in the key comparison. The key comparison started from June 2012, and finished its first rotation by five countries. The second rotation has been in operation and will finish August 2014. In the CCEM.RF-K5c.CL key comparison (KC) of scattering parameter measurements in 3.5 mm coaxial line (100 MHz to 33 GHz), nineteen countries participated in the key comparison. The key comparison started from June 2012 and finished its first rotation by five countries. The comparison will finish September 2015. In the APMC.EM.RF-S5.CL regional metrology organization supplementary comparison (SC) of characteristic impedance for coaxial lines, ten countries participated in the supplementary comparison. The supplementary comparison started from January 2014 and will finish November 2015.

The calibration services of the scattering parameters were started for PC7 and Type-N 50 ohm connectors in the frequency range of 9 kHz to 18 GHz, for Type-N 75 ohm connectors in the frequency range of 9 kHz to 3 GHz, and for WM-1651 (WR-6) rectangular waveguide in the frequency range of 110 kHz to 330 GHz. These calibration cervices are based on use of the originally-designed standard terminations in the range of 9 kHz to 10 MHz, and then the long-length air lines as the impedance standards are calibrated using a dimensional measurement and electrical-loss measurement. Subsequently, the dimensionally derived scattering-parameter calibration was started. The development of a scattering-parameter standard for rectangular waveguide in the frequency range of 50 GHz to 1.1 THz has been started.

NMIJ developed a new mm-wave power standard in the frequency range from 110 GHz to 170 GHz [Shimaoka, et. al, 2012a, 2013a]. It is an isothermal dry calorimeter, and has a WR-06 (WM-864) rectangular waveguide test port. Typical relative expanded uncertainties of a thermal power meter calibrated using the calorimeter range from 2.7 to 3.1%. NMIJ has also been developing two wideband waveguide calorimeters in the frequency ranges from 50 GHz to 75 GHz and 75 GHz to 110 GHz. We have reported work concerning their uncertainty evaluation [Shimaoka, et. al., 2013b]. Their measurement uncertainties have been under evaluation. NMIJ is developing a new microwave power standard based on the quantum effects. The measurement of microwave power using the Rabi frequency of vapor-phased cesium (Cs) atoms, which is proportional to the magnetic field strength of the microwaves, was reported until 2010. Incidentally, the Rabi frequency was measured by an atomic candle method, which was used for stabilization and as a reference of microwave strength. An optimization of the atomic candle is therefore important for the atomic microwave power standard. NMIJ optimized the atomic candle signal [Kinoshita et. al., 2012b, 2013c]. This optimization contributed to understanding the accuracy and precision of the atomic microwave power standard. In addition, NMIJ has started to improve the glass cell containing Cs atoms to reduce the uncertainty of the atomic measurement of microwave power. The new

cell enables converting from the magnetic field strength to the transmission power of the microwave without an electromagnetic simulation.

An accurate RF and microwave attenuation-measurement technique with a small mismatch uncertainty over broad continuous frequencies based on the loss measurements to the DUTs in four different phase networks was developed [Widarta, et. al. 2011a]. The four different phase-network configurations were realized by introducing two known phase-shift values of air lines into the system. A practical technique to apply the mismatch-loss correction in RF and microwave attenuation measurements of fixed attenuators as well as variable attenuators as devices under test has been also developed [Widarta, 2011b]. In the attenuation measurement, NMIJ developed a unique technique using step-attenuator measurements for evaluation of the complex reflection coefficients of the source [Widarta, 2012c]. In order to precisely measure high attenuation, a newly double step-attenuation measurement technique [Widarta, 2012d] and a broadband leakage investigation technique [Widarta, 2013d] have been developed. NMIJ has started to develop an attenuation standard based on the IF substitution method in the frequency range of 75 GHz to 110 GHz (W band). NMIJ has adopted the IF stabilization technique using a phase-locked loop in order to expand the frequency range of the attenuation measurement system into W band with high stability. The basic performance of the system was evaluated, and a good dynamic range, over 60 dB, was confirmed [Iida et al, 2013e].

NMIJ has been developing precision RF noise-measurement techniques. A variable noise source, using a rotary-vane attenuator, was studied in the frequency range of 50 GHz to 75 GHz [Iida et al, 2011c]. An experimental study for determining the resistivity and its temperature coefficient of a transmission line of a coaxial microwave noise source was performed [Iida et al, 2011d]. The uncertainty of a radiometer for RF and microwave noise temperature measurements was quantitatively evaluated [Iida et al, 2011e].

In recent years, NMIJ has started to study the accuracy evaluation of terahertz spectroscopy. In the attenuation (or transmittance) measurement by a terahertz time-domain spectrometer (THz-TDS), it is important to evaluate its linearity. For validation of the THz-TDS, NMIJ developed a metallized-film attenuator (MFA) that can be used in both focused and collimated THz beam configurations [Iida et al, 2012e, 2012f, 2013f]. A method of power linearity evaluation by using the metallized-film attenuator has been proposed [Iida et al, 2011f, 2012g, 2013g, 2013h].

In a joint research project with the National Physical Laboratory, UK, NMIJ achieved dimensional calibration capabilities of millimeter-wave coaxial line, i.e., 1.85 mm coaxial line, and waveguide, i.e., WM-864 waveguide. Good agreement between both laboratories was obtained [Horibe et al., 2010a, 2012i, 2012m, Shelton et. al. 2012r]. NMIJ had developed the metrology standards in both coaxial [Horibe et al., 2010b, 2011g, 2012k] and waveguide, with the uncertainty evaluation method of waveguide vector network analyzers (VNA) [Horibe et al., 2011h, 2012j, 2012n, 2012o, 2012p, 2013i] over 110 GHz up to 1.1 THz. In this research, NMIJ developed a new design of waveguide flange, a connection clamp, and vector network analyzer stage for establishing accurate and quick connections of waveguide standard devices and components [Horibe et al., 2011i, 2012l, 2013k, 2013m].

The calibration and testing methods of an artificial main network used in electromagnetic compatibility testing was developed using radio-frequency impedance standards [Kishikawa et al., 2012q, 2013j, 2013n]. NMIJ has begun to research material characterization and on-wafer measurement techniques in the frequency range between microwave and millimeter waves. In collaborate work with King Mongkut's Institute of Technology Ladkrabang (KMITL), Thailand, the uncertainty evaluation method and uncertainty optimization technique have been developed for material characterization based on the transmission and reflection method. Further material characterization techniques, split cylinder, ring-down cavity [Kato 2013o], and free-space measurement methods, are being researched. In the on-wafer techniques, a method to achieve a metrological traceability has been established [Horibe, 2013l].

4. Working Group Reports

Several topics are becoming of importance internationally, either in coordinating standards or developing the area. The Chair recommends the creation of at least two working groups to include:

- Time scale and the need for a redefinition
- Quantum-based metrology.

5. Sponsored Meetings

Several meetings have been sponsored technically, with a small financial sponsorship in one case. These meetings include the following:

- "Foundations and Frontiers of Computer, Communications, Electrical Engineering: Commemorating 150 years of Maxwell's Equations," West Bengal, India on January 9-10, 2015
- "International Conference on Signal Processing and Integrated Networks (SPIN-2014)," February 21-22, 2014, Noida, India
- "ICEAA – IEEE APWC Conference," Aruba, August 3-9, 2014
- "ICEAA – IEEE APWC – EMS," September 9-13, 2013 Torino, Italy

- "2013 Asia-Pacific Radio Science Conference (AP-RASC-13)," Taipei, Taiwan, September, 2013
- "RADIO 2014," April 7-10, 2014, Mauritius
- "International Conference on Microwaves and Photonics (ICMAP 2013)," December 13-15, 2013, Dhanbad, India
- "URSI EMTS 2013," Hiroshima, Japan, May 20-24, 2013
- "AES 2013, 2nd Advanced Electromagnetics Symposium," Sharjah-Dubai, United Arab Emirates, March 19-22, 2013
- "META'13, 4th International Conference on Metamaterials, Photonic Crystals and Plasmonics," Sharjah-Dubai, United Arab Emirates, March 18-22, 2013

6. Comments

The AP-RASC-13 conference participation was coordinated by the Vice Chair.

The ICEAA–IEEE APWC–EMS conference participation was coordinated between George Uslenghi (URSI VP), Patrizia Tavella (Italy), and Bill Davis (Commission A Chair). A large thanks to George and Patrizia for helping on this task. It was an enjoyable meeting.

Chair: Dr. William A. Davis, United States
E-mail: wadavis@vt.edu
Vice Chair: Dr. Yasuhiro Koyama, Japan
E-mail: koyama@nict.go.jp

COMMISSION B

1. GA 2011, Istanbul (Turkey)

The URSI Board approved the election of Giuliano Manara, Italy, as Chair, and Ari Sihvola, Finland, as Vice Chair, for the period 2011–2014.

2. International Electromagnetic Theory Symposium 2013 (EMTS 2013)

The 2013 URSI Commission B International Symposium on Electromagnetic Theory (EMTS 2013) was held in Hiroshima, Japan, May 20-24, 2013. The symposium attracted about 330 participants. It was organized by URSI Commission B in collaboration with the Electronics Society (ES) of The Institute of Electronics, Information and Communication Engineers (IEICE) of Japan. The Local Organizing Committee was co-chaired by Prof. Tsuneki Yamasaki (Nihon University, Japan) and Prof. Makoto Ando (Tokyo Institute of Technology, Japan).

EMTS 2013 was the 21st event in a triennial series of international symposia with a long history, started in 1953. It was organized in Japan for the first time. The main symposium venue was the International Conference Center of Hiroshima (ICCH), located in the Peace Memorial Park, where the opening reception, opening ceremony, all technical (oral and poster) sessions, technical exhibitions, and plenary talks, as well as Commission B business meetings were held. On the third day, the venue was moved to the Aki Grand Hotel at Miyajima-guchi, where two plenary talks and a poster session with the participation of all Young Scientist awardees (YSA) were given. After these sessions, participants could enjoy a late afternoon visit to the wonderful island of Miyajima, where they could enter the Itsukushima Shrine, a world heritage site, and watch the big Torii gate located in the sea. The visit was followed by the banquet at the ANA Crowne Plaza Hiroshima Hotel.

As for General Assemblies and Scientific Symposia (GASS), URSI Commission B symposia carefully maintain the tradition to support Young Scientists (YS). The Hiroshima symposium received 45 applications satisfying the criteria that the applicant must be the first author of a paper presented at the conference, and that her/he must be younger than 35. According to custom, for the Commission B symposia, the current Vice Chair of the Commission, Prof. Ari Sihvola, was responsible for handling the Young Scientists program. With the help of reviewers, 24 awardees were selected, and, as a matter of fact, due to the financial support of URSI and of the Local Organizing Committee, their registration fee was waived, they received a per diem, an invitation to the banquet, and free accommodation covering the full conference duration. Moreover, those from developing countries also received financial travel support.

Thanks to the support of the software company CST AG, a Young Scientist Best Paper Award was organized. The awardees were selected in the context of the poster session for YSA, organized at the Aki Grand Hotel. Finally, the awardees were announced during the banquet:

1. Ariel Epstein, Technion - Israel Institute of Technology, Israel, for the paper, "On the Relevance of Two-Dimensional Sources for Modeling Optical Emission from Layered Media"

2. Francesco Andriulli, Ecole Nationale Superieure des Telecomunications de Bretagne, France, for the paper, "Rapidly Converging Electromagnetic Simulations in the Entire Frequency Spectrum without the Search for Global Loops"

3. Martin Štumpf, Brno University of Technology, Czech Republic, for the paper, "Impulsive Electromagnetic Response of Thin Plasmonic Metal Sheets"

3. URSI Commission B School for Young Scientists

The decision of organizing URSI Commission B Schools for Young Scientists was taken in the business meetings of Commission B during GASS 2011 in Istanbul. The basic idea for the school was to encourage Young Scientists to learn the fundamentals and future directions in the area of electromagnetic theory from related lectures.

The first URSI Commission B School for Young Scientists was organized in the framework of EMTS 2013 in Hiroshima, Japan. The school was a one-day event, sponsored jointly by URSI Commission B and the EMTS 2013 Local Organizing Committee. The school offered a short, intensive course, where a series of lectures were delivered by two leading scientists in the Commission B community. The general title of the school was "Fundamentals of Numerical and Asymptotic Methods." It consisted of a couple of lectures of four hours each, given by Prof. Donald R. Wilton, "The Method of Moments (MoM) Applied to Problems in Electromagnetic Scattering, Radiation, and Guided Waves," and by Prof. Prabhakar H. Pathak (Dept. of ECE, The Ohio State University ElectroScience Laboratory, USA), "A Summary of Asymptotic High Frequency (HF) Methods for Solving Electromagnetic (EM) Wave Problems."

The second edition of the school will be organized at the URSI GASS 2014 in Beijing, China. Again, it will be a one-day event (two lectures of four hours each) given by Prof. Nader Engheta, University of Pennsylvania, USA. The title of the school is "Fields and Waves in Metamaterials."

4. International URSI Commission B Symposia 2016 and 2019

The 2016 International Symposium on Electromagnetic Theory (EMTS 2016) will be held on August 14-18, 2016, in Espoo, Finland. It will be organized by the Commission B (Fields and Waves) of the International Union of Radio Science (URSI) and Aalto University. A pre-announcement flyer was distributed during the Hiroshima Electromagnetic Theory Symposium. Questions about the symposium and its technical program can be directed to the present URSI Commission B Vice Chair, Prof. Ari Sihvola.

For the 2019 EMTS, the site will be chosen during the Commission B Business Meetings the Beijing GASS 2014. The present Chair has received a bid from the United States Commission B to hold the Symposium in San Diego, California, USA.

5. GASS 2014

With the help of conveners, Commission B has been able not only to fill its allocated slots for invited and submitted oral papers, but a substantial number of even high-ranking papers had to be moved to the two Commission B poster sessions. The Commission B Tutorial will be given by Prof. Stefano Maci, Italy, on the following topic: "Controlling Waves on Metasurfaces."

USNC Commission B member Nader Engheta, University of Pennsylvania, USA, will be awarded the Balthasar van der Pol Gold Medal, with the following citation: "For groundbreaking contributions and innovations in electromagnetic theory and applications of composite materials, metamaterials and nanoscale optics, bio-inspired imaging and sensing, and material-based optical nanocircuitry." Moreover, French Commission B Member Jean-Pierre Gabriel Berenger will be awarded the John Howard Dellinger Medal, with the citation: "For seminal work on the development of breakthrough absorbing boundary conditions for computational electromagnetics in radiosciences." Finally, Italian Commission B Member Francesco Paolo Andriulli will be awarded the Issac Koga Gold Medal, with the following citation: "For contributions to computational electromagnetics, specifically the development of preconditioned and stable integral equation solvers."

6. Vice-Chair Election 2014-2017

Two nominations have been received by the Commission:

- Kazuya Kobayashi, Japan
- Sembiam Rengarajan, USA

The appropriate ballot forms have been sent out by URSI. The final election will take place during the first Commission B Business Meeting during GASS 2014, and will have to be subsequently approved by the URSI Board.

7. Early Career Representative (ECR) Election 2014-2017

Two nominations have been received by the Commission:

- Joseph Costantine, USA
- Lian Lin Li, China, CIE

The appropriate ballot forms have been sent out by URSI. The final election will take place during the first Commission B Business Meeting during GASS 2014, and will have to be subsequently approved by the URSI Board.

8. Publication Matters

Papers presented during the 2013 International Commission B Symposium on Electromagnetic Theory were published on IEEE Xplore. Upon suggestions of session chairs and conveners, authors have been invited to contribute to a special section of *Radio Science*; submitted papers are presently under review.

For what concerns the tutorials for the *Radio Science Bulletin*, a paper on "The Dipole Moment (DM) and Recursive Update in Frequency Domain (RUFD) Methods: Two Novel Techniques in Computational Electromagnetics" was published in the September 2011 issue. The paper was coauthored by Raj Mittra, Chiara Pelletti, Kadappan Panyappan, and Agostino Monorchio. A paper on "Electromagnetism, Nanotechnologies and Biology: New Challenges and Opportunities" was published in the June 2012 issue. It was coauthored by Ovidio Mario Bucci and Enrico Bucci. Several other contributions have been invited, but it seems not so easy to obtain submissions.

9. URSI Atlantic Meetings and Asia-Pacific Radio Science Conferences (Midterm Symposia)

At the second meeting of the URSI Council on the occasion of the URSI GASS in Istanbul, the Board proposed to organize scientific meetings in the years in between the GASS. The three-year period in between the GASS meetings is felt to be too long for establishing and maintaining a sufficient level of contact and interaction within the URSI community. Since the URSI GASS in Istanbul, the Board has been looking into different options. On the occasion of the last meeting of the Coordinating Committee in April 2013, the proposal was made to have a yearly URSI meeting covering all 10 URSI Commissions. In order to avoid organizing duplicate meetings, it was proposed to incorporate the successful triennial AP-RASC URSI conference in this scheme, and to establish a new triennial event in the Atlantic region. Consequently, the year after the URSI GASS an URSI Atlantic Meeting will be organized in the European-American (Atlantic) region. Indeed, a new URSI Atlantic Meeting is already scheduled in the Gran Canaria, Spain, May 18-25, 2015.

Anyway, during the Commission B Business Meetings at EMTS 2013 in Hiroshima, members of Commission B unanimously decided that it is crucial for the Commission to continue the long tradition of organizing the triennial Electromagnetic Theory Symposia (EMTS). It was recommended to devote specific attention to avoid interference with the Asia-Pacific Radio Science Conference, which will be held in the same years as the EMTS.

Chair: Prof. G. Manara
E-mail: giuliano.manara@iet.unipi.it

COMMISSION D

This document provides the activity of Commission D during the triennium 2011-2014. It reports the main international conferences and workshops that received technical sponsorship or financial support from the Commission. The report also provides the scientific program scheduled for the next General Assembly and Scientific Symposium to be held in Beijing August 18-23, 2014. Finally, some activities of national Commissions are reported.

1. Officers of Commission D

During the period 2011-2014, the officers of Commission D were:

- Chair: Smail Tedjini, Grenoble-inp, France; e-mail: smail.tedjini@grenoble-inp.fr
- Vice Chair: Dr. Günter Steinmeyer, Max-Born-Institute, Berlin, Germany; e-mail: steinmey@mbi-berlin.de
- Past Chair: Prof. Franz X. Kärtner, MIT, USA; e-mail: kaertner@mit.edu

2. Terms of Reference of Commission D

Commission D is dedicated to Electronics and Photonics. In more detail, the reference terms approved during the last GASS of Istanbul in 2011 were defined as follows:

The Commission promotes research and reviews new development in:

- Electronic devices, circuits, systems and applications;
- Photonic devices, systems and applications;
- Physics, materials, CAD, technology and reliability of electronic and photonic devices down to nanoscale including quantum devices, with particular reference to radio science and telecommunications.

The Commission deals with devices for generation, detection, storage and processing of electromagnetic signals together with their applications from the low frequencies to the optical domain. Green technologies are also considered.

Year	Event	Support
2011	ICEAA-APWC 2011, Torino, Italy, 12-17 September 2011	Tech
2012	AES 2012, Paris, France, 16-19 April 2012	Tech
2012	META'12 - 3nd International Conference on Metamaterials, Photonic Crystals and Plasmonics, Paris, France, 16-19 April 2012	Tech
2012	International School of Physics "Enrico Fermi", Metrology and Physical Constants, Varenna, Italy, 17-27 July 2012	Tech
2012	ICEAA - International Conference on Electromagnetics in Advanced Applications, Cape Town, South Africa, 2-8 September 2012	Tech
2012	ISSSE 2012, Potsdam, Germany, 3-5 October 2012	Tech
2012	IEEE International Conference on RFID-Technology and Applications 2012, Nice, France, 5-7 November 2012	Tech
2013	META'13 - the 4th International Conference on Metamaterials, Photonic Crystals and Plasmonics, Sharjah-Dubai, U. A. Emirates, 18-22 March 2013	Tech
2013	AES 2013, the 2nd Advanced Electromagnetics Symposium, Sharjah-Dubai, United Arab Emirates, 19-22 March 2013	Tech
2013	MSMW '13 - 8th International Kharkov Symposium on Physics and Engineering of Microwaves, Millimeter and SubMillimeter Waves, Kharkiv, Ukraine, June 23 -28, 2013	Tech
2013	AP-RASC'13 - 2013 Asia-Pacific Radio Science Conference, Taipei, China SRS, 3-7 September 2013	Fin
2013	ICMAP 2013, Int Conf on Microwaves and Photonics, Dhanbad, India,13-15 December 2013	Tech
2014	Regional Conference in Radio Science, Pune, India, 2-5 January 2014	Tech
2014	RADIO 2014 - Radio and Antenna Days of the Indian Ocean, Mauritius, 7-10 April 2014	Tech
2014	EMC'2014, Tokyo, Japan, 13-26 May 2014	Tech
2014	ICEAA - IEEE APWC conference, Aruba, 3-9 August 2014	Tech
2014	Metamaterials 2014, Copenhagen, Denmark, 25-28 August 2014	Tech

Tech = Technical Support, Fin = Financial support

Table 1. Events sponsored by Commission D

3. Evolution of Topics in Commission D

As observed during this triennium 2011-2014, important topics such as nano-electronics, nano-photonics, metamaterials, and THz continue to growth in terms of interest and applications. Several sessions of the GASS 2014 are dedicated to these topics. By the way, the tutorial of Commission D is dedicated to THZ technologies. On the other hand, modeling and simulation techniques applied to complex and heterogeneous circuits and systems have seen several advances driven by the progress in computer science and high-performance computing systems. This topic is shared with Commission B.

Besides these conventional subjects, there are new topics that appeared or continue to gain in importance within the Commission. The most significant are related to:

- Wireless devices, such as RFID and sensors
- Energy harvesting and battery-less technologies (it is important to note that one of the general lectures of GASS 2014 is dedicated to energy harvesting, and was proposed by Commission D). Moreover, for the first time, one session is dedicated to that topic within the program of the Commission.
- Green technologies

It is worth remarking that these topics interest several other Commissions, in particular B and C. This fact is very relevant and clearly visible in the content of joint sessions DB, DC, and also DBC, at least for GASS 2014. It is expected that this trend will continue to progress and evolve to more joint sessions and topics.

4. Supported Conferences and Workshops

The commission has received several requests for either technical or financial sponsorship. Each request has been considered and positively agreed to when the topic of the event had a connection with the terms of Commission D.

In total, 17 sponsorships have been delivered, including one case of financial support to AP-RASC 2013. The list of the these events is provided in Table 1.

5. The Call for Papers for GASS 2014

After the meeting of the Coordinating Committee of April 2013, the call for papers was published. The deadline was February 15, 2014. All the scheduled sessions approved by Commission D received enough papers. We received

Technical Topic	Submitted (o,p,e)	Draft	Withdrawn	Total
D01,02: Micro and Nanophotonics	11 (9,1,1)	0	2	13
D03: New frontiers and applications of optical fibers	10 (9,1,0)	0	1	11
D04: Network Oriented Modeling of Electromagnetic Fields and Microwave Structures	12 (12,0,0)	0	1	13
DBC01: Energy Harvesting in Wireless Systems	6 (5,1,0)	0	3	9
D05: Trends in RFID, from Identification to sensing	12 (12,0,0)	0	0	12
DC01: Broadband Ubiquitous Network with Wired and Wireless convergence	9 (8,1,0)	0	2	11
DB01: RF MEMs and NEMS	4 (3,0,1)	0	0	4
DT: Tutorial D:	1 (1,0,0)	0	0	1
DA01: Quantum Optics, Quantum Information, Quantum Precise Measurement and Quantum Metrology	10 (3,3,4)	0	1	11
D06: Nonlinear Optics and Guided Wave Devices	5 (4,0,1)	1	0	6
D07: Hybrid and monolithic digital-RF integrated Circuits	5 (4,0,1)	0	0	5
DB02: Plasmonics	6 (3,1,2)	0	0	6
DBC02: Signal Processing Antenna	14 (6,2,6)	0	1	15
DB03,04: Multiphysics Modelling in Radio Frequency Nanoelectronics	9 (8,0,1)	0	0	9
D08: THz systems and applications	9 (8,1,0)	0	0	9
DFC01: Trends in THz Communications	6 (4,0,2)	0	0	6
D09,10: 60GHz Electronics	8 (7,0,1)	0	1	9
Other Topics (D)	12 (8,3,1)	0	2	14
Total	**149(114,14,21)**	**1**	**14**	**164**

Table 2. The submissions for the sessions managed by Commission D at the 2014 GASS.

164 papers, which was 20% larger than the Commission received in 2011. These are papers for Commission D only. There were also 100 papers submitted for joint sessions managed by Commissions B or C. The numbers of submissions for the sessions managed by Commission D are shown in Table 2.

6. The Sessions of Commissions D for GASS 2014

As presented in the previous section, the call for papers was successful, and the program was therefore organized in sessions scheduled from Monday, August 13, to Saturday, August 18. Table 3 lists the sessions, dates, and the conveners of these sessions.

7. The Joint Sessions with Other Commissions

Table 4 lists the joint sessions, mainly with Commissions B and C.

8. Contact With National Commissions

During this triennium, several pieces of information and requests have been sent to the national Chairs of local Commissions D. Unfortunately, there are several errors and items missing in the provided mailing list. It is necessary to clean and update this list.

In several countries, there are national URSI organizations and meetings, in particular, those of Commission D. As examples, annual national events are organized in France, Italy, and Germany, and certainly in other countries. To inventory these national events, a one-page report and summary of national Commission activity was sent to all the national Chairs, but only a few responses were received. Responses were received from Belgium, China, Czech Republic, France, Italy, Poland, Russia, and the United Kingdom. [These reports should be requested from the Chair of the Commission.]

Chair: Smail Tedjini
E-mail: smail.tedjini@grenoble-inp.fr

Vice Chair: Dr. Günter Steinmeyer
E-mail: steinmey@mbi-berlin.de

Session ID	Session Name	Day	Time	Location	Session Chairs
D01	Micro and Nanophotonics (1)	Monday, August 18	08:00-09:20	Commission D	Franz X Kärtner Mike Watts
D02	Micro and Nanophotonics (2)	Monday, August 18	9:40-11:00	Commission D	Franz X Kärtner Mike Watts
D03	New frontiers and applications of optical fibers	Monday, August 18	13:40-15:40	Commission D	Stefano Selleri
D04	Network Oriented Modeling of Electromagnetic Fields and Microwave Structures	Monday, August 18	19:00-20:40	Commission D	Peter Russer Yury Kuznetzov
D05	Trends in RFID, from Identification to sensing	Tuesday, August 19	9:40-12:00	Commission D	Gaetano Marrocco Smail Tedjini
D06	Nonlinear Optics and Guided Wave Devices	Wednesday, August 20	19:00-20:40	Commission D	Stefano Selleri
D07	Hybrid and monolithic digital-RF integrated Circuits	Thursday, August 21	08:00-09:20	Commission D	Achour Ouslimani Krishna Busawon
D08	THz systems and applications	Friday, August 22	13:40-15:40	Commission D	Jean-Louis Coutaz Taiichi Otsuji
D09	60GHz Electronics (1)	Saturday, August 23	08:00-09:20	Commission D	Kiat Seng YEO Kaixue Ma
D10	60GHz Electronics (2)	Saturday, August 23	9:40-10:40	Commission D	Kiat Seng YEO Kaixue Ma
DA01	Quantum Optics, Quantum Information, Quantum Precise Measurement and Quantum Metrology	Wednesday, August 20	13:40-15:40	Commission D	Guo Hong
DB01	RF MEMs and NEMS	Wednesday, August 20	08:00-09:20	Commission D	Roberto Sorrentino Fabio Coccetti
DB02	Plasmonics	Thursday, August 21	9:40-12:00	Commission D	Frédérique A de Fornel Nader Engheta
DB03	Multiphysics Modelling in Radio Frequency Nanoelectronics (1)	Friday, August 22	08:00-09:20	Commission D	Peter Russer Wenquan Che
DB04	Multiphysics Modelling in Radio Frequency Nanoelectronics (2)	Friday, August 22	9:40-10:40	Commission D	Peter Russer Wenquan Che

Table 3a. The sessions, dates, and conveners for the sessions of Commission D at GASS 2014.

Session ID	Session Name	Day	Time	Location	Session Chairs
DBC01	Energy Harvesting in Wireless Systems	Tuesday, August 19	08:00-10:00	Commission D	Apostolos Giorgiadis Luciano Tarricone
DBC02	Signal Processing Antenna	Thursday, August 21	13:40-15:40	Commission D	Yvan Duroc Alexander Yarovoy Yuan Yao
DC01	Broadband Ubiquitous Network with Wired and Wireless convergence	Tuesday, August 19	13:40-15:40	Commission D	Katsutoshi Tsukamoto Yuichi Kado Katsumi Iwatsuki
DFC01	Trends in THz Communications	Friday, August 22	19:00-21:00	Commission D	Tadao Nagatsuma Ci-Ling Pan Thomas Kuerner
DP1	DP1-Poster Session	Tuesday, August 19	19:00-21:00	Commission D	Mike Watts Franz X Kärtner G. Steinmeyer
DP2	DP2-Poster Session	Thursday, August 21	19:00-21:00	Commission D	Smail Tedjini Apostolos Giorgiadis
DT	Tutorial D:	Wednesday, August 20	9:40-10:00	Commission D	Smail Tedjini

Table 3b. The sessions, dates, and conveners for the sessions of Commission D at GASS 2014 (continued).

Session ID	Session Name	Day	Time	Managing commission	Session Chairs
AD01	Metrology of Optical Frequencies and Optical-Dimensional Measuring Techniques (1)	Tuesday, August 19	08:00-09:20	Commission A	Josef Lazar Juraj Poliak
AD02	Metrology of Optical Frequencies and Optical-Dimensional Measuring Techniques (2)	Tuesday, August 19	9:40-11:00	Commission A	Juraj Poliak Josef Lazar
BCD01	Reconfigurable Antennas for Cognitive Radio	Friday, August 22	19:00-20:40	Commission B	Agostino Monorchio Karu Esselle
BCD02	Emerging Wireless Technologies (1)	Saturday, August 23	08:00-09:20	Commission B	Smail Tedjini Paolo Nepa
BCD03	Emerging Wireless Technologies (2)	Saturday, August 23	9:40-10:40	Commission B	Jun-ichi Takada Sana Salous
BD01	Recent Advances in Metamaterials	Tuesday, August 19	9:40-12:00	Commission B	Christophe Caloz
BD02	Advanced Computational Techniques for Multi-Scale and Multi-Physics Electromagnetics	Wednesday, August 20	19:00-20:40	Commission B	Weng Cho Chew Jin-Fa Lee
BD03	General topics in electromagnetic scattering	Thursday, August 21	08:00-09:20	Commission B	Ismo V Lindell Ivan V. Andronov
CBDK01	Body-Area Networks(1)	Thursday, August 21	08:00-09:20	Commission C	Kamya Yekeh Yazdandoost Raffaele D'Errico
CD01	Circuit Technologies for Mobile Communications	Monday, August 18	19:00-20:40	Commission C	Shoichi Narahashi Ke Wu
CD02	Ultra-high bit rate radio communications (TeraHertz and 60 GHz) (1)	Friday, August 22	08:00-09:00	Commission C	Cyril Renaud Tadao Nagatsuma Thomas Kuerner
CD03	Signal Processing for radar systems	Friday, August 22	9:40-10:40	Commission C	Cyril Renaud Tadao Nagatsuma Thomas Kuerner

Table 4. The joint sessions of Commission D at the 2014 GASS.

COMMISSION F

During the triennium 2011-2014, Commission F has been involved with the organization of two specialist meetings: one concentrating on propagation characteristics for microwave and millimeter-wave communication systems (to be held in Ottawa, Canada), and another treating microwave remote sensing of the Earth, oceans, ice, and atmosphere (to be held in Espoo, Finland). These symposia initiated many of the session topics for the URSI Commission F General Assembly and Scientific Symposium (GASS) scheduled for Beijing, China, August 16-23, 2014. There, Simonetta Paloscia of Florence, Italy, will become the next URSI Commission F Chair.

In Memoriam

During this triennium, five well-known Commission F members have passed away. Four of them had their obituaries noted in issues of the *Radio Science Bulletin* (*RSB*). They are listed in order of the date of their death:

- David H. Staelin (1938-2011): early development of microwave-imaging orbital spectrometers for atmospheric monitoring (see *RSB*, December 2011).
- Gert Brussaard (1942-2012): propagation research in support of microwave communication and remote sensing. Chair of URSI Commission F, 1990-1993, President of URSI, 2008-2011 (see *RSB*, June, 2012).
- Hans Liebe (1934-2012): developed reliable expressions for the complex refractivity of moist air, which are basic to all millimeter-and sub-millimeter-wave propagation (see *RSB*, September, 2012).
- Martin Hall (1937-2012): one of the pioneers of dual-polarization radar for remote sensing of precipitation. Chair of URSI Commission F, 1996-1999 (see *RSB*, March 2013).
- Richard Moore (1923-2012): implemented radar technology for microwave remote sensing of land, sea, ice, and atmosphere; developed both the theory and the experiment; founder of the interdisciplinary Remote Sensing Laboratory at the University of Kansas; elected to US National Academy of Engineering, and Chair of URSI Commission F, 1993-1996.

Figure 1. A conversation between Roger Lang (l) and Robert Bultitude (c) over food and drink.

Commission F Symposium

At the Commission F business meeting in Istanbul, Turkey, 2011, it was agreed that the Commission would host two symposia during the triennium. The first URSI Commission F Triennial Symposium on Radiowave Propagation and Remote Sensing was held in Ottawa, and chaired by Robert Bultitude. The second symposium, URSI Commission F Specialist Symposium on Microwave Remote Sensing of the Earth, Oceans, Ice, and Atmosphere 2013, was held in Espoo, Finland, and chaired by Martti Hallikainen. Meeting reports are given below.

URSI Commission F Triennial Symposium on Radiowave Propagation and Remote Sensing, Ottawa, April 30 - May 2, 2013

Planning for the Ottawa symposium, proposed at the URSI General Assembly in Istanbul, began in earnest during the spring of 2012. Since planning discussions at the General Assembly involved only Canadian researchers from the radio propagation field, initial steps involved seeking partners from the Ottawa remote sensing community. This was easily accomplished. By May 2012, an organizing committee was formed, but because of the difficult worldwide economic conditions, it was difficult to obtain both sponsorship funding and the promise of participation from those who would have to travel to Ottawa from a great distance. Nevertheless, URSI's Canadian National Committee was eventually able to lend us sufficient funds to hire a conference organizer, and to begin making arrangements with various venue providers. Soon afterward, a Web site was launched, and e-mail invitations to attend were sent to scientists worldwide.

As anticipated, responses to invitations were slow, and submissions accompanied by early registrations were nonexistent. Critical mass for symposium attendance was not achieved until early spring, 2013; the new conference facilities at Carleton University then became the symposium's venue. This process – and its parsimonious

Figure 2. A group photo near one of the locks on the Rideau Canal.

Figure 3. The symposium attendees. First row, middle: Commission F Vice Chair Simonetta Paloscia, and on her right, Commission F Chair Roger Lang and Professor Martti Tiuri; on her, left symposium General Chair Martti Hallikainen, and TPC co-Chair Juha Kainulainen.

achievement – was greatly aided by the skill and hard work of the conference organizer, a small Ottawa-based consulting company named CHC.

In addition to helping with symposium planning, personnel from CHC also manned the registration desks at the symposium, and coordinated with the A/V staff and other service providers. At the close of registration, we had nearly fifty participants, some of whom were able to attend through funding assistance in the total amount of 4000 Euros provided by URSI at the international level. Participants arrived at the symposium from eighteen different administrations worldwide (including Canada, the US, the UK, Germany, Italy, France, Greece, Nigeria, The Netherlands, Belgium, China, Japan, Korea, India, Finland, Norway, Sweden, and Denmark). Others who could not personally attend – some from NASA in the US – presented papers via Webex. Care was taken that there were an equal number of sessions from the radio propagation and remote sensing disciplines. This included two keynote speakers from each area, who delivered fascinating presentations in their subject areas. These included backscatter from precipitation, mobile radio-channel modeling, rain attenuation on terrestrial line-of-sight radio paths, and two different aspects of radar remote sensing. In all, there were six half-day technical sessions in each of the two areas, with an average of eight, 20-minute oral presentations per session. There were no poster presentations.

A symposium dinner was held on the evening before the close of the symposium, where a moment was taken to remember our recently deceased Commission F colleagues, Gert Brussaard and Martin Hall.

Feedback from participants reflected that the symposium was enjoyed by all, with much exchange of both scientific and social communications. Figure 1 portrays a conversation between Robert Bultitude and Roger Lang. Figure 2 is a group photo taken along the side of the very famous Rideau Canal, which runs beside Carleton University. This canal was designed and constructed by the British Army's Royal Engineers, and is the oldest continuously operated canal in North America. The many locks, which raise and lower water traffic going from one section of the canal to another, are operated today much as they were when the canal first opened in 1832.

The symposium Web site, which includes the technical program and a copy of papers presented, remains open at www.ursi-f-ts.com. This will be accessible until approximately September 2014. Presenters at the symposium were asked to consider submissions for a special issue of *Radio Science* that included extended papers from the symposium. It was understood that this special issue will be published late in 2014.

Microwave Signatures 2013 October 28-31, 2013, Espoo, Finland

The URSI Commission F Specialist Symposium on Microwave Remote Sensing of the Earth, Oceans, Ice, and Atmosphere 2013 (Microwave Signatures 2013, for short) was held on the campus of Aalto University in Espoo, Finland, October 28-31, 2013. The meeting was the 11th of a series of meetings held, with the first one organized in Berne, Switzerland, in 1974.

Microwave Signatures 2013 provided an international forum for reporting and discussing recent achievements in instrumentation, methodology, and applications in the field of land, ocean, ice, and atmosphere sensing. The meeting attracted professionals from around the world (Figure 3), and consisted of a serial sequence of oral and poster sessions. The following invited sessions were organized:

- GNSS Reflectometry
  (organizer: Manuel Martin-Neira)

- L-Band Active/Passive Land Surface Retrievals and SMAP
  (Thomas Jackson and Andreas Colliander)
- Microwave Propagation in Vegetated and Snow Covered Soils: A Session in Honor of Paolo Pampaloni (Simonetta Paloscia)
- Remote Sensing of Snow and Ice: A Session in Memory of Richard K. Moore
  (Martti Hallikainen)
- Remote Sensing of Precipitation
  (V. Chandrasekar).

Other topics included:

- Radiometers and Calibration
- RFI in Remote Sensing
- Soils and Soil Moisture
- Remote Sensing of Forest and Vegetation
- Remote Sensing of Atmosphere

A total of 71 scientists attended the conference, and a total of 61 oral presentations and 18 poster presentations were given. A welcome reception was held on October 28 in the symposium venue. The banquet was held on October 30 in Helsinki, and was attended by 32 persons.

URSI Commission F provided travel stipends for several attendees. The symposium was also sponsored by Aalto University, with the IEEE Geoscience and Remote Sensing Society as a technical co-sponsor. The symposium home page is at http://frs2013.ursi.fi.

URSI General Assembly and Scientific Symposium, Beijing, China 2014

The URSI General Assembly will be held In Beijing, China, from August 17-23, 2014. Commission F has 153 accepted oral and poster papers. The tutorial will be given by Paolo Pampaloni of Florence, Italy, on "Looking at the Earth as a Planet: Passive Remote Sensing of Land Surfaces." Commission F has nine sessions and three joint sessions. These sessions represent a balance between remote sensing and wave propagation. The session titles are:

- Remote Sensing of Ice and Snow
- Millimeter Wave Propagation and Remote Sensing
- Advances in Spaceborne SAR Imaging and Applications
- Fixed Terrestrial Links: Measurements, Models and Planning Procedures
- Remote Measurement of Precipitation at Local, Regional, and Global Scales
- Microwave Remote Sensing of Vegetation and Terrestrial Snow
- Radio-Frequency Interference (RFI)
- Remote Sensing of Biomass
- Remote Sensing of Land and Sea at L band

The joint sessions are:

- Electromagnetic Modeling and Application of Underground Imaging (with B)
- Communications and Remote Sensing in Disaster Scenarios (with C)
- Trends in THz Communications (with D and C)

Commission F Chair, Dr. Roger Lang
E-mail: lang@gwu.edu

COMMISSION H

1. In Memoriam

Vladimir Fiala, a former Chair of URSI Commission H, died in Prague on September 8, 2012, at the age of 74. His research interests were in theoretical space plasma physics, antenna-plasma interactions, and propagation and excitation of plasma waves. He had a gift of sharing his enthusiasm with colleagues and students, and was always ready to help. Dr. Fiala was elected Vice Chair (1993) and became the Chair (1996-99) of URSI Commission H, and also worked as the President of the Czech National Committee of URSI.

2. Meeting Support

During the 2011-2014 triennium, 9000 Euros were allocated to each Commission to be spent for the support of meetings and attendance at the GASS. Commission H spent 6000 Euros to financially support the following meetings (mode B), with a contribution between 1000 to 2000 Euros each:

1. ISROSES II – International Symposium on Recent Observations and Simulations of the Sun-Earth System II, Borovets, Bulgaria, September 11-16, 2011

2. VERSIM 2012 – 5th VLF/ELF Remote Sensing of Ionosphere and Magnetospheres Workshop 2012, Sao Paulo, Brazil, September 2-8, 2012

3. AP-RASC'13 – 2013 Asia-Pacific Radio Science Conference, Taipei, China SRS, September 3-7, 2013

4. VERSIM 2014 – 6th VLF/ELF Remote Sensing of Ionosphere and Magnetospheres Workshop 2014, Dunedin, New Zealand, January 20-23, 2014

Commission H also allocated 3000 Euros to support participation of selected lecturers at the URSI GASS 2014. Propositions to support the presenters of papers in the Commission H lead sessions were solicited from all session conveners. With only three propositions received, the Commission Chair and Vice Chair decided to support the participation of all three proposed distinguished colleagues.

Commission H also provided support in mode A (without financial aid) for the following meetings:

1. ICEAA-APWC 2011, Torino, Italy, September 12-17, 2011
2. IRI 2011 Workshop, Hermanus, South Africa, October 10-14, 2011
3. ISEA 13 – 13th International Symposium on Equatorial Aeronomy, Paracas, Peru, March 12-17, 2012
4. AES 2012, Paris, France, April 16-19, 2012
5. META'12 – 3rd International Conference on Metamaterials, Photonic Crystals and Plasmonics, Paris, France, April 16-19, 2012
6. 39th COSPAR SA 2012 – Sessions D3.1 and PCB.1, Mysore, India, July 14-22, 2012
7. ICTRS 2012 – First International Conference on Telecommunications and Remote Sensing, Sofia, Bulgaria, August 29-31, 2012
8. ICEAA – International Conference on Electromagnetics in Advanced Applications, Cape Town, South Africa, September 2-8, 2012
9. RADIO 2012 – Radio and Antenna Days of the Indian Ocean, Mauritius, September 24-27, 2012
10. ISAP2012 – 2012 International Symposium on Antennas and Propagation, Nagoya, Japan, October 29 - November 2, 2012
11. ISSS-11 – 11th International School/ Symposium for Space Simulations, Jhongli City, China SRS
12. Galileo Science Symposium, Prague, Czech Republic, December 4-6, 2013
13. Regional Conference in Radio Science, Pune, India, January 2-5, 2014
14. COSMOS – COSPAR 2014, Moscow, Russia, August 2-10, 2014
15. ICEAA – IEEE APWC conference, Aruba, August 3-9, 2014

3. Working Group Activities

3.1 Working Groups of Commissions H, E, and J: Computer Simulations in Space Plasmas

co-Chairs for Commission H: Y. Omura (Japan) and B. Lembege (France)

The URSI Working Group of Computer Simulations in Space Plasmas contributed to organization of the ISSS-11 (The 11th International School/Symposium for Space Simulations), which was successfully held at Zhong Li, Taiwan, on July 21-28, 2013. A detailed conference report will be published in the *Radio Science Bulletin*. The next meeting of the ISSS series will be held in July 2015 in Prague.

3.2 Working Group of URSI and IAGA: VLF/ELF Remote Sensing of the Ionosphere and Magnetosphere (VERSIM)

co-Chair for URSI Commissions H and G: J. Lichtenberger (Hungary)

co-Chair for IAGA: C. J. Rodger (New Zealand), until 2013; J. Bortnik (USA), from 2013

This very active group aims to promote research in the ELF/VLF field by facilitating the exchange of ideas, information, and experience between active research workers and other interested scientists. This is done through regular meetings at IAGA and URSI Assemblies, a regular VERSIM community workshop, and via the circulation of a newsletter. The group has also been active in sponsoring scientific symposia at IAGA and URSI Assemblies in areas relevant to its field of interest, and in coordinating observational campaigns. At present, the main subjects of interest include plasma structures and boundaries – morphology and dynamics, wave-particle and wave-wave interactions, wave-induced particle precipitation, wave propagation in magnetosphere and ionosphere, sprites and the effects of lightning on the ionosphere. There are currently over 100 scientists from about 26 different countries on the VERSIM mailing list. The VERSIM Working Group maintains a Web site that is currently hosted by the institution of the past VERSIM co-Chair, C. J. Rodger, at http://www.physics.otago.ac.nz/versim/. A VERSIM newsletter is regularly posted on this Web site. Two VERSIM workshops have been organized during the last triennium:

5th VERSIM Workshop, Sao Paulo, Brazil, September 3-6, 2012

The 5th VERSIM Workshop took place in September 2012 at Mackenzie Presbyterian University (São Paulo, Brazil), organized by the Center for Radio Astronomy and Astrophysics Mackenzie (CRAAM), Engineering School, and supported by IAGA and URSI. This was a chance for the VERSIM IAGA/URSI joint working group to meet and discuss current issues, developments, and techniques, and was the first time the VERSIM workshop has taken place outside of Europe. The final day of the 5th VERSIM workshop was a special day devoted to geophysical and radio techniques to asses natural disasters and space

weather impacts on the Earth. This is part of an ICSU-funded URSI/SCOSTEP-supported program for South America. The workshop attracted 54 participants from five continents, although a significant number of participants were only present for the final day. A report on the 5th workshop was published in the *Radio Science Bulletin* issue No. 344, March 2013 (p. 40), and IAGA News 49 (December 2012, p. 9).

6th VERSIM Workshop, Dunedin, New Zealand from January 20-23, 2014

The 6th VERSIM workshop took place in January 2014 at the University of Otago (Dunedin, New Zealand), organized by the Space Physics Group of the Department of Physics, and supported by IAGA, URSI, and the Air Force Office of Scientific Research, Asian Office of Aerospace Research and Development. This was a chance for the VERSIM IAGA/URSI joint working group to meet and discuss current issues, developments, and techniques. The 6th VERSIM Abstract and Program Book is available online. The workshop attracted 35 participants from 14 countries, with 58 abstracts.

3.3 Working Group of Commissions E, G, and H: Seismo-Electromagnetics

co-Chair for Commission H: M. Parrot (France)

Since the last GASS in Istanbul, several dedicated meetings have been organized. An EMSEV (Electromagnetic Studies of Earthquakes and Volcanoes) workshop took place in Gotemba, Japan, at the end of September 2012. The next one is planned to be held in Poland in September 2014. Another team, with S. Pulinets (Russia) and D. Ouzounov (US) as leaders, has been accepted by ISSI (ESA) with the following topic: "Multi-Instrument Space-Borne Observations and Validation of the Physical Model of the Lithosphere-Atmosphere-Ionosphere-Magnetosphere Coupling," and regular working sessions have been held in Bern. Members of the Working Group and other interested scientists are still working with data from the DEMETER spacecraft mission, which was in operation from July 2004 until December 2010. Many other satellite data are also used, in particular TEC measurements. The Chinese satellite CSES is scheduled to be launched in 2016.

3.4 Working Group of Commissions A, B, D, F, G, H, J, and K: An Inter-Commission Working Group on Solar-Power Satellites

co-Chair for Commission H: K. Hashimoto (Japan)

Important progress was reported in the ITU-R Question on wireless power transmission (WPT) last year. A liaison statement was sent to many organizations, including URSI. The ITU-R WP1A meeting was held June 3-12, 2014. Report(s) or Recommendation(s) on ground applications of wireless power transmission will be compiled soon. A separate report on space application of solar-power satellite is planned to be compiled in the next few years. In order to make contributions for the report, a wide range of comments from the URSI Commissions will be important.

3.5 Working Group of Commissions G and H: Active Experiments in Space Plasmas

co-Chair for Commission H: B Thide (Sweden)

No reports on activities of this Working Group were received.

4. Preparations for the XXXIth URSI General Assembly and Scientific Symposium in Beijing, China, August 16-23, 2014

4.1 Scientific Sessions

Commission H has arranged:

1. Wave-particle Interactions and Their Effects on Planetary Radiation Belts: 17 oral presentations (H01, H02, H03, H05), three posters (HP3)
2. Laboratory Simulations of Space Plasma Waves: three oral papers (H04)
3. Boundary Layers in Terrestrial and Planetary Environments: Macro/Micro-Scale Kinetic Processes: 11 oral presentations (H06, H07), 14 posters (HP5)
4. Plasma Interactions with Solar System Bodies: nine oral presentations (H09, H10, H11), four posters (HP6)
5. Remote Sensing of the Plasmasphere: 10 oral presentations (H11, H12)
6. Commission H: Open session and latest results: 13 oral presentations (H08, H13, H14)

Common sessions with other commissions, lead by Commission H:

1. Active Experiments: Seven oral presentations (HG01, HG02), five posters (HP1)
2. Ionospheric, Magnetospheric and High Energy Effects of Lightning: 11 oral presentations (HGE01, HGE02), nine posters (HP2)

3. Drivers, Detection, and Ionospheric Impacts of Precipitation from the Radiation Belts: 11 oral presentations (HG03, HG04), four posters (HP4)

Other sessions related to Commission H:

1. Terrestrial and Planetary Electromagnetics: six oral presentations (EGH01)
2. Plasma Waves: six oral presentations (GH01)
3. Radio Sounding in Magnetospheres and Ionospheres: five oral presentations (GH02, GH03)
4. The Geospace Environment and Meteors: 10 oral presentations (GH04, GH05)
5. Electromagnetic Effects in Lithosphere-Atmosphere-Ionosphere Coupling: seven oral presentations (GHE01, GHE02)

4.2 Total Number of Papers and Trends From the Last GASS

For the upcoming URASI GASS in Beijing, Commission H accepted 132 papers (93 oral presentations and 39 posters). Every effort was made to maximize the number of scheduled oral presentations, and to use all available time slots in the program. There was a slight decrease in the total number of papers compared to the last URSI GASS in Istanbul in 2011, where Commission H accepted 144 papers (86 oral presentations and 58 posters).

4.3 Tutorial Lecture

The Commission H tutorial lecture, on "Theory and Simulations of Nonlinear Wave-Particle Interactions in the Planetary Radiation Belts," will be given by Prof. Yoshiharu Omura from the Research Institute for Sustainable Humanosphere, Kyoto University, Japan. The paper will be published in the *Radio Science Bulletin* before the 2014 General Assembly and Scientific Symposium.

4.4 Young Scientist Awards

The 2014 Young Scientists Awards will be given to seven young scientists from Commission H: Dr. Huishan Fu (China CIE), Dr. Wenlong Liu (China CIE), Dr. Eva Macusova (Czech Republic), Dr. Sebastien Celestin (France), Dr. Aaron T. Hendry (New Zealand), Dr. Wen Li (USA), and Dr. Lunjin Chen (USA). Two of these young scientists are being considered for an additional grant from URSI to cover part of their travel expenses to the 2014 General Assembly and Scientific Symposium.

4.5 Student Paper Competition

Three student papers were submitted through Commission H. After the review process, one of the submitted papers will be selected for the final round of the competition, where the students present their work during the 2014 General Assembly and Scientific Symposium.

5. Recipients of the URSI Awards 2014 related to Commission H

Appleton Prize

Dr. R. F. Benson, USA

Citation: "For fundamental contributions to knowledge of the interactions of space borne radio sounders with the Earth's plasma environment and to the use of sounders as diagnostic probes of that environment."

Santimay Basu Prize

Dr. M. B. Cohen, USA

Citation: "For contribution to ELF/VLF radio wave instrumentation, propagation, and generation, in the ionosphere and magnetosphere, and for initiating and fostering an international network of young scientists in developing countries."

The URSI awards will be presented to the awardees during the Opening Ceremony of the XXXIth General Assembly and Scientific Symposium at the Beijing Convention Center in Beijing, China, on August 17, 2014.

6. Commission H Vice Chair Election

The call for nominations for the new Commission H Vice Chair was sent out in December 2013. Two excellent candidates have been nominated, and voting is in progress. The final vote counting will take place during the first Commission H business meeting, which will be held on Monday, August 18, 2014 at the URSI GASS in Beijing.

7. Election of the Commission H Early Career Representative

The call for nominations for the newly introduced Commission H Early Career Representative was sent out in December 2013. Four excellent candidates have been nominated and voting is in progress. The final vote counting will take place during the first Commission H business meeting, which will be held on Monday, August 18, 2014 at the URSI GASS in Beijing.

8. Election of the Commission H Chair

The current Commission H Vice Chair, Meers Oppenheim, under usual circumstances would automatically become Chair after the 2014 URSI GASS in Beijing. In February 2014, he decided not to take this responsibility for serious personal reasons. After the decision of the URSI Board, the call for nominations for the Commission H Chair was sent out in May 2014, and one candidate was nominated. URSI President Phil Wilkinson will attend the first Commission H business meeting, which will be held on Monday, August 18, 2014, at the URSI GASS in Beijing, and organize the Chair election according to the URSI Statutes.

I would like to take this opportunity to thank the Commission H Vice Chair, Meers Oppenheim, as well as the Commission H past Chair, Yoshiharu Omura, for their valuable advice and support during the last triennium.

Chair: Ondrej Santolik
E-mail: os@ufa.cas.cz

Book Reviews for Radioscientists

Design of Reconfigurable Antennas Using Graph Models

by Joseph Constantine, Youssef Tawk, and Christos G. Christodoulou, San Rafael, CA, Morgan and Claypool Publishers, 2013; ISBN: 9781627050241 paperback; ISBN: 9781627050258 ebook; 148 pp.

As the title tells, this book deals with the design of reconfigurable antennas. This is not only a hot topic in RF communication techniques, but also a very broad field, since very different techniques are involved in order to change the behavior an antenna. Reconfigurable antennas are composed of a set of parts/subsystems that might be connected/disconnected or otherwise altered in an electrical and/or mechanical way in order to control the antenna's parameters.

The introduction of the book gives an overview of common reconfigurable antenna systems. The authors assume that the reader is familiar with switching elements, such as RF MEMS, varactor diodes, PIN diodes, and others. In other words, the book addresses advanced readers, and tries to offer a generic superstructure for the design.

The second chapter deals with graph theory. After a nice summary of its basic concepts and the description of graphs using matrices, the graph-theory concepts are applied to selected antenna structures. The highly abstract concept of a graph and its relationship to a real antenna system is explained in different ways for the selected structures. The chosen approaches are formulated as rules that are also used in later chapters.

In Chapter 3, the authors claim that "efforts in generating optimal reconfigurable antenna designs don't include any clear tactic." In the following, they give an iterative six-step procedure that should overcome this lack. However, this procedure simply formalizes what a designer usually does. Moreover, the procedure orients itself at examples that are given in advance. It therefore will not lead to creative new ideas unless the designer includes the respective options. Furthermore, the designer is dedicated to judging an intermediate result in the iteration process. The graph modeling occurs only in Step 4, and helps in formalizing the description of several states of the antenna, e.g., switches being on or off. However, at least for the given examples, it seems that the respective descriptions could easily be included in the procedure, even without explicitly using graph theory.

The benefit of graph modeling an antenna becomes more obvious in the following chapters, where larger antennas with many switches are treated. In this case, both redundancy and reliability play an important role. Graph modeling of antennas helps to discover redundant parts and, for example, in calculating the number of necessary switches for achieving a certain reliability, or finding optimum numbers of switches, taking into account complexity versus reliability versus cost, etc. A well-formalized description might even be helpful if a switch failure should be detected.

Again, graph modeling does not reduce the required simulation efforts in the design process, nor will it yield new antenna structures. A graph model is simply an abstract model for representing physical structures. A graph model thus may help to treat complex systems with many states in a well formalized manner. The book shows how graph theory can be useful both for the design process as well as during the operation of reconfigurable antennas.

Some of the statements in the book, including the statement cited above, seem very absolute. Graph modeling is not the one and only way leading to a more efficient handling of antennas, although it might be really useful. Graph theory will never replace what experienced antenna designers already know, but it might bring some additional order in their knowledge.

A final statement: The style of the presentation is sometimes lengthy. For example, the formulae for the reliabilities are written out with explicit numbers over and over, and the term "reconfigurable" occurs 410 times on 137 pages, in spite of a large number of pages with only figures, diagrams, and tables.

Pascal Leuchtmann
E-mail: pascal@ethz.ch

Have you written a book? Do you know a book written by a colleague that might be of interest for the URSI community? We would be glad to publish a review of such books in our URSI *Radio Science Bulletin*. Please contact our Associate Editor on book reviews, Kristian Schlegel (ks-ursi@email.de).

Conferences

CONFERENCE REPORTS

Report on ISSS

ZhongLi, Taiwan, 21 - 28 July 2013

The 11th International School/Symposium for Space Simulations (ISSS-11) was successfully held at ZhongLi, Taiwan, on July 21-28, 2013. Under the leadership of Prof. Lin Ni Hau from National Central University (Figure 1), as the Chair of the Local Organizing Committee, and Prof. Yoshiharu Omura from Kyoto University (Figure 2), as the Chair of the International Program Committee, ISSS-11 was the first Asian ISSS held outside Japan. ISSS-11 was sponsored in part by the National Science Council and the National Space Organization of Taiwan, with the International Union of Radio Science (URSI) as a technical cosponsor. ISSS was first held in Kyoto in 1982, initiated by Prof. M. Ashour-Abdualla (USA), Profs. H. Matsumoto and T. Sato (Japan), as well as Prof. R. Gendrin (France). The workshop has subsequently been held every two to three years for over 30 years. The most recent ISSS workshops were held in Alberta, Canada (2011, ISSS-10); Paris, France (2009, ISSS-9); and Hawaii, USA (2007, ISSS-8).

Figure 1. Prof. Lin Ni Hau presenting her invited

Figure 2. Prof. Yoshiharu Omura giving the opening speech.

Figure 3. A photo captured during a hands-on session.

This time, we received around 120 applications, with most of the participants coming from Japan, Taiwan, China, USA, Korea, Canada, France, Russia, India, Norway, and Romania (Figures 3 and 4). The events of the first two days, including the welcome banquet, were held in the Hotel Kuva Chateau, while the following events were held at the National Central University (NCU). Over the course of eight days, students were instructed in simulation lectures along with hands-on work, while the latest research results in the field were also presented. The school/symposium consisted

Figure 4. The poster session.

Figure 5. Prof. James F. Drake answering questions from the audience.

Figure 6. Prof. Norden Huang giving his plenary talk.

of 32 lectures, 12 tutorials, and five hands-on sessions. We were proud to have had invited Los Alamos National Laboratory (LANL) retiree Dr. Jeremiah Brackbill, Prof. Viktor Decyk from UCLA, Prof. James Drake from the University of Maryland, and Prof. Norden Huang E (Figures 5and 6) from NCU to join our school (Figure 7).

Following the ISSS tradition, ISSS-11 was held as a symposium, poster exhibit, and school, in order to facilitate the exposure of participants to a variety of subjects. An elegant welcome banquet, with the performance of an NCU string-quartet group, was held at the Hotel Kuva Chateau ballroom (Figure 8 and Figure 9). An additional dinner reception with the poster-prize award ceremony was held at the Pine Cone restaurant in NCU. Sunny days and mild warm weather allowed participants to enjoy the museums, shops, restaurants, and environment of Taiwan, including excursion trips to the town of JiuFen (Figure 10), and Taipei 101.

The dinner party was held at the Pine Garden Restaurant, and three poster prizes were awarded. We received more than 50 poster submissions, and with 90%

Figure 8. A concert performance by NCU's string quartet at the welcome banquet.

Figure 7. A group photo taken at NCU during the ISSS-11 meeting.

Figure 9. Participants enjoying their meal at the welcome banquet.

Figure 11a. Poster prize winner Mr. Patricio M. Sepulveda (l).

Figure 11b. Poster prize winner Mr. HaoMing Liang.

submitted by participants from outside of Taiwan, on a wide range of topics. The First Prize winner was Mr. Patricio M. Sepulveda of the Max-Planck Institute; the Second Prize winner was Mr. HaoMing Liang of UCLA; and the Third Prize winner was Ms. Yuni Lee from the University of Maryland (Figure 11).

Figure 10. An excursion trip to JiuFen, a famous touring place in Taiwan.

Figure 11c. Poster prize winner Ms. Yuni Lee.

ISSS-11 was concluded with a wonderful speech given by Prof. Bertrand Lembege. Such a ground-breaking event would not have been possible without the support of several domestic and international organizations, the time and effort of the invited lecturers, the hospitality of the hosts, and the enthusiastic participation of the attendees.

Prof. Lin Ni Hau, Chair of Local Organizing Committee, ISSS-11 2013
National Central University, Jhongli, Taiwan
E-mail: lnhau@jupiter.ss.ncu.edu.tw

Prof. Yoshiharu Omura, Chair International Organizing Committee, ISSS-11 2013
Kyoto University, Kyoto, Japan
Email: omura@rish.kyoto-u.ac.jp

Report on RADIO 2014

Wolmar, Flic-en Flac, 7 - 10 April 2014

Honorable Tassarajen Pillay Chedembrum, Minister of Information and Communication Technology, officially opened the second edition of the Radio and Antenna Days of the Indian Ocean (RADIO 2014), which was held at the Sugar Beach Resort, Wolmar, Flic-en-Flac, from April 7-10, 2014. The conference was organized by the Radio Society, Mauritius. The organizing committee consisted of researchers from the University of Mauritius and the University of Technology, Mauritius. It was chaired by Prof. Vikass Monebhurrun from SUPELEC, France.

For this second edition, RADIO 2014 brought together international experts from 20 different countries, spanning five continents (Australia, Botswana, Brazil, Canada, China, Denmark, France, India, Italy, Mauritius, The Netherlands, Poland, Reunion Island, Russia, South Africa, South Korea, Spain, Switzerland, United Kingdom, and USA).

Keynote speeches were delivered by Prof. Mérouane Debbah, SUPELEC, France; Prof. Steven Tingay, Curtin University, Australia; and Prof. Tapan Sarkar, Syracuse University, USA. The conference featured eleven oral sessions (Figure 1) and one poster session on state-of-the-art research themes, covering antenna design, computational electromagnetics, metamaterials and applications, radio astronomy, electromagnetic compatibility, RF exposure and health, and wireless applications. A gala dinner was held on Wednesday evening (Figure 2).

Figure 1. A Monday morning session.

Figure 2. A sega dance performance at the beach during the gala dinner on Wednesday evening.

Before the closing ceremony of the conference, prizes and certificates were awarded to young scientists and students. Partial support was provided to three young scientists to attend RADIO 2014. First and Second Best Paper prizes were awarded to student participants. We are grateful to our gold sponsors, CST and FEKO, as well as URSI, for their generous support. We are also grateful to IEEE AP-S and URSI for proving technical co-sponsorship.

As for the previous edition, four-page full papers submitted post-conference by the authors and accepted after a peer-reviewing process will be published in the IoP Conference Series: Materials Science and Engineering.

Following the success of RADIO 2014 and numerous requests from foreign delegates, the organizing committee is considering the organization of the next edition of the conference, again in Mauritius, in about a year and one-half.

Vikass Monebhurrun
General Chair, RADIO Conference
E-mail: Vikass.Monebhurrun@supelec.fr;
monebhurrun@supelec.fr

URSI CONFERENCE CALENDAR

August 2014

COSPAR 2014 ("COSMOS")
40th Scientific Assembly of the Committee on Space Research (COSPAR) and Associated Events
Moscow, Russia, 2-10 August 2014
Contact: COSPAR Secretariat, c/o CNES, 2 place Maurice Quentin, 75039 Paris Cedex 01, France, Tel: +33 1 44 76 75 10, Fax: +33 1 44 76 74 37, cospar@cosparhq.cnes.fr, http://www.cospar-assembly.org/

ICEAA 2014 - International Conference on Electromagnetics in Advanced Applications
Palm Beach, Aruba, 3-9 August 2014
Contact: Prof. P.L.E. Uslenghi, Dept. of ECE (MC 154), University of Illinois at Chicago, 851 So. Morgan St., Chicago, IL 60607-7053, USA, E-mail: uslenghi@uic.edu, http://www.iceaa.net/

URSI GASS 2014 - XXXIst General Assembly and Scientific Symposium of the International Union of Radio Science
Beijing, China CIE, 16-23 August 2014
Contact: URSI Secretariat, Sint-Pietersnieuwstraat 4, B-9000 Ghent, Belgium, E-mail: info@ursi.org, http://www.chinaursigass.com and http://www.ursi.org

Metamaterials 2014 - Eight International Congress on Advances Electromagnetic Materials in Microwaves and Optics
Copenhagen, Denmark, 25-28 August 2014
Contact: Prof. R.W. ZIOLKOWSKI, Dept. of Electrical and Computer Engineering, University of Arizona, 1230 E. Speedway Blvd., Tucson, AZ 85721-0104, USA, Fax : +1 520 621-8076, E-mail : ziolkowski@ece.arizona.edu
http://congress2014.metamorphose-vi.org

September 2014

EMC Europe 2014
Gothenburg, Sweden, 1-4 September 2014
Contacts: Symposium Chair: jan.carlsson@sp.se, Technical Program Chair: peterst@foi.se, http://www.emceurope2014.org/
Geospace Revisted 2014
Rhodes, Greece, 15-20 September 2014
Contact: Ioannis A. Daglis, University of Athens, Fax +30 210-7276725, E-mail: iadaglishys.uoa.gr
http://geospacerev.space.noa.gr/index.php

An up-to-date version of this conference calendar, with links to various conference web sites can be found at http://www.ursi.org/en/events.asp

October 2014

RADAR 2014 - International Radar Conference 2014 - "Catching the invisible"
Lille, France, 13-17 October 2014
Contact: Ms. Monique DECHAMBRE, LATMOS, Quartier des Garennes 11, Bd des Garennes F 78280 Guyancourt, France, monique.dechambre@latmos.ipsl.fr and exporadar2014@see.asso.fr
http://www.radar2014.org

November 2014

APMC 2014 – Asia-Pacific Microwave Conference
Sendai, Japan, 4-7 November 2014
Contacts: Prof. Noriharu Suematsu [Chair, Steering Committee] c/o Real Communications Corp., 3F Shinmatsudo S bldg., 1-409 Shinmatsudo, Matsudo 270-0034, Japan, Fax: +81-47-309-3617, E-mail: 2014secrt@apmc2014.org, http://apmc2014.org/

November 2014

APMC 2014 – Asia-Pacific Microwave Conference
Sendai, Japan, 4-7 November 2014
Contacts: Prof. Noriharu Suematsu [Chair, Steering Committee] c/o Real Communications Corp., 3F Shinmatsudo S bldg., 1-409 Shinmatsudo, Matsudo 270-0034, Japan, Fax: +81-47-309-3617, E-mail: 2014secrt@apmc2014.org
http://apmc2014.org/

January 2015

International Conference on Foundations and Frontiers of Computer, Electrical Engineering : commemorating 150 years of Maxwell's Equations
Hooghly, Westa Bengal, India, 9-10 January 2015
Contact: Prof. B.N. Biswas, Sir J.C. Bose School of Engineering, Supreme Knowledge Foundation Group of Institutions, 1, Khan Road, Mankundu, Hooghly-712139, West Bengal, India

May 2015

URSI Mid-Atlantic Meeting 2015
ExpoMeloneras Convention Centre, Gran Canaria, Spain, 18-25 May 2015
Contact: Prof. Peter Van Daele, URSI, Sint-Pietersnieuwstraat 41, B-9000 Gent, Belgium, E-mail: peter.vandaele@intec.ugent.be

News from the URSI Community

NEWS FROM A MEMBER COMMITTEE

FRANCE
Alain Baudry receives 2014 URSI France Medal

On March 25, 2014, during its annual meeting, the URSI France medal was presented to Alain Baudry by Pierre Encrenaz, member of the French Academy of Sciences.

Alain Baudry, born in 1942, is a researcher renowned for the development of radio astronomy in Europe, especially through the foundation of IRAM (Institut de Radioastronomie Millimétrique) in 1979. He also made a major contribution to the development of the Atacama Large Millimeter Array (ALMA) in Chile, now the largest radio interferometer in the world. He made major contributions to the successful observations of the Herschel Space Observatory satellite (in operation from May 2009 to June 2013).

Over a career of more than 40 years at the Observatoire de Bordeaux, he led, in perfect harmony, high-standard research activities and world-level instrumental projects, combining the experience of a researcher and of an engineer. He was at the origin of the first millimeter-wave radio astronomy interferometer, operational in 1973. In 1978, this led to the building of the POM millimeter telescope in Bordeaux, France. In spite of its moderate size (a diameter of approximately 2.5 m), this has been the instrument on which a generation of French mm-wave radio astronomers has been educated. Alain was subsequently solicited by IRAM in 1987 to lead, with other colleagues, the construction of the Plateau de Bure interferometer, in France. He also provided an impulse for the development of mm-wave very-long-baseline interferometry (mm-VLBI), and was at the origin, with a few other European colleagues, of the Joint Institute for VLBI in Europe (JIVE). JIVE, which is located in The Netherlands, processes observations using the European VLBI network. In the years 1990-2000, he managed the development of the high spectral resolution spectrometer of the HIFI instrument for the Herschel Space Observatory of ESA. Subsequently, Alain started and led for Europe the development and production of important parts of the ALMA back-end and correlator subsystems.

Figure 1. Presentation of the URSI France 2014 medal by Pierre Encrenaz to Alain Baudry on March 25, 2014

In parallel to these important instrumentation activities, Alain Baudry led high-level scientific research with international recognition. He supervised a large number of PhD theses, and published over 130 papers in high-impact journals. He became known as an expert in interstellar masers, based on his work on OH/IR stars and on sources in star-formation regions. Among his remarkable contributions, we can cite a 1971 paper that was a precursor of all what will be done in the following decades in terms of stellar formation observed in the far-infrared range, especially regarding the large data collection carried out by Herschel nearly 40 years later. Also in the 1980s were published the first millimeter-wave large-scale detections of the HCO+, HCN, HNC, and CCH interstellar molecules, the analysis of which is important for understanding the physical conditions around stars. Many of his students followed in bright careers with numerous discoveries.

Alain Baudry also helped towards supporting French research through his role as a director of the Laboratory of Astronomy and Astrophysics of the Bordeaux Observatory, as a member of the Scientific Advisory Committee of IRAM, then as a member of the executive board of this Institute, and as a member of the Conseil National des Astronomes et Physiciens, plus many other bodies. He was also Chair of Commission J of URSI France (1984-1992), and took an active part in the URSI General Assemblies of Lille (1996), Toronto (1999), Maastricht (2002), and Istanbul (2011).

Stimulating and co-ordinating, on an international basis, studies, research, applications, scientific exchange, and communication in the fields of radio science

Call for Papers

1st URSI Atlantic Radio Science Conference (URSI AT-RASC)

18 - 25 May 2015

ExpoMeloneras Convention Centre, Gran Canaria

The newly established triennial URSI Atlantic Radio Science Conference (URSI AT-RASC) is the 3rd URSI flagship conference besides the triennial URSI General Assembly and Scientific Symposium and the triennial AP-RASC conference (AsiaPacific Radio Science Conference).

This 1st URSI Atlantic Radio Science Conference will have an open scientific program composed of submitted papers within the domains covered by all ten Commissions of URSI:

Commission A: Electromagnetic Metrology
Commission B: Fields and Waves
Commission C: Radiocommunication and Signal Processing Systems
Commission D: Electronics and Photonics
Commission E: Electromagnetic Environment and Interference
Commission F: Wave Propagation and Remote Sensing
Commission G: Ionospheric Radio and Propagation
Commission H: Waves in Plasmas
Commission J: Radio Astronomy
Commission K: Electromagnetics in Biology and Medicine

Important deadlines

Paper submission
December 15, 2014

Notification
February 28, 2015

Early bird registration
March 31, 2015

Conference start
May 18, 2015

Paper submission Deadline: December 15, 2014

Authors must submit an abstract (minimum of 250 words) electronically by December 15, 2014. Each registered author may present no more than two papers. Organizers of special sessions should send a request to the appropriate commission Chair(s) by October 18, 2014 - details are found on the URSI website. Detailed information on Paper Submission as well as Travel Information will become available through the URSI website: www.at-rasc.org in September 2014. Papers presented at this 1st URSI AT-RASC will be submitted for posting to IEEE Xplore.

In addition, there will be special programs for young scientists, a student paper competition and programs for accompanying persons.

Technical Programme Committee: Prof. P.L.E. Uslenghi, Chair; Prof. P.S. Cannon, Vice-Chair; Dr. W.R. Stone, Publications

Organizing Committee: Prof. P. Lagasse, Chair, Prof. P. Van Daele, Vice-Chair

www.at-rasc.org

Contact:
uslenghi@uic.edu

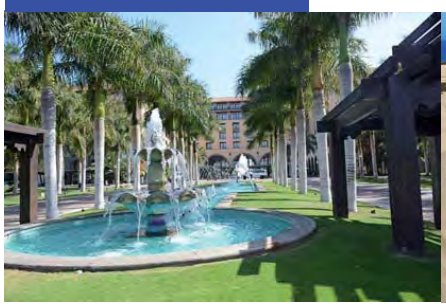

Information for authors

Content

The *Radio Science Bulletin* is published four times per year by the Radio Science Press on behalf of URSI, the International Union of Radio Science. The content of the *Bulletin* falls into three categories: peer-reviewed scientific papers, correspondence items (short technical notes, letters to the editor, reports on meetings, and reviews), and general and administrative information issued by the URSI Secretariat. Scientific papers may be invited (such as papers in the *Reviews of Radio Science* series, from the Commissions of URSI) or contributed. Papers may include original contributions, but should preferably also be of a sufficiently tutorial or review nature to be of interest to a wide range of radio scientists. The *Radio Science Bulletin* is indexed and abstracted by INSPEC.

Scientific papers are subjected to peer review. The content should be original and should not duplicate information or material that has been previously published (if use is made of previously published material, this must be identified to the Editor at the time of submission). Submission of a manuscript constitutes an implicit statement by the author(s) that it has not been submitted, accepted for publication, published, or copyrighted elsewhere, unless stated differently by the author(s) at time of submission. Accepted material will not be returned unless requested by the author(s) at time of submission.

Submissions

Material submitted for publication in the scientific section of the *Bulletin* should be addressed to the Editor, whereas administrative material is handled directly with the Secretariat. Submission in electronic format according to the instructions below is preferred. There are typically no page charges for contributions following the guidelines. No free reprints are provided.

Style and Format

There are no set limits on the length of papers, but they typically range from three to 15 published pages including figures. The official languages of URSI are French and English: contributions in either language are acceptable. No specific style for the manuscript is required as the final layout of the material is done by the URSI Secretariat. Manuscripts should generally be prepared in one column for printing on one side of the paper, with as little use of automatic formatting features of word processors as possible. A complete style guide for the *Reviews of Radio Science* can be downloaded from http://www.ips.gov.au/IPSHosted/NCRS/reviews/. The style instructions in this can be followed for all other *Bulletin* contributions, as well. The name, affiliation, address, telephone and fax numbers, and e-mail address for all authors must be included with

All papers accepted for publication are subject to editing to provide uniformity of style and clarity of language. The publication schedule does not usually permit providing galleys to the author.

Figure captions should be on a separate page in proper style; see the above guide or any issue for examples. All lettering on figures must be of sufficient size to be at least 9 pt in size after reduction to column width. Each illustration should be identified on the back or at the bottom of the sheet with the figure number and name of author(s). If possible, the figures should also be provided in electronic format. TIF is preferred, although other formats are possible as well: please contact the Editor. Electronic versions of figures *must* be of sufficient resolution to permit good quality in print. As a rough guideline, when sized to column width, line art should have a minimum resolution of 300 dpi; color photographs should have a minimum resolution of 150 dpi with a color depth of 24 bits. 72 dpi images intended for the Web are generally *not* acceptable. Contact the Editor for further information.

Electronic Submission

A version of Microsoft *Word* is the preferred format for submissions. Submissions in versions of T_EX can be accepted in some circumstances: please contact the Editor before submitting. *A paper copy of all electronic submissions must be mailed to the Editor, including originals of all figures.* Please do *not* include figures in the same file as the text of a contribution. Electronic files can be send to the Editor in three ways: (1) By sending a floppy diskette or CD-R; (2) By attachment to an e-mail message to the Editor (the maximum size for attachments *after* MIME encoding is about 7 MB); (3) By e-mailing the Editor instructions for downloading the material from an ftp site.

Review Process

The review process usually requires about three months. Authors may be asked to modify the manuscript if it is not accepted in its original form. The elapsed time between receipt of a manuscript and publication is usually less than twelve months.

Copyright

Submission of a contribution to the *Radio Science Bulletin* will be interpreted as assignment and release of copyright and any and all other rights to the Radio Science Press, acting as agent and trustee for URSI. Submission for publication implicitly indicates the author(s) agreement with such assignment, and certification that publication will not violate any other copyrights or other rights associated with the submitted material.

APPLICATION FOR AN URSI RADIOSCIENTIST

I have not attended the last URSI General Assembly, and I wish to remain/become an URSI Radioscientist in the 2012-2014 triennium. Subscription to *The Radio Science Bulletin* is included in the fee.

(please type or print in BLOCK LETTERS)

Name : Prof./Dr./Mr./Mrs./Ms. _____
Family Name First Name Middle Initials

Present job title: _____

Years of professional experience: _____

Professional affiliation: _____

I request that all information be sent to my ☐ home ☐ business address, i.e.:

Company name: _____

Department: _____

Street address: _____

City and postal/zip code: _____

Province/State: _____ Country: _____

Phone: _____ ext._____ Fax: _____

E-mail: _____

Areas of interest (Please tick)

☐ A Electromagnetic Metrology
☐ B Fields and Waves
☐ C Radio-Communication Systems & Signal Processing
☐ D Electronics and Photonics
☐ E Electromagnetic Environment & Interference
☐ F Wave Propagation & Remote Sensing
☐ G Ionospheric Radio and Propagation
☐ H Waves in Plasmas
☐ J Radio Astronomy
☐ K Electromagnetics in Biology & Medicine

I would like to order :

☐ An electronic version of the RSB downloadable from the URSI web site
(The URSI Board of Officers will consider waiving the fee if a case is made to them in writing.) 40 Euro

Method of payment : VISA / MASTERCARD (we do not accept cheques)

Credit card No ☐☐☐☐ ☐☐☐☐ ☐☐☐☐ ☐☐☐☐ Exp. date _____

CVC Code: _____ Date : _____ Signed _____

Please return this signed form to :

The URSI Secretariat
c/o Ghent University / INTEC
Sint-Pietersnieuwstraat 41
B-9000 GHENT, BELGIUM
fax (32) 9-264.42.88